



HAL
open science

Large-scale solar wind properties by Parker Solar Probe and shock-foreshock interaction near the Earth

Mingzhe Liu

► **To cite this version:**

Mingzhe Liu. Large-scale solar wind properties by Parker Solar Probe and shock-foreshock interaction near the Earth. Astrophysics [astro-ph]. Université Paris sciences et lettres, 2022. English. NNT : 2022UPSLO010 . tel-04203265

HAL Id: tel-04203265

<https://theses.hal.science/tel-04203265>

Submitted on 11 Sep 2023

HAL is a multi-disciplinary open access archive for the deposit and dissemination of scientific research documents, whether they are published or not. The documents may come from teaching and research institutions in France or abroad, or from public or private research centers.

L'archive ouverte pluridisciplinaire **HAL**, est destinée au dépôt et à la diffusion de documents scientifiques de niveau recherche, publiés ou non, émanant des établissements d'enseignement et de recherche français ou étrangers, des laboratoires publics ou privés.



THÈSE DE DOCTORAT
DE L'UNIVERSITÉ PSL

Préparée à Observatoire de Paris

**Large-Scale Solar Wind Properties by Parker Solar Probe
and Shock-Foreshock Interaction Near the Earth**

Soutenue par

Mingzhe Liu

Le 06 Décembre 2022

École doctorale n°127

**Astronomie et
astrophysique
d'Île-de-France**

Spécialité

**Astronomie & astro-
physique**

Préparée au

Laboratoire d'Etudes Spatiales et
d'Instrumentation en Astrophysique

Composition du jury :

Philippe SAVOINI Sorbonne Université & LPP/Ecole Polytechnique	<i>Président du jury</i>
Viviane PIERRARD Royal Belgian Institute for Space Aeronomy & Uni- versité catholique de Louvain	<i>Rapporteur</i>
Benoît LAVRAUD Laboratoire d'Astrophysique de Bordeaux, Univer- sité de Bordeaux, CNRS	<i>Rapporteur</i>
Marc PULUPA University of California, Berkeley	<i>Examineur</i>
Yannis ZOUGANELIS European Space Agency	<i>Examineur</i>
Karine ISSAUTIER LESIA, Observatoire de Paris, Université PSL, CNRS	<i>Directeur de thèse</i>

Acknowledgements

First of all, I would like to thank Prof. Karine Issautier to offer me this great opportunity to join her and the QTN team. This thesis would be impossible without her consistent scientific guidance and patient help on the administrative issues throughout the past three years. Also, I greatly appreciate her efforts to organize the group discussions on my work. Again, I would like to express deep gratitude to her for organizing everything besides the scientific supervision during my PhD.

I benefit a lot from the scientific discussions with Prof. Nicole Meyer-Vernet. She can always give me clear explanations on both the basic and complex concepts. Her continuous enthusiasms for science always inspire me to be a good researcher. Thanks a lot for her valuable comments on my work and warm encouragements even for a scientific presentation.

I am very grateful to Prof. Michel Moncuquet for sparing many afternoons in his office to explain and discuss the data analysis. I gain a lot from his knowledge and experience on the data processing. Also, his high-quality QTN datasets make my work much easier.

I would also show thanks to Prof. Milan Maksimovic for his patient help with the SWEAP datasets. I learn a lot from the discussions with him in his office, at the canteen and even at the bar, which removes many of my confusions with the instruments.

Furthermore, I want to thank Prof. Bertrand Lembege from LATMOS, Profs. Zhongwei Yang and Ying Liu from NSSC, Prof. Lynn Wilson III from NASA for productive discussions on shock physics and plasma waves. I also benefit a lot from the discussions on different topics with other collaborators including Jia, Siqi, Xiaowei, Lea, Mihailo, Vamsee, Wenwen, Nicolina, Shuailiang, and Jiuqi. Also, the acknowledgements should be given to Prof. Karl-Ludwig Klein and Prof. Carine Briand for some discussions on the radio emissions and Langmuir waves. Besides, I want to say thanks to Prof. Arnaud Zaslavsky and Prof. Baptiste Cecconi for some discussions on basic data analysis.

I want to thank all the people at LESIA who give me help and enrich my PhD life including Kristina, Sasha, Siyuan, Pietro, Laura, Srivani, Pearse, Etienne, Jean-Bapiste, Alain, Sasi, Lilia, Olga, Sudagar, Goran, Florence, Sylvaine, and Denis. I appreciate Prof. Phillippe Zark and Prof. Vincent Coudé du Foresto for their efforts as members of "Comité de suivi".

I want to acknowledge the FIELDS and SWEAP instrument teams to provide the pioneering solar wind data.

Again, I greatly thank Prof. Filippo Pantellini and Prof. Milan Maksimovic to spare their time to help me prepare for the PhD defense and improve the thesis together with Prof. Karine Issautier. Also, I appreciate the reviewers' nice comments/suggestions to improve the final thesis, and acknowledge all the jury members for their efforts to join my PhD defense.

In the past three years, my girlfriend gave me a lot of help and support in many different ways. Thanks a lot for her inspirations, encouragements, and accompanying the life.

Finally, I would like to thank my mother and my sister for their understanding and support as I have been abroad for several year's further education. Here, I want to memorize my father for his continuous encouragements to pursue my dreams.

Résumé

Le transport d'énergie dans la couronne et le vent solaires, qui n'est pas complètement compris, joue un rôle clé dans le chauffage de la couronne et l'accélération du vent. En raison de leur faible masse par rapport aux ions, les électrons dominent l'expansion thermique du vent solaire. Pour dériver leurs propriétés, la technique du bruit quasi-thermique (QTN) est un outil fiable : elle permet d'obtenir des mesures précises des paramètres des électrons dans le vent solaire, en particulier la densité électronique totale, sans aucun étalonnage. La technique QTN permet donc des vérifications croisées en routine pour les détecteurs de particules traditionnels. La sonde solaire Parker Solar Probe (PSP), en cours d'exploitation, dont les distances héliocentriques des périhélie de l'orbite passent de 35.7 rayons solaires (R_{\odot}) à 9.86 R_{\odot} en l'espace de cinq ans, offre une opportunité inédite d'examiner les propriétés du vent solaire au plus près du Soleil.

Tout d'abord, en utilisant les paramètres des électrons obtenus par la technique simplifiée du QTN et les paramètres des protons déduits des "coupes" de Faraday, nous avons étudié le flux d'énergie du vent solaire aussi près du Soleil que 27.8 R_{\odot} . Nous avons obtenu une valeur moyenne du flux d'énergie similaire aux résultats précédents basés sur des observations à long terme à de plus grandes distances et à diverses latitudes, ce qui confirme que cette quantité apparaît comme une constante solaire globale. De plus, les distributions normalisées du flux d'énergie sont presque symétriques et bien ajustées par des gaussiennes, ce qui implique des interactions limitées entre le vent solaire et les structures transitoires du plasma dans l'héliosphère interne.

Ensuite, nous avons examiné l'évolution radiale de la température totale des électrons (T_e), déduite de la technique du QTN en utilisant la partie haute fréquence des spectres radio, avec la distance héliocentrique variant d'environ 13 à 60 R_{\odot} . Nous obtenons que T_e décroît avec la distance comme $\sim R^{-0.66}$, qui est une variation beaucoup plus lente qu'un comportement adiabatique. La température T_e , basée sur les observations PSP, est cohérente avec la prédiction du modèle de vent solaire exosphérique extrapolé à 10 R_{\odot} , ainsi qu'aux observations Helios à 0.3 UA et aux observations de Wind à 1 UA, respectivement. De plus, lorsque le vent solaire est plus lent (ou dans un tube de flux avec un flux de masse plus important), les profils radiaux de V_p-T_e sont plus raides. Une anticorrélation plus prononcée de V_p-T_e est observée lorsque le vent solaire est plus lent et plus proche du Soleil. En complément, nous avons créé une base de données de spectres affectés par les ondes de Langmuir et/ou les émissions électromagnétiques, qui peut être utilisée pour une analyse plus approfondie et sera aussi utile pour un ajustement en routine sur la totalité du spectre QTN dans le vent solaire.

En plus des propriétés du vent solaire, nous avons étudié un choc interplanétaire (IP) quasi-perpendiculaire supercritique, interagissant avec le pré-choc terrestre. De nouvelles caractéris-

tiques sur les activités des ondes et la dynamique des particules, résultant de l'interaction choc-foreshock, ont été identifiées: (1) Des sursauts d'ondes de Langmuir intenses sont détectées en aval du choc IP, ce qui coïncide avec le fait que les faisceaux d'électrons pénétrant dans le pré-choc terrestre sont accélérés parallèlement au champ magnétique vers l'aval. (2) Le choc IP interagit avec les ondes/fluctuations d'Alfvén en amont, et est associé à un faisceau d'ions réfléchis en giration, d'intensité atypique par rapport à d'autres événements présentant des paramètres de choc similaires. Ces résultats soulèvent des questions et nécessitent des études supplémentaires concernant l'accélération des particules (par exemple par des whistlers précurseurs) et l'interaction choc-ondes d'Alfvén.

Mots clés : Parker Solar Probe, bruit quasi-thermique, vent solaire, chauffage et accélération, choc, ondes

Abstract

Heat transport in the solar corona and wind, which is not completely understood, plays a key role in corona heating and wind acceleration. Due to their small mass compared to ions, electrons dominate the thermally driven solar wind expansion. To derive their properties, the Quasi-thermal noise (QTN) technique is a reliable tool: it yields accurate measurements of the electron parameters in the solar wind especially the total electron density without any calibration. The QTN technique thus provides routine cross checking for traditional particle detectors. The ongoing pioneering Parker Solar Probe (PSP), whose heliocentric distances of orbit perihelia decrease from 35.7 solar radii (R_\odot) to 9.86 R_\odot within five years, offers an opportunity to examine the solar wind properties closer to the Sun than previously detected.

First, based on electron parameters obtained from the simplified QTN technique and the bulk proton parameters by Faraday Cups, we investigate the solar wind energy flux as close to the Sun as 27.8 R_\odot . We obtain that the averaged energy flux value is similar to the previous results based on long-term observations at greater distances and various latitudes, which confirms that this quantity appears as a global solar constant. Furthermore, the normalized energy flux distributions are nearly symmetrical and well fitted by Gaussians, implying the limited interactions between solar wind and transient plasma structures in the inner heliosphere.

Then, we examine the radial evolution of the total electron temperature (T_e), derived from the QTN technique using the high frequency part of the radio spectrum, with the heliocentric distance varying from about 13 to 60 R_\odot . We obtain that T_e decreases with the distance as $\sim R^{-0.66}$, which is much slower than an adiabatic behavior. The extrapolated T_e is consistent with the exospheric solar wind model prediction at around 10 R_\odot , Helios observations at 0.3 AU and Wind observations at 1 AU, respectively. Furthermore, when the solar wind is slower (or in flux tube with larger mass flux), the radial T_e profiles are steeper. More pronounced anticorrelated V_p - T_e is observed when the solar wind is slower and closer to the Sun. As a byproduct, we derive a database of spectra affected by bursty Langmuir waves and/or electromagnetic emissions, which will be useful for further analysis and routine full fit on the QTN spectra.

In addition to the solar wind properties, we study a supercritical quasi-perpendicular interplanetary (IP) shock interacting with the terrestrial foreshock via Wind observations. Some new features of wave activities and particle dynamics, resulting from the shock-foreshock interaction, are identified: (1) Intensive bursty Langmuir waves are detected downstream of the IP shock, coinciding with that the penetrating terrestrial foreshock electron beams are accelerated parallel to the magnetic field toward downstream. (2) The IP shock is interacting with the upstream Alfvén waves/fluctuations, and associated with atypically intensive beam-like gyrating-reflected

ions compared to other events with similar shock parameters. These findings raise questions and trigger further investigations regarding particle acceleration (i.e. through precursor whistlers) and interaction between a shock and Alfvén waves.

Keywords : Parker Solar Probe, Quasi-thermal noise, Solar Wind, heating and acceleration, Shock, Waves

Contents

Acknowledgements	i
Résumé	iii
Abstract	v
Contents	vii
List of Figures	x
List of tables	xviii
1 General Introduction	1
1 The Sun and the Heliosphere	2
1.1 Solar Interior and Atmosphere	2
1.2 Solar Wind and Heliosphere	4
2 General Properties of the Solar Wind	6
2.1 The Solar Wind Components	6
2.2 The Solar Wind Over Solar Cycles	9
2.3 The Solar Wind: A Laboratory for Fundamental Plasma Physics	11
3 Collisionless Shocks in the Heliosphere	15
3.1 Collisional Shocks Versus Collisionless Shocks	15
3.2 Definitions of Collisionless Shock Parameters and Types	16
3.3 General Terrestrial Foreshock Properties	20
4 Electron Quasi-Thermal Noise and Langmuir Waves	24
5 Motivation and Outline of the Thesis	26
2 Spacecraft and Instrumentation	28
1 Parker Solar Probe	29
1.1 FIELDS Instrument Suite	30
1.2 SWEAP Instrument Suite	30
1.3 Radio Frequency Spectrometer/FIELDS	31
2 Wind Spacecraft	37
2.1 Electrostatic Detectors: 3DP	39
2.2 Waves: Radio and Plasma Wave Investigation	40
2.3 Fluxgate Magnetometer: MFI	40

3	Solar Wind Energy Flux Observations in the Inner Heliosphere: First Results from Parker Solar Probe	41
1	Introduction	42
2	Data Analysis	43
2.1	n_α Estimation: Difference Between n_e and n_p	44
3	Observations and Results	45
3.1	Overview of E01, E02, E04 and E05	46
3.2	Distributions of Energy Flux and Variation with Distance	50
4	Discussion and Conclusions	53
4	Total Electron Temperature Derived from Quasi-Thermal Noise Spectroscopy In the Pristine Solar Wind: Parker Solar Probe Observations	55
1	Introduction	56
2	Data Analysis	58
2.1	Determination of T_e from QTN Spectroscopy	58
2.2	Preliminary Cross Checking	61
3	Observations and Results	64
3.1	Mean Radial Profiles of T_e	65
3.2	Temperature gradients for different solar wind populations	68
3.3	Anticorrelated parameters: V_p and T_e	69
4	Summary and Discussion	71
5	Properties of A Supercritical Quasi-perpendicular Interplanetary Shock Propagating in the Terrestrial Foreshock Region	74
1	Introduction	75
2	Observations and Data Analysis	77
2.1	Magnetic Connection between IP shock and Terrestrial Bow shock	77
2.2	Electron Dynamics at Kinetic Scales	81
2.3	Interactions between IP Shock and Alfvén Waves/Fluctuations	86
3	Summary and Discussions	91
5.A	Source of Transient Electron Beam	92
5.B	Exclusion of IP Shock as A Source	94
6	Quasi-Thermal Noise Spectroscopy: Application of Full Fittings on Parker Solar Probe Observations	96
1	Basics of Quasi-Thermal Noise Spectroscopy	97
2	Doppler-shifted Proton Thermal Noise	99
3	Antenna Impedance and Shot Noise	100
4	Gain Factor	101
5	Preliminary Numerical Results and Next Steps	101
6	Database of Spectra Affected by Langmuir Waves and/or Radio Emissions	103
7	Summary and Perspectives	108
1	Solar Wind Energy Flux	109
2	Radial Evolution of the Total Electron Temperature	109
3	Shock Physics	111
4	Full Fittings of the QTN Spectroscopy	112
A	Other Results	114
A.1	Estimation of Coulomb Collisions and Electron Plasma Beta	115

B Publications	118
B.1 Solar Wind Energy Flux Observations in the Inner Heliosphere: First Results from Parker Solar Probe	122
B.2 Total Electron Temperature Derived from Quasi-Thermal Noise Spectroscopy In the Pristine Solar Wind : Parker Solar Probe Observations	130
B.3 Properties of A Supercritical Quasi-perpendicular Interplanetary Shock Propagating in Terrestrial Foreshock Region	141
Bibliography	157
Résumé	177
Abstract	179

List of Figures

1.1	Schematic of the solar interior. This figure is courtesy of the WaLSA team. . . .	3
1.2	Basic structures of the heliospheric interface resulting from the interaction between the Local Interstellar Cloud (LIC) and the solar wind. The heliopause is a contact discontinuity, which separates the plasma of the solar wind from the interstellar plasma. The termination shock decelerates the supersonic solar wind. The bow shock may also exist in the supersonic interstellar wind. The heliospheric interface is thus divided into four regions: 1) supersonic solar wind; 2) subsonic solar wind in the region between the heliopause and termination shock; 3) disturbed interstellar plasma region (or "pileup" region) around the heliopause; 4) undisturbed interstellar medium. This image is adapted from Figure 2.1 in Izmodenov (2004).	5
1.3	A typical example of the 2D cut through 3D Helios ion velocity distribution function (VDF) measured at 0302 UT on March 11th, 1976. The background isocontours are fit to the measured ion VDF, and the magnetic field direction is shown by the dotted line. The ellipses distinguish identified ion populations and their temperature anisotropy. The left-hand panel reflects proton core-beam structure, and the right-hand panel treats all protons as one population, which together demonstrates the proton beam effect on the temperature determination. This image is adapted from Figure 2 in Němeček et al. (2021).	7
1.4	Diagram illustrating different populations of solar wind electrons, including the core, halo, and strahl.	8
1.5	(a–c) Polar plots of the solar wind speed, colored by IMF polarity for the <i>Ulysses</i> ' three polar orbits colored to indicate measured magnetic polarity. In each panel, the earliest times are on the left (nine o'clock position) and progress around counterclockwise. (d) Contemporaneous values for the smoothed sunspot number (black) and heliospheric current sheet tilt (red), lined up to match Figures 1a–1c. In Figures 1a–1c, the solar wind speed is plotted over characteristic solar images for solar minimum for cycle 22 (8/17/96), solar maximum for cycle 23 (12/07/00), and solar minimum for cycle 23(03/28/06). From the center out, images from the Solar and Heliospheric Observatory (<i>SOHO</i>) Extreme ultraviolet Imaging Telescope (Fe XII at 1950 nm), the Mauna Loa K coronameter (700–950 nm), and the <i>SOHO</i> C2 white light coronagraph are superimposed. This image is adapted from Figure 1 in McComas et al. (2008).	10

- 1.6 **(A)** OMNI/Lo helium abundance (A_{He}) as a function of solar wind speed (v_{sw}) and time. A_{He} is split into 10 v_{sw} -quantile, each indicated by a unique color and marker. The legend at the figure's top indicates each quantile's center in km s^{-1} . Within each v_{sw} -quantile, A_{He} is averaged down to 250-day resolution. Error bars indicate the standard error of the mean. The secondary y-axis plots the 13 month smoothed sunspot number (SSN). Vertical dash-dotted purple lines indicate Solar Cycle Minima, which conventionally indicate the start of a new solar cycle. Vertical dotted lines indicate the A_{He} Shutoff date averaged across v_{sw} -quantiles. Blue boxes at the top and bottom of each panel indicate the standard deviation of these shutoff dates. **(B)** Lyman- α ($L\alpha$, left) and F10.7 cm radio emission (right) solar activity indicators over the same period as A_{He} . Within one or two data points, A_{He} **increases across all but the one or two slowest v_{sw} -quantiles prior to plotted SSN Minima**. This image is adapted from Figure 1 in Alterman et al. (2020). 12
- 1.7 Panel (a): monthly solar sunspot number superimposed on *Helios* (green), *Ulysses* (red), and *Wind* (blue) heliocentric latitudes. Panel (b): solar wind speed measured by *Helios* (green), *Ulysses*/SWOOPS (red) and *Wind*/SWE (blue). Panel (c): solar wind energy flux obtained for *Helios*/E1 Plasma Experiment data (green), *Ulysses*/SWOOPS data (red), and *Wind*/SWE data (blue). Speed and energy-flux data are averaged over a solar rotation (taken as 27.2 days) and the energy flux is scaled to 1 AU for *Helios* and *Ulysses*. The time period between the *Helios* and *Ulysses* epochs have been removed. The yellow bands highlight intervals when *Ulysses* and *Wind* encounter very different solar wind conditions and at very different latitudes. This image is adapted from Figure 1 in Le Chat et al. (2012). 13
- 1.8 Cartoon showing examples of shocks in the heliosphere. Magnetic field lines are black, while the locations of shock fronts are labelled in red. The viewer is looking down on the ecliptic plane from above, except for the case of the bow shock interaction with the magnetized body, in which case the viewer is in the ecliptic plane. Arrows represent the flow speed of the solar wind, the Coronal Mass Ejection (CME), the interplanetary medium, or the LISM. This image is adapted from Figure 2.1 in Pulupa (2010). 17
- 1.10 A cartoon example of a possible terrestrial foreshock configuration. The interplanetary magnetic field (IMF) is represented by the dark blue lines, V_{sw} represents the bulk solar wind velocity, $\mathbf{V}_{E \times B}$ is the $\mathbf{E} \times \mathbf{B}$ -drift velocity due to the solar wind convection electric field, and \mathbf{V}_{FAB} is the reflected field-aligned ion beam (FAB) velocity. This figure is courtesy of Plate 1 in Tsurutani and Rodriguez (1981) and Figure 1 in Wilson (2016). 21
- 1.11 Examples of three types of superthermal ion distributions observed in the terrestrial ion foreshock region. (left) Relief plots of count rate in 2D velocity space integrated over $\pm 55^\circ$ of the elevation angle about the ecliptic plane. (Right) Contour plots of constant phase space density in 2D velocity space for the same events shown on left. This figure is adapted from Figure 4 in Parks et al. (2017). 23
- 1.12 Example of the QTN spectrum measured by a wire dipole antenna in a weakly magnetized plasma (*Ulysses*/URAP data in the solar wind). The main plasma parameters that can be deduced are indicated. This figure is adapted from Figure 2 in Meyer-Vernet et al. (2017). 25

1.13	Left: A group of typical thermal noise spectra with well-resolved plasma peaks measured by the PSP/FIELDS/RFS instrument. Right: A group of spectra affected by large-amplitude Langmuir waves from the same instrument.	26
2.1	Parker Solar Probe (PSP) and scientific payloads (Fox et al., 2016). Four instrument suites onboard PSP including Fields experiment (FIELDS) (Bale et al., 2016), Solar Wind Electrons Alphas and Protons investigation (SWEAP) (Kasper et al., 2016), Integrated Science Investigation of the Sun (IS \odot IS) (McComas et al., 2016), and Wide-field Imager for Solar PRobe (WISPR) (Vourlidas et al., 2016) are working together to provide both <i>in situ</i> and remote observations. The perihelia of PSP orbits are designed to decrease from 35.7 solar radii (R_{\odot}) to 9.86 R_{\odot} within five years. Courtesy of JHU/APL.	29
2.2	Detailed location configuration of FIELDS sensors on the Parker Solar Probe spacecraft. The coordinate systems of the spacecraft and the search coil magnetometer (SCM) are indicated in blue and red, respectively. The RFS receives inputs from the V1–V4 electric field antennas and (may also) the single axis medium-frequency (MF) winding of the SCM. The V5 and fluxgate magnetometer sensors on the magnetometer boom are not used as inputs to the RFS. This illustration is adapted from Malaspina et al. (2016) and Pulupa et al. (2017).	32
2.3	RFS block diagram. Inputs to the RFS are shown at the left. The RFS analog and digital sections are physically located on the DCB. This image is adapted from Figure 2 in Pulupa et al. (2017).	33
2.4	RFS signal and noise sources. The vertical axis is in units of the spectral density, referred to the input of the FIELDS HF preamplifiers. The vertical dotted line (19.2 MHz) denotes the upper bound of the RFS bandwidth, and corresponds to the Nyquist frequency at the sampling rate of $f_s = 38.4$ MHz. This image is adapted from Figure 3 in Pulupa et al. (2017).	34
2.5	Orbital trajectories of the Wind spacecraft in the GSE XY plane from November 1, 1994 to June 1, 2016. Colors denote time ranges as indicated. The dashed black circle indicates the lunar orbit. Note that the Wind orbit has not noticeably changed since June 1, 2016. This image is adapted from Figure 1 in Wilson et al. (2021).	37
2.6	Wind spacecraft and scientific payloads. <i>Wind</i> instruments can be divided into two categories: field and particle suites. Courtesy of Harten and Clark (1995).	38
3.1	Estimate of the difference between n_e measured by QTN and n_p measured by SPC (black dots): panels (a), (b), (c) and (d) show the results of encounters E01, E02, E04 and E05, respectively. Based on plasma neutrality, n_{α} shown in the figure is obtained with $n_{\alpha} = (n_e - n_p)/2.0$. On each panel, the expected values of n_{α}/n_e (from 1 % to 4 %, shaded areas) are plotted for reference (Alterman et al., 2020).	45
3.2	Solar wind density, speed and energy flux measurements by PSP during Encounter One (from 10/31/2018 00:00:00 to 11/12/2018 00:00:00 UTC). First panel: QTN electron density. Second panel: proton bulk speed. A red horizontal line ($V_p = 300$ km s $^{-1}$) is plotted for reference. Third panel: solar wind energy flux W . Fourth panel: solar wind energy flux normalized to one solar radius $W_{R_{\odot}}$ (black) with a red horizontal line ($W_{R_{\odot}} = 70$ W m $^{-2}$) superimposed for reference. The heliocentric distance (in unit of Solar radius R_{\odot}) is indicated at the top of the first panel and the black vertical line denotes the perihelion of the PSP orbit.	46

3.3	Solar wind density, speed and energy flux measurements by PSP for Encounter Two (03/30/2019 00:00:00 to 04/11/2019 00:00:00 UTC). This figure follows the same format as that of Figure 3.2.	47
3.4	Solar wind density, speed and energy flux measurements by PSP for Encounter Four (from 01/23/2020 00:00:00 to 02/04/2020 00:00:00 UTC), which follows the same format as that of Figure 3.2.	48
3.5	Solar wind density, speed and energy flux measurements by PSP for Encounter Five (from 06/01/2020 00:00:00 to 06/13/2020 00:00:00 UTC), which follows the same format as that of Figure 3.2.	49
3.6	Distributions of the solar wind energy flux (W_R) normalized to one solar radius with a ratio between α particle number density (n_α) and electron number density (n_e) ranging from 1% to 4% for Encounters E01, E02, E04 and E05. Figs (a), (b), and (c) assume $n_\alpha/n_e = 1\%$, 2.5% , and 4% , respectively to illustrate the uncertainty due to the absence of α measurements. Average and median values of each histogram are indicated with Gaussian fits superimposed in blue. Center value and standard deviation (full-width-half-maximum) of the Gaussian fit are also presented.	50
3.7	Variation of W and its components with heliocentric distance combining observations from Encounter One (E01), Two (E02), Four (E04) and Five (E05). From top to bottom, evolution of W , $W_{kinetic}/W$, $W_{enthalpy}/W$, and W_g/W with heliocentric distance are shown, respectively. The fitted profile (yellow) is superimposed on each corresponding panel, respectively.	52
4.1	Example of a voltage power spectrum (between 100 kHz and 10 MHz) recorded by the RFS receiver using the $ V1-V2 $ dipole electric antennas from FIELDS instrumentation (full black curve connected by crosses). The dot-dashed line gives the position of the local plasma peak (Moncuquet et al., 2020). The dotted horizontal line represents the pre-deployment RFS instrument noise (after launch) of $\sim 2.2 \times 10^{-17} \text{ V}^2\text{Hz}^{-1}$. The black dashed line shows the modelled radio galaxy noise. The blue and green lines represent the effective QTN signal and linear fit (f^{-3} variation that the QTN spectrum should follow when $f \gg f_p L_D/L$), respectively. The black dots on the blue line are used to derive the linear fit. The red line is the sum of the fitted QTN signal, the modelled radio galaxy noise and the instrument noise. The details are described in the text.	62

4.2	<p>Comparison of observations of solar wind electron temperatures derived from different methods on Parker Solar Probe (PSP). An example of 12-day measurements by PSP during Encounter One (from October 31, 2018 00:00:00 to November 12, 2018 00:00:00 UTC) is shown for reference. The heliocentric distance (in units of the solar radius R_{\odot}) is indicated at the top of the top panel and the black vertical line denotes the first perihelion of the PSP orbit. From the top to bottom panels, the total electron temperature derived from the linear fit QTN technique is displayed in black. In the top panel, the total electron temperature obtained by fitting the high-frequency part of the spectrum with the generalized Lorentzian QTN model (Maksimovic et al., 2020) is shown in blue for comparison. The bottom panel follows the same format as the first panel but for the core electron temperature derived from the simplified QTN technique (Moncuquet et al., 2020). The proton bulk speed from SPC/SWEAP is presented in the top panel for reference. An anticorrelation between V_p and T_e, which was also previously reported (Maksimovic et al., 2020), is visible during the time interval considered. Note that we have already smoothed $T_{e,QTN}(\text{Linear})$, $T_{c,QTN}$ and $T_{e,QTN}(\text{Kappa})$, so that the comparison between them is clear.</p>	63
4.3	<p>Radial variation of the total electron temperature (T_e) combining observations from Encounter One (E01) to Ten (E10) with E08 excluded. From top to bottom, T_e was fitted with the power law expression $T_e = T_0 \times (R/R_{\odot})^{\beta}$ (purple) and the expression given by the large distance exospheric solar wind model $T_e = T_0 + T_1 \times (R/R_{\odot})^{-4/3}$ (red), respectively. The fitted profile and expression with corresponding color are superimposed for comparison. The variations of the free parameters in the fitted expressions are the corresponding 1-sigma ($1-\sigma$) fit uncertainties. The vertical error bars indicate the $2-\sigma$ fit uncertainties, which in total covers about 95% data points.</p>	65
4.4	<p>(a)–(c): Histograms of the total electron temperature (T_e) scaled to 10 solar radii, 0.3 AU and 1 AU, based on observations displayed in Figure 4.3 and their corresponding power law modelling fit results. Gaussian fit is superimposed in blue on each histogram. The corresponding average and median values are also indicated together with the center value and $1-\sigma$ standard deviation of the Gaussian fit. . .</p>	68
4.5	<p>(a) We define the four wind families based on the proton bulk speed histogram. Each colored histogram has the same number of observations. (b) Outcome of the power law modelling in the form $T_e = T_0 \times (R/R_{\odot})^{\beta}$ for total electron temperature: β versus V_p. More details are described in the main text.</p>	69
4.6	<p>Follows the same format as Figure 4.5 but for the solar wind mass flux.</p>	70
4.7	<p>(a) 2-D histogram ditribution of T_e versus V_p with the color bar on the right side indicating the number of data points. Both the mean (red curve) and median values (black curve) are superimposed for reference. A clear anticorrelated (V_p, T_e) is displayed. (b) We define the four wind families based on the heliocentric distance histogram. Each colored histogram has the same number of observations. (c) Relation between V_p and T_e for each wind family, as defined in panel (b). The results are displayed in the same color as the corresponding heliocentric distance histogram in panel (b). More details are described in the main text.</p>	70

-
- 5.1 (Left) The *Wind* satellite orbits in the XY plane of Geocentric Solar Ecliptic (GSE) coordinate reference frame from 00:00:00 on September 10th, 1999 UTC to 12:00:00 on September 12th, 1999 UTC. The black solid line denotes the spacecraft trajectory. The empirical model bow shock (red solid line, see Peredo et al. (1995)) and magnetopause (blue solid line, see Roelof and Sibeck (1993)) are plotted for reference. The triangle and diamond respectively mark the start and end of *Wind* trajectory. The asterisk denotes the position where an IP shock was detected by *Wind*. The black arrows represents the projection of the average magnetic field vectors between the terrestrial bow shock and the IP shock. (Right) The *Wind* observations which correspond to the trajectory shown in the left. From top to bottom, the panels show the magnetic field magnitude, magnetic field components in GSE coordinate, pitch-angle distribution of 265 eV electrons obtained from the EESA-Low instrument onboard *Wind*/3DP, and electric field voltage dynamic spectrum from TNR onboard *Wind*/WAVES. The red and yellow dashed vertical lines mark the crossing of the terrestrial bow shock and the IP shock, respectively. 77
- 5.2 Five-hour expanded view of measurements from *Wind* around the IP shock detected at 03:57:56 on September 12th, 1999 UT. From top to bottom, the panels show the electron field voltage power spectrum from TNR onboard *Wind*/WAVES, omni-directional electron flux, electron flux at different pitch angles including the ones parallel, perpendicular and anti-parallel to the ambient magnetic field, and the ratio of the parallel to the perpendicular flux. For electron flux at different pitch angles, they are derived from the measurements by the EESA-Low instrument onboard *Wind*/3DP, and electrons from about 6 eV to 1106 eV are considered. The labelled energies have been corrected by considering the spacecraft potential. The red vertical line marks the time when the IP shock was detected. 80
- 5.3 Evolution of the stacked line plot of the pitch-angle distributions at the nine highest energies (after correcting the spacecraft potential) from the EESA-Low instrument onboard *Wind*/3DP. The top/bottom panel of each figure shows the electron pitch angle distribution of number/energy flux. The physical units are: the number flux is set in ($\#s^{-1}sr^{-1}cm^{-2}eV^{-1}$) and the energy flux is set in ($eVs^{-1}sr^{-1}cm^{-2}eV^{-1}$). 82
- 5.4 Wavelet analysis of the magnetic field measurements around the IP shock. From top to bottom, the panels show the magnetic field magnitude, GSE components of the magnetic field, wavelet analysis of the magnetic field magnitude $|B|$ and components including B_x , B_y and B_z respectively. The frequency range of the wavelet analysis is from 0.01 Hz to 5.5 Hz. The two blue arrows in panel (a) indicate the foot (left) and overshoot (right) structures, respectively. The white arrows in panels (c-f) indicate the precursor whistlers. The red vertical line marks the IP shock. In panels (c-f), the local proton cyclotron frequency (black horizontal line) and the 1/2 lower hybrid frequency (red horizontal line) are plotted for reference. 84

5.5	An example of MV analysis of the waves during the time period of 03:57:55 UT~03:57:57 UT (2.0 Hz <f <4.0 Hz in the spacecraft frame, ratio of the intermediate to minimum eigenvalues $\lambda_2/\lambda_3=59.71$, ratio of the maximum to intermediate eigenvalues $\lambda_1/\lambda_2=1.110$, $\hat{K}_{GSE} = [0.96715, 0.06149, -0.24665]$, $\theta_{kB} = 53.7^\circ$ (or 126.3°), $\theta_{kn} = 14.2^\circ$ (or 165.8°), $\theta_{kV} = 12.4^\circ$ (or 167.6°)). The hodograms in GSE and MV coordinates are shown. The [X, Y, Z]-MV coordinates represent the directions parallel to the minimum, intermediate and maximum variance eigenvectors, respectively. The projections of magnetic field (B) and wave vector (K) point outward of the paper.	85
5.6	From top to bottom, the panels show (a) the comparison between the magnetic field strength and the proton number density, (b-d) the comparison between X (Y, Z) component of magnetic field and proton bulk velocity in the GSE coordinate, (e) the proton plasma β_p , (f) the proton temperature anisotropy (black) with thresholds of ion cyclotron (red) and mirror-mode (blue) instabilities for comparison, (g) the compressibility (black) and alpha abundance (red), and (h) the cross-helicity, respectively. The red vertical line marks the IP shock propagating in the terrestrial foreshock region. The region denoted by the two blue dashed vertical lines downstream of the IP shock shows mirror mode features. More details about thresholds of ion cyclotron and mirror-mode instabilities are described in the main text.	87
5.7	Evolution of the ion distributions (in the solar wind frame) across the shock ramp obtained from the PESA-High/3DP instrument. The solar wind bulk flow velocities, which are used to transform particle distributions into the bulk flow rest frame, were determined from the measurements by the PESA-Low/3DP instrument. (a) Plot of a 20-second window of the magnetic field magnitude (11 samples/sec) around the IP shock. Foot-like magnetic enhancement (red curve) associated with precursor whistlers and magnetic overshoot can be clearly identified near the shock ramp. (b-d) Ion distributions corresponding to the time ranges of three color-coded shaded regions in panel (a). The contours show constant phase space density in the plane containing the ambient magnetic field (horizontal axis) and local solar wind velocity. Projected onto the planes are the following: shock normal direction (dashed red line), shock surface (solid red line), and solar wind velocity direction (solid black line). Gyration ions are indicated by the black arrows.	90
5.8	Five-hour expanded view of electron flux measurements, from the EESA-Low instrument onboard <i>Wind</i> /3DP, around the IP shock. From top to bottom, the panels show electron flux (from about 6 eV to 1106 eV) at parallel, sunward, antiparallel, and antisunward directions, respectively. The labelled energies have been corrected by considering the spacecraft potential. The red vertical line marks the time when the IP shock was detected.	93
5.9	Follows the same format as Figure 5.8 but for a 2-minute expanded view of electron flux measurements around the IP shock. Note that only the burst-mode particle dataset is considered in this plot.	95

6.1	A preliminary theoretical quasi-thermal noise (QTN) spectrum (blue line for the total noise) for the PSP/FIELDS/RFS. Three main different contributions are included: the electron QTN (yellow line), the doppler-shifted proton noise (green line), and the shot noise (red line). The electron QTN is calculated using a sum of two isotropic Maxwellians: a core and a halo. The solar wind parameters shown on the figure are: the total electron number density (n_e), the ratio of the halo to core electron number density ($n = \frac{n_h}{n_c}$), the ratio between the halo and core electron temperature ($t = \frac{T_h}{T_c}$), the core electron temperature (T_c), the proton temperature (T_p), and the proton bulk speed (V_{sw}).	102
6.2	Examples of electric field voltage spectra recorded by the PSP/FIELDS/RFS instrument. (a) A group of typical clean quasi-thermal noise (QTN) spectra with well-resolved plasma peaks. (b) A group of electric field voltage spectra affected by bursty Langmuir waves (near f_{pe}), unusual pollutions ($f \geq f_{pe}$), and LF plasma waves and/or dust impacts ($f < f_{pe}$). (c) A group of electric field voltage spectra affected by weak solar radio emissions ($f \gg f_{pe}$), and LF plasma waves and/or dust impacts ($f < f_{pe}$). (d) A group of electric field voltage spectra affected by strong solar radio emissions ($f \geq f_{pe}$), and LF plasma waves and/or dust impacts ($f < f_{pe}$).	104
6.3	A typical example of the identified spectrum disturbed by intensive Langmuir waves. The dataset is from PSP/FIELDS/RFS instrument.	105
6.4	(Left) Shape of an example Type III solar radio burst. The white crosses (red dots) are the lower bound (upper bound) frequency of the solar radio emissions on each spectrum. (Right) Radio spectrogram at the same time interval by combining all the frequency channels, which is adapted from Pulupa et al. (2020). The datasets are from PSP/FIELDS/RFS instrument.	106
A.1	Radial variation of the proton bulk speed (V_p), electron plasma beta (β_e), collision age (A_e), and Knudsen number (λ_{fp}/L_T), combining 12-day Parker Solar Probe observations around each perihelion from E01 to E07. For each panel, both the mean (black crosses) and median (red crosses) values of each radial bin are superimposed for reference.	116

List of tables

3.1 Energy Flux Average Value of Each Encounter 49

5.1 *Wind*/3DP Electron Parameters from EESA-Low Burst Mode Data. 86

Chapter 1

General Introduction

Objectives

This chapter gives an extremely brief and broad review about the Sun to introduce the corona heating problem, the concept of the solar wind, and the heliosphere. In particular, we make a brief summary about some general and basic solar wind properties relevant to this thesis. Moreover, we highlight some fundamental plasma processes in the solar wind, such as collisionless shocks, turbulence, magnetic reconnection, and plasma instabilities, to show the key questions on this environment. Since one part of the thesis concerns the Shock-Foreshock interaction near the Earth, we introduce collisionless shocks in the heliosphere, and give a short description about the basic physical picture of the terrestrial foreshock. Furthermore, the electron quasi-thermal noise and bursty Langmuir waves resulting from plasma instabilities are discussed. Finally, the motivation and outline of the thesis are given.

Contents

1	The Sun and the Heliosphere	2
1.1	Solar Interior and Atmosphere	2
1.2	Solar Wind and Heliosphere	4
2	General Properties of the Solar Wind	6
2.1	The Solar Wind Components	6
2.2	The Solar Wind Over Solar Cycles	9
2.3	The Solar Wind: A Laboratory for Fundamental Plasma Physics	11
3	Collisionless Shocks in the Heliosphere	15
3.1	Collisional Shocks Versus Collisionless Shocks	15
3.2	Definitions of Collisionless Shock Parameters and Types	16
3.3	General Terrestrial Foreshock Properties	20
4	Electron Quasi-Thermal Noise and Langmuir Waves	24
5	Motivation and Outline of the Thesis	26

1 The Sun and the Heliosphere

1.1 Solar Interior and Atmosphere

The Sun, the star of our solar system, is a middle-aged (~ 4.5 billion years), G-type, and main sequence star. It is a huge and massive ball of hot plasma, comprising around 99% of the total mass of the solar system (Woolfson, 2000). The chemical elements compositions of the Sun are primarily hydrogen ($\sim 75\%$), helium ($\sim 24\%$), and some other heavier elements (see Lodders, 2003; Hansen et al., 2004, and references therein). As is displayed in Figure 1.1 (top), the solar interior consists of layered structures, creating and radiating energy as light and other radiations out to the solar system. From the center to the surface, the layered structures are: the core, the radiative zone, convection zone, and the photosphere. The core of the Sun dominates the region from the center to $\sim 0.2\text{--}0.25$ solar radii (R_{\odot}) (García et al., 2007). The extremely high temperature¹ (~ 15 million Kelvin) and high pressure in the solar core region can convert the hydrogen into helium through nuclear fusion (Broggini, 2003), which produces a huge amount of thermal energy and drives the Sun to work. The region from the core out to about $\sim 0.7 R_{\odot}$ is the radiative zone where thermal radiation is the primary way to transfer energy, and the temperature decreases from ~ 7 million to ~ 2 million Kelvin². The convection zone (from $\sim 0.7 R_{\odot}$ to near the surface) of the Sun transfer the energy outward towards the solar surface (the photosphere) via a thermal convection process. We note that there is a thin transition layer, between the radiative zone and the convection zone, called the tachocline (Tobias, 2005). Specifically, the solar plasma heated at the tachocline carries energy to the solar surface and cools down. Then, the plasma with low temperature beneath the photospheric surface sinks back to the tachocline to start the convective cycle again. From the convection zone to the photospheric surface, the temperature drops to $\sim 5,700$ Kelvin.

Above the the photosphere, it is the surrounding solar atmosphere which consists of four distinct parts. From bottom to top, they are the chromosphere, the transition region, the corona, and the heliosphere. The chromosphere and the low solar corona are pointed out in Figure 1.1 (top). Figure 1.1 (bottom) shows the typical variation of the temperature versus the height of the solar atmosphere above the photospheric surface. There is a temperature minimum region ($\sim 4,100$ Kelvin) at about 500 km above the photosphere (Abhyankar, 1977; Solanki et al., 1994). The chromosphere is above the temperature minimum layer and extends about 2,000 km. Within the chromosphere, the temperature gradually increases with height and can reach around 20,000 Kelvin beneath the top (Edlén, 1945; Abhyankar, 1977; Solanki et al., 1994; Erdélyi and Ballai, 2007). Surprisingly, in a very thin (~ 200 km) transition region following the chromosphere, there is a very steep and sharp temperature increase from around 20,000 Kelvin in the upper chromosphere to ~ 1 million Kelvin in the low corona (Erdélyi and Ballai, 2007). This is the so-called corona heating problem, which still remains one of the most challenging problems of space/solar physics. The extremely high temperature in the solar corona contributes to produce a flow of plasma particles with a sufficient speed to overcome

1. <https://solarscience.msfc.nasa.gov/interior.shtml>

2. 1

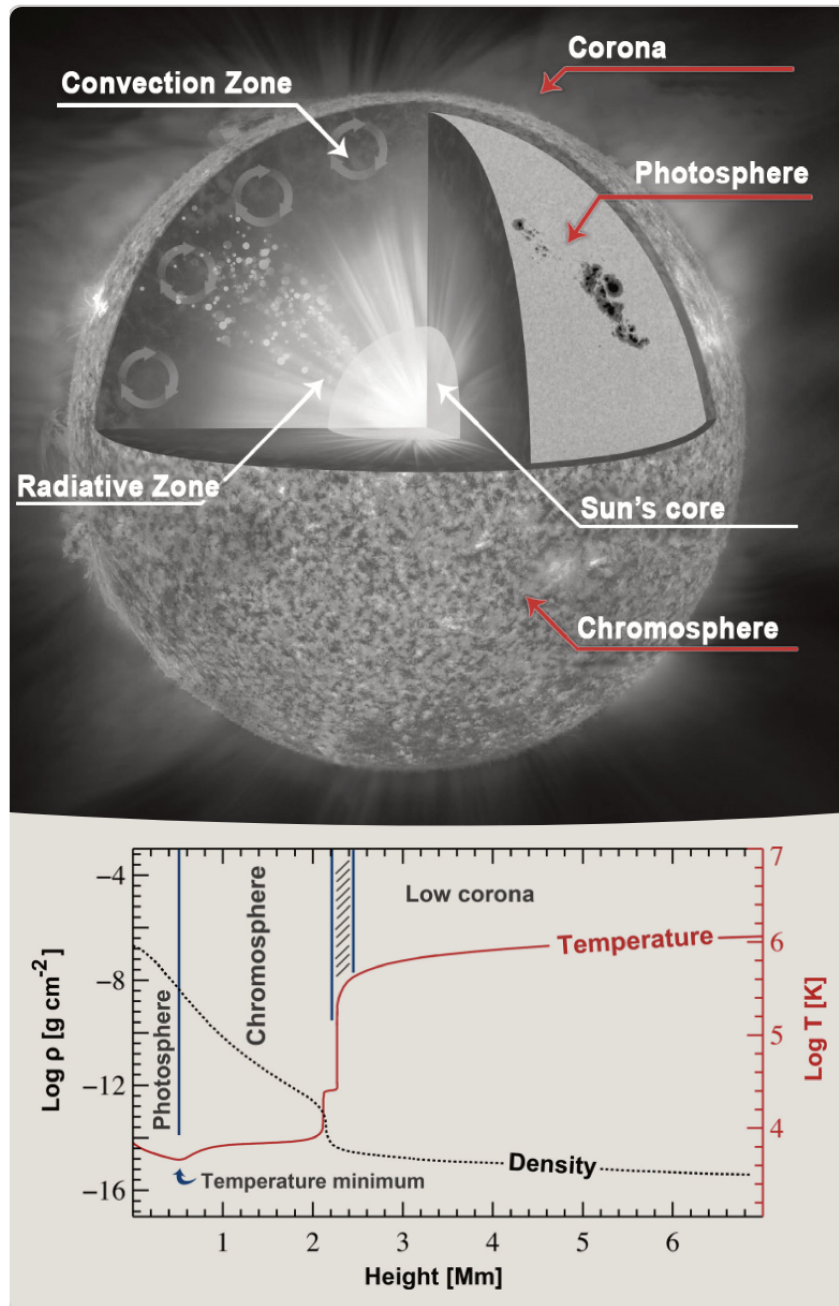


Figure 1.1 – (Top) Schematic of the solar interior. (Bottom) Variation of the temperature with respect to the height of the solar atmosphere above the photospheric surface. The thin layer with filled slashes denotes the transition region between the chromosphere and the low corona. This figure is courtesy of the [WaLSA team](https://walsa.team)^a.

^a. <https://walsa.team>

the Sun’s massive gravitational potential and escape into the interplanetary space. The steady flow of plasma expanding from the Sun and then into interplanetary space is the solar wind, which was theoretically predicted by E. Parker (Parker, 1958a; Parker, 1958b; Parker, 1965), and then confirmed by spacecraft measurements around 1960’s (Neugebauer and Snyder, 1962; Neugebauer and Snyder, 1966).

The outermost layer of the solar corona is defined to begin at the Alfvén surface (see Dwivedi and Parker, 2003; Emslie and Miller, 2003; Liu et al., 2021b; Kasper et al., 2021, and references therein). The Alfvén critical surface is at locations where the solar wind speed surpasses the local Alfvén speed, which is not smooth but rugged. The distance of the Alfvén critical surface locates at $\sim 10 R_{\odot}$ to $\sim 20 R_{\odot}$ (eg., Kasper et al., 2021; Liu et al., 2021b). Furthermore, this surface also differentiate the hot coronal plasma still connected to the Sun and the free-streaming solar wind in the interplanetary space. It is still unclear about the origin and acceleration of the solar wind, which is closely related to the unsolved corona heating problem mentioned above. Until now, several explanations about the energy sources to heat the corona are proposed including, among them, Alfvén waves (eg., Erdélyi and Ballai, 2007; De Pontieu et al., 2007; Chandran and Hollweg, 2009), magnetic reconnection (eg., Erdélyi and Ballai, 2007; Russell, 2001; Edmondson et al., 2009), and velocity filtration to explain high-corona temperatures from generalized Lorentzian electron distribution function (Scudder, 1992). This kind of distribution was introduced to explain high-energy tail in the solar wind and taken into account in exospheric models to enlighten basic mechanisms of the solar wind acceleration (e.g., Maksimovic et al., 1997; Meyer-Vernet and Issautier, 1998; Issautier et al., 1999a; Issautier et al., 2001a; Zouganelis et al., 2004; Pierrard et al., 2001; Pierrard and Pieters, 2014; Voitcu et al., 2014; Pierrard and Pieters, 2014). All these proposed mechanisms partially contribute to understand the corona heating and wind acceleration, but the final answer still remains debated.

1.2 Solar Wind and Heliosphere

In section 1.1, an extremely brief description about the Sun was made to introduce the corona heating problem and the concept of the solar wind. As is shown in Figure 1.2, the solar wind originates from the hot solar corona, expands supersonically into the interplanetary space, and terminates at the heliopause. The region filled with the steady flow of solar wind plasma and dominated by the solar influence is called the heliosphere (see Region 1&2 in Figure 1.2). Here, the inner heliospheric boundary is considered to be the Alfvén critical surface mentioned in section 1.1. The complex structure of the outer heliosphere and heliospheric interface is determined by the interaction between the solar wind and the Local Interstellar Cloud (LIC) (Izmodenov, 2004). As illustrated in Figure 1.2, from Region 1 to Region 2, the supersonically travelling solar wind is decelerated to subsonic speeds at the termination shock. From Region 4 to Region 3, the Local Interstellar Medium (LISM) plasma is decelerated to subsonic speeds at the heliospheric bow shock. The heliopause (boundary of Region 2&3 in Figure 1.2) separates the plasma flows of the LISM and the solar wind. Until now, the Voyager mission are the first and only human-made objects which crossed the termination shock (e.g., Burlaga et al., 2005; Burlaga et al., 2008; Decker et al., 2005), flew beyond the heliopause and entered the interstellar

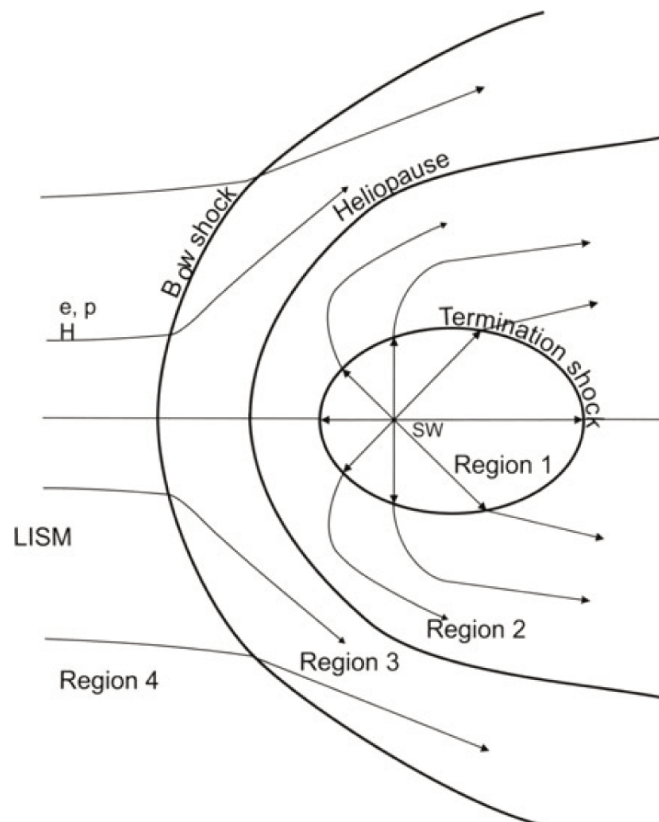


Figure 1.2 – Basic structures of the heliospheric interface resulting from the interaction between the Local Interstellar Cloud (LIC) and the solar wind. The heliopause is a contact discontinuity, which separates the plasma of the solar wind from the interstellar plasma. The termination shock decelerates the supersonic solar wind. The bow shock may also exist in the supersonic interstellar wind. The heliospheric interface is thus divided into four regions: 1) supersonic solar wind; 2) subsonic solar wind in the region between the heliopause and termination shock; 3) disturbed interstellar plasma region (or "pileup" region) around the heliopause; 4) undisturbed interstellar medium. This image is adapted from Figure 2.1 in Izmodenov (2004).

space (e.g., Richardson, 2013; Ocker et al., 2021; Croswell, 2021). Furthermore, the behavior of the heliosphere is intimately related to the periodic solar activities (e.g., the ~ 11 -year periodic flip of the solar magnetic poles), which is described in section 2.2.

2 General Properties of the Solar Wind

Since the prediction and discovery of the solar wind around 1960's (Parker, 1958a; Parker, 1958b; Parker, 1965; Neugebauer and Snyder, 1962; Neugebauer and Snyder, 1966), numerous spacecraft measurements have greatly improved our understanding about the solar wind properties. In this section, we make a brief introduction about some general and basic solar wind properties relevant to this thesis.

2.1 The Solar Wind Components

The solar wind is composed of electrons and ions (protons, alpha particles, and other minor heavy ions). The protons contribute to most of the solar wind mass, and the minor constituents can change the mean particle mass by at most 20% (Meyer-Vernet, 2007). The solar wind ion and electron properties have been examined with *in situ* spacecraft measurements for decades after the solar wind charged particles were confirmed to emanate continuously from the Sun (Neugebauer and Snyder, 1962; Neugebauer and Snyder, 1966). In particular, massive knowledge about the features of ion and electron velocity distributions have been achieved.

Ion Properties Figure 1.3 (left) gives a typical example of ion velocity distribution function (VDF) measured by the Helios spacecraft (Schwenn et al., 1975; Němeček et al., 2021). The solar wind ion distributions consist of three main typical populations: proton core, proton beam, and alpha particles. The whole proton distributions often deviate from the Maxwellian thermal equilibrium due to the role of the field-aligned proton beam. The field-aligned proton beam streams much faster than the proton core component along the direction parallel to the magnetic field. The speed difference between them is typically of the order of the local Alfvén speed (e.g., Asbridge et al., 1974; Feldman et al., 1974; Marsch et al., 1982; Goldstein et al., 2000; Tu et al., 2004; Alterman et al., 2018; Verscharen et al., 2019). By comparing the left-hand panel and the right-hand panel of Figure 1.3, the proton core component and the field-aligned proton beam should be treated separately. Otherwise, the temperature parallel to the magnetic field will be overestimated since the energy related to the large relative drift velocity between the beam and the core is considered as thermal energy. As is shown in Figure 1.3 (left), the alpha particles drifting with respect to the proton core component are also often observed, and the relative drifting speed is also of the order of the local Alfvén speed (e.g., Asbridge et al., 1974; Marsch et al., 1982; Verscharen et al., 2019). Furthermore, the proton distributions often display temperature anisotropy, i.e. $T_{p\perp}/T_{p\parallel} \neq 1$, where $T_{p\perp}$ and $T_{p\parallel}$ is the temperature perpendicular and parallel to the magnetic field direction, respectively. The proton distribution anisotropies seem to be constrained by mirror mode and/or ion cyclotron instabilities (upper bound), and firehose instabilities (lower bound) (e.g., Gary et al., 1997; Gary and Lee, 1994; Kasper et al.,

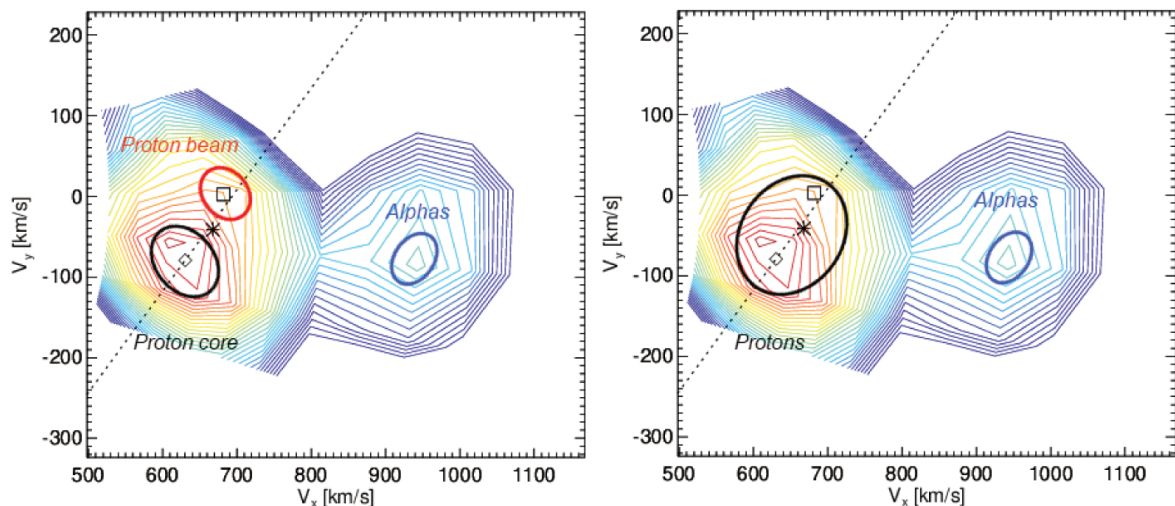


Figure 1.3 – A typical example of the 2D cut through 3D Helios ion velocity distribution function (VDF) measured at 0302 UT on March 11th, 1976. The background isocontours are fit to the measured ion VDF, and the magnetic field direction is shown by the dotted line. The ellipses distinguish identified ion populations and their temperature anisotropy. The left-hand panel reflects proton core-beam structure, and the right-hand panel treats all protons as one population, which together demonstrates the proton beam effect on the temperature determination. This image is adapted from Figure 2 in Němeček et al. (2021).

2002; Hellinger et al., 2006; Liu et al., 2006a; Liu et al., 2007; Liu et al., 2006b; Liu, 2007; Liu et al., 2018; Huang et al., 2020).

Electron Properties Although the electrons contribute much less to the solar wind mass than the ions do, the electrons still play a key role in the solar wind thermodynamics. Due to the large mass difference between ions and electrons, electrons mainly transport energy whereas ions transport momentum. Therefore, it is believed that electrons play a key role in the thermally driven solar wind expansion. Typically, the electron distribution are often made of three distinct populations including core, halo, and strahl components (e.g., Feldman et al., 1975; Rosenbauer et al., 1977; Pilipp et al., 1987; Lin, 1998; Maksimovic et al., 2000; Pierrard et al., 2001; Gosling et al., 2001; Salem et al., 2003; Maksimovic et al., 2005a; Štverák et al., 2008; Štverák et al., 2009; Verscharen et al., 2019). Figure 1.4 shows an illustration of typical electron distributions in the solar wind. The top row presents the 2D view of the eVDFs in the solar wind bulk flow rest frame, projected in the plane containing the directions parallel (horizontal axis) and perpendicular (vertical axis) to the ambient magnetic field. The bottom row presents the corresponding parallel cuts of the distributions which highlights each component. The basic and primary properties of the three distinctive electrons populations are summarized below:

- **Thermal core:** The core is usually well described by a bi-Maxwellian distribution (e.g., Feldman et al., 1975; Rosenbauer et al., 1977; Pilipp et al., 1987; Lin, 1998; Maksimovic et al., 2000; Gosling et al., 2001; Salem et al., 2003; Maksimovic et al., 2005a; Štverák et al., 2008; Štverák et al., 2009; Verscharen et al., 2019). The primary cool thermal core

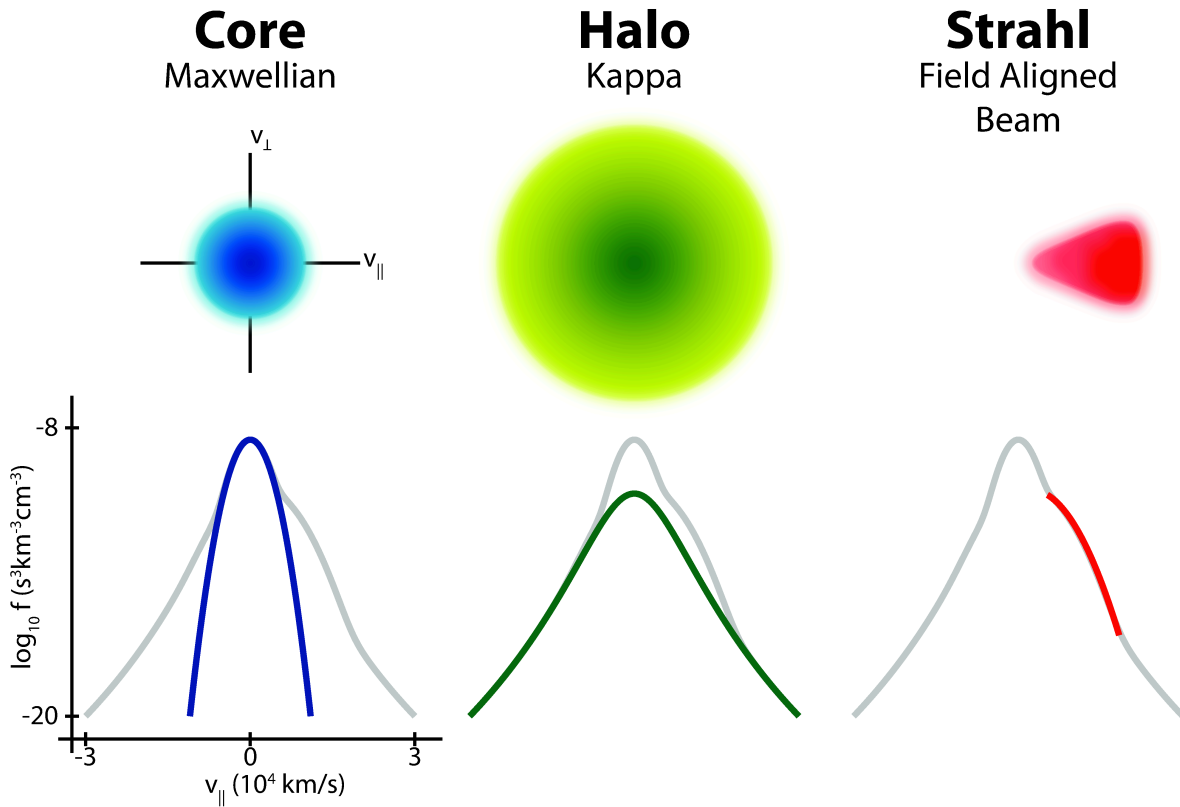


Figure 1.4 – Diagram illustrating different populations of solar wind electrons, including the core, halo, and strahl. The top row shows a 2-dimensional view of the eVDFs of these three distinctive components in the plasma rest frame, and the bottom row highlights each component in the corresponding parallel cuts along the magnetic field through the eVDFs. This figure is courtesy of Dr. Marc Pulupa ^a.

^a. <http://www.ssl.berkeley.edu/~pulupa/illustrations/>

contributes to $\sim 95\%$ of the total electron number density (n_e).

- **Suprathermal halo:** The halo population mostly follows a (bi-)kappa-distribution, which behaves as enhanced high-energy tails in the electron distribution (e.g., Feldman et al., 1975; Rosenbauer et al., 1977; Pilipp et al., 1987; Lin, 1998; Maksimovic et al., 2000; Gosling et al., 2001; Salem et al., 2003; Maksimovic et al., 2005a; Štverák et al., 2008; Štverák et al., 2009; Verscharen et al., 2019). The suprathermal halo component usually contributes to $\sim 4\%$ of n_e .
- **Field-aligned strahl:** The strahl electrons usually travel anti-Sunward along the ambient magnetic field and behaves as a field-aligned beam (e.g., Pilipp et al., 1987; Berčič et al., 2019; Berčič et al., 2020; Halekas et al., 2020b; Hammond et al., 1996; Ogilvie et al., 1999; Horaites et al., 2018; Verscharen et al., 2019). The strahl electrons contributes to $\sim 1\%$ of n_e . The strahl has a complicated cone-shaped structure, and its angular width highly depends on the electron energy and the solar wind bulk speed, and evolves with the heliocentric distance from the Sun.

Similar to the proton populations, each of the three electron populations also often exhibits

temperature anisotropies (e.g., Feldman et al., 1975; Štverák et al., 2008; Štverák et al., 2015; Halekas et al., 2020b; Verscharen et al., 2019; Salem et al., 2003; Salem et al., 2021). Furthermore, there are rather large relative drifts along the ambient magnetic field among the three distinctive electron populations and the solar wind ions (e.g., Feldman et al., 1975; Štverák et al., 2008; Pulupa et al., 2014b; Verscharen et al., 2019; Salem et al., 2021). The electron properties on the three populations and their corresponding temperature anisotropies strongly depend on the proton bulk speed (e.g., Pierrard et al., 2001; Salem et al., 2003; Marsch, 2006; Verscharen et al., 2019). Regarding the radial evolution of eVDFs, the relative density of the halo electrons radially increases, whereas that of the strahl electrons decreases (e.g., Maksimovic et al., 2005a; Štverák et al., 2009; Halekas et al., 2020b; Verscharen et al., 2019), which indicates the conversion of strahl electrons to halo electrons. This is consistent with the result that the strahl angular width increases with distance (e.g., Hammond et al., 1996; Graham et al., 2017; Berčič et al., 2019; Berčič et al., 2020; Verscharen et al., 2019). The exact mechanisms still remain unclear, and both Coulomb collisions and wave–particle interactions are good candidates. Besides the three typical electron populations, the eVDFs sometimes display the fourth component called super-halo electrons with energies from about 2 to 200 keV, of which the origin remains poorly understood (e.g., Lin, 1980; Wang et al., 2015; Wang et al., 2015; Yang et al., 2015).

2.2 The Solar Wind Over Solar Cycles

The inherent magnetic field of the Sun completely flips roughly every 11 years (e.g., Monin, 1980; Ossendrijver and Hoyng, 2002; Hathaway, 2010; Hathaway, 2015), thus forming the so-called 22-year solar cycle. A complete whole solar cycle goes through periods called solar maximum and solar minimum which defined based on the number of sunspots on the solar surface. The solar activity affected by the Sun’s magnetic field evolves following the solar cycle. The periodical variations of the Sun’s magnetic field impact the solar wind expansion from the Sun into the interplanetary space. Past investigations showed that the fast and slow solar winds originate from different regions on the Sun: during solar minimum, (1) the fast wind comes from the polar coronal holes (polar regions with open magnetic field lines); and (2) the slow wind comes from the equatorial streamer belt regions (regions near the equator with closed magnetic field) (see McComas et al., 2008; Issautier et al., 2008; Hansteen, 2009, and references therein).

Figure 1.5 shows how the polar solar wind speed distribution evolves with the solar cycle based on *Ulysses* measurements over all its three orbits. In Figure 1.5 (d), the smoothed sunspot number (black) and the corresponding averaged current sheet tilt angles relative to the solar equator (red) are plotted for reference. The solar conditions for each *Ulysses* orbit are summarized as: solar minimum in solar cycle 22 for the first orbit, solar maximum in solar cycle 23 for the second orbit, and solar minimum in solar cycle 23 for the third orbit. During the solar minimum (Figure 1.5 (a) and (c)), the polar distributions of the solar wind speed variations are well defined. The solar wind flows are emitted out almost radially and the speed variations strongly depend on latitudinal variations. This is because the polar coronal holes and the equator streamer belts are well separated at solar minimum. Figure 1.5 (a) in general looks very similar to Figure 1.5 (c) except for the reversed solar magnetic field directions. Near the solar

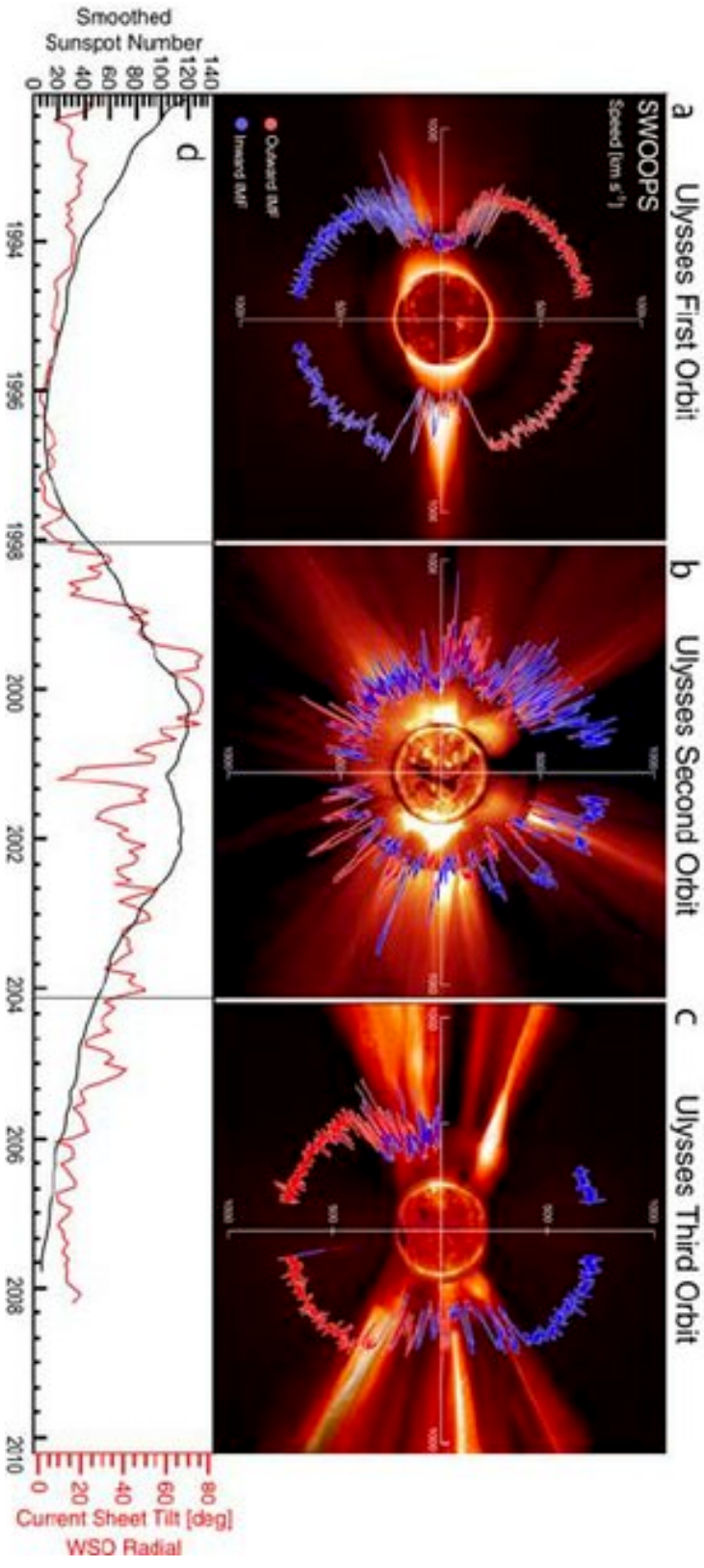


Figure 1.5 – (a-c) Polar plots of the solar wind speed, colored by IMF polarity for the *Ulysses*' three polar orbits colored to indicate measured magnetic polarity. In each panel, the earliest times are on the left (nine o'clock position) and progress around counterclockwise. (d) Contemporaneous values for the smoothed sunspot number (black) and heliospheric current sheet tilt (red), lined up to match Figures 1a–1c. In Figures 1a–1c, the solar wind speed is plotted over characteristic solar images for solar minimum for cycle 22 (8/17/96), solar maximum for cycle 23 (12/07/00), and solar minimum for cycle 23(03/28/06). From the center out, images from the Solar and Heliospheric Observatory (*SOHO*) Extreme ultraviolet Imaging Telescope (Fe XII at 1950 nm), the Mauna Loa K coronameter (700–950 nm), and the *SOHO* C2 white light coronagraph are superimposed. This image is adapted from Figure 1 in McComas et al. (2008).

maximum (Figure 1.5 (b)), the separation between the coronal holes and the streamer belts are very complex, which explains the complexity of the polar distributions of the solar wind speed.

Furthermore, the α particle abundance ($A_{He} = n_{\alpha}/n_p$) also varies as a function of the solar wind speed and the heliographic latitude over the solar cycles (e.g., Kasper et al., 2007; Alterman et al., 2020). Figure 1.6 summarizes the A_{He} variations at one AU as a function of proton bulk speed and time over two solar cycles. Generally, A_{He} reaches its maxima (minima) near the solar maximum (minimum), indicating that A_{He} can serve as a solar activity indicator. Also, near the solar minimum, A_{He} variations clearly depend on the proton bulk speed and the heliolatitude, and these dependences disappear during the solar maximum (Kasper et al., 2007).

As described above, the solar wind can be classified into two basic states based on the proton bulk speed (see also Neugebauer and Snyder, 1962; Neugebauer and Snyder, 1966). The fast and slow solar wind have quite different properties, and they originate from different coronal sources. Despite their large differences in properties and coronal sources, both fast and slow solar winds turn out to have a similar energy flux (e.g., Schwenn and Marsch, 1990; Meyer-Vernet, 2006a; Le Chat et al., 2009; Le Chat et al., 2012). Figure 1.7 presents the solar wind energy flux (scaled to one AU) variations as a function of time over almost a complete solar cycle. The solar wind energy flux is compared to the solar wind speed measurements, the monthly sunspot number (a proxy of the solar activity) and the latitude of each spacecraft. To summarize, based on *in situ* plasma measurements from *Helios*, *Ulysses*, and *Wind* covering a large range of latitudes and time, the solar wind energy flux is confirmed to be independent of the solar wind speed and latitude within 10%, and vary weakly over the solar cycle (Le Chat et al., 2012). The solar wind energy flux appears as a global solar constant, which explains well the anti-correlation between the solar wind speed and density (Le Chat et al., 2012). Furthermore, stellar winds from solar-like and cool-giant stars have a similar value for their stellar-wind energy flux, suggesting that there might be a shared fundamental physical process at the origin of stellar winds (Le Chat et al., 2009).

2.3 The Solar Wind: A Laboratory for Fundamental Plasma Physics

In addition to the unresolved coronal heating and the solar wind acceleration problems, the solar wind gets involved with many fundamental plasma processes such as collisionless shocks, turbulence, magnetic reconnection, plasma instabilities (and the associated plasma waves), and so on. Thus, the solar wind provides a natural laboratory which may help us to improve the understanding of the fundamental plasma physics. Further understanding of the mentioned fundamental plasma processes may in turn shed light on the coronal heating and the solar wind acceleration processes. For example, two main mechanisms proposed to explain coronal heating include turbulence (e.g., Erdélyi and Ballai, 2007; Alfvén, 1947; Sturrock and Uchida, 1981) and magnetic reconnection (e.g., Erdélyi and Ballai, 2007; Parker, 1988). Since this thesis is in part related to the shock–foreshock interaction near the Earth, some basic aspects of collisionless shocks in the heliosphere are described in section 3 of this chapter.

Turbulent flows exist almost everywhere and have triggered active investigations for more than a century, but yet are still not comprehensively understood (e.g., Sreenivasan, 1999; Meyer-

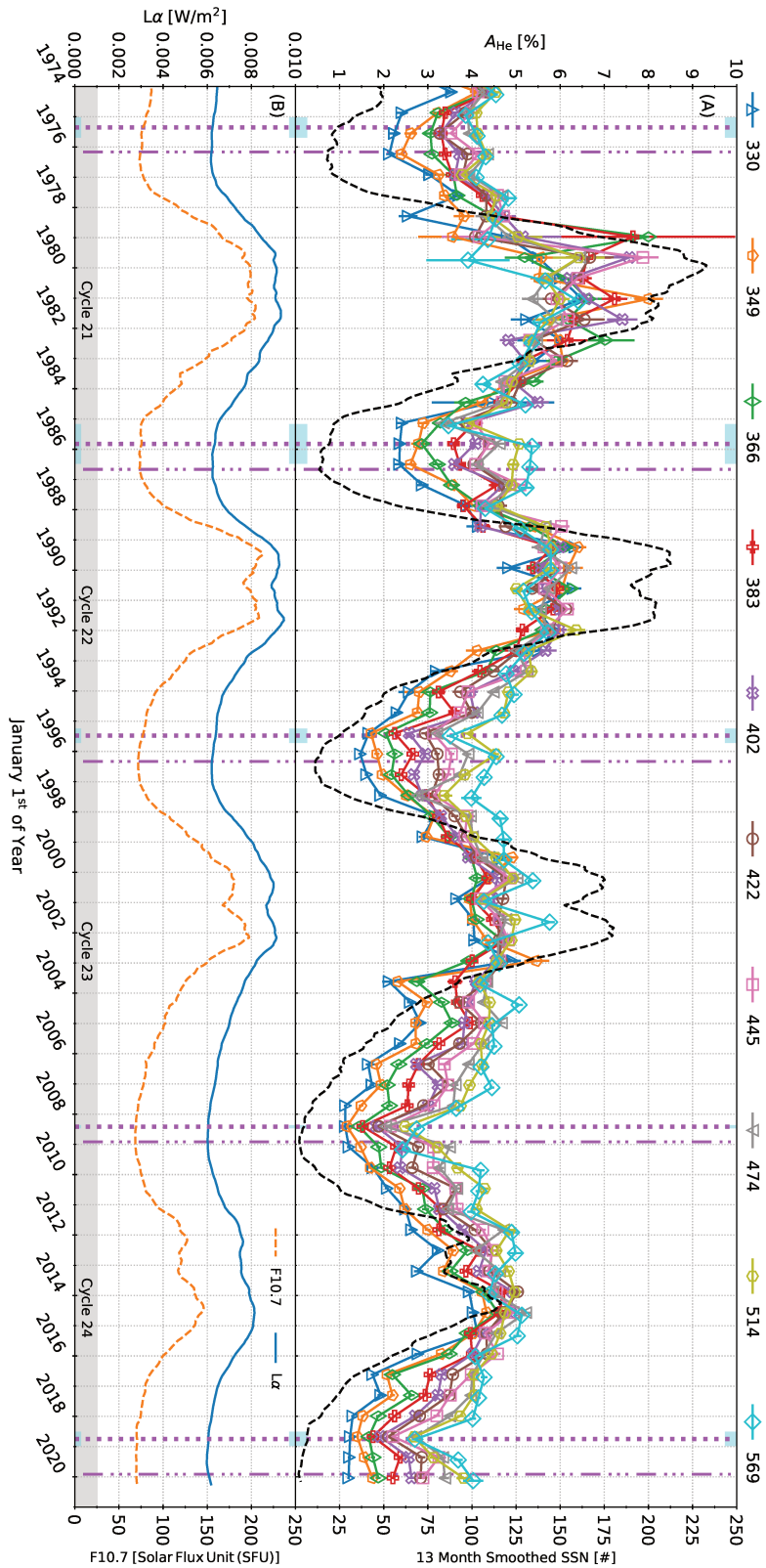


Figure 1.6 – (A) OMNI/Lo helium abundance (A_{He}) as a function of solar wind speed (v_{sw}) and time. A_{He} is split into 10 v_{sw} -quantile, each indicated by a unique color and marker. The legend at the figure's top indicates each quantile's center in km s^{-1} . Within each v_{sw} -quantile, A_{He} is averaged down to 250-day resolution. Error bars indicate the standard error of the mean. The secondary y-axis plots the 13 month smoothed sunspot number (SSN). Vertical dash-dotted purple lines indicate Solar Cycle Minima, which conventionally indicate the start of a new solar cycle. Vertical dotted lines indicate the A_{He} Shutoff date averaged across v_{sw} -quantiles. Blue boxes at the top and bottom of each panel indicate the standard deviation of these shutoff dates. (B) Lyman- α ($L\alpha$, left) and F10.7 cm radio emission (right) solar activity indicators over the same period as A_{He} . Within one or two data points, A_{He} increases across all but the one or two slowest v_{sw} -quantiles prior to plotted SSN Minima. This image is adapted from Figure 1 in Alterman et al. (2020).

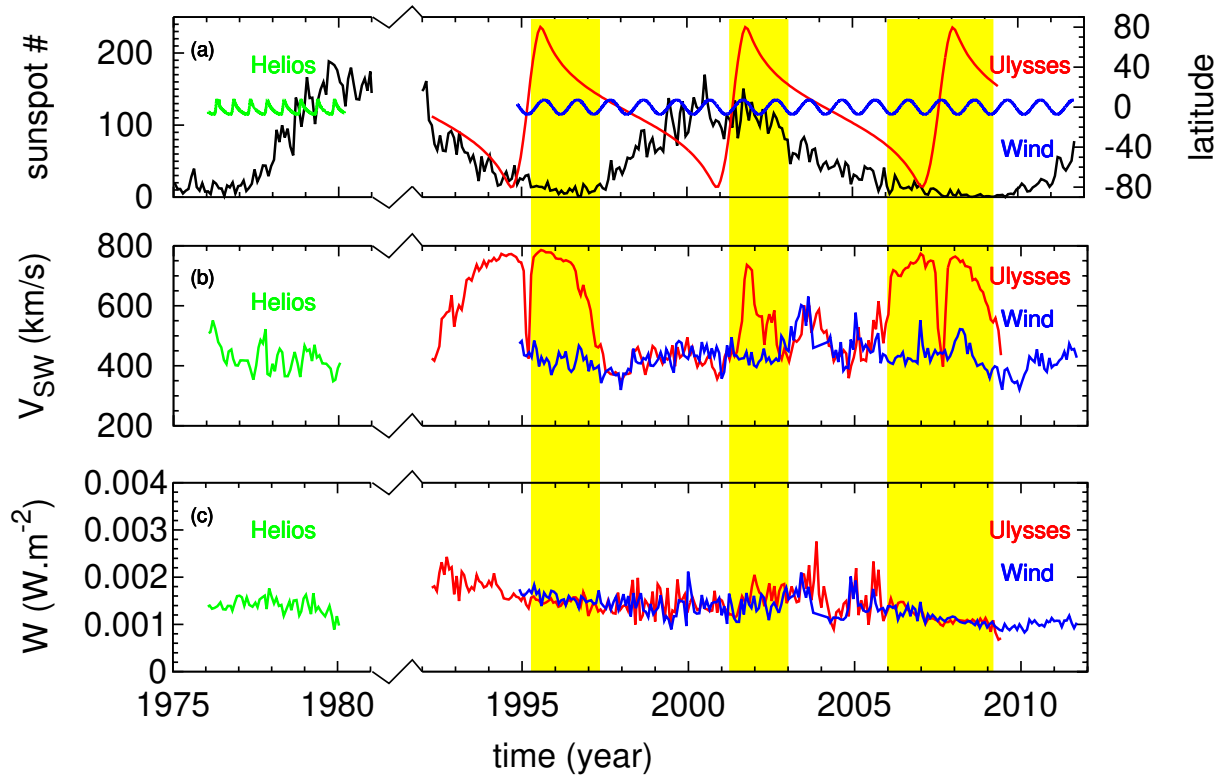


Figure 1.7 – Panel (a): monthly solar sunspot number superimposed on *Helios* (green), *Ulysses* (red), and *Wind* (blue) heliocentric latitudes. Panel (b): solar wind speed measured by *Helios* (green), *Ulysses*/SWOOPS (red) and *Wind*/SWE (blue). Panel (c): solar wind energy flux obtained for *Helios*/E1 Plasma Experiment data (green), *Ulysses*/SWOOPS data (red), and *Wind*/SWE data (blue). Speed and energy-flux data are averaged over a solar rotation (taken as 27.2 days) and the energy flux is scaled to 1 AU for *Helios* and *Ulysses*. The time period between the *Helios* and *Ulysses* epochs have been removed. The yellow bands highlight intervals when *Ulysses* and *Wind* encounter very different solar wind conditions and at very different latitudes. This image is adapted from Figure 1 in Le Chat et al. (2012).

Vernet, 2007). Generally, fluid turbulence consists of disordered and/or swirling fluid motions that occurs irregularly in space and time. In a plasma like the solar wind, turbulence becomes more complicated due to the roles of electric and magnetic fields. Experimental work have shown that Alfvén modes play key roles in the solar wind turbulence (e.g., Bale et al., 2005; Podesta, 2009; Zhao et al., 2022; Zhao et al., 2021a), which can be described well by MHD models (e.g., Zank and Matthaeus, 1993; Goldreich and Sridhar, 1995; Makwana and Yan, 2020).

Magnetic reconnection is another physical phenomenon, which occurs universally in the heliosphere. It rearranges the magnetic topology, and converts magnetic energy into kinetic energy and/or thermal energy. The concept of magnetic reconnection was first proposed by James Dungey to explain the coupling between the solar wind and the terrestrial magnetosphere (e.g., Dungey, 1961; Lockwood, 2016), which opens a new window for both space weather and fundamental plasma physics. The phenomenon of magnetic reconnection has been found in the planetary magnetosphere (e.g., Phan et al., 2000; Deng and Matsumoto, 2001; Lavraud et al., 2006; Burch et al., 2016; Phan et al., 2018; Zhao et al., 2021b; Zhao et al., 2021c) and the free solar wind (e.g., Phan et al., 2006; Phan et al., 2009; Pulupa et al., 2014a; Phan et al., 2021; Lavraud et al., 2021; Phan et al., 2022). Near the Sun, magnetic reconnection is considered as one of the main candidate mechanisms to explain the corona heating and the solar wind acceleration (i.e. via the roles of large solar flares or nanoflares near the Sun) (e.g., Parker, 1988; Erdélyi and Ballai, 2007).

Recent work showed that there are striking interconnections between shocks, turbulence, and magnetic reconnection (Karimabadi et al., 2014). Numerous evidences indicate the existence of magnetic reconnection in the transition region and/or downstream of collisionless shocks (e.g., Lu et al., 2021; Wang et al., 2019; Bessho et al., 2019). Besides, the interaction between upstream magnetic turbulence and a quasi-perpendicular shock plays a key role in particle acceleration (e.g., Giacalone, 2005; Zank et al., 2006; Lu et al., 2009; Andreopoulos et al., 2000; Zank et al., 2003; Donzis, 2012). The turbulence in a plasma provides the environment (i.e. current sheet) to excite magnetic reconnection, and magnetic reconnection in turn plays a key role in dissipation of turbulence (e.g., Loureiro and Boldyrev, 2017; Eastwood et al., 2009; Servidio et al., 2009; Matthaeus and Lamkin, 1986).

3 Collisionless Shocks in the Heliosphere

Shock waves occur ubiquitously throughout the universe as one kind of discontinuity. They form both in collision dominated media (i.e. ordinary hydrodynamic (HD) media) and in collisionless media (i.e. interstellar and/or interplanetary magnetohydrodynamic (MHD) media). In Chapter 5, we analyze how an interplanetary (IP) shock modifies the terrestrial foreshock electron and ion dynamics via *Wind* measurements. In this section, we present a brief introduction about the collisionless shocks in the heliosphere including: (1) a comparison between the collisional hydrodynamic (HD) and collisionless magnetohydrodynamic (MHD) shocks; (2) definitions of some basic collisionless shock parameters and types; and (3) a short review about the terrestrial foreshock.

3.1 Collisional Shocks Versus Collisionless Shocks

When a physical object travels through a collisional hydrodynamic (HD) medium, a shock forms ahead of the physical object if the relative speed between the physical object and the ambient medium exceeds the local sound speed. HD shocks form due to the nonlinear steepening of acoustic pressure waves. The region of the media which has been disturbed by the shock is called the downstream region. In contrast, the region which has not yet been disturbed is defined as the upstream region. The discontinuous transition between the upstream and downstream regions is the so-called shock ramp. In the rest frame of a hydrodynamic shock, the incoming fluid is slowed down below the downstream sound speed and heated via binary particle collisions (i.e. viscosity $\nu \approx \lambda v_{th}$, where λ is the mean free path and v_{th} is the thermal speed of particles in the fluid) (e.g., Shu, 1992; Miles, 1978; Whitham, 1999). In collisional (viscous) media, the shock thickness is of the order of the particle mean free path (Shu, 1992). Thus, the number of binary collisions is sufficient for the irreversible energy dissipation (from kinetic to thermal energy) via viscous heating effects. As a result, from upstream to downstream region of the shock, the entropy increases and the bulk flow properties (i.e. density, velocity, temperature, thermal pressure, etc) change abruptly.

In the heliosphere, the solar wind can be approximately treated as an ideal magnetohydrodynamic (MHD) fluid. The ideal MHD approximation ignores the resistive and viscous effects, and is only valid in the low frequency and large scale regime of the plasma. Under such conditions, MHD shocks are expected to propagate in the heliosphere (Gold, 1955; Gold, 1962; Kellogg, 1962). The newly added electromagnetic effects in the MHD fluid, however, result in new types of shocks with numerous phenomena which are not present at conventional hydrodynamic shocks. Based on the ideal MHD theory, there are three propagating wave modes (Nishikawa and Wakatani, 1994; Gurnett and Bhattacharjee, 2005; Meyer-Vernet, 2007): the fast magnetosonic mode (phase speed V_f), the Alfvén mode (intermediate mode, phase speed V_i), and the slow magnetosonic mode (phase speed V_s). Shocks in the MHD fluid result from the nonlinear steepening of these three linear MHD wave modes. Therefore, there are three types of MHD shocks: fast shock, intermediate shock, and slow shock. Furthermore, in the shock rest frame, the MHD fluid can be classified into four states by comparing the fluid bulk speed (V_{bulk})

and the phase speeds of the three MHD wave modes (e.g., Wu, 1990; Feng and Wang, 2008; Pulupa, 2010): state 1 ($V_{bulk} > V_f$), state 2 ($V_i < V_{bulk} < V_f$), state 3 ($V_s < V_{bulk} < V_i$), state 4 ($V_{bulk} < V_s$). From upstream to downstream of the shock, state 1 \rightarrow 2 and state 3 \rightarrow 4 shocks correspond to fast and slow shocks, respectively. The remaining four transitions, including state 1 \rightarrow 3, state 1 \rightarrow 4, state 2 \rightarrow 3, and state 2 \rightarrow 4, correspond to intermediate shocks (Wu, 1990; Chao et al., 1993; Feng and Wang, 2008; Pulupa, 2010). For all the four different types of intermediate shocks, the pre-shock flow is super-Alfvénic ($V_{bulk} > V_i$) and the post-shock flow is sub-Alfvénic ($V_{bulk} < V_i$).

The typical thickness of a MHD shock is on the order of the proton gyroradius and/or proton inertial length (about tens of kilometers) (e.g., Newbury et al., 1998; Guo and Giacalone, 2010; Yang et al., 2013; Yang et al., 2020a; Yang et al., 2020b; Balikhin and Gedalin, 2022). The average Coulomb collisional mean free path for both protons and electrons in the solar wind is on the order of 1 AU (Livi et al., 1986; Salem et al., 2003; Pulupa, 2010). Thus, shock waves existing in the heliosphere cannot rely upon binary particle collisions for energy dissipation (bulk kinetic energy \rightarrow thermal energy). Stated in another way, the shocks in the interplanetary or interstellar medium are in nature collisionless. This raises the question concerning the energy dissipation mechanisms at the shock transition regions without collisions since the prediction (Gold, 1955; Gold, 1962; Kellogg, 1962) and discovery (Ness et al., 1964; Burlaga, 1971) of collisionless shocks. Furthermore, the ideal MHD cannot be applied to examine the internal dynamics of collisionless shocks (Parks, 2004), though many basic macroscopic bulk features of collisionless shocks are well described based on ideal MHD approximation. Due to the complex nature of the shock transitions and limitations of MHD theory, investigations of energy dissipation mechanisms (i.e. at small scales) at collisionless shocks requires kinetic treatments. How the thermalization across the shocks could be achieved without collisions still remains unclear and various collisionless energy dissipation mechanisms may operate such as wave dispersion (e.g., Wu, 1982; Mellott and Greenstadt, 1984; Stone and Tsurutani, 1985; Tsurutani and Stone, 1985; Gary and Sanderson, 1970; Gary, 1970; Gary, 1972; Gary and Mellott, 1985; Wilson, 2010; Parks et al., 2017), anomalous resistivity due to wave-particle interactions (e.g., Gary, 1981; Mellott and Greenstadt, 1984; Wilson, 2010), particle reflection (e.g., Paschmann et al., 1980; Leroy et al., 1982; Edmiston and Kennel, 1984; Sckopke et al., 1983; Kennel, 1987; Parks et al., 2017; Wilson, 2010; Liu, 2018; Parks et al., 2017), turbulence (e.g., Wu, 1982; Stone and Tsurutani, 1985; Tsurutani and Stone, 1985; Tokar et al., 1987), and plasma instabilities (e.g., Gary et al., 1981; Gary, 1985; Gary, 1981; Wilson, 2010; Liu, 2018; Parks et al., 2017). Regardless of the energy dissipation mechanisms within the shock transitions, across both HD collisional and MHD collisionless shocks, conservation of mass, momentum, and energy must be maintained, which are described by the Rankine-Hugoniot (RH) relations (Macquorn Rankine, 1870; Chéret, 1992; Fomin, 2016).

3.2 Definitions of Collisionless Shock Parameters and Types

Figure 1.8 summarizes the locations where collisionless shocks form in the heliosphere. These shocks include stream interaction region (SIR) associated interplanetary (IP) shocks (e.g., Smith

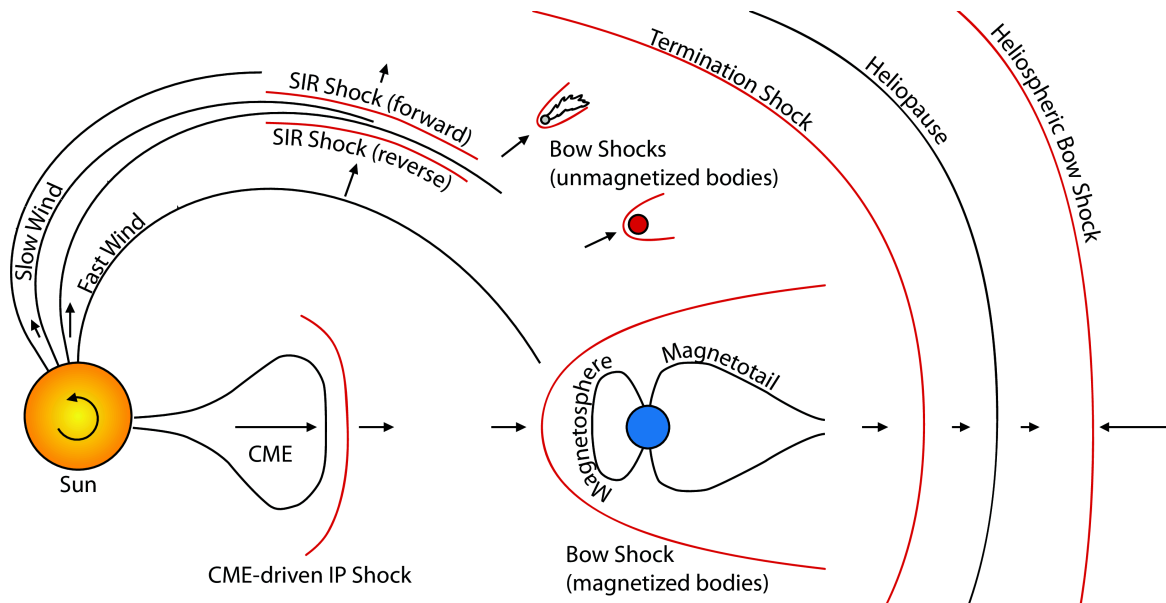


Figure 1.8 – Cartoon showing examples of shocks in the heliosphere. Magnetic field lines are black, while the locations of shock fronts are labelled in red. The viewer is looking down on the ecliptic plane from above, except for the case of the bow shock interaction with the magnetized body, in which case the viewer is in the ecliptic plane. Arrows represent the flow speed of the solar wind, the Coronal Mass Ejection (CME), the interplanetary medium, or the LISM. This image is adapted from Figure 2.1 in Pulupa (2010).

and Wolfe, 1976; Gosling and Pizzo, 1999; Jian et al., 2006; Wei et al., 2022), coronal mass ejection (CME) associated IP shocks (e.g., Liu et al., 2012; Möstl et al., 2012; Lugaz et al., 2015; Liu, 2018; Zhao et al., 2019b), bow shocks associated with magnetized bodies (e.g., Parks et al., 2017; Pulupa, 2010; Yang et al., 2020a), bow shocks associated with unmagnetized bodies (e.g., Luhmann, 1986; Mazelle et al., 2004; Cravens and Gombosi, 2004; Schubert and Lichtenstein, 1974), and shocks in the outer heliosphere (e.g., Chao et al., 1993; Feng and Wang, 2008; Burlaga et al., 2005; Decker et al., 2005; Burlaga et al., 2008; Yang et al., 2015; Lembège and Yang, 2016; Lembège and Yang, 2018). These shocks can be classified into two categories: travelling IP shocks and standing bow shocks. The two are in nature equivalent to each other since they differ simply by a Galilean frame shift. A travelling IP shock is defined as a forward (reverse) shock if it travels away from (towards) the Sun in the solar wind frame of reference. Note that both forward and reverse IP shocks travel away from the Sun in the heliocentric inertial reference frame. There is no difference in the physics of forward and reverse shocks but their temporal profiles look different in the spacecraft rest reference frame (see Figure 1.9). The structure of collisionless shocks depends on various parameters, which makes a simple classification impossible. Hereafter, a few general and useful concepts/definitions to categorize them are listed below.

Fast, Slow, and Intermediate Shocks As is discussed in section 3.1, there are three types of MHD shocks, including fast, slow and intermediate shocks. In the heliosphere, the bow shocks driven by magnetized (i.e. the planets with internal dynamos such as Earth, Mercury, Jupiter,

Uranus, and Neptune) and/or unmagnetized (the planets without internal dynamos such as Venus and Mars, and some comets) bodies are exclusively fast shocks. For the travelling IP shocks, most are fast shocks, and only a minority are identified as slow shocks. The existence of intermediate shocks is still debated, and only a few cases have been detected in the outer heliosphere (see Chao et al., 1993; Feng and Wang, 2008). Figure 1.9 shows typical plasma and magnetic field signatures of fast and slow IP shocks in the spacecraft rest reference frame, combining sense of travel (forward or reverse) defined above. Therefore, there are four types of IP shocks: fast-forward (FF), slow-forward (SF), fast-reverse (FR), and slow-reverse (SR). The differences between fast and slow shocks are: magnetic field strength increases (decreases) across the fast (slow) shocks (from upstream to downstream).

Supercritical and Subcritical shocks Typically, the shock strength is defined in terms of a fast magnetosonic Mach number $M_f = \frac{V_{up}}{V_f}$ and/or an Alfvén Mach number $M_A = \frac{V_{up}}{V_A}$. Here, V_{up} is the upstream bulk velocity along the shock normal in the shock rest frame of reference, whereas V_f and V_A are the local fast magnetosonic and Alfvén speed upstream the shock, respectively. The energy dissipation mechanisms at collisionless shocks strongly depend on the Mach number. Generally, particle reflection dominates at high Mach number shocks (Paschmann et al., 1980; Leroy et al., 1982; Mellott and Greenstadt, 1984), while wave dispersion and anomalous resistivity are more important at low Mach number shocks (Mellott and Greenstadt, 1984; Wilson et al., 2007). Indeed, when M_f exceeds the critical Mach number (M_{cr}), resistive energy dissipation through plasma instabilities at the shock ramp is not efficient enough to heat the plasma. In this event, a fraction of the incoming ions are reflected towards upstream by the electromagnetic field at the shock front participating in the evacuation of energy through an upstream directed heat flux (Edmiston and Kennel, 1984; Kennel, 1987; Parks et al., 2017; Wilson, 2010). M_{cr} is determined by assuming that the downstream normal flow speed is equal to the downstream acoustic speed. Shocks with $M_f > M_{cr}$ are called supercritical shocks and those with $M_f < M_{cr}$ are called subcritical shocks. Early theory showed that $M_{cr} \approx 2.7$ for a perpendicular shock (shock normal angle, $\theta_{Bn} = 90^\circ$) under cold plasma approximations. For typical solar wind conditions and θ_{Bn} orientations, the critical Mach number is generally only $M_{cr} \sim 1-2$ (Edmiston and Kennel, 1984; Kennel, 1987; Parks et al., 2017; Wilson, 2010), which indicates that the particle reflection may play a role even at low Mach number shocks (i.e. most IP shocks).

Obliquity: Shock normal angle θ_{Bn} In a plane shock, θ_{Bn} is the angle between the shock normal vector \mathbf{n} and the upstream magnetic field \mathbf{B} , which is an important parameter that organizes the shock geometry. The shock is classified into several categories based on the shock normal angle θ_{Bn} : (1) parallel shock when $\theta_{Bn} = 0^\circ$; (2) quasi-parallel shock when $0^\circ < \theta_{Bn} < 45^\circ$; (3) quasi-perpendicular shock when $45^\circ < \theta_{Bn} < 90^\circ$; and (4) perpendicular shock when $\theta_{Bn} = 90^\circ$. In general, the transition region of a quasi-perpendicular shock is relatively smooth and laminar, whereas that of a quasi-parallel shock is usually turbulent and associated with large-amplitude plasma waves. It should be mentioned that even though the transition is generally

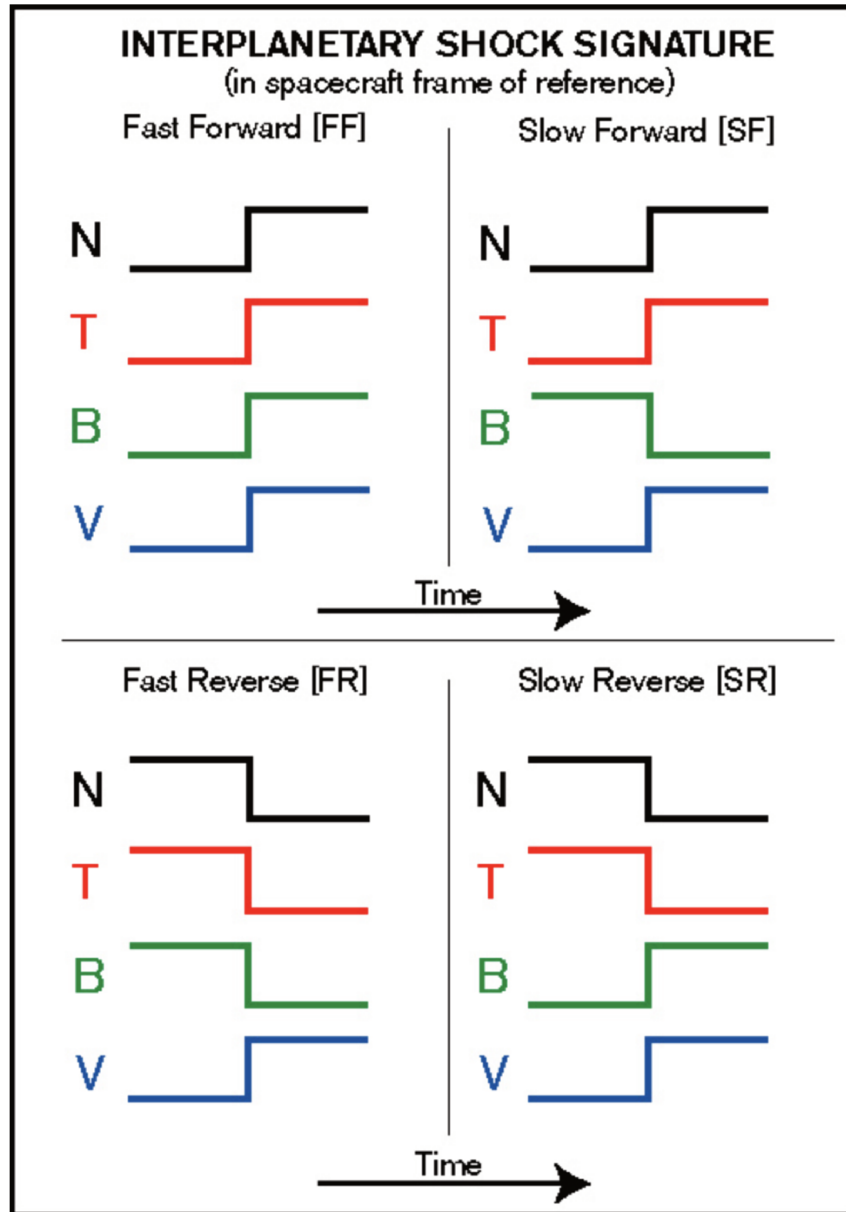


Figure 1.9 – Schematic view of solar wind parameter profiles across four different types of interplanetary shocks: velocity V , temperature T , density N , and magnetic field strength B . The profiles are for the spacecraft frame of reference. In each case, the time increases from the left to the right as indicated by the arrows. This figure is courtesy of the *Wind*/MFI team ^a.

^a. https://wind.nasa.gov/mfi/ip_descr.html

extremely sharp at low Mach number quasi-perpendicular shocks, extended wave trains (i.e. low-frequency magnetic whistler precursors) are sometimes expected and observed upstream of low Mach number quasi-perpendicular shocks (e.g., Wilson et al., 2007; Wilson et al., 2009; Liu, 2018; Liu et al., 2018).

We note that collisionless shocks are very large-scale structures, whose shape and locations vary rapidly in response to the varying ambient solar wind bulk properties (magnetic field, thermal pressure, etc.). For example, the Mach number strength and the shock normal angle θ_{Bn} at different regions of a collisionless shock differ. The relative significance of different energy dissipation mechanisms at collisionless shocks depend on the shock types, the Mach number strength and the shock normal angle θ_{Bn} , which are complex and not well understood.

3.3 General Terrestrial Foreshock Properties

Upstream of a collisionless shock, the region magnetically connected to the shock is called the foreshock. Foreshocks are only present at the collisionless shocks but do not exist at conventional hydrodynamic shocks. In this section, we take the terrestrial foreshock as an example to discuss some basic foreshock physics. This is because the terrestrial bow shock and foreshock have been extensively studied (e.g., Kellogg et al., 1996; Bale et al., 2002; Kellogg, 2003; Kellogg et al., 1996; Bale et al., 1996; Bale et al., 1998; Kellogg et al., 1999; Kellogg, 2003; Wilson et al., 2013; Wang et al., 2015; Parks et al., 2017), with a huge amount of experimental results. In addition, though the sizes of the observed foreshock source regions upstream of IP shocks are comparable to the size of the terrestrial foreshock (e.g., Bale et al., 1999; Pulupa and Bale, 2008), the timespan of the IP foreshock region observed by the spacecraft is usually less than one minute due to the high travelling speed of IP shocks (e.g., Bale et al., 1999; Hoang et al., 2007; Pulupa and Bale, 2008). This makes it more difficult to well resolve the IP foreshock compared to the terrestrial foreshock.

It is well-known and long investigated that the terrestrial foreshock region is dominated by waves and backstreaming particles (Wilson, 2016; Parks et al., 2017). Figure 1.10 shows a possible foreshock geometry assuming that the interplanetary magnetic field (IMF in the figure) follows the standard Parker spiral at 1 AU with an angle of $\sim 45^\circ$ with respect to Sun-Earth direction. Due to the $\mathbf{E} \times \mathbf{B}$ drift and large mass ratio between ions and electrons, a clear separation appears between the ion and electron upstream foreshock boundaries, which can be well described by the single particle theory (see Parks et al., 2017). Specifically, the foreshock boundary can be defined by the guiding centers (GCs) of the backstreaming foreshock particles (in the Earth rest frame). As is shown in Figure 1.10, the total velocity of the GCs (in the Earth rest frame) is given by

$$\begin{aligned} V_{gc} &= \mathbf{V}_{FAB} + \mathbf{V}_{E \times B} \\ &= \mathbf{V}_{FAB} + \mathbf{B} \times \frac{\mathbf{V}_{sw} \times \mathbf{B}}{B^2}. \end{aligned} \quad (1.1)$$

For a given \mathbf{V}_{sw} and IMF \mathbf{B} , the second term of the right hand side in Equation 1.1 is a constant. The angle between the terrestrial foreshock boundary and the IMF \mathbf{B} is given by γ ,

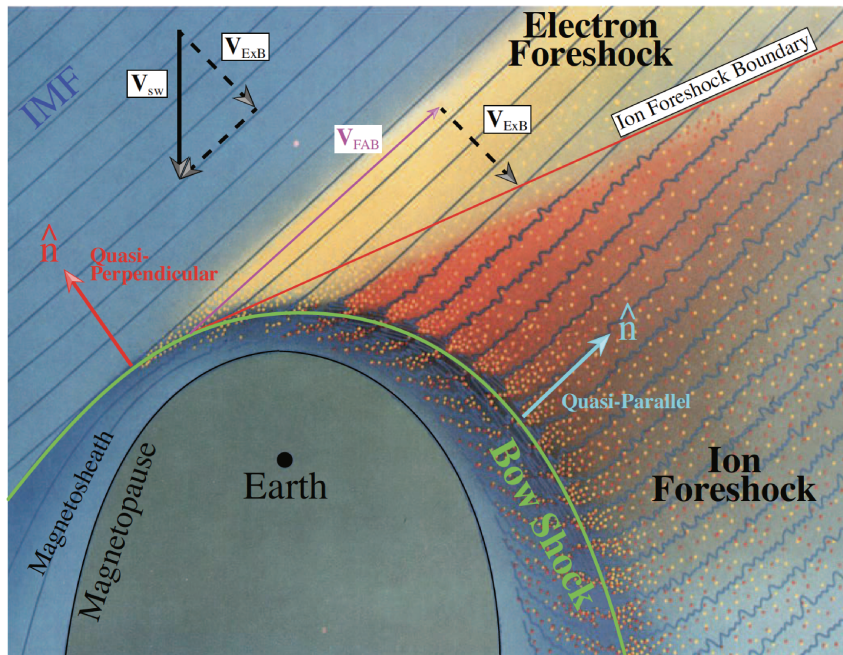


Figure 1.10 – A cartoon example of a possible terrestrial foreshock configuration. The interplanetary magnetic field (IMF) is represented by the dark blue lines, V_{sw} represents the bulk solar wind velocity, $\mathbf{V}_{E \times B}$ is the $\mathbf{E} \times \mathbf{B}$ -drift velocity due to the solar wind convection electric field, and \mathbf{V}_{FAB} is the reflected field-aligned ion beam (FAB) velocity. This figure is courtesy of Plate 1 in Tsurutani and Rodriguez (1981) and Figure 1 in Wilson (2016).

$$\tan \gamma = \frac{V_{E \times B}}{V_{FAB}}. \quad (1.2)$$

For the backstreaming ions from the terrestrial bow shock, \mathbf{V}_{FAB} is related to the incident solar wind bulk speed and is thus typically of the same order (Gosling et al., 1982; Paschmann et al., 1980; Leroy et al., 1982). In contrast, only suprathermal electrons (halo and/or strahl) are reflected at most collisionless shocks, and \mathbf{V}_{FAB} for reflected electrons is of the order or larger than the electron thermal speed (i.e. much larger than $\mathbf{V}_{E \times B}$). Thus, as shown in Figure 1.10, the ion and electron foreshock boundaries are clearly separated. Closer to the electron (ion) foreshock boundary, the reflected electrons (ions) are more energetic. Also, downstream of the ion foreshock boundary, there is a ultra-low frequency (ULF) wave boundary (not shown) (e.g., Le, 1991; Le and Russell, 1992a; Le and Russell, 1992b). Consistently, in the region between the ion and electron foreshock boundaries, only backstreaming electrons are detected. In contrast, in the ion foreshock region, both backstreaming ions and electrons are observed. Some key features of the electron foreshock and ion foreshock are discussed below.

- **Electron foreshock:** The backstreaming electrons can exhibit a "bump on tail" electron velocity distribution function that is unstable to the growth of Langmuir waves via Landau resonance (see Savoini and Lembège, 2001; Pulupa et al., 2011; Pulupa et al., 2012, and references therein). Backstreaming electrons may be shock reflected electrons or electrons leaking from the downstream region (Savoini and Lembege, 2009). Furthermore, the most

intense Langmuir waves are detected at the leading edge of the electron foreshock where the most energetic backstreaming electron beams above 1 keV are observed (e.g., Kasaba et al., 2000; Bale et al., 2000; Pulupa et al., 2012). In contrast, in the deeper region of the terrestrial electron foreshock, Langmuir waves are weaker in association with less energetic backstreaming electrons below 1 keV (e.g., Matsumoto et al., 1997; Kasaba et al., 2000; Pulupa et al., 2011). Interestingly, electromagnetic $2f_{pe}$ emissions are also frequently observed in the terrestrial electron foreshock (e.g., Yoon et al., 1994; Reiner et al., 1996; Kasaba et al., 2000). Langmuir waves and $2f_{pe}$ emissions in the terrestrial electron foreshock are the counterpart of Type II solar radio emissions in the IP foreshock. Langmuir waves in the IP electron foreshock and Type II radio emissions are discussed in section 1.3 of Chapter 2.

- **Ion foreshock:** As shown in Figure 1.11, backstreaming ions including field-aligned ion beams, intermediate ions, and diffuse ions are detected in the terrestrial ion foreshock (Wilson, 2016; Parks et al., 2017). The backstreaming ions near the ion foreshock boundary are field-aligned and become more diffuse and isotropic when traveling deeper into the foreshock and/or approaching the quasi-parallel shock region (Wilson, 2016). Due to the interaction between the incoming solar wind and backstreaming foreshock ions, large-amplitude waves/fluctuations covering a broad frequency range are generated in the quasi-parallel foreshock region (e.g., low frequency Alfvén/ion cyclotron waves, fast magnetosonic or magnetosonic-whistler waves). Indeed, Alfvén waves and/or Alfvén-like oscillations were frequently detected in the quasi-parallel terrestrial foreshock region most likely due to the left-hand resonant ion/ion instability (e.g., Wang et al., 2015; Wilson, 2016, and references therein). Furthermore, nonlinear structures, including hot flow anomalies, foreshock cavities, density holes, shocklets and SLAMS, are also frequently detected in the terrestrial ion foreshock (Wilson, 2016; Parks et al., 2017), which can further locally heat and accelerate ions.

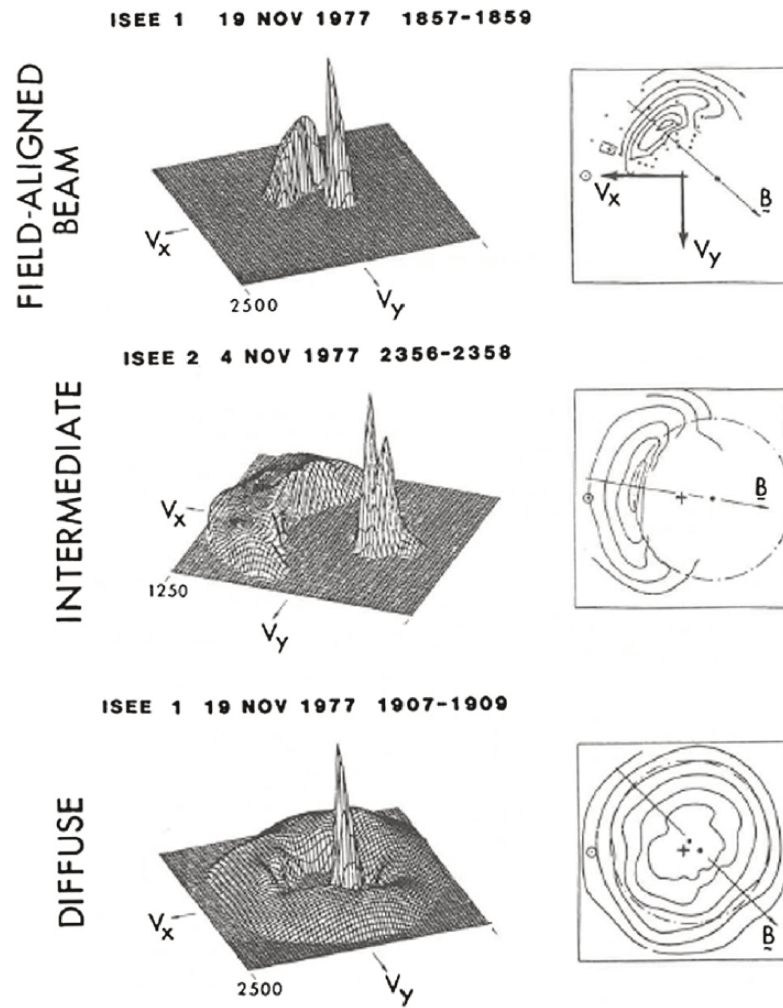


Figure 1.11 – Examples of three types of superthermal ion distributions observed in the terrestrial ion foreshock region. (left) Relief plots of count rate in 2D velocity space integrated over $\pm 55^\circ$ of the elevation angle about the ecliptic plane. (Right) Contour plots of constant phase space density in 2D velocity space for the same events shown on left. This figure is adapted from Figure 4 in Parks et al. (2017).

4 Electron Quasi-Thermal Noise and Langmuir Waves

The electron quasi-thermal noise (QTN) is ubiquitous. Observed by spacecraft electric antenna around the electron plasma frequency (f_{pe}), QTN can be used for *in situ* plasma diagnosis. Another important phenomenon frequently observed near f_{pe} is the bursty Langmuir waves due to plasma instabilities (i.e. bump on tail instabilities). As is discussed in section 1.3 of Chapter 2, solar radio emissions (i.e. Type IIs and IIIs) are closely related to the bursty Langmuir waves resulting from plasma instabilities. The purpose of this section is to provide some basic physical explanations about the electron QTN spectrum, and discuss the bursty Langmuir waves resulting from plasma instabilities. For the detailed analytical formulae to calculate the QTN spectroscopy and some applications on the spacecraft antenna, please refer to Chapters 4 and 6.

When a passive electric antenna is immersed in a plasma like the solar wind, the thermal motions of the ambient electrons generate electrostatic fluctuating signals at the antenna. This noise was first examined in the 1960's (e.g., de Pazzis, 1969; Fejer and Kan, 1969), but it was later misinterpreted as electromagnetic emissions and/or plasma instabilities (e.g., Brown, 1973; Shaw and Gurnett, 1975; Harvey et al., 1979; Birmingham et al., 1981). This (quasi) thermal noise depends on both the ambient electron distributions and the properties of the measuring antenna. The concept of "quasi" is due to the fact that the electron distributions in the solar wind is not a unique Maxwellian (with a unique thermal temperature) but is more complicated (see section 2.1 of this chapter) leading to different electron temperatures. When the antenna is configured in a proper way (see Meyer-Vernet et al., 2017; Meyer-Vernet and Moncuquet, 2020), the quasi-thermal noise (QTN) spectra will be completely determined by the particle velocity distributions of the ambient plasma provided that it is stable (i.e. without plasma instabilities). Therefore, resolving the QTN spectroscopy can in turn provide accurate electron plasma properties (i.e. density and temperature). After a long-history extension and theoretical developments (i.e. including the Doppler-shifted proton noise), the QTN spectroscopy has been recognized as a powerful technique (e.g., Meyer-Vernet, 1979; Meyer-Vernet et al., 1986; Meyer-Vernet and Perche, 1989; Issautier et al., 1996; Issautier et al., 1999b; Meyer-Vernet et al., 2017; Moncuquet et al., 2020; Martinović et al., 2022), which also provides routine cross-checking for the conventional particle detectors (e.g., Maksimovic et al., 1995; Issautier et al., 2001c; Salem et al., 2001).

The QTN spectrum around the electron plasma frequency (f_{pe}) contains a wealth of information about the solar wind, whose basic shape can be explained based on simple plasma physics (Meyer-Vernet and Perche, 1989). Figure 1.12 gives a typical example of the QTN spectrum illustrating the different contributions to the spectrum. The quasi-thermal motion of the ambient plasma electrons passing by the antenna induces electric voltage pulses. At time scales exceeding $1/(2\pi f_{pe})$ (corresponding to frequencies $f < f_{pe}$), the electrons are Debye shielded so that each ambient thermal electron passing closer than L_D produces on the antenna an electric voltage pulse with a duration (roughly equal to $1/(2\pi f_{pe})$) shorter than the inverse frequency of observation. Thus, the Fourier transform of such a pulse is a constant for $f < f_{pe}$, producing a plateau whose amplitude is determined by the bulk of the thermal electrons (cold electrons

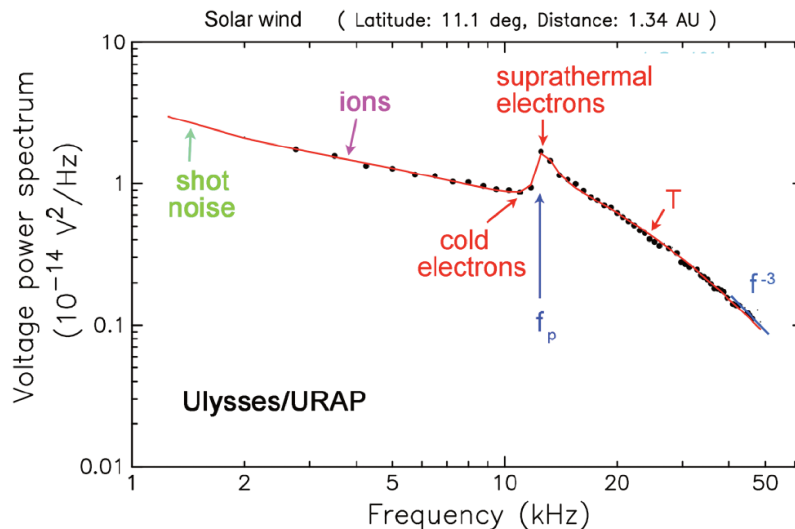


Figure 1.12 – Example of the QTN spectrum measured by a wire dipole antenna in a weakly magnetized plasma (Ulysses/URAP data in the solar wind). The main plasma parameters that can be deduced are indicated. This figure is adapted from Figure 2 in Meyer-Vernet et al. (2017).

in Figure 1.12). In contrast, at higher frequencies ($f > f_{pe}$), the electron quasi-thermal motion excites Langmuir waves, thereby producing a spectral peak near f_{pe} as well as a power spectrum proportional to the total electron pressure at high frequencies (Meyer-Vernet and Perche, 1989; Meyer-Vernet et al., 2017). Furthermore, the height of the peak near f_{pe} depends on the mean energy of suprathermal electrons, whereas the peak width depends on suprathermal electron concentration (Chateau and Meyer-Vernet, 1991; Meyer-Vernet et al., 2017).

Unlike measurements of the electron QTN, both bursty Langmuir waves and radio emissions can be measured with less dependence on the measuring antenna. For example, the electric antenna onboard Stereo/WAVES (Bougeret et al., 2008; Bale et al., 2008) cannot be used to routinely resolve the QTN plasma peaks except in some high-density transient plasma structures. Nevertheless, the bursty Langmuir waves due to plasma instabilities can still be detected. Langmuir waves were first identified by Langmuir Irving at the beginning of the last century (Langmuir, 1928). Briand (2015) gave a comprehensive review about Langmuir waves detected by spacecraft in different plasma environments in the heliosphere. They can be detected in the planetary environments (i.e. the foreshock, the ionosphere and the magnetotail), in the quiet free solar wind, and in the interplanetary medium associated with Type II/III radio emissions during solar activities (like solar flares or interplanetary shocks). These Langmuir waves are exclusively generated/enhanced by the release of free energy from unstable electron distributions associated with bump-on-tail instabilities. The unstable electron distributions are produced by accelerated electron beams via magnetic reconnections and/or shocks, and time-of-flight effects of halo/strahl electrons transmitting the transient plasma structures (i.e. magnetic holes).

Recently, large-amplitude Langmuir waves were detected in the free pristine solar wind by PSP (eg., Bale et al., 2019; Pulupa et al., 2020; Jagarlamudi et al., 2021), which indicates the presence of the transient electron beams near the Sun. Figure 1.13 shows a group of typical

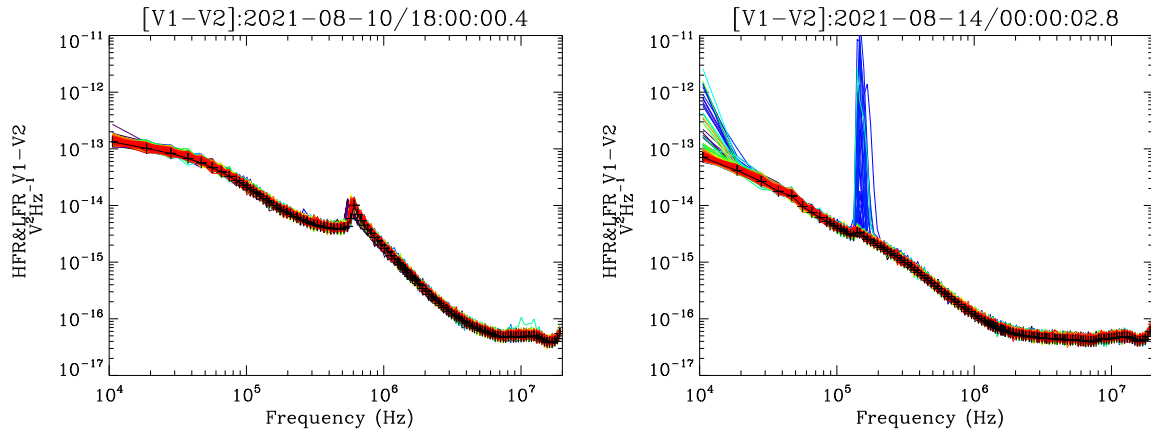


Figure 1.13 – Left: A group of typical thermal noise spectra with well-resolved plasma peaks measured by the PSP/FIELDS/RFS instrument. Right: A group of spectra affected by large-amplitude Langmuir waves from the same instrument.

thermal noise spectra (left panel) versus the spectra affected by strong Langmuir wave activity (right panel). The presence of bursty Langmuir waves can modify the shape and amplitude of the QTN plasma peak, which prevents to derive the suprathermal electron temperature (and sometimes core electron temperature) based on the QTN technique (Moncuquet et al., 2020). We note that the electron number density can still be accurately derived based on the unusual plasma peaks. Langmuir waves induced by the particle quasi-thermal motions are electrostatic, leading to a local measurement of the plasma. In contrast, Langmuir waves due to plasma instabilities get involved with plasma processes of radio emissions (electromagnetic).

5 Motivation and Outline of the Thesis

This chapter gives a brief introduction about the Sun, the heliosphere, and some properties of the solar wind. In particular, the corona heating and solar wind acceleration problems are of prime interest for the space physics community. The heat and/or energy transport processes in the solar wind are key to answer the questions, but still remain not fully understood. Measuring the electron properties can provide important clues to understand the transport properties. Quasi-thermal noise (QTN) spectroscopy, which is less affected by spacecraft photoelectrons and charging effects than traditional particle detectors, is a reliable tool to give accurate measurements of electron properties. Especially the total electron density from the QTN technique is yielded without any calibration. Thus, electron measurements from the QTN technique provide routine cross checking for traditional particle detectors. The ongoing pioneering Parker Solar Probe (PSP), whose heliocentric distances of orbit perihelia decrease from 35.7 solar radii (R_{\odot}) to 9.86 R_{\odot} within five years, offers an opportunity to examine the solar wind properties closer to the Sun than previously detected. This thesis, based on PSP observations, examines the solar wind energy flux, derives electron properties from the QTN technique, and studies the radial evolution of the total electron temperature.

In addition, terrestrial bow shock and IP shocks are important collisionless plasma struc-

tures. It is well-known that the terrestrial foreshock region is dominated by plasma waves and backstreaming particles (Wilson, 2016; Parks et al., 2017). When IP shocks are Earth-directed, they interact with the terrestrial foreshock region. Thus, an interesting question arises regarding how an IP shock modifies the terrestrial foreshock particle dynamics and wave properties. Thanks to the high-quality data and the special orbit design, *Wind* has shown its high capability to examine the shock physics (i.e. particle distributions and wave analysis), which makes it practical to examine wave activities and particle dynamics resulting from the interaction between an IP shock and the terrestrial foreshock.

Based on the above introduction and discussions, the thesis is organized as follows:

1. Chapter 2 outlines and summarizes the Parker Solar Probe and *Wind* spacecraft instrumentations used herein.
2. Chapter 3 studies the solar wind energy flux as close to the Sun as $27.8 R_{\odot}$.
3. Chapter 4 applies the QTN technique using the high frequency part of the radio spectra on Parker Solar Probe observations to derive the total electron temperature (T_e) and examines the radial evolution of the derived T_e with the heliocentric distance varying from about 13 to $60 R_{\odot}$.
4. Chapter 5 reports some new features of wave activities and particle dynamics resulting from the interaction between an IP shock and the terrestrial foreshock via *Wind* observations.
5. Chapter 6 shows the work in progress to derive the electron properties with smaller uncertainties by fitting the whole QTN spectrum. Specifically, the QTN spectroscopy is explained, progresses and caveats of performing full fittings on the QTN spectra are summarized.
6. Chapter 7 briefly summarizes main results of the thesis and describes perspectives for future work.

Chapter 2

Spacecraft and Instrumentation

Objectives

In this chapter, we give a brief introduction of the spacecraft and instrumentations used in this thesis. The results presented in this thesis depend on the measurements of the thermal and suprathermal plasma, and electric and magnetic field from Parker Solar Probe (PSP) (i.e. Chapters 3, 4 and 6) and *Wind* spacecraft (i.e. Chapter 5). For PSP, an extremely brief introduction about the FIELDS and SWEAP instrument suites is made followed by a relatively detailed summary of the Radio Frequency Spectrometer/FIELDS. For the *Wind* scientific payloads, the electrostatic particle analyzers (*Wind*/3DP), and the electric and magnetic field detectors (*Wind*/WAVES and *Wind*/MFI) are summarized.

Contents

1	Parker Solar Probe	29
1.1	FIELDS Instrument Suite	30
1.2	SWEAP Instrument Suite	30
1.3	Radio Frequency Spectrometer/FIELDS	31
2	Wind Spacecraft	37
2.1	Electrostatic Detectors: 3DP	39
2.2	Waves: Radio and Plasma Wave Investigation	40
2.3	Fluxgate Magnetometer: MFI	40

1 Parker Solar Probe

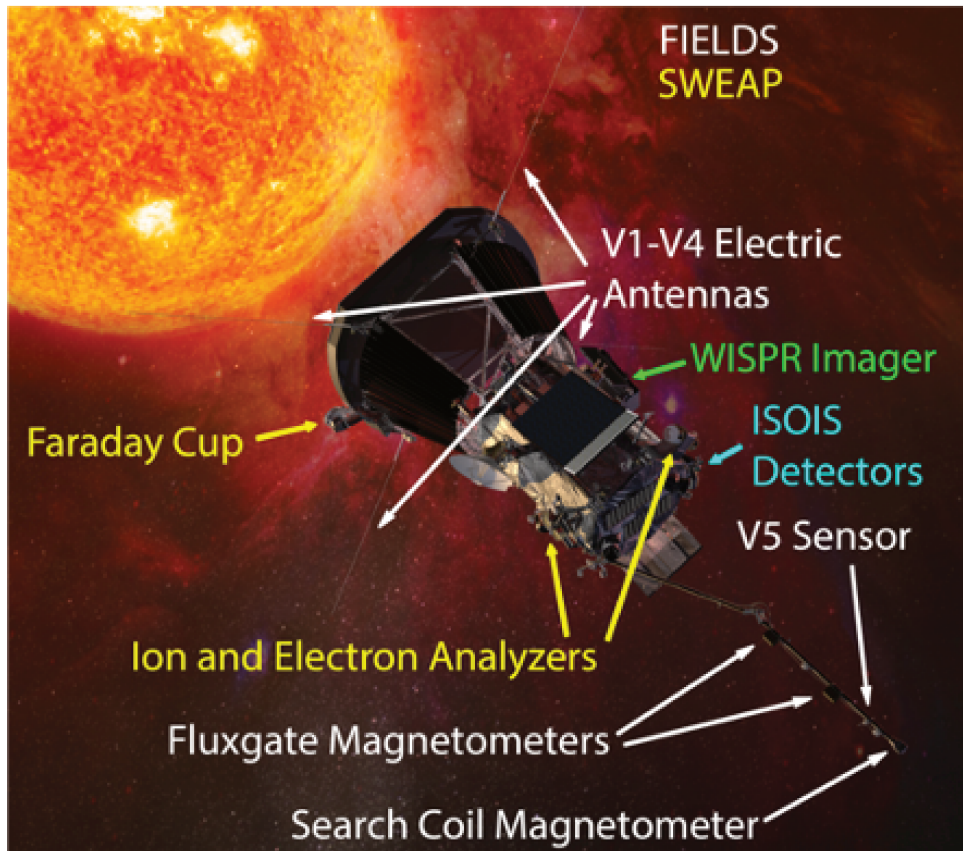


Figure 2.1 – Parker Solar Probe (PSP) and scientific payloads (Fox et al., 2016). Four instrument suites onboard PSP including Fields experiment (FIELDS) (Bale et al., 2016), Solar Wind Electrons Alphas and Protons investigation (SWEAP) (Kasper et al., 2016), Integrated Science Investigation of the Sun (IS \odot IS) (McComas et al., 2016), and Wide-field Imager for Solar PRobe (WISPR) (Vourlidas et al., 2016) are working together to provide both *in situ* and remote observations. The perihelia of PSP orbits are designed to decrease from 35.7 solar radii (R_{\odot}) to 9.86 R_{\odot} within five years. Courtesy of JHU/APL.

The Parker Solar Probe (PSP; Fox et al., 2016), a NASA mission, was launched into space on August 12, 2018 UTC. Its primary scientific objectives are to examine: (1) the physics of the solar corona heating and the solar wind acceleration; (2) the structure and dynamics of the plasma and magnetic fields at the corona; (3) mechanisms of the energetic particle acceleration and transport. The PSP spacecraft was designed to gradually shrink its highly elliptical orbits around the Sun and lower the perihelia from 35.7 solar radii (R_{\odot}) to 9.86 R_{\odot} via Venus flybys. In total, from 2018 to 2025, PSP makes twenty-four orbits around the Sun and seven Venus flybys. Figure 2.1 presents the PSP spacecraft and the four selected instrument suites including Fields experiment (FIELDS) (Bale et al., 2016), Solar Wind Electrons Alphas and Protons investigation (SWEAP) (Kasper et al., 2016), Integrated Science Investigation of the Sun (IS \odot IS) (McComas et al., 2016), and Wide-field Imager for Solar PRobe (WISPR) (Vourlidas et al., 2016). Together, the unique orbit design of PSP enables these four scientific payloads to measure

the plasma, fields, and energetic particle environment of the inner heliosphere closer to the Sun than previous spacecraft. This thesis uses the FIELDS and SWEAP instrument suites which are briefly introduced in section 1.1 and section 1.2, respectively.

1.1 FIELDS Instrument Suite

FIELDS makes use of three magnetic field sensors and five electric field sensors to make direct measurements of electric (from DC to 19.2 MHz) and magnetic (from DC up to 1MHz) fields, respectively. The FIELDS magnetic field sensors are comprised of two identical fluxgate magnetometers (FGMi and FGMo) (Bale et al., 2016; Bowen et al., 2020) and a search coil magnetometer (SCM) (Bale et al., 2016; Bowen et al., 2020; Dudok de Wit et al., 2022), of which all three sensors are mounted on a boom extending behind the spacecraft. The fluxgate and search coil magnetometers are standard devices for measuring low frequency (DC) and wave (AC) magnetic fields, respectively. Together, the magnetometers contribute to determine the structure and dynamics of the magnetic fields at the sources of the fast and slow solar wind, study the coronal processes that lead to solar corona heating and wind acceleration, and explore the roles of shocks, reconnection, and turbulence in accelerating energetic particles (Bale et al., 2016). The FIELDS electric field sensors contain four identical monopole electric field antennas (V1–V4) and a fifth (V5) dipole antenna. The four V1–V4 antennas are two meters long, and are deployed beyond the spacecraft’s heat shield and into the sunlight. The V5 antenna is 21 centimeters long and mounted on the magnetometer boom. The electric field measurements further give properties of *in situ* plasma waves, electron density and temperature profiles, and solar/interplanetary radio emissions (Bale et al., 2016; Malaspina et al., 2016; Pulupa et al., 2017; Moncuquet et al., 2020). These magnetic and electric field sensors provide inputs to receivers within the FIELDS Main Electronics Package (MEP). The MEP contains the Antenna Electronics Board (AEB), Data Controller Board (DCB), Radio Frequency Spectrometer (RFS) (Pulupa et al., 2017), Digital Fields Board (DFB) (Malaspina et al., 2016), Low Noise Power Supply (LNPS), Time Domain Sampler (TDS) (Goetz et al., 2018), and Magnetometer control boards (MAG) (Bowen et al., 2020). RFS is closely related to this thesis, and is introduced in a detailed way in section 1.3.

1.2 SWEAP Instrument Suite

SWEAP provides complete measurements of the most abundant particles (the electrons, the protons, and the ionized helium) of solar wind and/or coronal plasma. The instrument suite consists of the Solar Probe Cup (SPC) and the Solar Probe Analyzers (SPAN) (Kasper et al., 2016; Livi et al., 2018; Case et al., 2020; Whittlesey et al., 2020). SPC is a fast Faraday Cup designed to look directly at the Sun and provide the one dimensional velocity distribution function (VDF) of ions and sometimes electrons. The raw data from SPC are the currents measured on each collector plate which can be converted into differential energy flux and then the VDF (phase space density) (Case et al., 2020). In the case of SPC, the VDF is only measured in one dimension (along the flow direction into the aperture of the instrument), which

is the so-called "reduced distribution function". SPAN is a combination of ion (SPAN-B) and electron (SPAN-A and SPAN-B) electrostatic analyzers (ESAs) operated to provide the full three dimensional VDFs of ions (Livi et al., 2018) and electrons (Whittlesey et al., 2020). SPAN makes use of curved plates to discriminate the incoming particles based on the corresponding energy/charge ratios, multiple anodes to make measurements from different azimuth angles, and electrostatic deflectors to scan through elevation angles. The raw data of SPAN are measured in units of counts, and the conversion to differential energy flux and/or phase space density needs to consider the instruments efficiency, deadtime, accumulation time, and optical geometric factor (Bordoni, 1971; Goruganthu and Wilson, 1984; Meeks and Siegel, 2008; Curtis et al., 1989; Paschmann and Daly, 1998; Wüest et al., 2007; Wilson et al., 2016). Furthermore, the VDF measurements from both SPC and SPAN allow to give plasma parameters such as number density, bulk flow velocity, thermal pressure/temperature, and heat flux.

1.3 Radio Frequency Spectrometer/FIELDS

The Radio Frequency Spectrometer (RFS) is one part of the FIELDS suite, which is equipped with the V1–V4 electric field antennas and the X axis of the search coil magnetometer (SCM) (Bale et al., 2016; Pulupa et al., 2017). The RFS is a two-channel digital receiver and spectrometer, optimized for remote sensing observations of radio waves and *in situ* measurements of electrostatic and/or electromagnetic fluctuations in the solar wind and corona plasma. The RFS covers the highest-frequency bandwidth (from 10 kHz to 19.2 MHz) among the receivers of the FIELDS suite. Figure 2.2 shows that the four 2-meter electric field antennas (V1–V4) are mounted near the heat shield in the spacecraft X-Y plane. The signals measured at the V1–V4 antenna terminals are amplified by preamplifiers mounted near the base of the antennas, and provide low-frequency (LF), medium-frequency (MF), and high-frequency (HF) outputs. As is shown in Figure 2.3, the RFS is designed to use the HF output of the FIELDS electric field preamplifiers. Each RFS channel can select antennas via multiplexers, thereby using as the input either the difference between any two antennas (dipole mode) or the difference between any antenna and the spacecraft body (monopole mode). Moreover, both RFS channels are digitally sampled simultaneously, allowing to derive auto spectra for each channel and cross spectra between the two channels based on the selected inputs. The SCM X axis is parallel to the spacecraft X-Z plane with a 45° angle oriented from the spacecraft X-Y plane. Each axis of the SCM is designed to have a LF winding sensitive to the magnetic field fluctuations from 10 Hz to 50 kHz. In addition, the SCM X axis also has a MF winding (see Figure 2.3), sensitive to the magnetic field fluctuations from 1 kHz to 1 MHz, which may also be used as an input to the RFS. In this thesis, we mainly focus on the electric field measurements, and therefore the introduction below is only related to the electric field observations. Here, we only briefly summarize the data products and operation modes, and in particular discuss the science signals of interests to trigger the RFS instrument configuration.

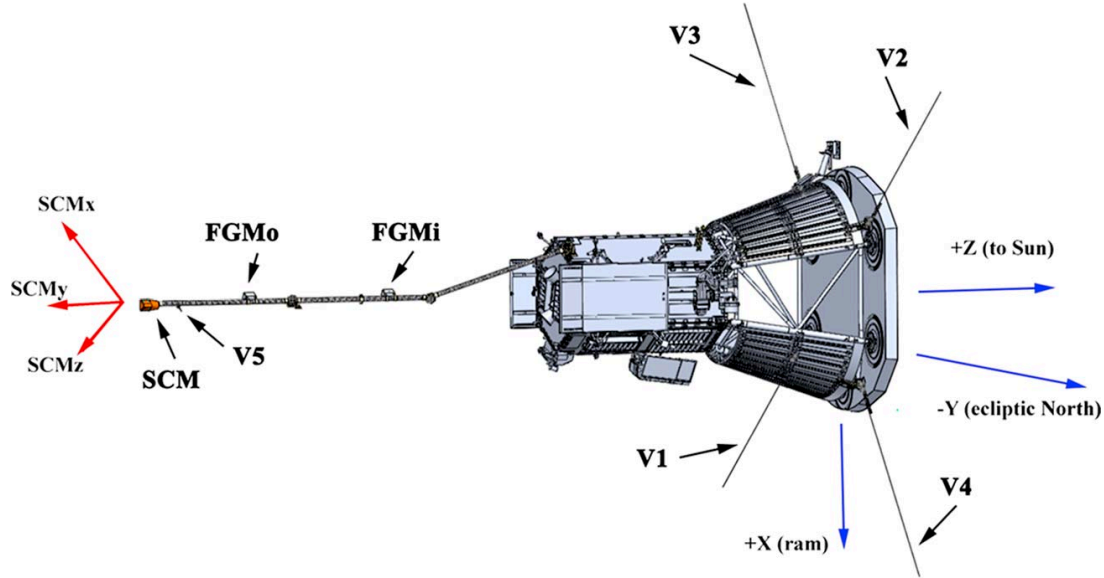


Figure 2.2 – Detailed location configuration of FIELDS sensors on the Parker Solar Probe spacecraft. The coordinate systems of the spacecraft and the search coil magnetometer (SCM) are indicated in blue and red, respectively. The RFS receives inputs from the V1–V4 electric field antennas and (may also) the single axis medium-frequency (MF) winding of the SCM. The V5 and fluxgate magnetometer sensors on the magnetometer boom are not used as inputs to the RFS. This illustration is adapted from Malaspina et al. (2016) and Pulupa et al. (2017).

Data Products The primary data products from the RFS are autospectra and cross spectra derived from the selected inputs of the V1–V4 electric field antennas. Like any previous spacecraft, the numerous spacecraft subsystems and instruments on board PSP can generate noise emissions. The noise emissions can be radiated as electromagnetic waves and/or conducted between different subsystems/instruments via the electrical connections, which can overwhelm the low-amplitude science signals. Therefore, a polyphase filter bank is applied to calculate the spectra (Pulupa et al., 2017), which enables the measurement of the low-amplitude signals of interest in the presence of high-amplitude narrowband spacecraft-generated noises. The waveforms from the selected inputs are processed onboard the spacecraft into the averaged autospectra and cross spectra, which are then telemetered to the ground. Specifically, the RFS consists of the Low-Frequency Receiver (LFR) and High-Frequency Receiver (HFR) to cover the frequency ranging from 10 kHz to 19.2 MHz. The default operating configuration makes full use of two channels (see Figure 2.3), with one channel receiving inputs from the V1–V2 dipole antenna, and the other channel connecting to V3–V4 dipole antenna. This default configuration of RFS alternates between LFR and HFR modes. As a result, the final telemetered data product is an averaged spectrum for both LFR and HFR data, which reduces the statistical noise. In the normal mode, the telemetered spectra will consist of 64 selected frequencies for each receiver, covering the range 10 kHz–1.7 MHz for LFR and 1.3 MHz–19.2 MHz for HFR. The chosen frequencies will be pseudo-logarithmically spaced, keeping a consistent relative frequency spacing $\Delta f/f$ of $\sim 4\%$ throughout the respective frequency range for each receiver. The time resolution of telemetered spectra is 7 s (or 3.5 s) during the PSP encounter phase, and 56 s during the PSP

survey phase. For more details about the working principles of the RFS, please refer to Pulupa et al. (2017).

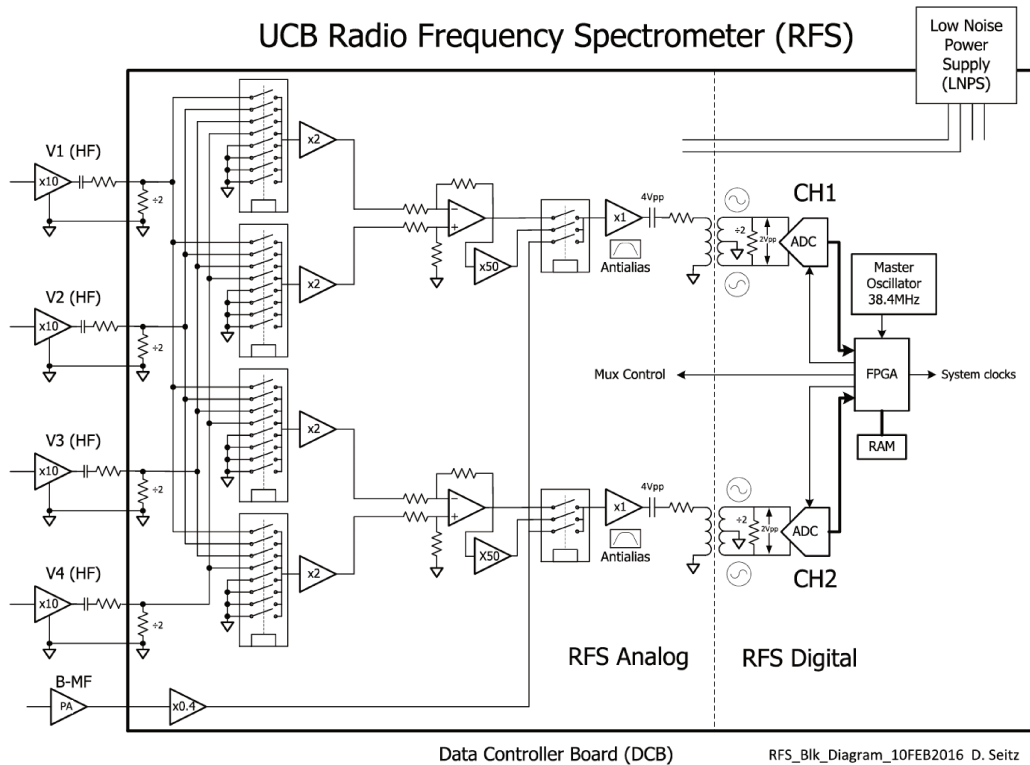


Figure 2.3 – RFS block diagram. Inputs to the RFS are shown at the left. The RFS analog and digital sections are physically located on the DCB. This image is adapted from Figure 2 in Pulupa et al. (2017).

Science Signals of Interests The RFS bandwidth covers the frequency range (from 10 kHz to 19.2 MHz), and the plasma frequency (f_{pe}) during the PSP encounter phase is expected to typically range from ~ 100 to ~ 750 kHz (Bale et al., 2016; Pulupa et al., 2017). Figure 2.4 presents an overview of the expected science signal sources, as well as the measurement of the system noise. The expected science signal sources mainly includes the radio galaxy noise ($f \gg f_{pe}$), the solar radio emissions ($f \geq f_{pe}$), and the quasi-thermal noise (near f_{pe}). Recent studies (eg., Bale et al., 2019; Pulupa et al., 2020; Jagarlamudi et al., 2021) showed that large-amplitude electrostatic Langmuir waves near f_{pe} are detected by RFS/LFR. Moreover, electron Bernstein waves near the local electron cyclotron frequency (f_{ce}) are visible in the RFS/LFR spectrogram (from ~ 10 to ~ 30 kHz) (eg., Malaspina et al., 2020; Pulupa et al., 2020; Ma et al., 2021b).

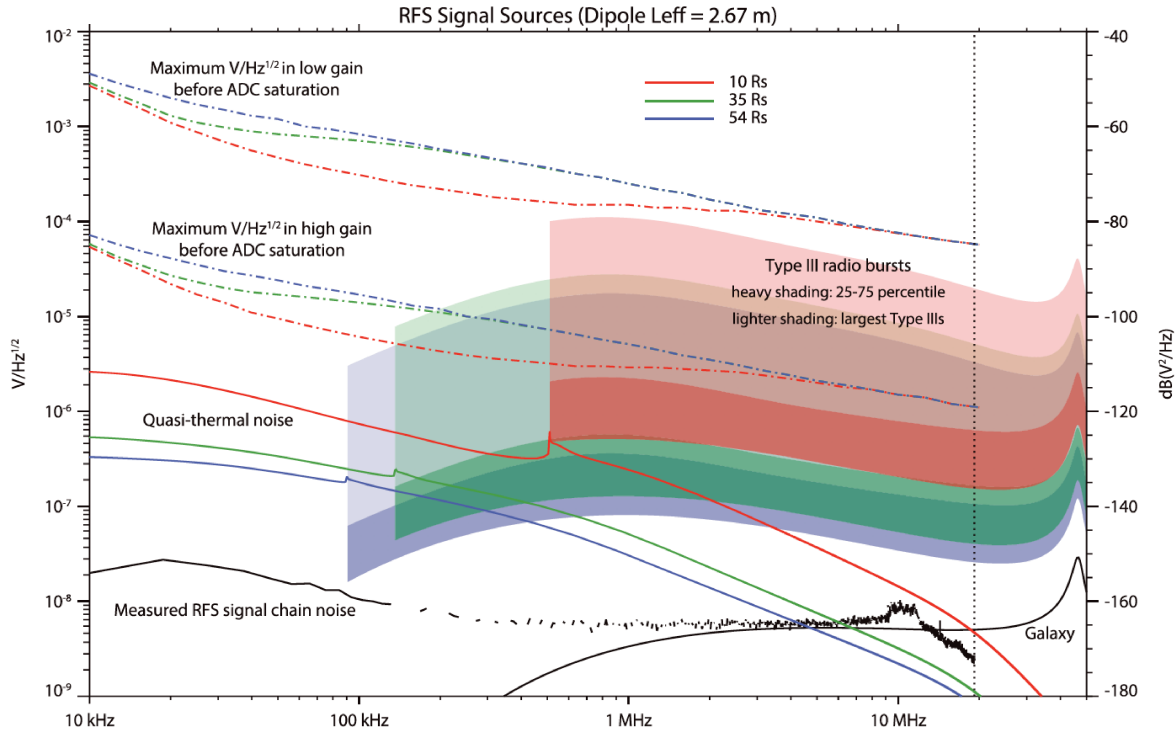


Figure 2.4 – RFS signal and noise sources. The vertical axis is in units of the spectral density, referred to the input of the FIELDS HF preamplifiers. The vertical dotted line (19.2 MHz) denotes the upper bound of the RFS bandwidth, and corresponds to the Nyquist frequency at the sampling rate of $f_s = 38.4$ MHz. This image is adapted from Figure 3 in Pulupa et al. (2017).

- **Radio galaxy noise** ($f \gg f_{pe}$): For the galactic radio background noise, it is almost constant in time and nearly isotropic in angular distribution with the modulation as a function of the observed solid angle being less than 20% in the considered frequency range (Manning and Dulk, 2001). Therefore, it was frequently used to accurately calibrate the antennas on board previous spacecraft missions (e.g., Zarka et al., 2004; Eastwood et al., 2009; Hillan et al., 2010; Zaslavsky et al., 2011). The galaxy noise spectrum has a broad peak near 1 MHz, which lies within the RFS frequency bandwidth. However, due to the short length (2 m for a monopole) of the PSP/FIELDS V1-V4 electric antennas compared to the previous spacecraft antennas (i.e. 6 m for Stereo/WAVES (Bougeret et al., 2008; Bale et al., 2008), tens of meters for Wind/Waves (Bougeret et al., 1995) and Ulysses/URAP (Stone et al., 1992)), it is a significant challenge for the RFS to detect the radio galaxy noise. Therefore, the preamplifier and receiver were carefully designed and calibrated to improve the sensitivity of the RFS, so that the radio galaxy noise can be accurately distinguished from the instrument noise. So the radio galaxy noise is the driver for configuring the lower bound of the RFS dynamic range. In particular, PSP/FIELDS electric antennas were calibrated by relating the measured radio galaxy noise spectrum to the modelled flux of the source during the spacecraft commissioning (Maksimovic et al., 2020). The measured radio galaxy noise spectrum was obtained by comparing the

spectrum measured by the antenna predeployment and during the quietest postdeployment time interval. The PSP spacecraft commissioning occurred shortly after launch, when PSP was at a heliocentric distance of slightly less than 1 AU. In this way, the effects from the quasi-thermal noise and other radio emissions, which can challenge the antenna calibration, were avoided.

- **Solar radio emissions ($f \geq f_{pe}$):** Type II and Type III solar radio bursts are the main sources of the solar radio emissions, which are of comparable scientific interest for the RFS/FIELDS. Here, they are briefly introduced in a parallel way, in order to illustrate the similarities and differences between the two. Type II and III solar radio bursts are generated by electron beams accelerated from the Sun into the interplanetary space. Velocity dispersion of the electron beams along interplanetary magnetic field (IMF) lines can exhibit a bump on tail electron velocity distribution function that is unstable to the growth of electrostatic Langmuir waves near the local f_{pe} via Landau resonance. The electrostatic Langmuir waves can in turn be converted to transverse electromagnetic radio emission near f_{pe} and/or its harmonics ($2f_{pe}$). As the accelerated electron beams travel outward from the Sun into the interplanetary space along the IMF lines, f_{pe} decreases, and therefore the frequency of Type II and III emissions decreases accordingly. This is the so-called frequency drift of Type II and III radio emissions. The difference between them is that Type II solar radio bursts are generated by electron beams accelerated by the shock driven by coronal mass ejections (CMEs) (e.g., Bale et al., 1999; Pulupa and Bale, 2008; Liu et al., 2009, and references therein), whereas Type III radio emissions are driven by flare-accelerated electrons (e.g., Dulk, 1985; Dulk, 2000; Gopalswamy, 2004; Reid and Ratcliffe, 2014). The frequency drift of Type III radio emissions is much quicker than that of Type II radio emissions. Type II frequency drift can be used to track the CME propagation (e.g., Liu et al., 2017; Zhao et al., 2017; Zhao et al., 2019b, and references therein). Analysis of the Type III frequency-drifting signal can not only provide rich information about flare-accelerated electrons and the structure of the IMF lines (e.g., Reiner et al., 2009; Reiner and MacDowall, 2015, and references therein), but also help to derive an electron density model all along the trajectory of the burst (Leblanc et al., 1998). The amplitude of the Type II emissions is much lower than that of Type IIIs. So, in Figure 2.4, the upper bound of the RFS dynamic range is determined based on the statistical distribution of the Type III flux density (Krupar et al., 2014). The high sensitivity of the RFS, configured to measure the radio galaxy noise, allows to measure weak solar radio emissions (e.g., Pulupa et al., 2020; Ma et al., 2021a; Ma et al., 2022).
- **Quasi-thermal noise (near f_{pe}):** The quasi-thermal motion of the ambient plasma electrons (mainly) and ions passing by the antenna induces electric voltage pulses, and thereby generate the quasi-thermal noise (QTN) spectrum. The QTN spectra depend on both the ambient plasma properties and the antenna configuration (Meyer-Vernet and Perche, 1989; Meyer-Vernet et al., 2017). When the antenna is configured in a proper way (see Meyer-Vernet et al., 2017; Meyer-Vernet and Moncuquet, 2020), the QTN spectra will be completely determined by the particle velocity distributions of the ambient

plasma. The electric antenna should be both long enough and thin enough (i.e. $a < L_D < L$) to obtain a very prominent and well-resolved plasma peak near f_{pe} . Here, L is the electric antenna length, L_D is the local Debye length, and a is the electric antenna radius. Performing full QTN fits on the spectrum with a very prominent and well-resolved plasma peak can provide a full set of solar wind plasma parameters (i.e. core electron density and temperature, suprathermal electron density and temperature, and the proton bulk speed and temperature) (Issautier et al., 1996; Issautier et al., 1999b). For the first several encounters, PSP is still not close enough to the Sun and therefore L_D is, for most of the time, still larger than the antenna length ($L \simeq 2$ m). Nevertheless, the plasma peak emerged because of the suprathermal electrons (Meyer-Vernet et al., 2022). Recent investigations (see Moncuquet et al., 2020; Maksimovic et al., 2020; Martinović et al., 2022; Liu et al., 2022) have already applied this technique on PSP to derive the electron density and temperature based on the electric voltage spectra acquired by the RFS/FIELDS. Since the electron density from QTN is deduced from a spectral peak, this measurement is independent of gain calibrations, and serves routinely to calibrate other instruments. Until now, on PSP, the electron number density provided by QTN technique has been playing an important role as a calibration standard for scientific analysis (e.g., Kasper et al., 2021; Zhao et al., 2021a; Liu et al., 2021a; Liu et al., 2021b). As shown in Figure 2.4, the plasma peak of the QTN spectrum becomes more and more prominent closer to the Sun, which makes it more practical to implement a full fit on the QTN spectrum. In contrast, at the orbits of the closest approach, the effects of spacecraft charging will be the strongest for SWEAP suite (Ergun et al., 2010; Guillemant et al., 2012). The electron parameters provided by the QTN Spectroscopy are expected to play a more important role for both the scientific analysis and calibrations for the plasma instrumentations.

- ***In situ* Plasma waves and Dust impacts ($f < f_{pe}$ or near f_{pe}):** As shown in Figure 2.4, the electrostatic Langmuir waves and/or electromagnetic radio emission associated with Type IIs/IIIs may be detected *in situ* (e.g., Pulupa et al., 2020; Ma et al., 2021a; Ma et al., 2022), when the spacecraft is magnetically connected to the source regions of Type IIs/IIIs, which can overwhelm the QTN spectrum at $f \geq f_{pe}$. Also, near f_{pe} , large-amplitude Langmuir waves are detected in the free pristine solar wind by RFS/LFR (eg., Bale et al., 2019; Pulupa et al., 2020; Jagarlamudi et al., 2021), which changes the shape of the QTN plasma peak. At $f < f_{pe}$, the transverse electromagnetic radio waves generated remotely cannot propagate through the plasma, and the measurements made by RFS/FIELDS must be due to the *in situ* plasma waves and/or turbulent fluctuations. For example, the large-amplitude, wideband, Doppler-shifted, Ion Acoustic Waves (from ~ 10 to 15 kHz) (Mozer et al., 2020) and electron Bernstein waves (from ~ 10 to ~ 30 kHz) (eg., Malaspina et al., 2020; Pulupa et al., 2020; Ma et al., 2021b) are visible in the RFS/LFR spectrogram, which can distort the RFS spectra at $f < f_{pe}$ together with dust impacts (Meyer-Vernet et al., 2009; Zaslavsky et al., 2012; Malaspina et al., 2016). All the *in situ* plasma waves and dust impacts discussed here should be carefully dealt with when implementing the QTN Spectroscopy.

2 Wind Spacecraft

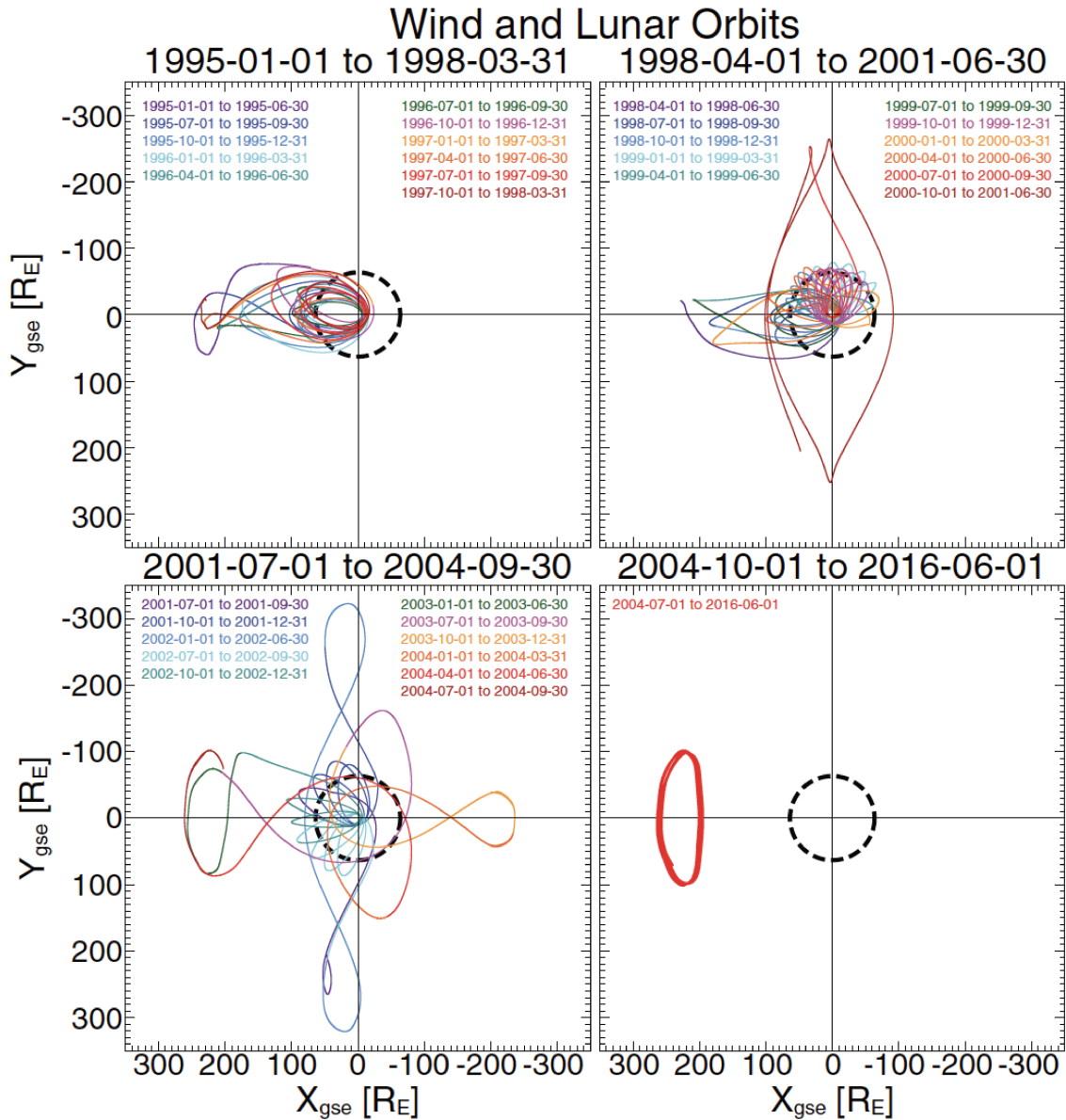


Figure 2.5 – Orbital trajectories of the Wind spacecraft in the GSE XY plane from November 1, 1994 to June 1, 2016. Colors denote time ranges as indicated. The dashed black circle indicates the lunar orbit. Note that the Wind orbit has not noticeably changed since June 1, 2016. This image is adapted from Figure 1 in Wilson et al. (2021).

Wind is a spin stabilized spacecraft which was launched into a lunar swingby orbit on November 1, 1994. It is a NASA mission as part of the International Solar Terrestrial Physics (ISTP) program, which is designed to study the plasma and waves in the solar wind (at the L1 Lagrangian point) and terrestrial magnetosphere. The *Wind* orbit trajectories in the GSE XY plane from November 1, 1994 to June 1, 2016 is summarized in Figure 2.5. After 2004 until now, *Wind* has been staying in a stable 'halo' orbit around L1. Before 2004, *Wind* made

numerous crossings of the terrestrial bow shock and spent significant time in the terrestrial foreshock region. This provides good opportunities to study the plasma physics intrinsic to the collisionless terrestrial bow shock and the foreshock upstream of the shock. Also, *Wind* can monitor the interplanetary (IP) shocks, which is important for both space weather predictions and fundamental plasma physics.

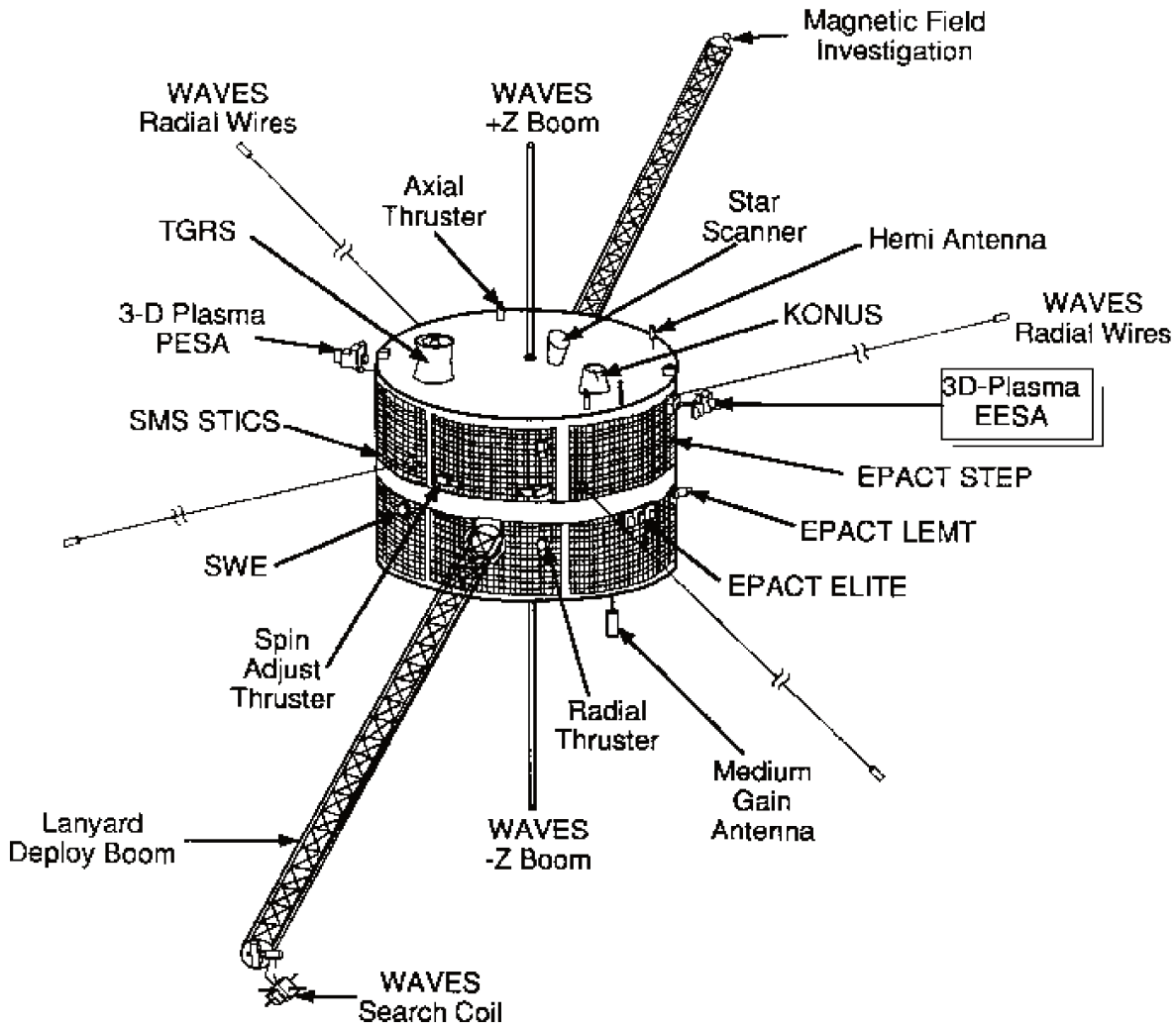


Figure 2.6 – *Wind* spacecraft and scientific payloads. *Wind* instruments can be divided into two categories: field and particle suites. Courtesy of Harten and Clark (1995).

An array of instruments are deployed onboard *Wind*, which can be divided into two categories (field and particle suites). As is shown in Figure 2.6, the scientific payloads include: the Magnetic Field Investigation (MFI) (Lepping et al., 1995), the Radio and Plasma Wave Investigation (WAVES) (Bougeret et al., 1995), Three-Dimensional Plasma and Energetic Particle Investigation (3DP) (Lin et al., 1995), the Solar Wind Experiment (SWE) (Ogilvie et al., 1995), the Solar Wind and Suprathermal Ion Composition Experiment (SMS) (Gloeckler et al., 1995), the Energetic Particles: Acceleration, Composition, and Transport (EPACT) investigation (von

Rosenvinge et al., 1995), KONUS (Aptekar et al., 1995), and the Transient Gamma-Ray Spectrometer (TGRS) (Owens et al., 1995).

After the launch, *Wind* continues to provide excellent measurements of plasma and waves in spite of its advanced age. Due to the high-quality data and the special orbit design, *Wind* has shown its high capability to examine the shock physics (i.e. particle distributions and wave analysis) under various plasma environments: terrestrial bow shock (e.g., Kellogg et al., 1996; Bale et al., 2002; Kellogg, 2003), terrestrial foreshock (e.g., Kellogg et al., 1996; Bale et al., 1996; Bale et al., 1998; Kellogg et al., 1999; Kellogg, 2003; Wilson et al., 2013; Wang et al., 2015), and IP shock (e.g., Bale et al., 1999; Kellogg, 2003; Wilson et al., 2007; Wilson et al., 2009; Wilson et al., 2012; Wilson et al., 2017; Pulupa and Bale, 2008; Pulupa et al., 2011; Liu et al., 2006a; Liu et al., 2018; Liu, 2018). Most of these studies depend on the measurements from *Wind*/MFI, *Wind*/WAVES, *Wind*/3DP, and *Wind*/SWE. In Chapter 5 of this thesis, *in situ* measurements from *Wind*/MFI, *Wind*/3DP and the thermal noise receiver (TNR) onboard *Wind*/WAVES (Bougeret et al., 1995) have been used to do the analysis. PSP inherits most of its scientific payloads from *in situ* detectors onboard *Wind*, which have been introduced in section 1 of this chapter. Also, some details about the detectors onboard *Wind* are presented in a parallel way with the scientific analysis in Chapter 5. Below, *Wind*/3DP, *Wind*/WAVES, and *Wind*/MFI are summarized in a brief way.

2.1 Electrostatic Detectors: 3DP

Wind/3DP is an instrument suite designed to make measurements of the full three-dimensional distribution of thermal, suprathermal and energetic electrons and ions in the solar wind (Lin et al., 1995). It consists of two sensor packages mounted on short radial booms (0.5 m) extended out from the spacecraft body (see Figure 2.6), including electrostatic analyzers and solid-state telescopes. Here, we focus on the electrostatic analyzers which contain a pair of ion detectors (PESA-Low and PESA-High) and a pair of electron detectors (EESA-Low and EESA-High). Different detectors are set with different geometry factors to cover different ranges of energies. The EESA-Low analyzer covers the energy range from 3 eV to 1.1 keV, whereas the EESA-High analyzer detects electrons of 300 eV to 30 keV. Both instruments have operational fields of view of $180^\circ \times 14^\circ$ and 15 logarithmically spaced energy channels. The PESA-Low instrument measures ions from as low as 100 eV to as high as 10 keV with 14 different energy channels, which is designed primarily to provide solar wind bulk properties (i.e. ion density, velocity, and temperature). Since PESA-Low is designed to orient itself along the bulk flow direction to capture the solar wind flow, it covers a narrower range of pitch-angle compared to the other three detectors. The PESA-High instrument measures ions of 80 eV to 30 keV at 15 different energies. Each detector sweeps out $4 \times \pi$ steradians in space to give a full distribution in one spacecraft spin (with the spin period being 3 seconds). The data are combined onboard with 88 angular bins for each detector. We note that SPAN-E (SPAN-I) onboard PSP/SWEAP (see section 1.2) is inherited from EESA-Low (PESA-Low) on board *Wind*/3DP.

2.2 Waves: Radio and Plasma Wave Investigation

Wind/WAVES instrument suite has similar scientific goals and measurement objectives as PSP/FIELDS (see section 1.1). *Wind*/WAVES detects electric fields and high-frequency magnetic fields, but not low-frequency magnetic fields (Bougeret et al., 1995). As is shown in Figure 2.6, *Wind*/WAVES sensors are composed of three orthogonal electric field dipole antennas for measuring electric field and three orthogonal search coil magnetometers for measuring high-frequency (AC) magnetic fields. *Wind*/WAVES receivers include Low Frequency FFT receiver called FFT (0.3 Hz to 11 kHz), Thermal Noise Receiver called TNR (4–256 kHz), Radio receiver band 1 called RAD1 (20–1040 kHz), Radio receiver band 2 called RAD2 (1.075–13.825 MHz), and the Time Domain Sampler called TDS. The combinations of TNR, RAD1 and RAD2 share similar measurement objectives and instrument configurations with RFS/FIELDS (see section 1.3) regardless of different receiver design, which are of interests for this thesis. TNR, RAD1 and RAD2 are connected to the 2×50 m thin wire electric dipole antennas (before broken by dust impacts), designed to measure remote radio wave emission and *in situ* quasi-thermal noise. TNR is especially designed to measure electron quasi-thermal noise combining five logarithmically spaced (overlapping) frequency bands (A, B, C, D and E, with the standard frequency resolution being $\Delta f/f = 4.3\%$). Typically, in normal mode of operation (ACE mode), spectra are acquired every 4.5 s. The dynamic and frequency ranges of RAD1 and RAD2 are designed to cover Type II and III radio bursts from several radii above the surface of the Sun to 1 AU. Furthermore, *in situ* ion acoustic and Langmuir waves are also visible in TNR.

2.3 Fluxgate Magnetometer: MFI

Wind/MFI is composed of dual triaxial fluxgate magnetometers (see Figure 2.6), designed to measure low-frequency magnetic fields (Lepping et al., 1995). The MFI has a very flexible commandable dynamic range of ± 4 nT to $\pm 65,536$ nT, with the corresponding digital resolution ranging from ± 0.001 nT to ± 16 nT. The sensor noise level is very low (< 0.006 nT) for 0–10 Hz signals. The sample rates are typically 10.87 samples/s and can sometimes reach to 44 samples/s, which are of interests for wave analysis (i.e. low-frequency magnetic whistler waves) in this thesis.

Chapter 3

Solar Wind Energy Flux Observations in the Inner Heliosphere: First Results from Parker Solar Probe

Objectives

Based on *in situ* plasma measurements from *Helios*, *Ulysses*, and *Wind* at greater distances and various latitudes, the solar-wind energy flux appears as a global solar constant, which is independent of the solar-wind speed and latitude within 10%, and varies weakly over the solar cycle (Le Chat et al., 2012). *In situ* field and plasma measurements from Parker Solar Probe offer us an opportunity to estimate the solar wind energy flux closer to the Sun than previously derived. In this chapter, we investigate the solar wind energy flux as close to the Sun as $27.8 R_{\odot}$. Main results and large parts of the text are extracted from Liu et al., 2021 (A&A).

Contents

1	Introduction	42
2	Data Analysis	43
2.1	n_{α} Estimation: Difference Between n_e and n_p	44
3	Observations and Results	45
3.1	Overview of E01, E02, E04 and E05	46
3.2	Distributions of Energy Flux and Variation with Distance	50
4	Discussion and Conclusions	53

1 Introduction

The question of how the solar wind is produced and accelerated is unsolved since its discovery about sixty years ago (Parker, 1958a; Neugebauer and Snyder, 1962) and "we cannot state at the present time why the Sun is obliged by the basic laws of physics to produce the heliosphere" (Parker, 2001). An important property of the solar wind is its energy flux, which is similar in the whole heliosphere and in the fast and slow wind (eg., Schwenn and Marsch, 1990; Meyer-Vernet, 2006b; Le Chat et al., 2009; Le Chat et al., 2012), and much more so than the particle flux itself. The energy flux is of a similar fraction of the luminosity for Solar-like and cool giant stars, which suggests that stellar winds may share a basic process for their origin and acceleration (Le Chat et al., 2009). Investigations of the solar wind energy flux in the inner heliosphere are of significant importance for astrophysics but still very few.

The average solar wind energy flux scaled to one solar radius of about 70 W m^{-2} from long-term Helios and Ulysses observations is close to 10^{-6} times the solar luminosity - a fraction similar to that of a number of other stars (Meyer-Vernet, 2006b; Meyer-Vernet, 2007). With a much larger solar wind data set from several spacecraft at various distances and latitudes, an average value of $79 \pm 18 \text{ W m}^{-2}$ was found between 1976 and 2012 (Le Chat et al., 2012), whereas an average value of about 60 W m^{-2} was found with OMNI data at 1 AU between 2011 and 2014 (McComas et al., 2014). Helios 1 and 2 orbits ranged from 0.3 to 1 AU (Schwenn et al., 1975), whereas Ulysses operated between 1 and 4 AU (Wenzel et al., 1992). The ongoing pioneering mission Parker Solar Probe (PSP) (Fox et al., 2016) orbits with perihelia of heliocentric distances decreasing from 35.7 solar radii (R_{\odot}) to $9.86 R_{\odot}$ within five years. Four instruments onboard PSP including Fields experiment (FIELDS) (Bale et al., 2016), Solar Wind Electrons Alphas and Protons investigation (SWEAP) (Kasper et al., 2016), Integrated Science Investigation of the Sun (IS \odot IS) (McComas et al., 2016), and Wide-field Imager for Solar PRobe (WISPR) (Vourlidas et al., 2016) are working together to provide both *in situ* and remote observations. *In situ* field and plasma measurements of the inner heliosphere from FIELDS/PSP and SWEAP/PSP offer an opportunity to estimate the solar wind energy flux closer to the Sun than previously derived.

FIELDS/PSP provides accurate electron density and temperature measurements via Quasi-thermal noise (QTN) spectroscopy. This technique has been used in a number of space missions (eg., Meyer-Vernet, 1979; Meyer-Vernet et al., 1986; Meyer-Vernet et al., 2017; Issautier et al., 1999b; Issautier et al., 2001b; Issautier et al., 2008; Maksimovic et al., 1995; Moncuquet et al., 2005; Moncuquet et al., 2006), and is an effective and efficient tool. Recently, preliminary solar wind electron measurements were derived from the plasma QTN spectra observed by the Radio Frequency Spectrometer (RFS/FIELDS) (see Pulupa et al., 2017; Moncuquet et al., 2020; Maksimovic et al., 2020). SWEAP/PSP consists of the Solar Probe Cup (SPC) and the Solar Probe Analyzers (SPAN) (Kasper et al., 2016; Case et al., 2020; Whittlesey et al., 2020). SPC is a fast Faraday Cup designed to measure the one dimensional velocity distribution function (VDF) of ions and sometimes electrons and SPAN is a combination of three electrostatic analyzers operated to measure the three dimensional VDFs of ions and electrons. Due to the instrument

design, SPAN-Ai instrument cannot observe the complete core of the solar wind ions in the first several encounters and SPC can provide ion observations during SPAN's observational gaps by pointing at the Sun during the encounter phase of each orbit although SPC sometimes cannot see the whole distribution (Kasper et al., 2016; Whittlesey et al., 2020; Case et al., 2020).

Therefore, we calculate the solar wind energy flux with both the RFS/FIELDS/PSP (electron) and SPC/SWEAP/PSP (ion) observations during Encounters one (E01), two (E02), four (E04) and five (E05) (Section 2). The minimum heliocentric distance is $35.66 R_\odot$ for E01 and E02 and around $27.8 R_\odot$ for E04 and E05. In Section 3, we analyze the relationship between the energy flux, the bulk speed and the plasma density (Section 3.1). How the total energy flux and each component of it evolve with increasing heliocentric distance is studied in Section 3.2. In Section 4, the results are summarized and discussed.

2 Data Analysis

The solar wind energy flux (W), which includes the kinetic energy ($W_{kinetic}$), the enthalpy ($W_{enthalpy}$), and the heat flux (Q), is expressed as

$$W = W_{kinetic} + W_{enthalpy} + W_g + Q \quad (3.1)$$

where we have neglected the wave energy flux and added the flux equivalent to the energy required to overcome the solar gravitation W_g (Schwenn and Marsch, 1990). Q is the sum of the electron heat flux q_e and proton heat flux q_p . Values of q_e range from 10^{-4} to 10^{-3} W m^{-2} during E01, E02, E04 and E05 of PSP orbits (Halekas et al., 2020a; Halekas et al., 2020b), which can be neglected (See section 3). Note that at 1 AU, q_e measured with Helios is $q_e \approx 10^{-6} \text{ W m}^{-2}$ (Pilipp et al., 1990), while q_p ranges from about 10^{-7} (1 AU) to 10^{-5} (0.3 AU) W m^{-2} (Hellinger et al., 2011). We therefore neglect both the electron and proton heat flux compared to the other components, so that

$$W = W_{kinetic} + W_{enthalpy} + W_g \quad (3.2)$$

where the expressions of the different components are given below. Note that the enthalpy can be neglected at 1 AU (eg., Le Chat et al., 2012). However, this contribution cannot be ignored closer to the Sun, where it contributes to about 5% of the total energy flux (See section 3.2).

$$W_{kinetic} = n_p m_p V_p \frac{V_p^2}{2} + n_\alpha m_\alpha V_\alpha \frac{V_\alpha^2}{2} \quad (3.3)$$

$$\begin{aligned} W_{enthalpy} &= n_e V_p \frac{5k_B T_e}{2} + n_p V_p \frac{5k_B T_p}{2} + n_\alpha V_\alpha \frac{5k_B T_\alpha}{2} \\ &\approx n_e V_p \frac{5k_B T_e}{2} + n_p V_p \frac{5k_B T_p}{2} \end{aligned} \quad (3.4)$$

$$W_g = (n_p m_p V_p \frac{GM_\odot}{R_\odot} + n_\alpha m_\alpha V_\alpha \frac{GM_\odot}{R_\odot}) (1 - \frac{R_\odot}{r}) \quad (3.5)$$

Here, n_p , m_p , n_α , and m_α denote the proton number density, proton mass, α particle number density, and α particle mass, respectively. V_p (V_α) is the solar wind proton (α) bulk speed, n_e the electron number density, k_B the Boltzmann constant, T_p (T_e) the proton (electron) temperature, G the gravitational constant, M_\odot the solar mass, R_\odot the solar radius, and r the heliocentric distance of PSP. Note that T_e is derived from the core electron temperature T_c and suprathermal electron temperature T_h with $T_e = T_c + (n_h/n_e)T_h$, where n_h denotes the suprathermal electron density and n_h/n_e is assumed to be 0.1 (see Moncuquet et al., 2020; Štverák et al., 2009). In Equations 3.3, 3.4 and 3.5, we assume that $V_\alpha \approx V_p$, and ignore the enthalpy of the α particles since n_α is much smaller than n_e (and both V_α and T_α are not available). The energy flux is scaled to one solar radius as written below, yielding the total energy required at the base to produce the wind - a basic quantity for understanding the wind production and comparing the Sun to other wind-producing stars.

$$W_{R_\odot} = W(r) \frac{r^2}{R_\odot^2} \quad (3.6)$$

We use the level-3 ion data (moments) from SPC/SWEAP (Kasper et al., 2016; Case et al., 2020) and the electron parameters deduced from the simplified QTN method with the observations from RFS/FIELDS (Moncuquet et al., 2020; Pulupa et al., 2017). For each encounter, only 12-day high-time-resolution observations near the perihelion are considered: SPC collects one sample or more every 0.874 seconds and the QTN datasets have a 7-sec resolution. Since the resolution of the datasets from SPC is different from that of the QTN datasets, we interpolate them to the same resolution to do the calculations. At the beginning of the PSP mission, α particle observations obtained directly from SPC/SWEAP cannot be used due to calibration issues. Also, n_p is too different from n_e (being smaller than n_e by more than 30% on average) with an estimation of $\langle n_\alpha/n_e \rangle = \langle (n_e - n_p)/(2 \times n_e) \rangle \approx 16.0\%$, which implies unrealistic values for n_α obtained based on plasma neutrality. We propose to use n_e from the QTN technique to in turn derive n_α and then n_p , which is detailed in section 2.1. The resulting values of n_α and n_p are used to calculate W and then W_{R_\odot} .

2.1 n_α Estimation: Difference Between n_e and n_p

As mentioned above, α particle observations obtained directly from SPC/SWEAP/PSP are not suggested for scientific analysis due to calibration problems. Another possible solution is to deduce n_α from n_p and n_e based on plasma neutrality. Figure 3.1 (a), (b), (c) and (d) present the estimated n_α/n_e of E01, E02, E04 and E05, respectively. The values of n_α/n_e are obtained with n_p (from SPC) and n_e (from QTN), where $\langle n_\alpha/n_e \rangle$ is around 16% for all the four encounters. The difference between n_p and n_e is too large to be reasonable, suggesting that the measurements of n_p are in general underestimated. Past studies (e.g., Kasper et al., 2007; Kasper et al., 2012; Alterman and Kasper, 2019; Alterman et al., 2020) showed that the α particle abundance ($A_{He} = n_\alpha/n_p$) rarely exceeds $A_{He} \sim 5\%$ especially when the bulk speed of the solar wind is below $V_p = 400 \text{ km s}^{-1}$. Recent work (Alterman et al., 2020) showed that at 1 AU A_{He} ranges from 1% to 5% during the Solar Cycle 23 and 24 and predicted that 1%

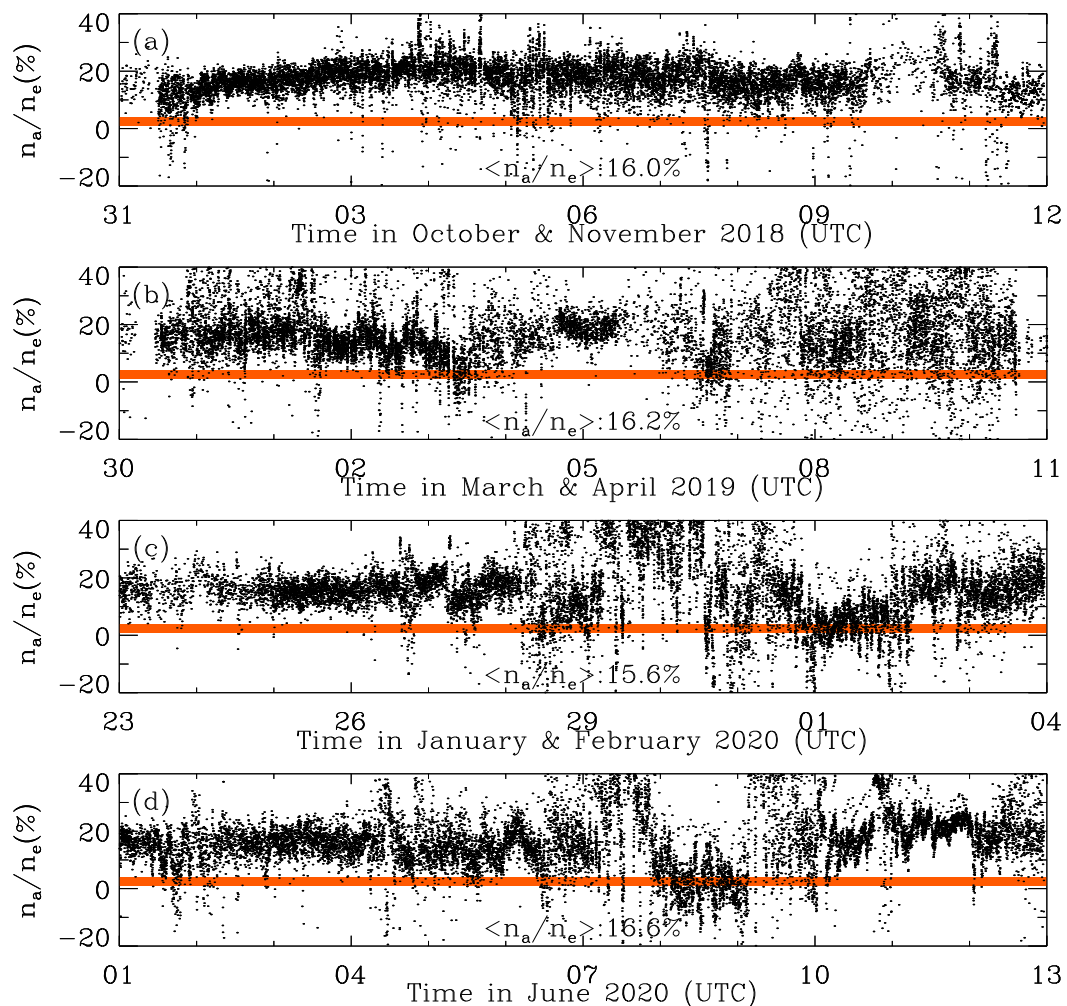


Figure 3.1 – Estimate of the difference between n_e measured by QTN and n_p measured by SPC (black dots): panels (a), (b), (c) and (d) show the results of encounters E01, E02, E04 and E05, respectively. Based on plasma neutrality, n_α shown in the figure is obtained with $n_\alpha = (n_e - n_p)/2.0$. On each panel, the expected values of n_α/n_e (from 1 % to 4 %, shaded areas) are plotted for reference (Alterman et al., 2020).

$< A_{He} < 4\%$ at the onset of Solar Cycle 25 (solar minimum). We assume that A_{He} (which is almost the same as n_α/n_e) of the solar wind remains the same when it propagates from the inner heliosphere to 1 AU (Viall and Borovsky, 2020). As a result, we deduce n_α with n_e where n_α/n_e is a free parameter ranging from 1% to 4% (Alterman et al., 2020). Then, this enables us to determine n_p based on the plasma neutrality.

3 Observations and Results

During the first and second encounter of PSP, it reached the perihelion of $35.66 R_\odot$ (~ 0.17 AU) on November 06th, 2018 and April 5th, 2019, respectively. For both E04 and E05, PSP arrived at the perihelion of $27.8 R_\odot$ (~ 0.13 AU) on January 29th, 2020 and June 7th, 2020, respectively. In section 3.1, we give an overview of the PSP measurements of solar wind density,

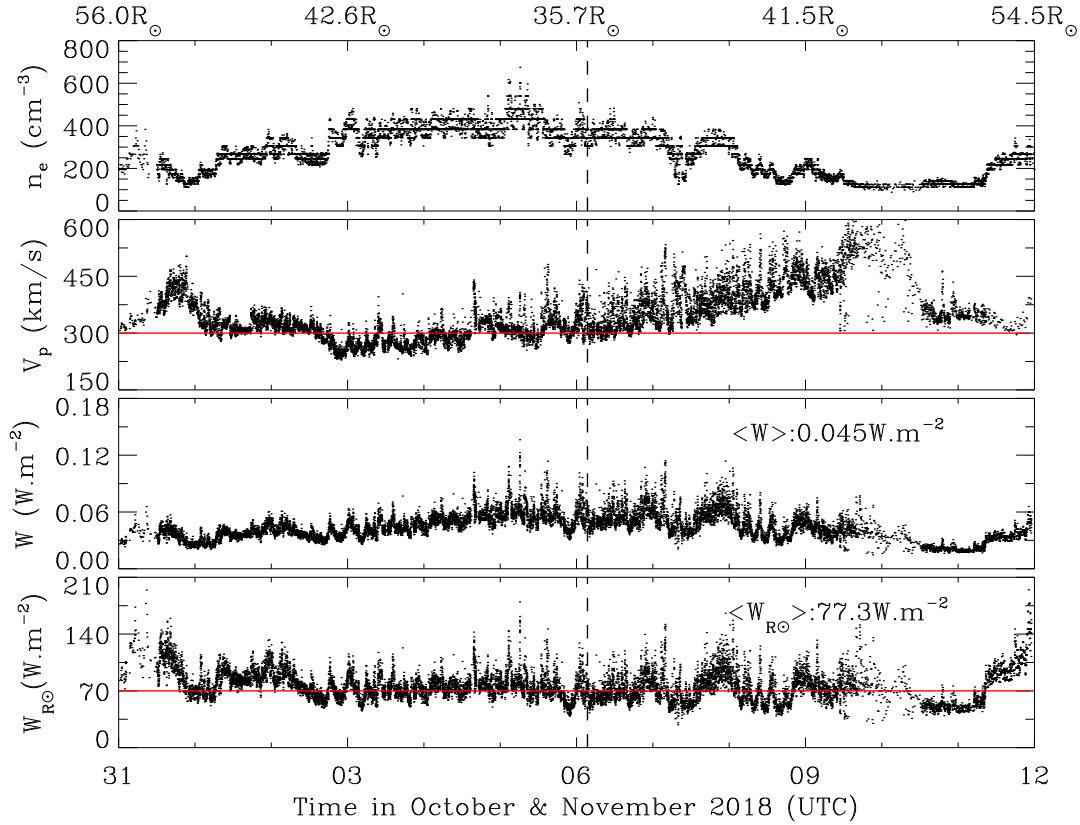


Figure 3.2 – Solar wind density, speed and energy flux measurements by PSP during Encounter One (from 10/31/2018 00:00:00 to 11/12/2018 00:00:00 UTC). First panel: QTN electron density. Second panel: proton bulk speed. A red horizontal line ($V_p = 300 \text{ km s}^{-1}$) is plotted for reference. Third panel: solar wind energy flux W . Fourth panel: solar wind energy flux normalized to one solar radius W_{R_\odot} (black) with a red horizontal line ($W_{R_\odot} = 70 \text{ W m}^{-2}$) superimposed for reference. The heliocentric distance (in unit of Solar radius R_\odot) is indicated at the top of the first panel and the black vertical line denotes the perihelion of the PSP orbit.

speed and energy flux for all available encounters including E01, E02, E04, and E05. Note that E03 observations are not considered due to the lack of SPC observations near the perihelion. For each encounter, 12-day observations around the perihelion are used for calculations. The heliocentric distance for both E01 and E02 ranges from 35.66 to about $55 R_\odot$, and it ranges from 27.8 to about $57 R_\odot$ for both E04 and E05. In section 3.2, we combine the observations from E01, E02, E04, and E05 to show the histogram distributions and the evolution of the energy flux as a function of the heliocentric distance.

3.1 Overview of E01, E02, E04 and E05

Figure 3.2 shows an overview of the PSP measurements of the solar wind density, speed and energy flux during E01 (from 10/31/2018 00:00:00 to 11/12/2018 00:00:00 UTC). The top panel presents the electron number density (n_e) obtained by the QTN method. In the second panel, the proton bulk speed is shown. The third and fourth panels present the solar wind energy flux (W , from equation 3.2) and its value scaled to one solar radius (W_{R_\odot} , from equation

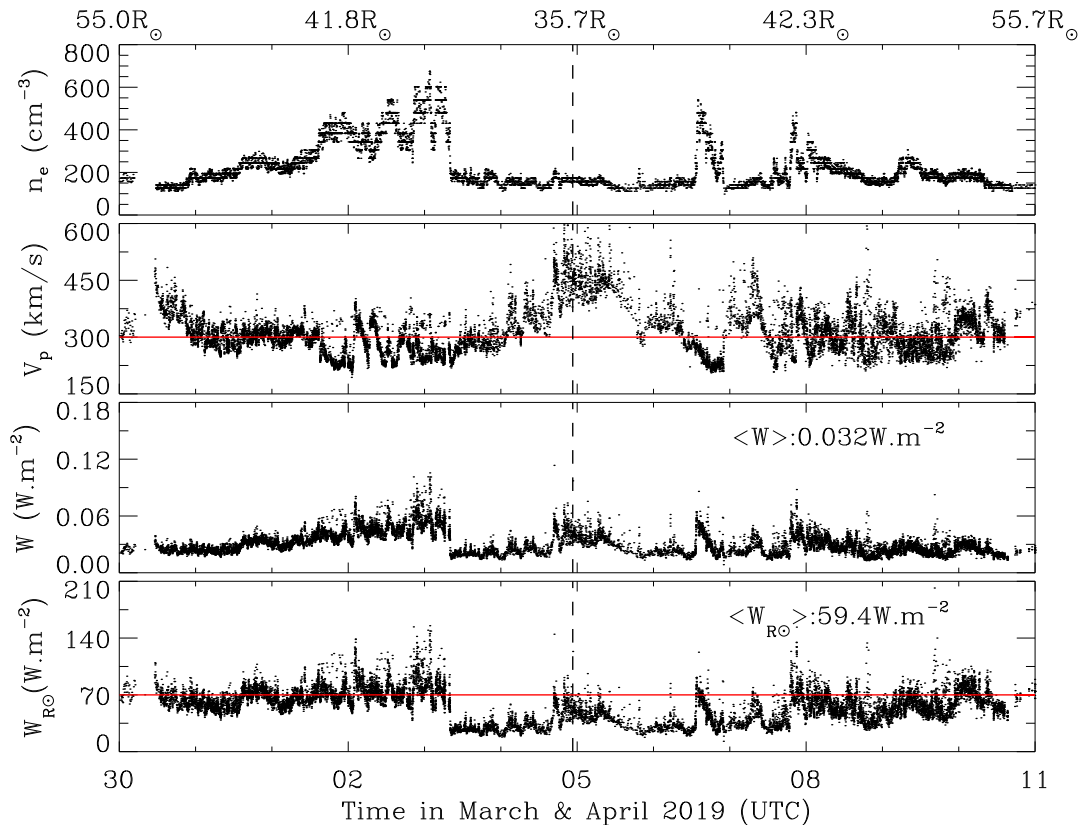


Figure 3.3 – Solar wind density, speed and energy flux measurements by PSP for Encounter Two (03/30/2019 00:00:00 to 04/11/2019 00:00:00 UTC). This figure follows the same format as that of Figure 3.2.

3.6), respectively. In Figure 3.2, n_α and n_p are computed from n_e based on $n_\alpha/n_e = 2.5\%$ for calculating W and W_{R_\odot} . Most of the time, V_p varies around 300 km s^{-1} , and W_{R_\odot} varies around 70 W m^{-2} . The average values of W and W_{R_\odot} are 0.045 W m^{-2} and 77.3 W m^{-2} , respectively. The average value of W_{R_\odot} of E01 is consistent with the previous long-term observations (eg., Le Chat et al., 2012) (around 79 W m^{-2}). Note that W_{R_\odot} does not vary much with V_p when V_p increases abruptly (i.e. from November 8th to 10th, 2018).

Figure 3.3, which follows the same format as Figure 3.2, summarizes the PSP measurements of solar wind density, speed and energy flux during E02 (from 03/30/2019 00:00:00 to 04/11/2019 00:00:00 UTC). Note that n_e shows two successive low plateaus near the perihelion of E02 (from April 3rd to 8th, 2019 UT), as shown in the first panel of Figure 3.3, whereas V_p shows two high peaks. This is in agreement with the well-known anticorrelation between the solar wind speed and density (eg., Richardson et al., 1996; Le Chat et al., 2012). Both W_{R_\odot} and W also show two low plateaus near the perihelion of E02 (from April 3rd to 8th, 2019 UT), similar to the solar wind density. Elsewhere, V_p remains around 300 km s^{-1} and W_{R_\odot} varies around 70 W m^{-2} . The mean values of W and W_{R_\odot} during E02 are 0.032 W m^{-2} and 59.4 W m^{-2} , respectively.

Similarly, Figure 3.4 illustrates the PSP observations during E04 (from 01/23/2020 00:00:00 to 02/04/2020 00:00:00 UTC). It shows that V_p varies around 375 km s^{-1} before January 29th,

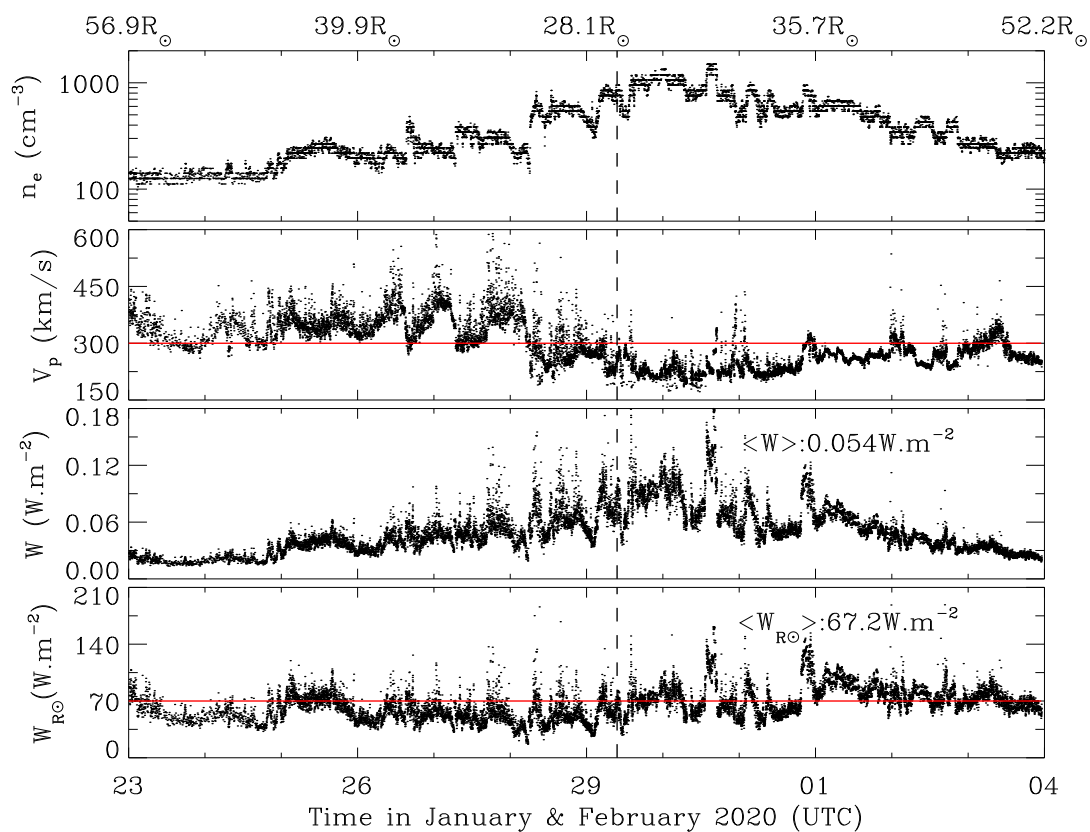


Figure 3.4 – Solar wind density, speed and energy flux measurements by PSP for Encounter Four (from 01/23/2020 00:00:00 to 02/04/2020 00:00:00 UTC), which follows the same format as that of Figure 3.2.

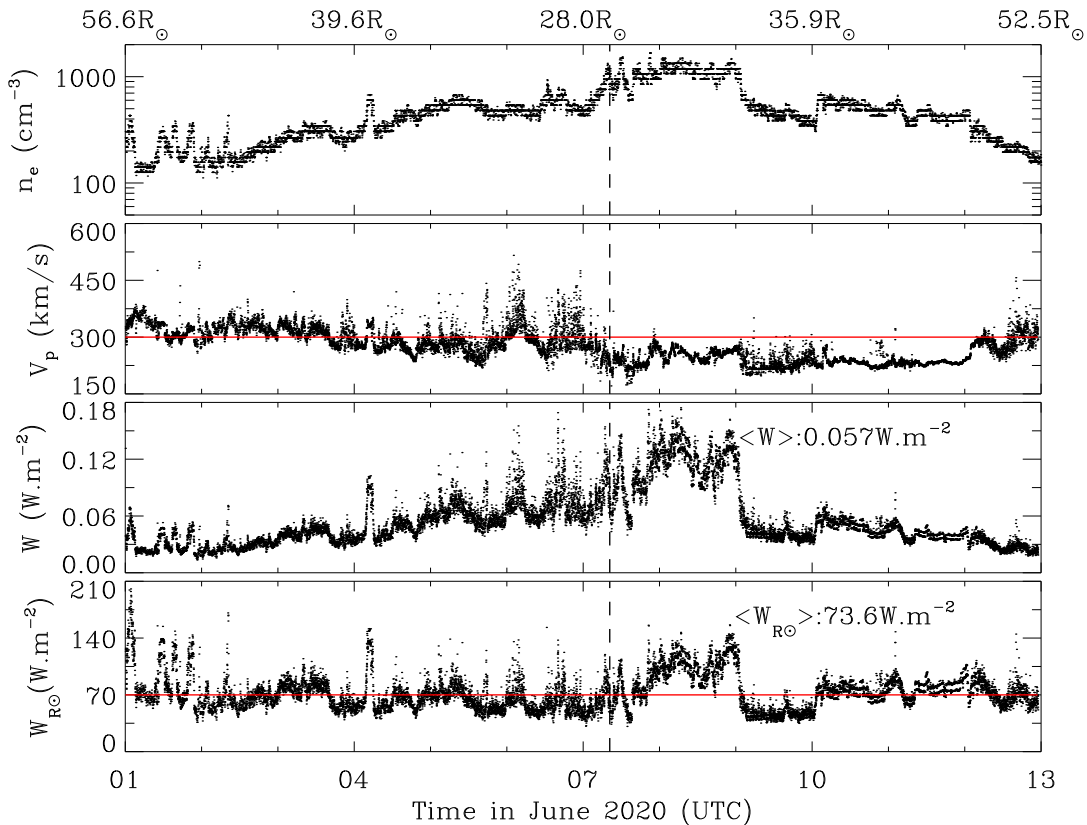


Figure 3.5 – Solar wind density, speed and energy flux measurements by PSP for Encounter Five (from 06/01/2020 00:00:00 to 06/13/2020 00:00:00 UTC), which follows the same format as that of Figure 3.2.

Table 3.1 – Energy Flux Average Value of Each Encounter

Energy Flux (W m^{-2})	E01	E02	E04	E05
$\langle W \rangle$	0.045	0.032	0.054	0.057
$\langle W_{R_{\odot}} \rangle$	77.3	59.4	67.2	73.6

2020 and is predominantly 225 km s^{-1} afterward. $W_{R_{\odot}}$ varies around 70 W m^{-2} and does not change significantly even when V_p decreases sharply from January 28th to 30th, 2020. The average values of W and $W_{R_{\odot}}$ for E04 are 0.054 W m^{-2} and 67.2 W m^{-2} , respectively.

Figure 3.5 is similar to Figure 3.2, 3.3 and 3.4 but for E05 (from 06/01/2020 00:00:00 to 06/13/2020 00:00:00 UTC). During this encounter, V_p usually stays at around 300 km s^{-1} except from June 7th to 12th, 2020 during which V_p remains approximately at 225 km s^{-1} . For E05, $W_{R_{\odot}}$ is predominantly about $W_{R_{\odot}} = 70 \text{ W m}^{-2}$. From June 7th to 10th, 2020, both W and $W_{R_{\odot}}$ experience sharp changes which results from sharp variation of n_e . The corresponding values of both W and $W_{R_{\odot}}$ are larger (smaller) than the ambient values at the beginning (in the end) of this time period. The average values of W and $W_{R_{\odot}}$ for E05 are 0.057 W m^{-2} and 73.6 W m^{-2} , respectively.

Table 3.1 summarizes the average values of the energy flux $\langle W \rangle$ and the values normalized

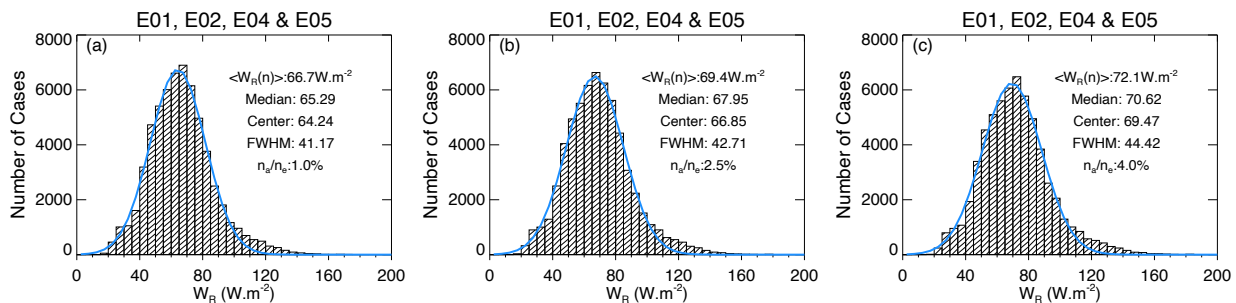


Figure 3.6 – Distributions of the solar wind energy flux (W_R) normalized to one solar radius with a ratio between α particle number density (n_α) and electron number density (n_e) ranging from 1% to 4% for Encounters E01, E02, E04 and E05. Figs (a), (b), and (c) assume $n_\alpha/n_e = 1\%$, 2.5%, and 4%, respectively to illustrate the uncertainty due to the absence of α measurements. Average and median values of each histogram are indicated with Gaussian fits superimposed in blue. Center value and standard deviation (full-width-half-maximum) of the Gaussian fit are also presented.

to one solar radius $\langle W_{R_\odot} \rangle$ for the four PSP encounters mentioned above. Note that the sequence difference between $\langle W_{R_\odot} \rangle$ and $\langle W \rangle$ results from the r^{-2} normalization when deriving W_{R_\odot} , whereas the individual flux tubes vary differently. It is remarkable that these values of $\langle W_{R_\odot} \rangle$ are close to those found previously (Meyer-Vernet, 2006b; Le Chat et al., 2012) despite the smaller time durations and latitude extensions of PSP observations. Note the relatively low $\langle W_{R_\odot} \rangle$ of E02 and the low solar wind density near the perihelion of PSP orbit (see Figure 3.3). The dilute transient solar wind structure observed around the perihelion contributes to explain this relatively low value compared to the previous long-term observations of Le Chat et al. (2012). The origins for the low plateaus of plasma density related to high peaks of bulk speed are discussed by Rouillard et al. (2020). In the previous work (Le Chat et al., 2012), the values have been averaged over a solar rotation (~ 27.2 days) to reduce the effect of transient events such as Coronal Mass Ejections (CMEs) or Co-rotating Interaction Regions (CIRs). Although CMEs or small-scale flux ropes are observed by PSP during E01 (e.g. Hess et al., 2020; Zhao et al., 2020; Korreck et al., 2020; Lavraud et al., 2020; Szabo et al., 2020), $\langle W_{R_\odot} \rangle$ of E01 (77.3 W m^{-2}) is almost the same as the long-term averaged value (see Le Chat et al., 2012).

3.2 Distributions of Energy Flux and Variation with Distance

Figure 3.6 shows the distributions of W_{R_\odot} combining the observations from E01, E02, E04 and E05. Based on the assumption that n_α/n_e ranges from 1.0% to 4.0%, we calculate W_{R_\odot} with $n_\alpha/n_e = 1.0\%$, 2.5%, and 4.0%, and the corresponding results are shown in Figure 3.6 (a), (b), and (c), respectively. Each histogram distribution is fitted with a Gaussian function (blue line) and the center value (the most probable value) and standard deviation (full-width-half-maximum which is short for FWHM) are shown together with the mean and median values. It is remarkable that the histograms of W_{R_\odot} are very symmetrical and nearly Gaussian. The difference between the average, median, and most probable fit value of W_{R_\odot} is very small (less than 3%). With a fixed n_α/n_e ratio, the uncertainties of $\langle W_{R_\odot} \rangle$ resulting from the uncertainties

of the plasma parameters n_e , V_p , T_e , and T_p are 10.0%, 4.1%, 0.85%, and 0.28%, respectively. We use the uncertainty of n_e provided by the QTN method and the uncertainty of T_e is estimated to be around 20% (Moncuquet et al., 2020). The estimated uncertainties of V_p and T_p are 3.0% and 19%, respectively (Case et al., 2020). When n_α/n_e increases from 1.0% to 2.5% and then to 4.0%, $\langle W_{R_\odot} \rangle$ also increases from 66.7 W m⁻² to 69.4 W m⁻² and then to 72.1 W m⁻², as well as the values of FWHM (see Figure 3.6). We thus deduce that the uncertainty of W_{R_\odot} resulting from the variation of n_α/n_e is around 4%. $\langle W_{R_\odot} \rangle$ from the E01, E02, E04, and E05 observations is around 69.4 W m⁻² with a total uncertainty that we estimate to be at most 20.0%, which is consistent with previous results (e.g. Schwenn and Marsch, 1990; Meyer-Vernet, 2006b; Le Chat et al., 2009; Le Chat et al., 2012; McComas et al., 2014).

Figure 3.7 presents W , $W_{kinetic}/W$, $W_{enthalpy}/W$, and W_g/W as a function of heliocentric distance in units of solar radius R_\odot , which includes the observations from E01, E02, E04 and E05. Levenberg-Marquardt least-squares fit is performed to each quantity and the fitted functions are shown in the figure. Note that the power index for W is -1.92 (near to -2.0), in agreement with Equation 3.6 used to scale the solar wind energy flux to one R_\odot . When PSP moves from 57.1 R_\odot to 27.8 R_\odot , $W_{kinetic}$, in order of magnitude, ranges from 10⁻³ to 10⁻² W m⁻², while $W_{enthalpy}$ and W_g range from 10⁻³ to 10⁻² W m⁻², and from 10⁻² to 10⁻¹ W m⁻², respectively. Further, as shown by Figure 3.7, W_g is the dominant term for W , $W_{kinetic}$ is the second dominant one and $W_{enthalpy}$ is the least. Even though the contribution of $W_{enthalpy}$ to W is still the least among the three components in the inner heliosphere, it reaches about 30% of the kinetic energy flux at the smallest distances and we cannot neglect it there anymore ($\langle W_{enthalpy} \rangle / \langle W \rangle \approx 5\%$). Note that since W_g exceeds $W_{kinetic}$ by a factor of about four, most of the energy supplied by the Sun to generate the solar wind serves to overcome the solar gravity. As is shown in the first panel of Figure 3.7, the energy flux can reach $W \approx 10^{-1}$ W m⁻² near the perihelia of PSP orbits whereas the corresponding electron heat flux is $q_e \approx 10^{-3}$ W m⁻² (see Halekas et al., 2020a; Halekas et al., 2020b). At most, q_e contributes to 1.0% of W , and proton heat flux q_p is usually much less than q_e . Therefore, neglecting the heat flux will not affect the conclusions in this work.

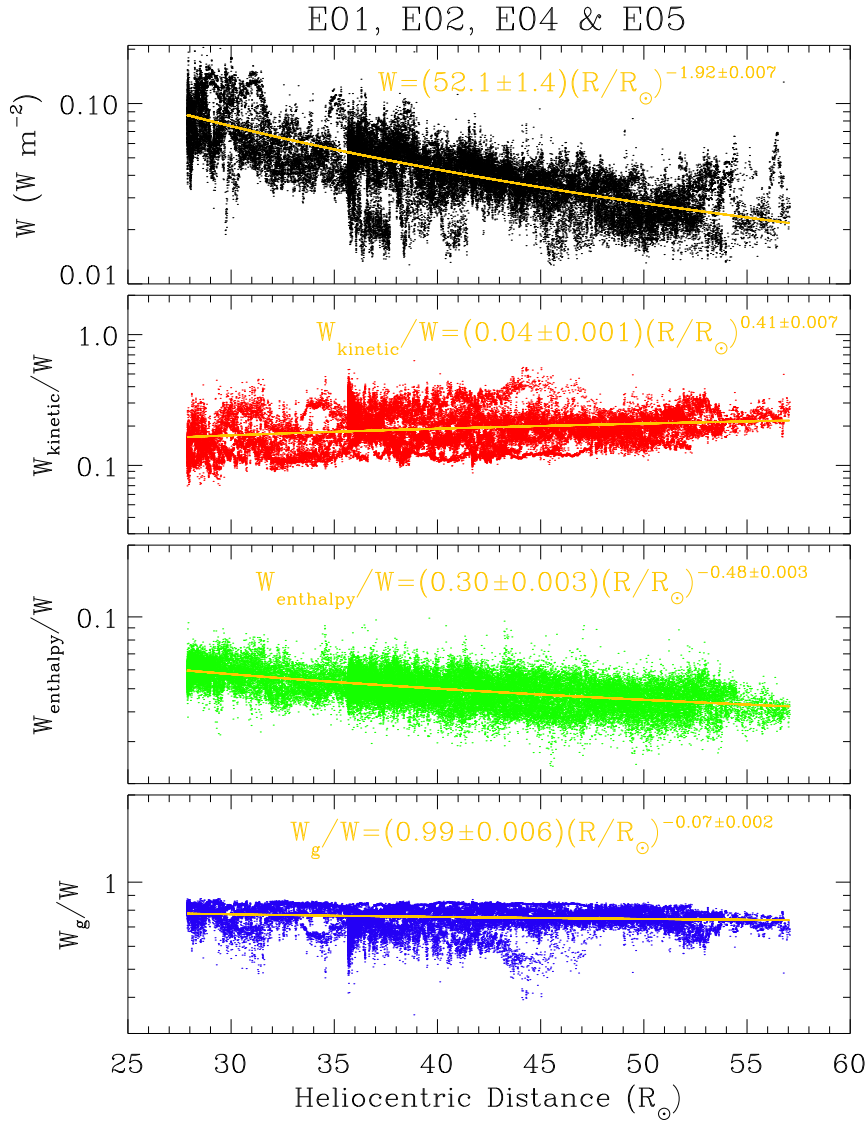


Figure 3.7 – Variation of W and its components with heliocentric distance combining observations from Encounter One (E01), Two (E02), Four (E04) and Five (E05). From top to bottom, evolution of W , W_{kinetic}/W , W_{enthalpy}/W , and W_g/W with heliocentric distance are shown, respectively. The fitted profile (yellow) is superimposed on each corresponding panel, respectively.

4 Discussion and Conclusions

This work presents the first analysis of the solar wind energy flux in the inner heliosphere (adding the flux equivalent to the energy necessary to move the wind out of the solar gravitational potential) with PSP observations. This covers heliocentric distances from 0.13 AU ($\sim 27.8 R_{\odot}$) to 0.27 AU ($\sim 57.1 R_{\odot}$) combining data from E01, E02, E04, and E05. This enables us to study the solar wind energy flux in the inner heliosphere, which is of great importance to understand the acceleration of the solar wind. Note that E03 is excluded due to the lack of the SPC observations near perihelion.

We find that the average value of $W_{R_{\odot}}$, $\langle W_{R_{\odot}} \rangle$, is about 69.4 W m^{-2} with a total uncertainty of at most 20%, which is similar to previous results based on long-term observations at greater distances and various latitudes (eg., Schwenn and Marsch, 1990; Meyer-Vernet, 2006b; Le Chat et al., 2009; Le Chat et al., 2012; McComas et al., 2014). This result confirms that this quantity appears as a global solar constant, which is of importance since it is often used to deduce the solar wind density from the speed (or the reverse) in global heliospheric studies and modelling (eg., Shen et al., 2018; McComas et al., 2014; McComas et al., 2017; McComas et al., 2020; Krimigis et al., 2019; Wang et al., 2020).

It is remarkable that the distributions of $W_{R_{\odot}}$ are nearly symmetrical and well fitted by Gaussians. This may be explained by the limited interactions between the solar wind and transient structures (e.g. CMEs, CIRs and so on) in the inner heliosphere (below 0.27 AU).

Normalizing the solar wind energy flux as $1/r^2$ assumes a radial expansion of solar wind, which does not hold true for individual flux tubes, especially close to the Sun. However, this normalization holds true when integrating over a whole sphere surrounding the Sun, so that a large data set is necessary to obtain a reliable result. It is thus noteworthy that with only 12-day observations for each encounter (E01, E02, E04 and E05) and a limited latitude exploration, we find the same normalized energy flux as previous long-term studies at various latitudes. This is consistent with the fact that our dataset yields an energy flux varying with heliocentric distance with a power index close to -2. It is also interesting to note that this normalized energy flux represents a similar fraction of solar luminosity as observed for a large quantity of stars (Meyer-Vernet, 2006b; Le Chat et al., 2012). Since this quantity represents the energy flux to be supplied by the Sun for producing the wind (eg., Meyer-Vernet, 1999; Schwadron and McComas, 2003), this similarity may provide clues to the physical processes at the origin of stellar winds (eg., Johnstone et al., 2015).

In this work, the heat flux is neglected when calculating the energy flux. When PSP gets much closer to the Sun, the contribution of the electron heat flux will become larger (see Halekas et al., 2020a; Halekas et al., 2020b). Furthermore, the solar wind protons often consist of two populations, a core and a beam drifting with respect to each other. The speed difference between them is typically of the order of the local Alfvén speed (Alterman et al., 2018). It is likely that the proton heat flux will also be more important closer to the Sun. Therefore, the heat flux will be considered in future work. Due to the lack of alpha particle observations, we make an assumption that $V_{\alpha} \approx V_p$. In fact, the differential speed between protons and alpha particles is

also typically of the order of the local Alfvén speed (e.g. Steinberg et al., 1996; Āurovcová et al., 2017; Alterman et al., 2018), so that it may affect the energy flux closer to the Sun. We await more data to come in the future PSP encounters to perform a long-term statistical study, with recovery of the well calibrated alpha parameters.

Chapter 4

Total Electron Temperature Derived from Quasi-Thermal Noise Spectroscopy In the Pristine Solar Wind: Parker Solar Probe Observations

Objectives

To accurately measure the radial electron temperature profile not only helps us to understand the energy transport in the solar wind but also provides an important ingredient to constrain thermally driven solar wind models. In this chapter, we apply the Quasi-thermal noise (QTN) technique using the high frequency part of the radio spectra on Parker Solar Probe (PSP) observations to derive the total electron temperature (T_e). Then, the radial evolution of T_e is examined with the heliocentric distance varying from about 13 to 60 R_\odot . We find that T_e decreases with the heliocentric distance as $\sim R^{-0.66}$, which is much slower than an adiabatic behavior. Furthermore, the T_e variations for different solar wind populations (i.e. divided by proton bulk speed (V_p) and mass flux) and the anticorrelated V_p - T_e are discussed. The main results and large part of texts are extracted from Liu et al., 2022 (A&A).

Contents

1	Introduction	56
2	Data Analysis	58
	2.1 Determination of T_e from QTN Spectroscopy	58
	2.2 Preliminary Cross Checking	61
3	Observations and Results	64
	3.1 Mean Radial Profiles of T_e	65
	3.2 Temperature gradients for different solar wind populations	68
	3.3 Anticorrelated parameters: V_p and T_e	69
4	Summary and Discussion	71

1 Introduction

Heat transport in the solar corona and wind, which is not completely understood, plays a key role in coronal heating and wind acceleration. Due to the large mass difference between ions and electrons, electrons mainly transport energy whereas ions transport momentum. Therefore, electrons are expected to play a key role in the thermally driven solar wind expansion. Furthermore, the accurately measured electron temperature radial profile is not only of prime interest to understand the energy transport in the solar wind but also an important ingredient to constrain the thermally driven solar wind models (e.g., Meyer-Vernet and Issautier, 1998; Issautier et al., 1999a; Issautier et al., 2001a; Maksimovic et al., 1997; Zouganelis et al., 2004). For simplicity, the electron temperature is generally assumed to be fitted with a power law of the distance to the Sun, assuming no large-scale temporal variations: $T_e = T_0 \times (R/R_\odot)^\beta$. β is observed to range between 0 (isothermal) and $-4/3$ (adiabatic), which indicates that electrons cool off with radial profiles spanning from nearly isothermal to almost adiabatic (e.g., Marsch et al., 1989; Pilipp et al., 1990; Issautier et al., 1998; Le Chat et al., 2011; Maksimovic et al., 2000; Štverák et al., 2015; Moncuquet et al., 2020). The large scatter in the measurements of β is not surprising and may be due to several reasons: i) it is difficult to separate genuine variations along stream flux tubes from those across them; ii) transient structures such as coronal mass ejections, co-rotating interaction regions and interplanetary shocks can cause nongeneric effects; iii) the observations from different spacecraft have been carried out in different latitudinal and radial ranges and/or in different phases of the solar activity; iv) classification of data based on the solar wind speed, Coulomb collisions and plasma beta has not always been done. In contrast, the exospheric solar wind models give another theoretical radial profile of the total electron temperature with the expression $T_e = T_0 + T_1 \times (R/R_\odot)^{-4/3}$ for $(R/R_\odot)^2 \gg 1$ (e.g., Meyer-Vernet and Issautier, 1998; Meyer-Vernet et al., 2003; Issautier et al., 2001a), which yields a profile that flattens at large distances, in agreement with Helios measurements (between 0.3 and 1 AU) (Marsch et al., 1989; Pilipp et al., 1990). Since this model has the same number of free parameters as the power-law model, it is difficult to distinguish both models from observations in a small radial range. Le Chat et al., 2011 has verified this fact with the Ulysses observations of high-speed solar wind during its first pole-to-pole latitude scan (from 1.5 to 2.3 AU).

Observations from Parker Solar Probe (PSP; Fox et al., 2016) indicate that there is an anticorrelation between the proton bulk speed V_p and the electron temperature T_e close to the Sun (e.g., Maksimovic et al., 2020; Halekas et al., 2020b; Halekas et al., 2022), whereas the correlation between the proton bulk speed V_p and the proton temperature T_p persists throughout the heliosphere (see Lopez and Freeman, 1986; Totten et al., 1995; Matthaeus et al., 2006; Démoulin, 2009, and references therein). Specifically, Maksimovic et al., 2020 found that the anticorrelation between V_p and T_e observed below 0.3 AU disappears as the wind expands, evolves and mixes with different electron temperature gradients for different wind speeds. The exospheric solar wind model (e.g., Maksimovic et al., 1997; Maksimovic et al., 2001) showed that the fast wind from the polar coronal hole regions (low-temperature regions) might be produced by the non-thermal electron distributions in the corona, which might explain the anticorrelated

(V_p, T_e) close to the Sun. Furthermore, the exospheric model predicted that the temperature profile is flatter in the fast wind as previously observed (Meyer-Vernet and Issautier, 1998). However, exospheric models use simplified hypotheses and challenging questions remain about the heating and cooling mechanisms for electrons. The PSP observations close to the Sun therefore give us an opportunity to investigate the solar wind electron thermal dynamics in the inner heliosphere.

The Quasi-thermal noise (QTN) technique yields accurate electron density and temperature measurements in the solar wind. It has been used in a number of space missions (e.g., Meyer-Vernet, 1979; Meyer-Vernet et al., 1986; Meyer-Vernet et al., 1993a; Meyer-Vernet et al., 2017; Issautier et al., 1999b; Issautier et al., 2001b; Issautier et al., 2001c; Issautier et al., 2005; Issautier et al., 2008; Maksimovic et al., 1995; Maksimovic et al., 2005b; Moncuquet et al., 1995; Moncuquet et al., 1997; Moncuquet et al., 2005; Moncuquet et al., 2006; Martinović et al., 2020; Le Chat et al., 2011; Salem et al., 2001; Salem et al., 2021; Lund et al., 1994; Schippers et al., 2013). Recent investigations (see Moncuquet et al., 2020; Maksimovic et al., 2020; Martinović et al., 2022) have already applied this technique on PSP based on electric voltage spectra acquired by the Radio Frequency Spectrometer (RFS/FIELDS) (Pulupa et al., 2017). Besides, SWEAP/PSP consists of the Solar Probe Cup (SPC) and the Solar Probe Analyzers (SPAN) (Kasper et al., 2016; Case et al., 2020; Whittlesey et al., 2020; Livi et al., 2022). SPC is a fast Faraday cup designed to measure the one dimensional velocity distribution function (VDF) of ions. SPAN is a combination of three electrostatic analyzers operated to measure the three dimensional ion and electron VDFs. Usually, traditional particle analyzers are affected by spacecraft photoelectrons and charging effects. Since the QTN electron density is deduced from a spectral peak, this measurement is independent of gain calibrations. Due to its reliability and accuracy, the electron number density derived from the QTN spectroscopy is called the gold standard density and serves routinely to calibrate other instruments (e.g., Maksimovic et al., 1995; Issautier et al., 2001c; Salem et al., 2001; Salem et al., 2021). Until now, on PSP, electron number density provided by the QTN technique has been playing an important role as a calibration standard for scientific analysis (e.g., Kasper et al., 2021; Zhao et al., 2021a; Liu et al., 2021a; Liu et al., 2021b).

We derived the total electron temperature from the QTN spectroscopy in the so-called pristine or nascent solar wind observed by PSP. Specifically, a combination of 12-day observations around each perihelion from Encounter One (E01) to Ten (E10) of PSP are presented with the heliocentric distance varying from about 13 to 60 R_\odot . Currently, observations from E08 are not considered due to the unusual biasing setting for the electric antenna at that time. In Section 2, we describe a simple but practical and effective way to deduce the total electron temperature with the high-frequency part of the quasi-thermal noise spectra provided by the dipole electric antenna onboard PSP. The corresponding results are compared to those from Maksimovic et al. (2020) (T_e from a different QTN technique), and Moncuquet et al. (2020) (T_e from a simplified QTN technique) for a preliminary cross-checking. In Section 3, we first provide the mean radial electron temperature profile, and then investigate the electron temperature gradients for different solar wind populations classified by the proton bulk speed and the solar wind mass flux,

respectively. Also, we examine how the anticorrelation between V_p and T_e are affected by radial evolution. In Section 4, the results and their implications for the electron thermal dynamics are summarized and discussed.

2 Data Analysis

The QTN spectroscopy technique provides in situ macroscopic plasma properties by analyzing the power spectrum of the electric field voltage induced on an electric antenna by the plasma particle quasi-thermal motions. The QTN spectra are determined by both the ambient plasma properties and the antenna configuration because of the strong coupling between the plasma particles and the electric field. For an ideal electric antenna configuration, the longer and thinner the electric antenna is set, the better the QTN technique performs. Specifically, the length of the electric antenna (L) should exceed the local Debye length L_D to ensure accurate temperature measurements. Fat antennas (with thick radius a) collect or emit more electrons so that the corresponding shot noise may exceed the quasi-thermal noise. Therefore, the electric antenna should be both long enough and thin enough ($a < L_D < L$) so that the QTN technique can work well. When the antenna is configured in a proper way (see Meyer-Vernet et al., 2017; Meyer-Vernet and Moncuquet, 2020), the QTN spectra are completely determined by the particle velocity distributions of the ambient plasma.

For the first several encounters, PSP is still not close enough to the Sun and therefore L_D generally exceeds the antenna length ($L \simeq 2$ m). Nevertheless, the plasma peak emerged because of the suprathermal electrons (Meyer-Vernet et al., 2022). Therefore, Moncuquet et al., 2020 gave the first results of QTN measurements on PSP based on a simplified QTN technique. The preliminary results include the electron number density n_e , the core electron temperature T_c and an estimation of the suprathermal electron temperature T_h (contribution of both the halo and strahl electron thermal pressure). Based on the derived n_e from Moncuquet et al., 2020, Maksimovic et al., 2020 yields the total electron temperature T_e during the first encounter of PSP by fitting the high-frequency part of the QTN spectra recorded by RFS/FIELDS. In this chapter, we apply another simple, fast but effective method on PSP observations to derive T_e . In the next subsection, we provide details of the method that enables us to derive the total electron temperature from the high-frequency part of the electric field voltage spectra measured by RFS/FIELDS. Finally, we present the preliminary cross-checking between the total electron temperature derived in this work and those obtained via different QTN techniques.

2.1 Determination of T_e from QTN Spectroscopy

In practice, the measured electric field voltage power spectrum at the receiver ports is expressed as

$$V_R^2 = \Gamma_R^2 (V_{electron}^2 + V_{proton}^2 + V_{shot}^2) + V_{noise}^2 + V_{galaxy}^2 \quad (4.1)$$

where $V_{electron}^2$, V_{proton}^2 , V_{shot}^2 , V_{noise}^2 , and V_{galaxy}^2 represent the electron QTN, the doppler-

shifted proton thermal noise, the shot noise, the instrument noise, and the galactic radio background noise, respectively. In Equation 4.1, Γ_R^2 is the gain factor of the receiver, which is expressed as

$$\Gamma_R^2 \simeq \frac{C_A^2}{(C_A + C_B)^2} \quad (4.2)$$

where C_A and C_B are the dipole antenna capacitance and the (dipole) stray capacitance, respectively. Since V_R^2 is the power spectrum at the receiver ports, Γ_R^2 is in factor of the first three terms. Note that Γ_R^2 has already been included in the expression of V_{galaxy}^2 (see below). For the frequencies satisfying $fL/(f_p L_D) \gg 1$, the electron QTN can be approximated as $V_{electron}^2 \simeq \frac{f_p^2 k_B T_e}{\pi \epsilon_0 L' f^3}$ (Meyer-Vernet and Perche, 1989), where f_p is the local electron plasma frequency, L' equals to the physical length (L) of one boom (or arm) of the dipole antenna when it is long enough (i.e. $L \gg L_D$), k_B is the Boltzmann constant, and ϵ_0 is the permittivity of free space. PSP/FIELDS antennas are separated by the heat shield and the physical separation is ~ 3 meters for both $|V1-V2|$ and $|V3-V4|$ dipole antennas. Since the antenna physical length ($L \simeq 2$ m) is not long enough, the gap should be considered for L' with $L' = 3.5$ m. The high-frequency electron QTN (above f_p) is proportional to the electron kinetic temperature whatever the shape of the velocity distribution is like. For the frequency ranges considered, $C_A \simeq \pi \epsilon_0 L / [\ln(L/a) - 1]$ (Meyer-Vernet et al., 2017) and $C_B \simeq 18$ pF (Moncuquet et al., 2020), where $L \simeq 2$ m is the electric antenna physical length and $a \simeq 1.5$ mm is the wire radius. Note that, when performing the fitting using the whole QTN spectra, the derived electron temperatures depend on the choice of the velocity distribution function for the electrons (Meyer-Vernet and Perche, 1989). This is similar to the analysis to fit the velocity distribution functions observed by the particle analyzer. However, in the present work, the derived total electron temperature is not model dependent. This is because, when deriving the expression of $V_{electron}^2 \simeq \frac{f_p^2 k_B T_e}{\pi \epsilon_0 L' f^3}$, T_e is defined directly from the second moment of the electron velocity distribution functions, and no models are assumed (Meyer-Vernet and Perche, 1989; Chateau and Meyer-Vernet, 1991; Meyer-Vernet et al., 2017).

When $fL/(f_p L_D) \gg 1$, the the doppler-shifted proton thermal noise and the shot noise are negligible compared to the electron QTN (Meyer-Vernet et al., 2017). Note that the periodic antenna biasing performed for measuring the DC electric fields, which affects the shot noise, does not perturb our results, contrary to the perturbations these biasing bring to the QTN at smaller frequencies. In contrast, the contributions of the galactic radio background noise (Novaco and Brown, 1978; Cane, 1979; Zaslavsky et al., 2011) and the instrument noise become important and need to be subtracted to obtain the effective electron QTN spectrum at high frequency. The galaxy noise is almost constant in time and nearly isotropic in angular distribution with the modulation as a function of the observed solid angle being less than 20% in the considered frequency range (Manning and Dulk, 2001). Therefore, it was frequently used to calibrate the antenna onboard previous spacecraft missions (e.g., Zaslavsky et al., 2011; Maksimovic et al., 2020). Specifically, the calibration is performed by relating the measured radio background radiation of the galaxy to the modelled flux of the source. The use of the empirical isotropic

galaxy noise model from Novaco and Brown, 1978 was justified by displaying a good agreement between the data and the model. Due to the high sensitivity of RFS/FIELDS/PSP (Pulupa et al., 2017), the galaxy noise lies within the RFS bandwidth and can be accurately measured. As a result, following the method outlined in Zaslavsky et al., 2011, Maksimovic et al., 2020 used an RFS spectrum measured when PSP was close to 1 AU to derive an accurate absolute value of the reduced effective length of $|V1-V2|$ dipole antenna. Below, the galaxy noise measured by RFS/FIELDS/PSP is modelled based on the newly derived reduced effective length of $|V1-V2|$ dipole antenna. The pre-deployment internal noise of RFS/FIELDS (after launch) in the considered frequency range was estimated to be $V_{noise}^2 \sim 2.2 \times 10^{-17} \text{ V}^2\text{Hz}^{-1}$ (Pulupa et al., 2020; Maksimovic et al., 2020). The background radio galactic noise is modelled following the procedures of Zaslavsky et al., 2011 and Maksimovic et al., 2020. The specific steps are summarized below.

The background radio galactic noise is modelled according to Equation (11) from Zaslavsky et al. (2011), $V_{galaxy}^2 = \frac{4\pi}{3} Z_0 \Gamma_R^2 L_{eff}^2 B_{model}$, where $Z_0 = \sqrt{\mu_0/\epsilon_0} \simeq 120\pi$ is the impedance of vacuum, $\Gamma_R L_{eff} = 1.17$ is the reduced effective length (see Maksimovic et al., 2020), and B_{model} is the empirical model for the isotropic sky background brightness (Novaco and Brown, 1978), expressed as

$$B_{model} = B_0 f_{MHz}^{-0.76} e^{-\tau} \quad (4.3)$$

where $B_0 = 1.38 \times 10^{-19} \text{ W/m}^2/\text{Hz}/\text{sr}$, f_{MHz} is the frequency expressed in MHz, and $\tau = 3.28 f_{MHz}^{-0.64}$.

Figure 4.1 presents a typical example of electric field voltage power spectrum plot ranging between 100 kHz and 10 MHz measured by the FIELDS $|V1-V2|$ dipole antenna connected to the RFS receiver. We obtain the observations (crosses connected by the black curve) by merging the spectra measured by LFR/RFS and that by HFR/RFS. The dotted horizontal line represents pre-deployment internal noise of RFS/FIELDS as mentioned above. The black dashed line is the radio galaxy background noise calculated as described above. Both the instrument noise and radio galaxy noise are deducted from the observed electric field voltage spectrum so that the so-called pure QTN spectrum $\Gamma_R^2 V_{electron}^2 \simeq V_R^2 - V_{noise}^2 - V_{galaxy}^2$ (blue curve line) is derived following the similar requirement set by Maksimovic et al., 2020. Specifically, the data points are selected as: (1) the lower-frequency limit is set as $fL/(f_p L_D) \geq 2$ so that both the proton thermal noise and the shot noise can be neglected; (2) the derived so-called pure QTN spectrum should be larger than both the instrument noise and radio galaxy noise, which is used to set the higher-frequency limit. Then, we further select the dataset for the linear fitting to derive T_e following $fL/(f_p L_D) \geq 8$, which is a much more strict requirement. The green line represents the linear fitted results and there is only one free parameter which is the total electron temperature. The electron plasma frequency used for each fitted spectrum is derived from the plasma peak tracking technique (see Moncuquet et al., 2020). In Figure 4.1, the vertical black dashed-dotted line, which represents the location of the local electron plasma frequency, is plotted for reference. Specifically, we perform the numerical process by fitting the theoretical voltage spectral density $\log(V_R^2)$ to each measured spectrum via minimizing the χ^2 merit function with

the implementation of a nonlinear least-squares Levenberg-Marquardt technique (Markwardt, 2009). χ^2 is defined as $\chi^2 = \sum_{i=1}^N \frac{(O_i - E_i)^2}{O_i}$, where O_i is the value of the measured spectrum, and E_i is the corresponding expected value (theoretical one). All the electric field voltage spectra measured by the RFS/FIELDS are fitted following the same procedure mentioned above. The spectra fitted in this work usually comprise a number of frequency points ranging between ~ 5 and ~ 15 . We further quantify the quality of the fit with the overall standard deviation (σ_{fit}) of the numerical fitted values to the corresponding measurements. In general, $\sigma_{fit} < 2.5\%$ indicates the goodness of the fittings. The physical uncertainty of T_e is estimated from the uncertainty of the plasma frequency, the uncertainty of the so-called pure QTN spectrum and the uncertainty of the numerical process. The uncertainty of the plasma frequency is about 4% ($\sim 8\%$ for f_p^2) (Moncuquet et al., 2020), which is the standard frequency resolution of the RFS/FIELDS. The uncertainty of the so-called pure QTN spectrum comes from the variations of the instrument noise and the empirical isotropic galaxy noise model, which is in total less than 20% (see Manning and Dulk, 2001; Zaslavsky et al., 2011; Pulupa et al., 2017; Maksimovic et al., 2020). The uncertainty for the sum of the instrument noise and the empirical isotropic galaxy noise model mainly affect the pure QTN spectrum at the highest selected frequency, whereas it is negligible at the lowest selected frequency. For simplicity, the mean uncertainty of the so-called pure QTN spectrum is estimated to be about 10%. Therefore, the physical uncertainty of the derived T_e is at most 20%, which is almost the same as that of T_c (see Moncuquet et al., 2020; Liu et al., 2020; Liu et al., 2021a). This estimated physical uncertainty for T_e is consistent with the statistical uncertainty for T_e shown in Figure 4.4.

Note that the high-frequency part of the QTN spectrum can be strongly perturbed by the electromagnetic emissions (e.g., Type II and/or III radio emissions) and therefore cannot be used for deriving T_e . Especially, such electromagnetic emissions were frequently detected during E02 (Pulupa et al., 2020) and should be carefully removed. In this work, when the QTN technique cannot be implemented in the presence of electromagnetic emissions, no T_e value is set. The electric field voltage power spectrum below f_p in general remains unperturbed and both n_e and T_c can still be obtained (Moncuquet et al., 2020). As a byproduct, we managed to derive a database of spectra affected by bursty Langmuir waves and/or electromagnetic emissions (see Chapter 6).

2.2 Preliminary Cross Checking

Figure 4.2 shows an overview of the solar wind electron temperatures and the proton bulk speed measured by PSP during E01 (from October 31, 2018 to November 12, 2018 UTC). The electron temperatures derived from different techniques including T_e from QTN (this study) and T_c from QTN are compared for cross-checking. In the top panel, we present T_e (in black, labelled as $T_{e,QTN}(\text{Linear})$) derived from our linear fit QTN technique explained above and compare it to T_e (in blue, $T_{e,QTN}(\text{Kappa})$) derived from the generalized Lorentzian QTN model (Maksimovic et al., 2020). In general, they are in broad agreement with each other. Therefore, both the absolute values and variations of $T_{e,QTN}(\text{Linear})$ should be reliable. Similarly, T_c from QTN (Moncuquet et al., 2020) is displayed in blue in the bottom panel and are compared to

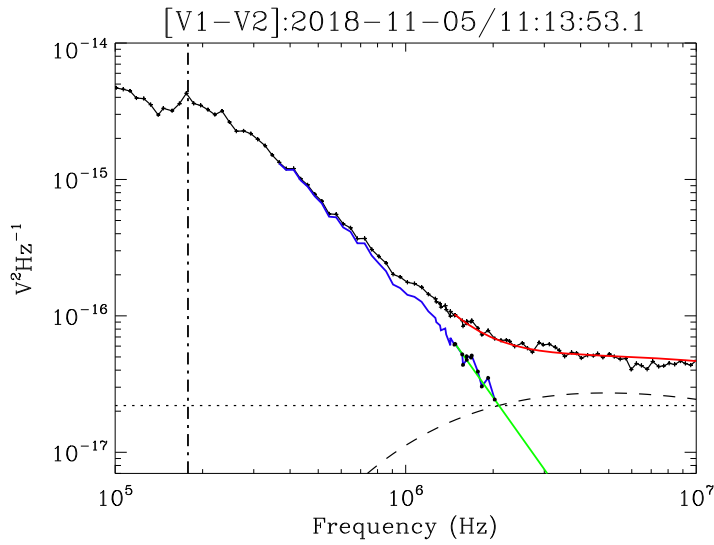


Figure 4.1 – Example of a voltage power spectrum (between 100 kHz and 10 MHz) recorded by the RFS receiver using the $|V1-V2|$ dipole electric antennas from FIELDS instrumentation (full black curve connected by crosses). The dot-dashed line gives the position of the local plasma peak (Moncuquet et al., 2020). The dotted horizontal line represents the pre-deployment RFS instrument noise (after launch) of $\sim 2.2 \times 10^{-17} \text{ V}^2\text{Hz}^{-1}$. The black dashed line shows the modelled radio galaxy noise. The blue and green lines represent the effective QTN signal and linear fit (f^{-3} variation that the QTN spectrum should follow when $f \gg f_p L_D/L$), respectively. The black dots on the blue line are used to derive the linear fit. The red line is the sum of the fitted QTN signal, the modelled radio galaxy noise and the instrument noise. The details are described in the text.

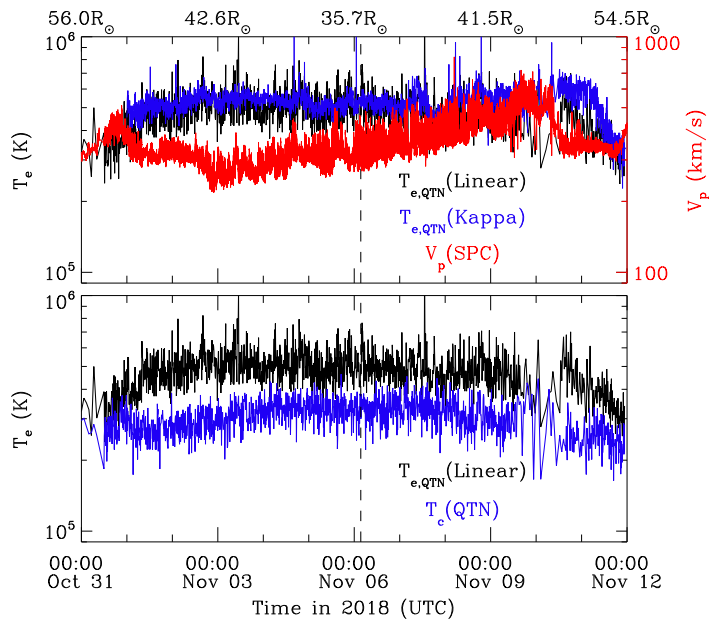


Figure 4.2 – Comparison of observations of solar wind electron temperatures derived from different methods on Parker Solar Probe (PSP). An example of 12-day measurements by PSP during Encounter One (from October 31, 2018 00:00:00 to November 12, 2018 00:00:00 UTC) is shown for reference. The heliocentric distance (in units of the solar radius R_{\odot}) is indicated at the top of the top panel and the black vertical line denotes the first perihelion of the PSP orbit. From the top to bottom panels, the total electron temperature derived from the linear fit QTN technique is displayed in black. In the top panel, the total electron temperature obtained by fitting the high-frequency part of the spectrum with the generalized Lorentzian QTN model (Maksimovic et al., 2020) is shown in blue for comparison. The bottom panel follows the same format as the first panel but for the core electron temperature derived from the simplified QTN technique (Moncuquet et al., 2020). The proton bulk speed from SPC/SWEAP is presented in the top panel for reference. An anticorrelation between V_p and T_e , which was also previously reported (Maksimovic et al., 2020), is visible during the time interval considered. Note that we have already smoothed $T_{e,QTN}(\text{Linear})$, $T_{c,QTN}$ and $T_{e,QTN}(\text{Kappa})$, so that the comparison between them is clear.

$T_{e,QTN}(\text{Linear})$ (in black). The ratio T_e/T_c reflects the contribution of suprathermal electrons and should not be a constant. The median value of the $T_{e,QTN}(\text{Linear})/T_{c,QTN}$ is about 1.41, which is close to the median value of $T_{e,QTN}(\text{Kappa})/T_{c,SPAN-E}$ (~ 1.47) (see Maksimovic et al., 2020). $T_{c,SPAN-E}$ is the core electron temperature derived from SPAN-E (Halekas et al., 2020a; Halekas et al., 2020b). Finally, the proton bulk speed from SPC/SWEAP is presented in the top panel for reference. The example time interval considered also shows an anticorrelation between V_p and T_e , which was previously reported in Maksimovic et al., 2020. We will further discuss this result in section 3.3.

We note that the ratio of T_e/T_c mentioned in this paper seems to disagree with that discussed by Halekas et al., 2020b, especially near the perihelion (i.e. ≤ 0.2 AU). This may be due to a systematic discrepancy in measuring the suprathermal electrons between the QTN technique and the SPAN-E. For the SPAN-E instrument, measurements of suprathermal electrons are very

difficult for essentially three reasons (see Whittlesey et al., 2020; Halekas et al., 2020b; Halekas et al., 2022). First, closer to the Sun, the temperature increase of thermal electrons means that, at the constant energy range, the number of energy bins of SPAN-E to characterize the halo electrons decreases as the radial distance decreases (see Maksimovic et al., 2021). Second, the strahl electrons, which contribute as much as the halo electrons to the total temperature, are more difficult to observe close to the Sun, when the magnetic field is more radial (Whittlesey et al., 2020; Berčič et al., 2020). These electrons can disappear from the SPAN-E field of view by being blocked by the heat shield. Finally, the geometrical factors of the SPAN-E instrument are not sufficient to properly characterize the halo electrons near the Sun (see for example Figure 1 of Halekas et al., 2022, where the halo electron VDF is clearly seen at the one count level of the instrument). Even though the low geometric factor of SPAN-E cannot explain the low total fractional supra-thermal density, but it indeed increases the difficulty to accurately measure the fractional halo and strahl density and their corresponding conversion process. These three effects combined make it more complicated to accurately measure the total electron temperature by SPAN-E than the core electron temperature. For the QTN spectroscopy, as is discussed in section 2.1, it is a passive method, thus the analysis of the additional contribution (instrument noise and galaxy noise) to the power level can lead to the uncertainty of the QTN electron temperature. All these factors may at least partly contribute to the systematic difference, but they cannot explain the magnitude of the difference. Therefore, an accurate and detailed comparison of the QTN total electron temperature with the one by SPAN-E should be made with more care and will be a future work. Similarly, an in-depth comparison between the core temperatures measured by the QTN (e.g., Moncuquet et al., 2020) and SPAN-E (e.g., Halekas et al., 2020b; Halekas et al., 2022) would also be useful, but is out of the scope of the present paper which is focused on the total electron temperature measurements from the high frequency part of the QTN spectra.

3 Observations and Results

PSP was designed to gradually shrink its orbit around the Sun and get closer step by step via seven Venus gravity assist flybys within about seven years. In this work, we focus on the 12-day period of observations around each perihelion from E01 to E10 (E08 not included) with the heliocentric distance varying from about 13.0 to 60.0 R_\odot . During its first three encounters, PSP followed similar trajectories and reached the perihelion of 35.66 R_\odot (~ 0.17 AU). In the following two orbits (from E04 to E05), PSP travelled closer to the Sun and reached perihelion of 27.8 R_\odot (~ 0.13 AU). The perihelia of PSP orbits became about 20.8 R_\odot for both E06 and E07 and about 16 R_\odot for both E08 and E09. During E10, PSP reached as close to the Sun as 13 R_\odot . In Section 3.1, we provide an overview of the radial evolution of the total electron temperature derived from the QTN technique, combining the datasets from E01 to E10 (E08 not included). In Section 3.2, we analyze and discuss the electron temperature gradients for different solar wind populations classified by the proton bulk speed and the solar wind mass flux, respectively. In Section 3.3, we investigate the radial evolution of anticorrelation between

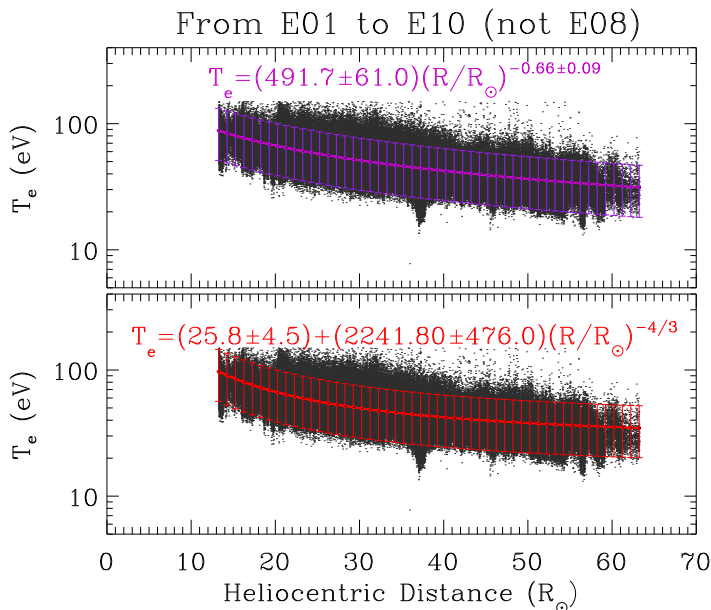


Figure 4.3 – Radial variation of the total electron temperature (T_e) combining observations from Encounter One (E01) to Ten (E10) with E08 excluded. From top to bottom, T_e was fitted with the power law expression $T_e = T_0 \times (R/R_\odot)^\beta$ (purple) and the expression given by the large distance exospheric solar wind model $T_e = T_0 + T_1 \times (R/R_\odot)^{-4/3}$ (red), respectively. The fitted profile and expression with corresponding color are superimposed for comparison. The variations of the free parameters in the fitted expressions are the corresponding 1-sigma ($1-\sigma$) fit uncertainties. The vertical error bars indicate the $2-\sigma$ fit uncertainties, which in total covers about 95% data points.

V_p and T_e .

3.1 Mean Radial Profiles of T_e

Figure 4.3 presents the total electron temperature derived from the QTN technique as a function of the heliocentric distance in units of solar radius R_\odot , combining 12-day period of observations near the perihelion of each encounter from E01 to E10 (E08 not included). Since PSP almost corotates with the Sun near the perihelion of each encounter, its observations only cover a very small heliographic latitude and longitude span (Kasper et al., 2019; Halekas et al., 2020a). This means that, in each encounter, PSP detects the solar wind from only a limited number of sources. Therefore, a large data set from different encounters is necessary to remove/reduce the effects of transient structures such as CMEs or small-scale flux ropes (e.g., Hess et al., 2020; Zhao et al., 2020; Korreck et al., 2020; Chen et al., 2021), switchbacks (e.g., Bale et al., 2019; Dudok de Wit et al., 2020; Martinović et al., 2021; Fargette et al., 2021), magnetic holes associated with slow shock pairs (e.g., Chen et al., 2021; Zhou et al., 2022), and so on. As explained below, we fit the total electron temperature with respect to the heliocentric distance with both the power law model and the exospheric model to get their mean radial profiles.

Specifically, we perform the fittings for each model by minimizing the χ^2 value with the

implementation of a nonlinear least-squares Levenberg-Marquardt technique (Markwardt, 2009). This technique takes into account the heliocentric distance and all the data points, as is generally the case for previous studies (e.g., Issautier et al., 1998; Štverák et al., 2015; Hellinger et al., 2013; Moncuquet et al., 2020). In total, there are $N \sim 882,361$ data points and there are two adjustable free parameters for each model fit. Therefore, the degree of freedom is $DOF = N - 2 = 882,359$. χ^2 is defined as $\chi^2 = \sum_{i=1}^N (\frac{O_i - E_i}{\sigma_i})^2$, where O_i is the value of the observations (T_e), E_i is the corresponding expected value (fit), and σ_i is the uncertainty of the measured T_e . As shown in section 2.1, we estimate that $\sigma \sim 0.2 \times T_e$. The power-law model is derived with $\chi^2 \simeq 1178937$ and the so-called reduced/normalized $\chi_\nu^2 = \chi^2/DOF \simeq 1.34$. The exospheric model is derived with $\chi^2 \simeq 1235002$ and the so-called reduced/normalized $\chi_\nu^2 = \chi^2/DOF \simeq 1.40$. Since χ_ν^2 for both model fits are close to unity and are comparable in the two cases, one can conclude that the exospheric temperature model of the form $T_e = T_0 + T_1 \times r^{(-4/3)}$ is as good as the power law approximation in fitting the observed total electron temperature gradient in the small radial range considered. The fitted profiles and expressions for both models are shown on Figure 4.3. Furthermore, both the mean and median values of $\overline{T_e}/T_e$ are very close to unity for both model fits, where $\overline{T_e}$ is the fitted value and T_e is the measured value. This again indicates the goodness of both model fittings. 1- σ value of $\overline{T_e}/T_e$ for both model fits is around 0.2, based on which the uncertainties of the two free parameters for each model fit are derived. 2- σ fit uncertainties are plotted in Figure 4.3 for reference, which in total covers about 95% data points.

The total electron temperature fitted by the power law model ($T_e \propto r^{-0.66}$, where r is the heliocentric distance in unit of solar radius) is displayed in purple. The derived total electron temperature profile is flatter than that of the core electron temperature ($T_c \propto r^{-0.74}$, see Moncuquet et al., 2020), which is consistent with the results in the outer heliosphere (e.g., Issautier et al., 1998; Le Chat et al., 2011). The total electron temperature consists of the contribution of the core, halo and strahl electron thermal pressure. Therefore, the flatter radial profile of T_e may be explained by the nearly isothermal behaviour of suprathermal electrons (see Moncuquet et al., 2020). We note that in that study, the suprathermal temperature is the total contribution of both the halo and strahl electron thermal pressures. Based on the SPAN-E observations (Berčič et al., 2020), there is no strong trend in variation of the strahl electron temperature with radial distance. Also, the strahl electrons are more pronounced closer to the Sun while the density ratio between the halo and strahl electrons increases with the radial distance (Maksimovic et al., 2005a; Štverák et al., 2009), which suggests a conversion of some strahl electrons into halo ones. As a result, the fact that the T_e profile is flatter than the T_c one may mainly be due to the flatness of the strahl electron temperature profile. The recent results from PSP (see Abraham et al., 2022) suggest that the physical picture is somewhat different from a simple conversion of strahl to halo as discussed above. PSP results instead show that the overall suprathermal electron fraction (halo + strahl) increases with respect to the heliocentric distance below 0.25 AU, and that the halo and strahl relative density are quite small near perihelion. However, as is discussed in Section 2.2, close to the Sun, both the halo and strahl electrons may be missed by SPAN-E due to the instrument limitations. Therefore, since the overall suprathermal fraction

(halo + strahl) closer to the Sun (e.g., Abraham et al., 2022; Maksimovic et al., 2021) may be underestimated, both of which should be treated with more care.

Then, based on the power-law fitted T_e profile ($T_e \propto r^{-0.66}$), we extrapolate T_e to $10 R_\odot$, 0.3 AU, and 1 AU, respectively. Figure 4.4 (a), (b), and (c) show the corresponding distributions of the scaled T_e combining the observations from E01 to E10 (E08 not included). A Gaussian function (blue line) was fitted on each histogram distribution and the corresponding center value (the most probable value) and $1\text{-}\sigma$ standard deviation of Gaussian fit are shown in comparison with the mean and median values. The histogram distributions of T_e are very symmetrical and almost Gaussian. Again, the difference between the mean, median, and the center value of Gaussian fit is quite small (less than 6%). This may be explained by the fact that we combine observations from several different encounters (different types of wind from different sources). The exospheric solar wind model indicates that for $r < 10 R_\odot$, the T_e radial profile becomes less steep (Zouganelis et al., 2004). So, when extrapolating T_e back to the Sun with a constant slope, we stop the extrapolation at about $10 R_\odot$. The value of T_e scaled to $10 R_\odot$ is around 100.6 ± 19.9 eV. The predicted absolute values here are somewhat larger than the predictions shown in Bale et al., 2016; however, they are similar to the strahl electron temperature measured by SPAN-E/SWEAP (Berčić et al., 2020; Maksimovic et al., 2021). The strahl electron temperature is considered to be closely related to or almost equal to the coronal electron temperature. At $10 R_\odot$, this extrapolated temperature is also consistent with the exospheric solar wind model prediction derived from an electron velocity distribution with a Kappa index ranging between 4 and 6 (Zouganelis et al., 2004), which indicates that the electron distribution has a suprathermal tail as measured by the QTN measurements (e.g., Maksimovic et al., 2020). That same model yields a solar wind bulk speed between 250 and 350 km s⁻¹. Note that the Kappa index mentioned here is based on one unique generalized Lorentzian or Kappa function that is an alternative to the Maxwellian core plus Kappa/Maxwellian halo model. But the suprathermal tail itself may have a large kappa index, as found by SPAN-E near perihelion (e.g., Maksimovic et al., 2021; Abraham et al., 2022). Indeed, Zouganelis et al., 2004 showed that the acceleration provided by the exospheric model does not require specifically a Kappa function, but results more generally from nonthermal distributions. Our results show that the agreement between the extrapolated T_e based on PSP observations and the exospheric solar wind model prediction is quite good, given the simplifications made in both the T_e measurements and the solar wind model. Note that, T_e scaled to 0.3 AU is $\sim 29.3 \pm 5.8$ eV, which is consistent with the Helios observations at the same heliocentric distance (Maksimovic et al., 2005a). For T_e scaled to 1 AU, the value is $\sim 13.1 \pm 2.6$ eV, which is almost the same as the long-term (~ 10 years) Wind observations (Wilson et al., 2018). T_e scaled to 1 AU is also approximately the same as the mean/median value of the one-year statistical analysis based on STEREO observations (Martinović et al., 2016). Note also that the extrapolated electron temperatures from the exospheric model fit (not shown here) are always higher than but still comparable to those from the power law model fit.

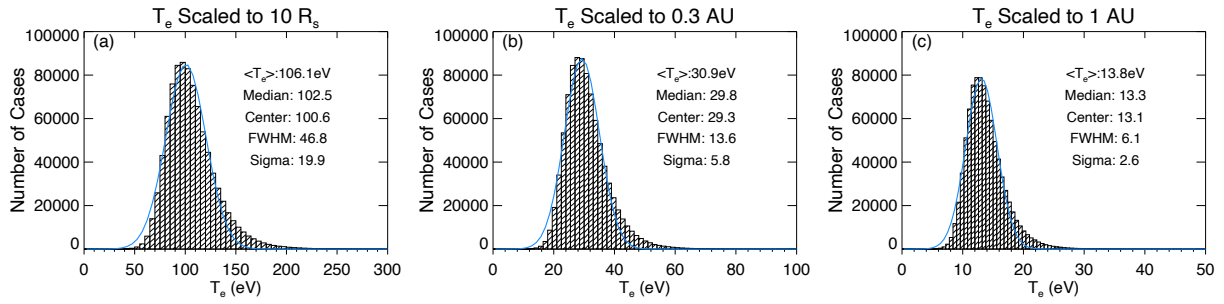


Figure 4.4 – (a)–(c): Histograms of the total electron temperature (T_e) scaled to 10 solar radii, 0.3 AU and 1 AU, based on observations displayed in Figure 4.3 and their corresponding power law modelling fit results. Gaussian fit is superimposed in blue on each histogram. The corresponding average and median values are also indicated together with the center value and 1- σ standard deviation of the Gaussian fit.

3.2 Temperature gradients for different solar wind populations

As presented/discussed in previous investigations (e.g., Meyer-Vernet and Issautier, 1998; Le Chat et al., 2011; Maksimovic et al., 2005a; Štverák et al., 2009; Štverák et al., 2015; Maksimovic et al., 2020), solar wind classified based on the proton bulk speed may have different electron heating and cooling behaviours. Therefore, in order to do direct comparisons with the previous studies, we also separate solar wind populations based on the proton bulk speed. The dataset was split into four proton bulk speed bins as illustrated by Figure 4.5 (a). In this way, each proton bulk speed bin contains the same number of data points, which is $882,361/4 \sim 220590$. We used the total proton bulk speed (V_p) provided by SPC/SWEAP for E01 and E02 and those from SPAN-I/SWEAP after E02 (Kasper et al., 2016; Case et al., 2020). For each proton bulk speed bin, we fit the T_e radial profile with a power-law model using the method described in section 3.1. The derived power law indices are plotted against the corresponding proton bulk speed in Figure 4.5 (b). We use the proton bulk velocity measured in the RTN coordinate system. The radial component of the velocity (V_R) measured by SPC and SPAN-I are in good agreement, but there is a systematic discrepancy for the tangential component (V_T) (Woodham et al., 2021). However, V_R is the main component of V_p (total proton bulk speed), and their absolute values are very close to each other. Furthermore, we use both V_R and V_p to cross-check the results below in this section and in section 3.3. We verify that the measurement uncertainty of V_p does not affect our conclusions.

The T_e radial gradients have a tendency (though weak) for the slower wind electrons to cool down with a steeper profile than the faster wind ones. It is noteworthy to mention that with only 12-day observations for each encounter (from E01 to E10, with E08 excluded) and a limited latitude exploration, we find similar behaviour for electrons in the inner heliosphere as previous long-term investigations (e.g., Maksimovic et al., 2005a; Štverák et al., 2015; Maksimovic et al., 2020) at various latitudes and longitudes and much larger span of heliocentric distances in the outer heliosphere. This is also consistent with the exospheric model predictions as shown in Meyer-Vernet and Issautier, 1998. Also, we note that the T_e radial gradient within each proton

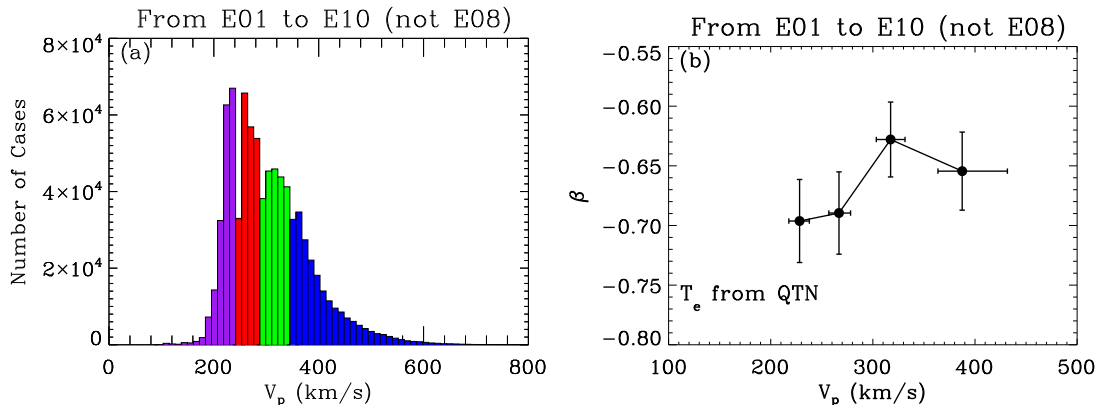


Figure 4.5 – (a) We define the four wind families based on the proton bulk speed histogram. Each colored histogram has the same number of observations. (b) Outcome of the power law modelling in the form $T_e = T_0 \times (R/R_\odot)^\beta$ for total electron temperature: β versus V_p . More details are described in the main text.

bulk speed bin is steeper than that in the outer heliosphere based on Ulysses observations ($T_e \propto r^{-0.53}$, see Le Chat et al., 2011). This may verify the exospheric model prediction that the electron temperature profile becomes steeper when getting closer to the Sun (Meyer-Vernet and Issautier, 1998).

Moreover, since PSP is very close to the Sun during the encounter phase where the solar wind is still under acceleration, the proton bulk speed detected by PSP may not be the final speed. Therefore, because of the different types of winds coming from different source regions, we further use another basic physical quantity to partition the dataset based on almost constant streamline, i.e., the solar wind mass flux $F_w = n_e m_p V_p r^2$ (e.g., Wang and Sheeley, 1990; Bemporad, 2017). The resulting histogram distribution of F_w is shown in Figure 4.6 (a). The derived values ($F_w \sim 2 \times 10^{10} - 3 \times 10^{11} \text{ g s}^{-1}$) are in agreement with the remote-sensing observations from SOHO at altitudes higher than $3.5 R_\odot$ (Bemporad, 2017), in situ measurements from ACE at 1 AU (Wang, 2010), and in situ data by Ulysses from ~ 1.4 to ~ 1.8 AU (Issautier et al., 2008; Wang, 2010). As expected, this indicates the conservation of the solar wind mass flux. Wang, 2010 showed that the solar wind mass flux at the corona base increases roughly with the footpoint field strength. This indicates, to some degree, both the corona base conditions and the propagation effects are considered for F_w , in contrast to the proton bulk speed. Thus, as displayed in Figure 4.6 (a), we split the dataset into four solar wind mass flux tubes and check the corresponding electron temperature gradients. Figure 4.6 (b) shows that solar wind electrons within the flux tube with larger mass flux cool down faster.

3.3 Anticorrelated parameters: V_p and T_e

As shown in section 2.2, PSP observations display a clear anticorrelation between V_p and T_e during E01. A similar anticorrelation was observed during E04, E05, E07 and E09. During E02 and E10, frequent Type III radio emissions were detected by PSP and fewer effective data points of T_e derived from the QTN technique were obtained than during other encounters. This

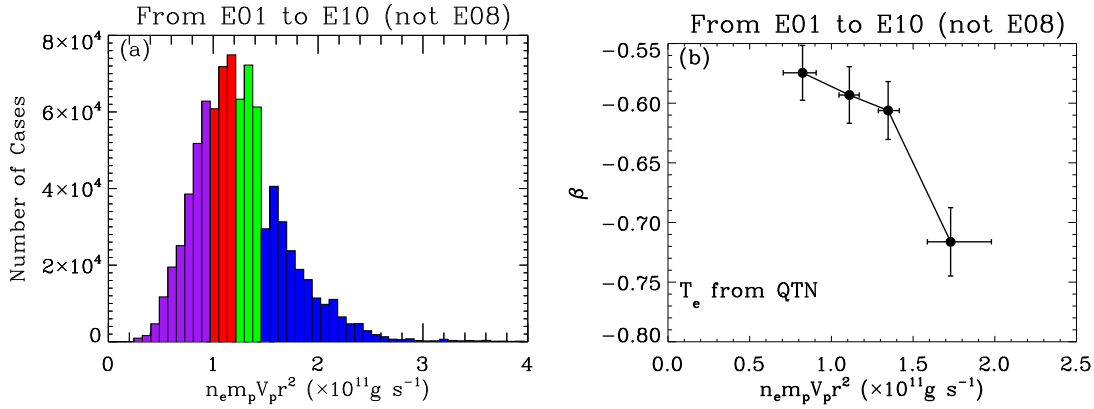


Figure 4.6 – Follows the same format as Figure 4.5 but for the solar wind mass flux.

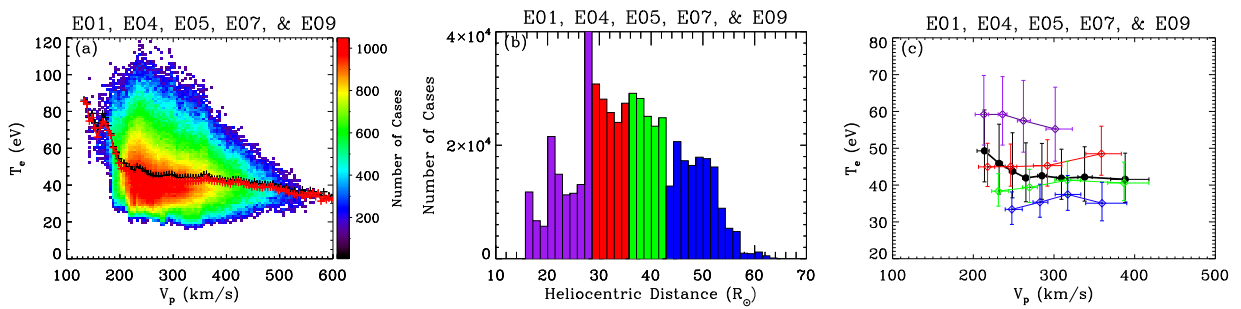


Figure 4.7 – (a) 2-D histogram distribution of T_e versus V_p with the color bar on the right side indicating the number of data points. Both the mean (red curve) and median values (black curve) are superimposed for reference. A clear anticorrelated (V_p , T_e) is displayed. (b) We define the four wind families based on the heliocentric distance histogram. Each colored histogram has the same number of observations. (c) Relation between V_p and T_e for each wind family, as defined in panel (b). The results are displayed in the same color as the corresponding heliocentric distance histogram in panel (b). More details are described in the main text.

may affect the analysis of the relation between V_p and T_e . In contrast, slight correlated (V_p , T_e) were observed during E03 and E06 based on the QTN observations. The V_p – T_e relation measured in the solar wind may indeed depend on both the source region (Griton et al., 2021) and the radial evolution (Maksimovic et al., 2020; Pierrard et al., 2020; Halekas et al., 2022). The complexity of the electron temperature behaviours, especially the anticorrelation between V_p and T_e , contrasts with the correlation between the proton temperature and the wind speed that persists throughout the heliosphere (see Maksimovic et al., 2020, and references therein). We selected the data points from E01, E04, E05, E07 and E09, and further analyzed the effect of the radial evolution on the anticorrelation between V_p and T_e .

Figure 4.7 (a) compares T_e and V_p combining observations from E01, E04, E05, E07 and E09. A clear anticorrelated (V_p , T_e) is displayed. We also equally split the dataset into four radial distance bins as illustrated by Figure 4.7 (b). For each radial distance bin, the datasets are equally split into four proton bulk speed bins following the method mentioned in section 3.2. We then compute the median values of V_p and T_e for each proton bulk speed bin. The

calculated median values of V_p and T_e belonging to each radial distance bin are presented in the same color in Figure 4.7 (c). For comparison, median values of V_p and T_e of the whole dataset equally divided into eight proton bulk speed bins are plotted in black.

We find that the (V_p, T_e) anticorrelation is stronger when the solar wind is slower (see black curve in Figure 4.7 (c)). For the solar wind considered, most of them are slow wind and on average they are being accelerated during the expansion. Therefore, the slower solar wind is detected closer to the Sun. This is consistent with the fact that the most pronounced anticorrelated V_p-T_e is observed close to the Sun (see purple curve in Figure 4.7 (c)). The results may also indicate that the (V_p, T_e) anticorrelation is reduced/removed during the acceleration process of the slow solar wind. Based on both the Helios and PSP measurements, Berčič et al., 2020 found a clear anticorrelation between the parallel strahl electron temperature $T_{s\parallel}$ (proxy coronal electron temperature) and the local solar wind speed. Halekas et al., 2022 grouped the PSP observations by the asymptotic wind speed, and found that both the *in situ* electron temperature (parallel core electron temperature $T_{c\parallel}$) and the proxy coronal electron temperature ($T_{s\parallel}$) are anticorrelated with the asymptotic wind speed. As a result, the anticorrelated (V_p, T_e) herein may be the remnants of the coronal conditions.

4 Summary and Discussion

In this work, we have implemented a simple, fast and effective method, based on the QTN spectroscopy, on PSP observations to derive the total electron temperature. To do so, we used a linear fit on the high frequency part of the QTN spectra observed by RFS/FIELDS. The derived total electron temperature are in general agreement with T_e obtained from the QTN model with Lorentzian velocity distribution functions (Maksimovic et al., 2020). We present the radial evolution of the total electron temperature by combining 12-day observations around each perihelion from E01 to E10 (E08 not included) with the heliocentric distance ranging from about 13 to 60 R_\odot .

The radial profile of the total electron temperature ($T_e \propto r^{-0.66}$) in the inner heliosphere falls within the range between adiabatic and isothermal and is flatter than that of the electron core temperature ($T_c \propto r^{-0.74}$, see Moncuquet et al., 2020). This is consistent with previous Helios and Ulysses observations farther out (e.g., Pilipp et al., 1990; Issautier et al., 1998; Le Chat et al., 2011). Furthermore, the flatness of the radial profile of T_e may mainly be due to the contribution of the strahl electrons. The extrapolated T_e to 0.3 AU and 1 AU using the fitted power law are almost the same as the Helios and Wind observations at the same heliocentric distance (see Maksimovic et al., 2005a; Wilson et al., 2018), respectively. Similarly, T_e was also extrapolated back to 10 R_\odot . The corresponding extrapolated measurements are almost the same as the solar corona strahl electron temperature (Berčič et al., 2020). This may confirm that the strahl electron temperature is closely related to or even almost equals to the coronal electron temperature. The temperature extrapolated back to 10 R_\odot is also consistent with the exospheric solar wind model prediction assuming an electron velocity distribution with the Kappa index ranging between 4 and 6 (Zouganelis et al., 2004). The extrapolated T_e based on the exospheric

solar wind model is systematically higher (but still comparable to) than that derived from the power-law model fit.

The radial T_e profiles in the slower solar wind are relatively steeper than those in the faster solar wind. Stated in another way, electrons in the slower solar wind cool down more quickly than those in the faster wind. It is remarkable that with only 12-day observations for each encounter (from E01 to E10 with E08 excluded) and a limited latitude exploration, we find the same conclusions about electron cooling and heating behaviours in the inner heliosphere as previous long-term investigations (e.g., Maksimovic et al., 2005a; Štverák et al., 2015; Maksimovic et al., 2020) with a much larger span of the latitude, longitude and heliocentric distance explorations in the outer heliosphere. In general, the radial T_e profile observed in the pristine solar wind is steeper than that in the outer heliosphere, which to some degree verify the exospheric model prediction in the inner heliosphere (Meyer-Vernet and Issautier, 1998). This indicates that the exospheric solar wind model explains partially the electron behaviour in the inner heliosphere. Furthermore, the solar wind mass flux derived from the in situ dataset in the inner heliosphere from PSP is in agreement with that even closer to the corona base (Bemporad, 2017) and further out in the interplanetary space (Issautier et al., 2008; Wang, 2010). Interestingly, the electron temperature cools down faster within flux tubes with larger mass flux. Given the solar wind mass flux conservation and the fact that the mass flux at the corona base increases with the footpoint field strength (Wang, 2010), it can be used as an effective physical quantity to distinguish the solar wind into different populations. This considers both the corona base conditions and the propagation effects in contrast to the proton bulk speed. Especially, the solar wind at PSP orbit perihelia may be still accelerating, the speed should not be considered as the final speed.

With PSP observations from E01, E04, E05, E07 and E09, we find that the (V_p, T_e) anticorrelation is more pronounced when the solar wind is slower in the inner heliosphere. During the time period considered, most of the detected solar wind is slow wind, which on average is still being accelerated during the spherical expansion. Furthermore, the results may indicate that the slow solar wind acceleration during the expansion reduces/removes the strong (V_p, T_e) anticorrelation detected near the Sun. This is verified by the fact that the most pronounced anticorrelated V_p-T_e is observed close to the Sun, in agreement with Maksimovic et al. (2020). The solar wind V_p-T_e relation is still an interesting issue, which may depend on both the source region at the Sun (Griton et al., 2021) and the radial evolution during the expansion (Maksimovic et al., 2020; Pierrard et al., 2020). To comprehensively understand the V_p-T_e relation, more work is needed to distinguish and/or connect the effects from the source region, spherical expansion and the transient structures detected locally.

Based on the Helios and preliminary PSP observations (e.g., Maksimovic et al., 2005a; Štverák et al., 2009; Halekas et al., 2020a; Halekas et al., 2020b; Berčič et al., 2020), the strahl electrons will become more pronounced when PSP gets closer to the Sun. However, the QTN technique currently cannot resolve the strahl electrons well, which needs further theoretical/model extensions. When PSP gets closer to the Sun, L/L_D is expected to become larger. This will enable us to derive the electron properties (e.g., n_e , T_e , and kappa index) with smaller uncertainties by fitting the whole QTN spectrum with the generalized Lorentzian (or so-called

kappa) QTN model. We await for well calibrated fixed T_e from SPAN-E for all encounters to make systematic cross-checking with T_e provided by the QTN technique, which should benefit to both methods.

Chapter 5

Properties of A Supercritical Quasi-perpendicular Interplanetary Shock Propagating in the Terrestrial Foreshock Region

Objectives

The interaction between an interplanetary (IP) shock and the terrestrial foreshock is of great significance for both space weather predictions and fundamental plasma physics. In this chapter, we investigate the properties of an IP shock ($M_f = 2.1$, $\theta_{Bn} = 80^\circ$), which was detected by *Wind* on September 12th, 1999, magnetically connected to the terrestrial bow shock. Here, we focus on the wave activities and corresponding particle dynamics, suggesting that such wave and particle features result from the interaction of the IP shock with the terrestrial foreshock. Furthermore, implications behind the new features are discussed. The main results and texts are extracted from Liu et al., 2022 (APJS).

Contents

1	Introduction	75
2	Observations and Data Analysis	77
2.1	Magnetic Connection between IP shock and Terrestrial Bow shock	77
2.2	Electron Dynamics at Kinetic Scales	81
2.3	Interactions between IP Shock and Alfvén Waves/Fluctuations	86
3	Summary and Discussions	91
5.A	Source of Transient Electron Beam	92
5.B	Exclusion of IP Shock as A Source	94

1 Introduction

Collisionless shocks are important plasma structures, and appear ubiquitous in the solar wind and around planets. From the Sun to the Earth, interplanetary (IP) shocks are typically driven by coronal mass ejections (CMEs) or fast solar wind (e.g., Liu et al., 2012; Liu et al., 2014b; Liu et al., 2014a; Möstl et al., 2012; Lugaz et al., 2015; Zhao et al., 2019b). Near the Earth, the bow shock forms in front of the Earth due to the interaction between the solar wind and the Earth’s magnetosphere. Upstream of the terrestrial bow shock, the region magnetically connected to the shock is called the terrestrial foreshock. It is well-known and long investigated that the terrestrial foreshock region is dominated by waves and backstreaming particles (Wilson, 2016; Parks et al., 2017). When IP shocks are Earth-directed, they may interact with the terrestrial foreshock region, which is of great significance for both space weather predictions and fundamental plasma physics (e.g., Přeč et al., 2009; Šafránková et al., 2007a; Šafránková et al., 2007b; Goncharov et al., 2018). Past studies mainly focused on how the mutual interaction modifies the geometry, propagation and strength of the IP shock. The studies on how an IP shock modifies terrestrial foreshock electron and ion dynamics and associated waves, however, are still very few.

Terrestrial foreshocks are identified by enhanced fluxes of backstreaming particles. Due to the $\mathbf{E} \times \mathbf{B}$ drift and large mass ratio between the ions and electrons, a clear separation appears between the ion and electron foreshock boundaries (see Parks et al., 2017). In the region between the ion and electron foreshock boundaries, only backstreaming electrons are detected. In contrast, in the ion foreshock region, both backstreaming ions and electrons are observed. The backstreaming electrons can exhibit a bump on tail electron velocity distribution function that is unstable to the growth of Langmuir waves via Landau resonance (see Savoini and Lembège, 2001; Pulupa et al., 2011; Pulupa et al., 2012, and references therein). Savoini and Lembège (2001) showed that local backstreaming electron distributions consist of two components: (i) a high energy component characterized by a field-aligned bump on tail or beam signature, and/or (ii) a low-energy component characterized by a loss cone signature. Also, electrons locally accelerated in the deep downstream region may escape back into the upstream region (Savoini and Lembege, 2009). Furthermore, it is in the leading edge of the electron foreshock region that the most intense Langmuir waves around the local electron plasma frequency (f_{pe}) are generally observed associated with more energetic backstreaming electron beams above 1 keV (e.g., Kasaba et al., 2000; Bale et al., 2000; Pulupa et al., 2012). Besides, in the deeper region of the terrestrial foreshock, weaker Langmuir waves are detected in association with less energetic backstreaming electrons below 1 keV (e.g., Matsumoto et al., 1997; Kasaba et al., 2000; Pulupa et al., 2011). The $2f_{pe}$ emissions, frequently detected in the terrestrial foreshock, are considered to be generated by backstreaming-electron-driven Langmuir waves and correlated with the amplitude of Langmuir waves. Then, $2f_{pe}$ emission source region is confirmed to be the leading region of the electron foreshock (e.g., Yoon et al., 1994; Reiner et al., 1996; Kasaba et al., 2000). When backstreaming electrons and associated electrostatic Langmuir waves/fluctuations are detected upstream of the terrestrial bow shock, the spacecraft is considered magnetically

connected to the terrestrial bow shock. Thus, an interesting question arises regarding how an IP shock modifies the terrestrial foreshock electron dynamics, when the IP shock is magnetically connected to the terrestrial bow shock.

The backstreaming ions near the ion foreshock boundary are field-aligned and become more diffuse and isotropic when traveling deeper into the foreshock and/or approaching the quasi-parallel shock region (Wilson, 2016). Due to the interaction between the incoming and backstreaming ions, numerous large-amplitude waves/fluctuations that fall in a broad frequency range were detected in the quasi-parallel foreshock region (e.g., low frequency Alfvén/ion cyclotron waves, fast magnetosonic or magnetosonic-whistler waves). Alfvén waves and/or Alfvén-like oscillations were frequently detected in the quasi-parallel terrestrial foreshock region in association with the left-hand resonant ion/ion instability (e.g., Wang et al., 2015; Wilson, 2016, and references therein). In particular, when a quasi-perpendicular IP shock is Earth-directed, it may interact with Alfvén waves/fluctuations in the quasi-parallel terrestrial foreshock. In the past, many theoretical and simulation investigations focused on the interaction of Alfvén waves with shocks (e.g., McKenzie and Westphal, 1969; Lu et al., 2009). The amplitude of the Alfvén waves is enhanced by the shock (e.g., McKenzie and Westphal, 1969; Lu et al., 2009) and Alfvén waves detected in the shocked plasma are separated into two branches propagating in opposite directions (Lu et al., 2009). Furthermore, clear ripples were identified at the front of the perpendicular shock due to the interaction with the upstream Alfvén waves based on two-dimensional hybrid simulations (Lu et al., 2009). The ripples at the shock front can affect both reflected ion and electron dynamics (e.g., Lembège and Savoini, 2002; Lembege et al., 2004; Saito and Umeda, 2011; Yang et al., 2012; Yang et al., 2018). Interactions between the Alfvén waves/fluctuations and a quasi-perpendicular shock is still an interesting issue which is far from completely understood. Examining the features of the particle populations and waves around the IP shock interacting with Alfvén waves/fluctuations may provide new insights.

In this work, we report properties of an IP shock propagating in the quasi-parallel terrestrial foreshock region, which was observed by *Wind* (Wilson et al., 2021) at 03:57:56 UT on September the 12th, 1999. Specifically, *in situ* measurements of the solar wind from *Wind*/MFI (Lepping et al., 1995), *Wind*/3DP (Lin et al., 1995) and the thermal noise receiver (TNR) on-board *Wind*/WAVES (Bougeret et al., 1995) have been used to do the analysis. In section 2.1, we confirm that the IP shock is magnetically connected to the terrestrial bow shock via a comprehensive analysis of magnetic field measurements, electron pitch angle distributions, and wave observations. Then, with the high-cadence magnetic field data (11 samples per second) and the burst-mode particle data (a full distribution per three seconds), we investigate how the IP shock modifies the electron dynamics of the terrestrial foreshock at kinetic scales in section 2.2. Furthermore, the interactions between the IP shock and the Alfvén waves/fluctuations detected in the terrestrial foreshock region are reported in section 2.3, including the properties of Alfvén waves/fluctuations around the IP shock and the IP shock-reflected ion dynamics. In the end, main results are summarized and discussed in section 3.

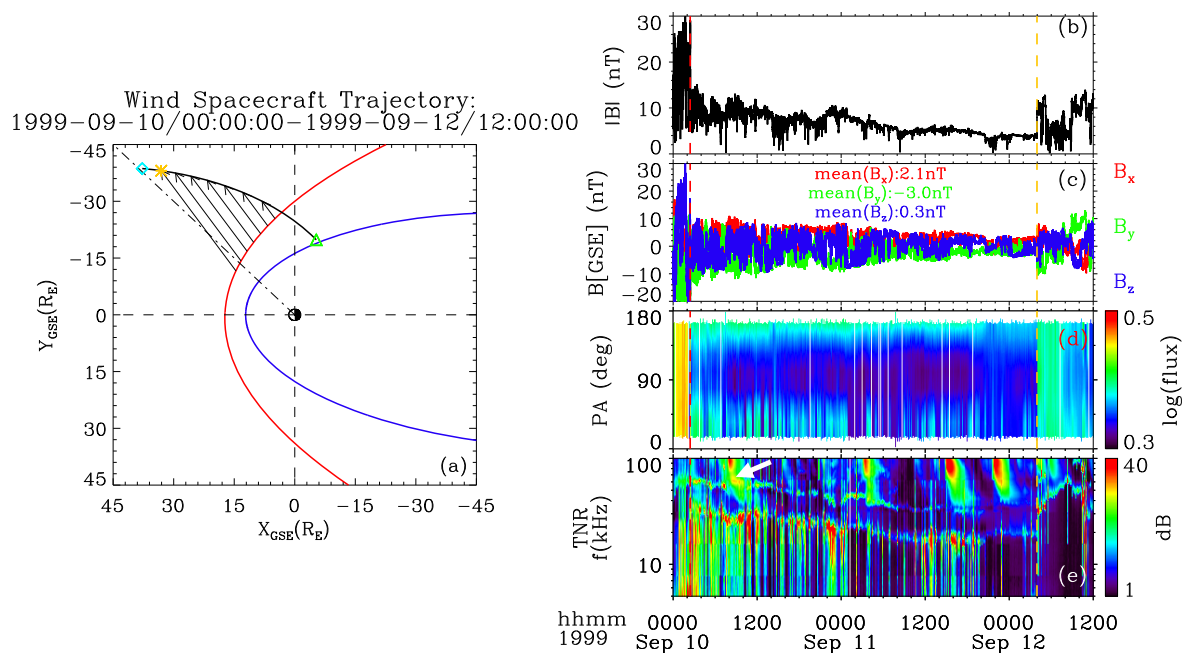


Figure 5.1 – (Left) The *Wind* satellite orbits in the XY plane of Geocentric Solar Ecliptic (GSE) coordinate reference frame from 00:00:00 on September 10th, 1999 UTC to 12:00:00 on September 12th, 1999 UTC. The black solid line denotes the spacecraft trajectory. The empirical model bow shock (red solid line, see Peredo et al. (1995)) and magnetopause (blue solid line, see Roelof and Sibeck (1993)) are plotted for reference. The triangle and diamond respectively mark the start and end of *Wind* trajectory. The asterisk denotes the position where an IP shock was detected by *Wind*. The black arrows represents the projection of the average magnetic field vectors between the terrestrial bow shock and the IP shock. (Right) The *Wind* observations which correspond to the trajectory shown in the left. From top to bottom, the panels show the magnetic field magnitude, magnetic field components in GSE coordinate, pitch-angle distribution of 265 eV electrons obtained from the EESA-Low instrument onboard *Wind*/3DP, and electric field voltage dynamic spectrum from TNR onboard *Wind*/WAVES. The red and yellow dashed vertical lines mark the crossing of the terrestrial bow shock and the IP shock, respectively.

2 Observations and Data Analysis

2.1 Magnetic Connection between IP shock and Terrestrial Bow shock

Figure 5.1 (left) shows the *Wind* spacecraft trajectory (black solid curve) projected in the XY-GSE plane, which covers the time period from 00:00:00 on September 10th, 1999 UTC to 12:00:00 on September 12th, 1999 UTC. Projections of the model terrestrial bow shock (red solid curve, see Peredo et al. (1995)) and magnetopause (blue solid curve, see Roelof and Sibeck (1993)) locations are also plotted for reference. The model bow shock parameters are adjusted to match the average location of the observed crossings by the spacecraft. During the time period considered, the spacecraft traveled across the quasi-parallel side of the terrestrial bow shock from the downstream (magnetosheath) to the upstream and then detected an IP shock (yellow asterisk). The projection of the average magnetic field vector was determined by averaging the

magnetic field during the time period between the last crossing of the terrestrial bow shock and detection of the IP shock. As a result, *Wind* may generally be magnetically connected to the terrestrial bow shock along the trajectory between the terrestrial bow shock and the IP shock. The IP shock passed the *Wind* spacecraft at 03:57:56 UT on September 12th, 1999. The IP shock that is supercritical with a fast magnetosonic Mach number $M_f \sim 2.1$ and an Alfvén Mach number $M_A \sim 3.0$, and it propagates in a plasma with proton plasma beta $\beta_p \approx 1$. It is a fast-mode, quasi-perpendicular shock, with a shock normal angle $\theta_{Bn} = 80^\circ$ and a shock speed $V_{shn} = 532.8 \pm 3.3 \text{ km s}^{-1}$. The basic parameters of the IP shock are obtained by the Shock Discontinuities Analysis Tool (Vinas and Scudder, 1986), which are consistent with those from the shock database maintained by J. C. Kasper¹.

Figure 5.1 (right) presents an overview plot of the *Wind* observations along the spacecraft trajectory mentioned above. Figure 5.1 (b-c) gives the magnetic field magnitude and GSE components of the magnetic field, respectively. From the terrestrial bow shock (red vertical dashed line) to the IP shock (yellow vertical dashed line), the magnetic field magnitude in general decreases. Furthermore, the X-GSE component (in red) of the magnetic field is in general positive ($\langle B_x \rangle \sim 2.1 \text{ nT}$) and Y-GSE component (in green) of the magnetic field is usually negative ($\langle B_y \rangle \sim -3.0 \text{ nT}$). This implies that the observed ambient magnetic field generally directs sunward. Therefore, electrons with pitch angles close to 0° are traveling towards the Sun and may be backstreaming from the bow shock. In contrast, electrons with pitch angles close to 180° are traveling antisunward and may be incident to the bow shock. Figure 5.1 (d) presents the pitch-angle distribution of 265 eV electrons measured by EESA-Low/3DP for reference. Typically, the relevant electron populations of this energy are the halo and/or strahl in the quiet solar wind or bi-directional streams of suprathermal electrons within CMEs (Gosling et al., 1987). Here, the strahl electrons from the Sun are apparent in the direction antiparallel to the magnetic field, whereas terrestrial foreshock electron beams (backstreaming electrons from the bow shock) are clearly identified as enhancements when pitch angles are less than 90° . Figure 5.1 (e) shows the electric field voltage dynamic spectrum measured by TNR onboard *Wind*/WAVES. The TNR radio receiver onboard *Wind*/WAVES, which is connected to the $2 \times 50 \text{ m}$ thin wire electric dipole antennas (before broken by dust impacts), measures electric fields ($\sim 4\text{--}256 \text{ kHz}$) combining five logarithmically spaced (overlapping) frequency bands (with the standard frequency resolution being $\Delta f/f = 4.3\%$). The TNR radio receiver is especially designed to measure electrostatic fluctuations produced by the quasi-thermal noise due to the thermal motion of the ambient electrons and ions. The quasi-thermal plasma line is clearly visible (between 20 kHz and 40 kHz before and after the IP shock) and can be used to determine straightforwardly the local electron density (e.g., Meyer-Vernet and Perche, 1989; Meyer-Vernet et al., 2017). The Langmuir wave activity can be identified as the intense enhancement near the plasma line. As expected, intense Langmuir waves are associated with transient enhancements of electron flux in the parallel direction. Also, $2f_{pe}$ emissions are clearly detected during the time period considered. Again, observations of the terrestrial foreshock electron beams along the magnetic field and the associated Langmuir wave activity indicate that *Wind* may in general be

1. <https://www.cfa.harvard.edu/shocks/>

magnetically connected to the terrestrial bow shock along the trajectory between the terrestrial bow shock and the IP shock. In addition, the timespan of the electron foreshock region of a quasi-perpendicular IP shock observed by the spacecraft is usually less than one minute (e.g., Bale et al., 1999; Hoang et al., 2007; Pulupa and Bale, 2008). Therefore, we exclude the possibility that the terrestrial foreshock electrons and strahl electrons are disturbed by the IP foreshock electrons. More details are described in Appendix 5.A and 5.B.

We note that the terrestrial foreshock electron beams are observed intermittently, whereas the strahl electrons from the Sun are observed constantly. This may be due to the dynamic nature of the terrestrial bow shock, especially the large-scale bow shock expansion (i.e. back and forth movements) due to the solar wind compression. For the time period considered, *Wind* crossed the bow shock three times due to the expansion from 02:00:00 to 03:00:00 on September 10th, 1999 UTC. Besides, the ambient magnetic field is slightly rotating. As a result, it may connect to different regions on the bow shock and/or disconnect to the bow shock. In contrast, in Figure 5.1 (a), both the model bow shock and the projected upstream magnetic field lines are assumed to be static. Therefore, *Wind* may not always be magnetically connected to the bow shock (though it did for most of the time considered), which may be the main reason to explain the intermittent features of the terrestrial foreshock electron beams. Furthermore, when *Wind* is magnetically connected to the quasi-perpendicular terrestrial bow shock, Lembège and Savoini (2002) showed that electrons may not be reflected uniformly by the bow shock based on two dimensional full particle electromagnetic simulation. Instead, packs of reflected electrons may be formed along the rippled shock front. This may also contribute to the intermittent features of the terrestrial foreshock electron beams. Also, a few weak Type III radio bursts were observed with the cutoff frequency much higher than local f_{pe} (except the one indicated by the white arrow in Figure 5.1 (e)). This indicates that most Langmuir waves detected between the terrestrial bow shock and the IP shock are not associated with the energetic electrons from the Sun, whereas driven by the terrestrial foreshock electron beams.

An expanded view of 5-hour observations around the IP shock (indicated by red verticle line) is shown in Figure 5.2. The plasma line is apparent and both local f_{pe} and $2f_{pe}$ are overplotted as white dots in Figure 5.2 (a) for reference. Accurate measurements of local f_{pe} are derived by tracking the plasma peaks based on the neural network method whose accuracy is verified by the full fit of the quasi-thermal noise spectrum (see Salem et al., 2001; Issautier et al., 2005, and references therein). Moreover, Figure 5.2 (b–e) show that the transient electron flux enhancements around the IP shock mainly come from the direction parallel to the ambient magnetic field. More details about the detectors and specific definition of the directions are given in Appendix 5.A. Thereby, we verified that the transient parallel electron flux enhancements exclusively come from the terrestrial bow shock and therefore correspond to the terrestrial foreshock electrons. Indeed, intermittent Langmuir waves (Figure 5.2 (a)) driven by transient terrestrial foreshock electron beams are observed around the IP shock. We note that a weak Type III burst was observed around the IP shock. The cutoff frequency of the Type III burst is much higher than local f_{pe} , which means that the corresponding flare-accelerated energetic electrons did not reach the spacecraft. We further checked the EESA-High/3DP ($\sim 300 \text{ eV} \leq$

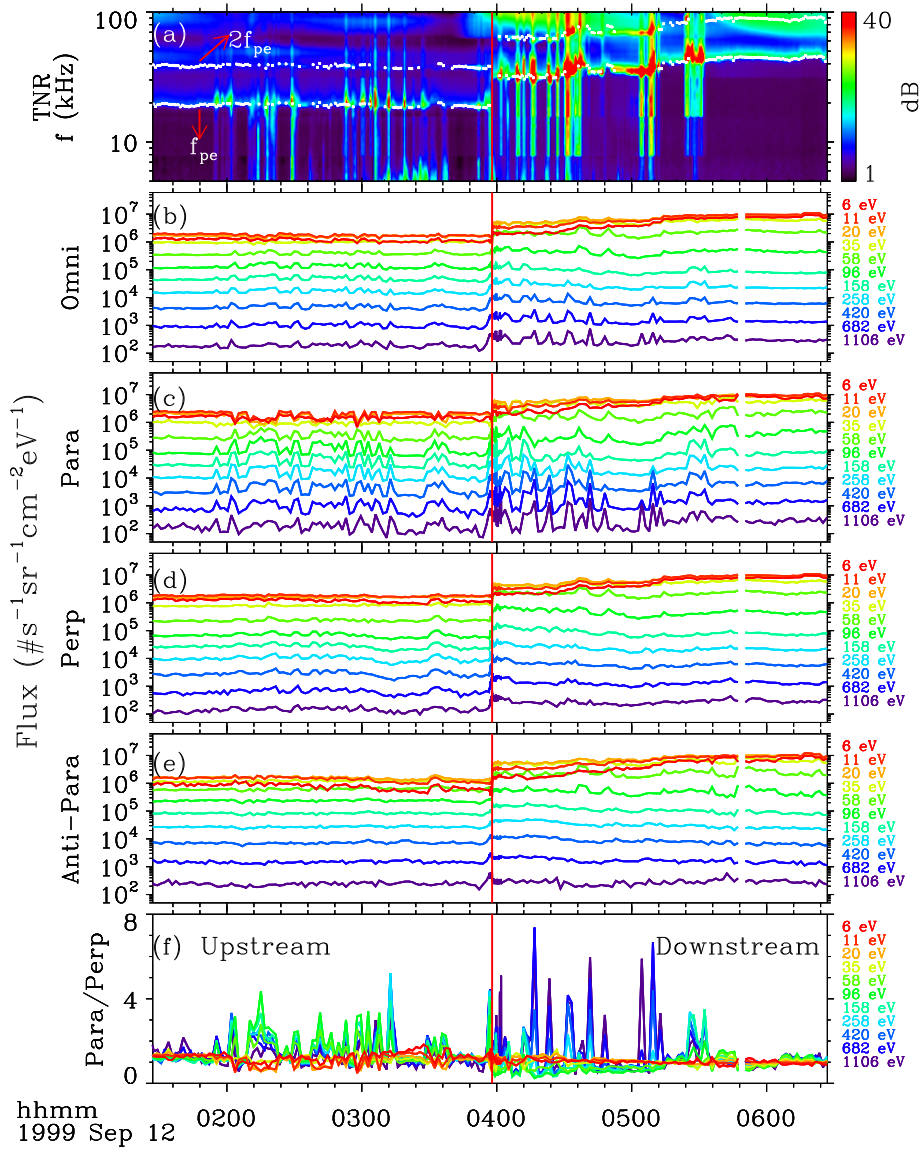


Figure 5.2 – Five-hour expanded view of measurements from *Wind* around the IP shock detected at 03:57:56 on September 12th, 1999 UT. From top to bottom, the panels show the electron field voltage power spectrum from TNR onboard *Wind*/WAVES, omni-directional electron flux, electron flux at different pitch angles including the ones parallel, perpendicular and anti-parallel to the ambient magnetic field, and the ratio of the parallel to the perpendicular flux. For electron flux at different pitch angles, they are derived from the measurements by the EESA-Low instrument onboard *Wind*/3DP, and electrons from about 6 eV to 1106 eV are considered. The labelled energies have been corrected by considering the spacecraft potential. The red vertical line marks the time when the IP shock was detected.

$E \leq 30$ keV) and SST-Foil/3DP (~ 20 keV $\leq E \leq 500$ keV) measurements and indeed found no apparent enhancements of the antisunward energetic electron flux (not shown here). Therefore, we confirm that the Langmuir waves detected around the IP shock were exclusively driven by the terrestrial foreshock electrons and not associated with the energetic electrons from the Sun. Thus, it is quite striking to mention that the intensity of the bursty Langmuir waves detected downstream of the IP shock is much higher than those upstream of the IP shock. Figure 5.2 (a) and (f) show that the detected Langmuir wave intensity is closely related to the ratio between the parallel and perpendicular electron flux. When the terrestrial foreshock electrons and the associated Langmuir waves are detected, the ratio of the parallel to the perpendicular electron flux is larger than the ambient values in the free solar wind. Upstream of the IP shock, the ratio of the parallel to the perpendicular electron flux is the largest for the terrestrial foreshock electrons with energy from 96 eV to 258 eV (see green lines in Figure 5.2 (f)). In contrast, downstream of the IP shock, the energy of the dominant terrestrial foreshock electrons (with larger ratio of the parallel to the perpendicular electron flux) is higher than 420 eV (see dark blue and/or purple lines in Figure 5.2 (f)). Across the IP shock, the energy of the dominant terrestrial foreshock electrons and the corresponding ratio of the parallel to the perpendicular electron flux are greatly enhanced. This coincides with the enhanced Langmuir wave activity downstream of the IP shock. The possible driving mechanisms are explained in section 2.2.

2.2 Electron Dynamics at Kinetic Scales

In this section, we investigate how the electron features are modified across the IP shock at kinetic scales, which are associated with the mechanisms of wave generations/enhancements. Full electron pitch angle distributions (PADs) around the IP shock are plotted in Figure 5.3. The labelled energies in Figure 5.3 are the mean values of the nine highest energy channels of EESA-Low/3DP after correcting the estimated spacecraft potential (Salem et al., 2001). Figure 5.3 (a–b) present the observations upstream of the IP shock; Figure 5.3 (c) covers the foot, ramp and overshoot structures of the IP shock; and Figure 5.3 (d–f) give the observations downstream of the IP shock. The foot, ramp and overshoot structures are clearly displayed in both Figure 5.4 (a) and Figure 5.7 (a). In Figure 5.3 (a–b), both the electron (with energy higher than 35 eV) number flux and energy flux along the magnetic field (including both parallel (PA $< 45^\circ$) and anti-parallel (PA $> 135^\circ$)) are higher than those perpendicular (PA = 90°) to the magnetic field. We confirm that IP foreshock electrons were not detected by *Wind* in Appendix 5.B. Therefore, suprathermal electrons flowing parallel (anti-parallel) to the ambient magnetic field correspond to the terrestrial foreshock electron beams (strahl electrons from the Sun). This gives further confirmation that the IP shock is indeed magnetically connected to the terrestrial bow shock.

We note that both the suprathermal electron number flux and energy flux perpendicular to the ambient magnetic field (i.e. PA = 90°) increase from upstream to the shock ramp position (see Figure 5.3 (a–c)). This enhancement may be explained by the pitch-angle scattering by the whistler heat flux instabilities observed near the shock ramp together with the normal betatron acceleration of electrons (see below). Downstream of the IP shock, the parallel suprathermal (especially with the energy higher than 258 eV) electron flux (PA $< 45^\circ$) is in general higher

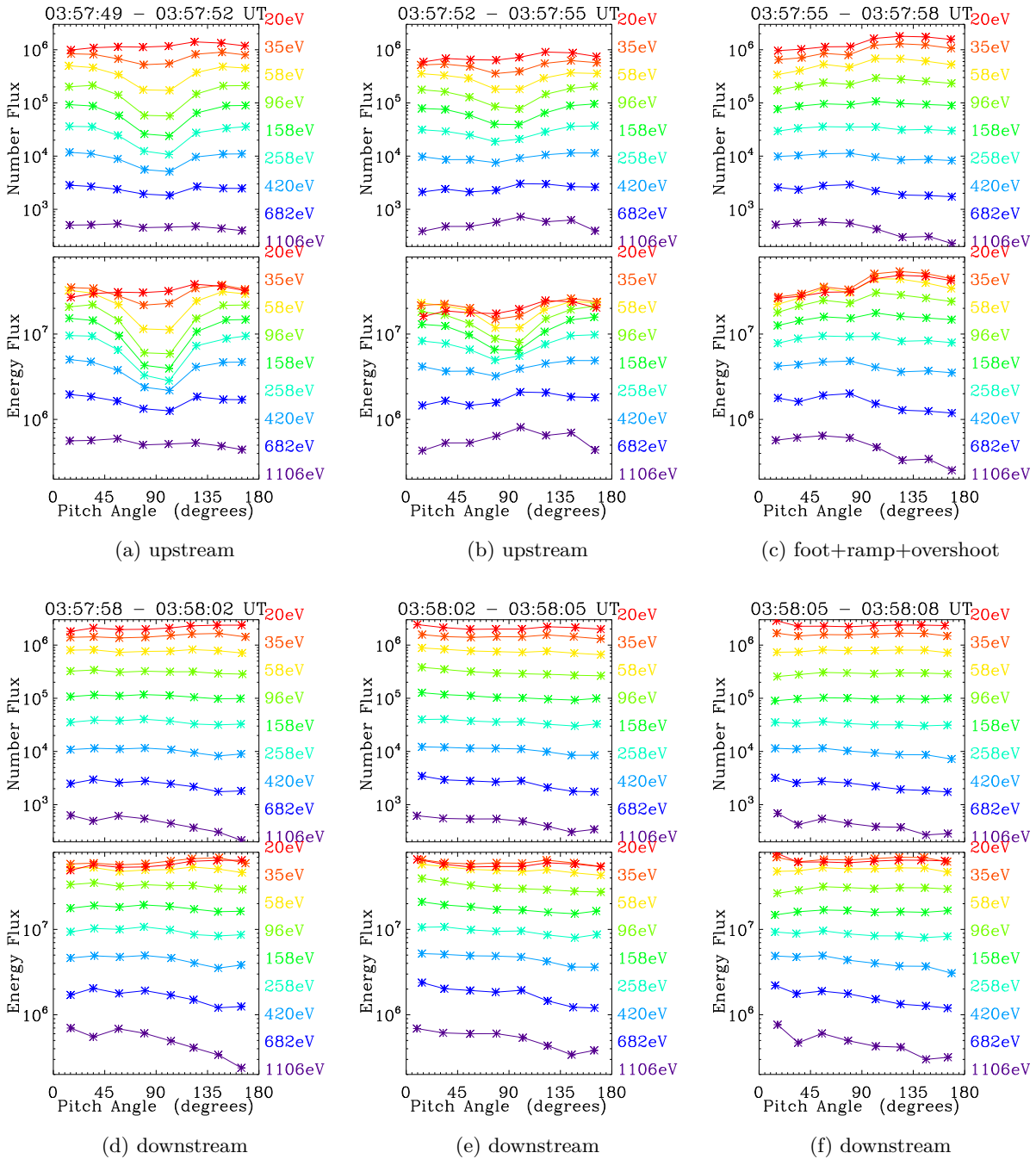


Figure 5.3 – Evolution of the stacked line plot of the pitch-angle distributions at the nine highest energies (after correcting the spacecraft potential) from the EESA-Low instrument onboard *Wind*/3DP. The top/bottom panel of each figure shows the electron pitch angle distribution of number/energy flux. The physical units are: the number flux is set in $(\#s^{-1}sr^{-1}cm^{-2}eV^{-1})$ and the energy flux is set in $(eVs^{-1}sr^{-1}cm^{-2}eV^{-1})$.

than those anti-parallel ($PA > 135^\circ$) and perpendicular ($PA = 90^\circ$) to the ambient magnetic field. This is consistent with the enhanced ratio between the parallel and the perpendicular suprathermal electron flux across the IP shock mentioned in section 2.1 (see Figure 5.2 (f)). This may account for the generation and/or enhancement of intensive Langmuir wave activity downstream of the IP shock. When the transient terrestrial foreshock electrons penetrate the IP shock, the parallel terrestrial foreshock electron flux is enhanced accordingly. Stated in another way, the transient electron flux enhancements upstream of the IP shock are further enhanced when penetrating the IP shock (e.g., Figure 5.2). Downstream the IP shock, the further enhanced terrestrial foreshock electron beams may contribute to create larger bump on tail distributions. In Figure 5.2 (f), the higher energy parallel electron fluxes can sometimes reach the lower energy parallel fluxes (higher than 258 eV) when the terrestrial foreshock electrons are detected, which may be remnants of positive slopes. Indeed, despite the fact that the parallel electron fluxes in higher energies are enhanced (see both Figure 5.2 (f) and Figure 5.3), they are not as large as to produce positive slopes on the tail of the electron distributions. There are two possible explanations: (i) the bump (the region with a positive slope) on the tail of the distribution function has already been relaxed to generate and/or enhance the Langmuir waves; (ii) the bump still exists, but the EESA instruments onboard Wind/3DP has insufficient energy resolution to resolve it. Based on the quasilinear theory of beam relaxation (e.g., Grogard, 1975; Pulupa et al., 2012; Zhao et al., 2021c, and references therein), positive slopes on bump on tail electron velocity distributions can be mediated by Landau resonance and then further generate/enhance Langmuir waves. The intensity of the Langmuir waves depends on both the energy of the electron beam and the height of the bump on tail distribution, which could explain well the more intense Langmuir waves downstream of the IP shock.

Figure 5.4 gives the wavelet analysis of the magnetic field at a high cadence of 11 samples/s around the IP shock with a 2-minute time interval considered. The magnetic foot associated with the precursor whistlers and the magnetic overshoot are indicated by two arrows in Figure 5.4 (a), respectively. A detailed view of the magnetic foot and overshoot is shown in Figure 5.7 (a). Across the IP shock, the magnetic field magnitude is enhanced. This field jump (at the foot and ramp of the shock) lasts for about 5 seconds, much longer than the electron cyclotron period T_{ce} ($0.0038 \text{ s} < T_{ce} < 0.0086 \text{ s}$). Therefore, the first adiabatic invariant $\mu = E_{\perp}/B$ should be conserved during the compression, which means that normal betatron acceleration of electrons may exist. Normal betatron acceleration of electrons mainly occurs before and at the IP shock (at the foot and ramp of the shock), as the variation of the magnetic field magnitude almost remains relatively small downstream of the IP shock. The normal betatron acceleration of electrons may contribute to the change of the pitch angle of electrons (Liu et al., 2018). Precursor whistlers (indicated by the white arrows in Figure 5.4 (c-f)) are observed at $2.0 \text{ Hz} < f < 4.0 \text{ Hz}$ (in spacecraft frame) near the shock ramp. Figure 5.5 shows an example of minimum variance (MV) analysis (Khrabrov and Sonnerup, 1998) of the magnetic fluctuations at $2.0 \text{ Hz} < f < 4.0 \text{ Hz}$ (in spacecraft frame) at the foot/precursor region of the IP shock. The hodograms in GSE and MV coordinates are shown in the left and right panels, respectively. The wave event is right-handed polarized with respect to the local magnetic field, which is consistent with the

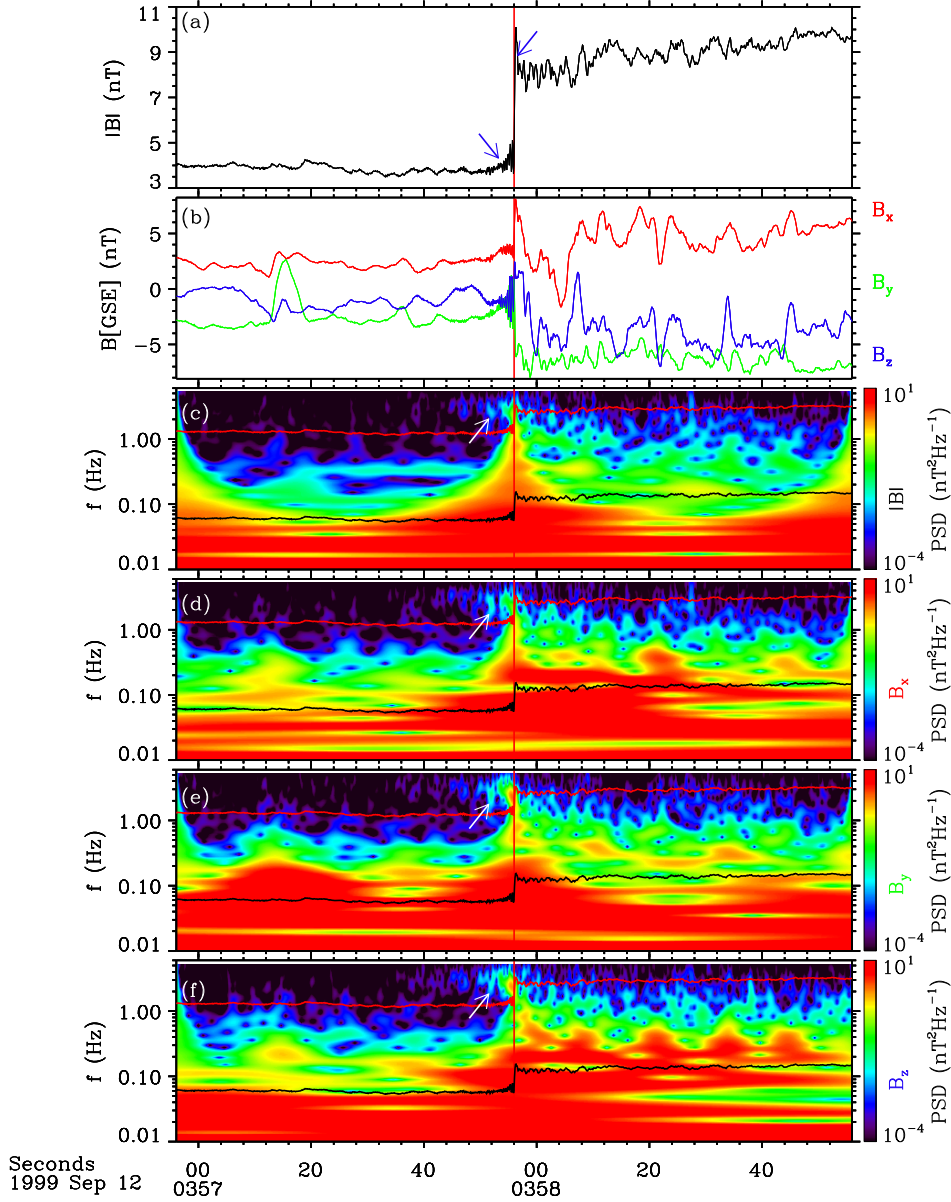


Figure 5.4 – Wavelet analysis of the magnetic field measurements around the IP shock. From top to bottom, the panels show the magnetic field magnitude, GSE components of the magnetic field, wavelet analysis of the magnetic field magnitude $|B|$ and components including B_x , B_y and B_z respectively. The frequency range of the wavelet analysis is from 0.01 Hz to 5.5 Hz. The two blue arrows in panel (a) indicate the foot (left) and overshoot (right) structures, respectively. The white arrows in panels (c–f) indicate the precursor whistlers. The red vertical line marks the IP shock. In panels (c–f), the local proton cyclotron frequency (black horizontal line) and the 1/2 lower hybrid frequency (red horizontal line) are plotted for reference.

whistler properties. The wave event is also right-handed polarized with respect to the wave vector \hat{K}_{GSE} . However, there is an ambiguity of the sign of \hat{K}_{GSE} due to projection effects, which results from using only single spacecraft magnetic field measurements (Khrabrov and Sonnerup, 1998; Wilson et al., 2017). Since $\theta_{kB} > 0^\circ$, the whistlers observed around the shock are oblique whistler waves. The shock angle $\theta_{kn} > 0^\circ$, so they are not likely to be phase standing

(Mellott and Greenstadt, 1984).

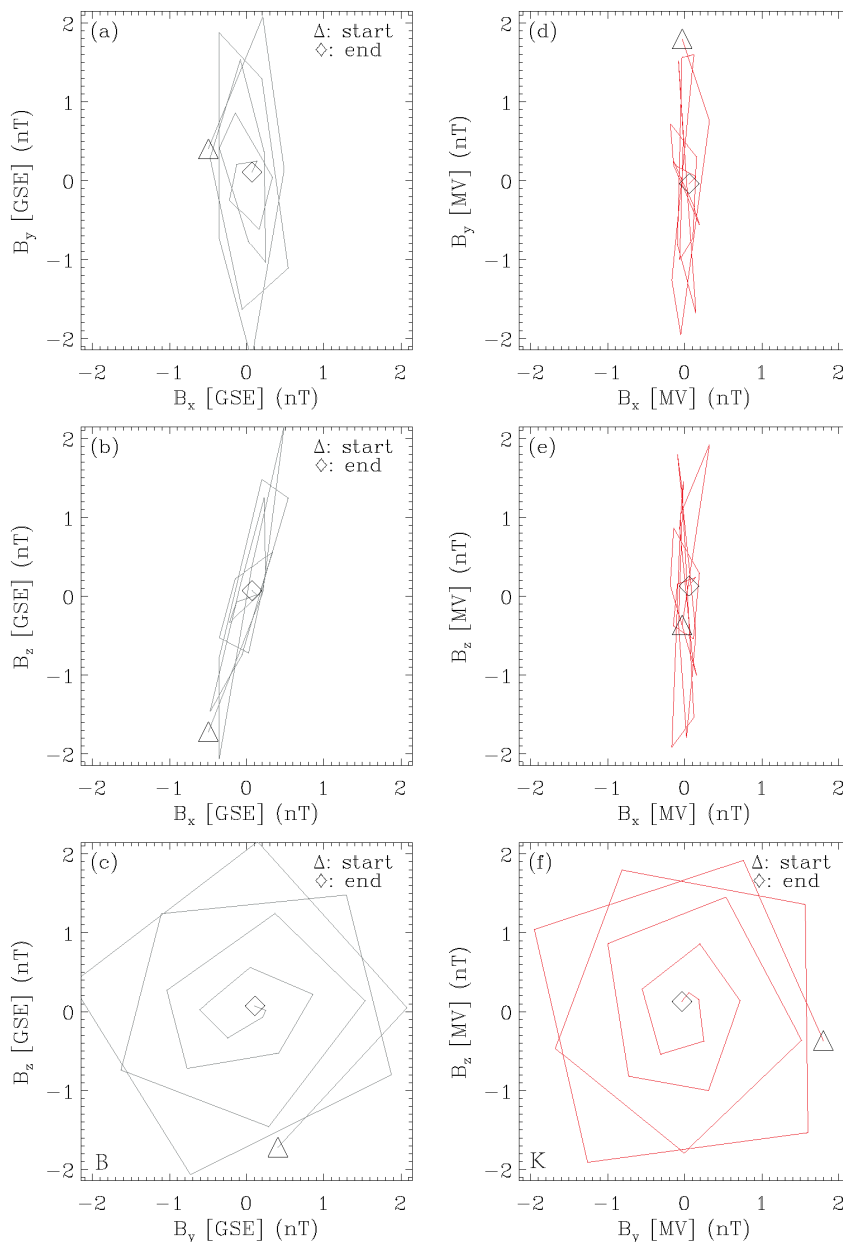


Figure 5.5 – An example of MV analysis of the waves during the time period of 03:57:55 UT~03:57:57 UT ($2.0 \text{ Hz} < f < 4.0 \text{ Hz}$ in the spacecraft frame, ratio of the intermediate to minimum eigenvalues $\lambda_2/\lambda_3=59.71$, ratio of the maximum to intermediate eigenvalues $\lambda_1/\lambda_2=1.110$, $\hat{K}_{GSE} = [0.96715, 0.06149, -0.24665]$, $\theta_{kB} = 53.7^\circ$ (or 126.3°), $\theta_{kn} = 14.2^\circ$ (or 165.8°), $\theta_{kV} = 12.4^\circ$ (or 167.6°)). The hodograms in GSE and MV coordinates are shown. The [X, Y, Z]-MV coordinates represent the directions parallel to the minimum, intermediate and maximum variance eigenvectors, respectively. The projections of magnetic field (B) and wave vector (K) point outward of the paper.

Precursor whistlers are generated through dispersive radiation from the shock ramp or indirectly due to instabilities excited by reflected particles (see Wilson et al., 2012; Wilson et al.,

2017, and references therein). Besides, precursor whistlers can be generated (and/or enhanced) by whistler heat flux instabilities and/or whistler anisotropy instabilities (Wilson et al., 2009; Liu et al., 2018), which are discussed below. Gary et al. (1999) demonstrated that the heat-flux-driven whistler mode is always unstable when the temperature anisotropy of halo electrons $T_{\perp h}/T_{\parallel h} > 1.01$ and always stable when the parallel beta of core electrons $\beta_{\parallel c} \leq 0.25$. The primary influence of whistler heat flux instabilities is to pitch-angle scatter halo electrons through a cyclotron resonance. Table 5.1 shows the electron parameters derived from the 3DP/EESA-Low data around the IP shock. Electron parameters were derived by fitting core electrons to Bi-Maxwellian distributions and halo electrons to Bi-Kappa distributions (Mace and Sydora, 2010). For more details about the fitting algorithm, please refer to Wilson et al. (2009) and Liu et al. (2018). From 03:57:55 UT to 03:58:05 UT, whistler heat flux instabilities can be excited, which is a possible driver of the whistler waves. In Table 5.1, a clear increase in $T_{\perp h}/T_{\parallel h}$ is seen across the shock (03:57:55–03:57:58 UT), which may result from the normal cyclotron resonance that can increase the transverse energy of the suprathermal electrons and the normal betatron acceleration of electrons mentioned above. These results illustrate that (when passing through the IP shock) whistler heat flux instabilities may contribute to the increase of the perpendicular suprathermal number flux and energy flux (see Figure 5.3) through pitch-angle scattering together with the normal betatron acceleration of electrons.

Time(UT)	$T_{\perp c}/T_{\parallel c}$	$T_{\perp h}/T_{\parallel h}$	$T_{\parallel h}/T_{\parallel c}$	$\beta_{\parallel c}$	$n_{ce}(\text{cm}^{-3})$	$n_{he}(\text{cm}^{-3})$	n_{he}/n_{ce}
03:57:49–03:57:52	0.71	0.65	9.85	1.61	3.61	0.27	0.075
03:57:52–03:57:55	0.72	0.89	6.90	1.67	2.27	0.20	0.087
03:57:55–03:57:58	1.10	1.09	7.56	0.84	4.27	0.27	0.063
03:57:58–03:58:02	1.03	1.10	10.31	1.10	7.35	0.10	0.014
03:58:02–03:58:05	0.98	1.07	10.31	1.23	7.20	0.10	0.015

Table 5.1 – *Wind*/3DP Electron Parameters from EESA-Low Burst Mode Data.

2.3 Interactions between IP Shock and Alfvén Waves/Fluctuations

Figure 5.6 presents the *in situ* solar wind observations around the IP shock from *Wind* including the magnetic field and the plasma measurements. Figure 5.6 (b-d) show that magnetic field components are in phase with the proton bulk velocity components, indicating signatures of Alfvén waves/fluctuations both upstream and downstream of the IP shock. This means that the IP shock is interacting with the ambient Alfvén waves/fluctuations. We further analyze the features of Alfvén fluctuations with the corresponding compressibility C_p (Figure 5.6 (g)), and cross helicity σ_c (Figure 5.6 (h)). Compressibility C_p is defined as $C_p(t) = \frac{\langle \delta N_p^2 \rangle}{\bar{N}_p^2} \frac{\bar{B}^2}{\langle \delta \mathbf{B} \cdot \delta \mathbf{B} \rangle}$ (Gary, 1986; Yao et al., 2013; Zhao et al., 2021a), where \bar{N}_p is the mean proton density, \bar{B} is the mean magnetic field magnitude, δN_p is the fluctuation of the ambient proton density, and $\delta \mathbf{B}$ is the ambient magnetic field fluctuation. Cross helicity σ_c is defined as $\sigma_c(t) = \frac{2\langle \delta \mathbf{V} \cdot \delta \mathbf{V}_A \rangle}{\langle \delta \mathbf{V}^2 + \delta \mathbf{V}_A^2 \rangle}$ (Matthaeus and Goldstein, 1982; Yao et al., 2013), where $\delta \mathbf{V}$ is the proton bulk velocity fluctuation and $\delta \mathbf{V}_A$ is the fluctuation of the ambient Alfvén velocity. Following the procedure of Yao et al. (2013), we

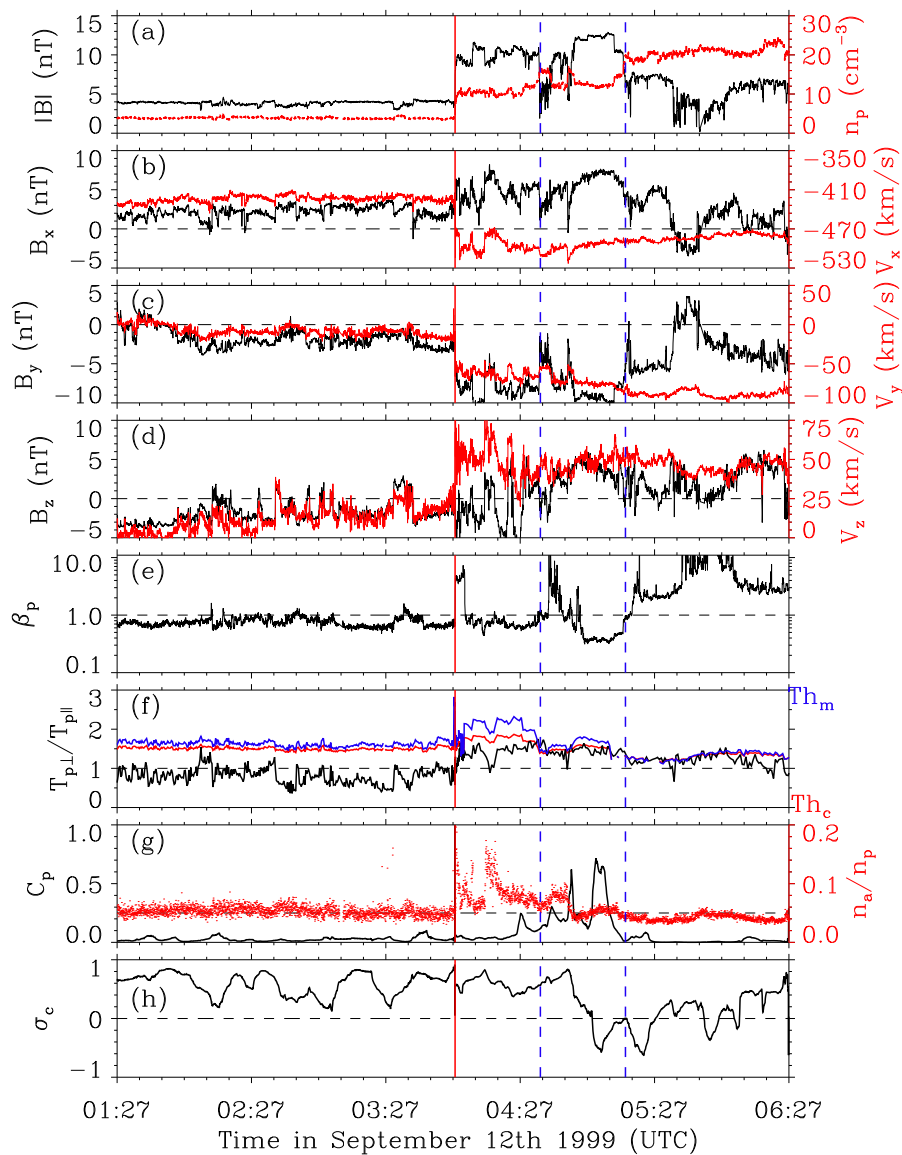


Figure 5.6 – From top to bottom, the panels show (a) the comparison between the magnetic field strength and the proton number density, (b-d) the comparison between X (Y, Z) component of magnetic field and proton bulk velocity in the GSE coordinate, (e) the proton plasma β_p , (f) the proton temperature anisotropy (black) with thresholds of ion cyclotron (red) and mirror-mode (blue) instabilities for comparison, (g) the compressibility (black) and alpha abundance (red), and (h) the cross-helicity, respectively. The red vertical line marks the IP shock propagating in the terrestrial foreshock region. The region denoted by the two blue dashed vertical lines downstream of the IP shock shows mirror mode features. More details about thresholds of ion cyclotron and mirror-mode instabilities are described in the main text.

used a moving time window width of 10 minutes to calculate the background quantities (mean values) and then the corresponding fluctuating quantities. Also, a moving time step of 3 seconds was used to do the calculations, so that C_p and σ_c were obtained for each 3-sec time interval.

A quasi-perpendicular shock can show preferential perpendicular heating (i.e. enhanced $T_{p\perp}/T_{p\parallel}$ downstream of the shock) (e.g., Liu et al., 2007; Liu et al., 2018). Plasma instabilities due to the temperature anisotropy can provide free energy to enhance the magnetic fluctuations. We thus also examine these instabilities as possible mechanisms to generate associated wave modes which may interact with the Alfvén waves/fluctuations mentioned above. The onset thresholds for plasma instabilities associated with the proton temperature anisotropy are expressed as (see Gary and Lee, 1994; Liu et al., 2006a; Liu, 2007):

$$\frac{T_{\perp p}}{T_{\parallel p}} - 1 = \frac{S}{\beta_{\parallel p}^{\alpha}}, \quad (5.1)$$

The parallel plasma beta is defined as $\beta_{\parallel p} = \frac{n_p k_B T_{\parallel p}}{B^2/2\mu_0}$. The free parameters, S and α , are determined from solutions to the single-fluid MHD equations or to the Vlasov dispersion relation. For firehose instabilities, $S = -2$ and $\alpha = 1$ (Parker, 1958a). The ion cyclotron instabilities at the maximum growth rate $\gamma = 0.01\Omega_p$ have $S = 0.64$ and $\alpha = 0.41$ (Gary et al., 1997). Here, Ω_p is the proton cyclotron frequency. For ion mirror mode instabilities at the maximum growth rate $\gamma = 0.01\Omega_p$, $S = 0.87$ and $\alpha = 0.56$. When the values $\frac{T_{\perp p}}{T_{\parallel p}}$ reach $1 + \frac{S}{\beta_{\parallel p}^{\alpha}}$, the corresponding plasma instabilities may be excited.

Upstream of the IP shock, for most of the time, σ_c is close to one whereas C_p is close to zero, which indicates signatures of shear Alfvén waves. Since $\sigma_c > 0$ and the ambient magnetic field is in general sunward, the detected Alfvén waves purely propagate antisunward. Also, Figure 5.6 (f) shows that the upstream plasma ($\frac{T_{p\perp}}{T_{p\parallel}} \sim 1.0$) inhibits ion mirror mode and cyclotron instabilities. Downstream of the IP shock, (1) the IP shock shows evidence for preferential perpendicular ion heating by the enhanced $T_{p\perp}/T_{p\parallel}$ across the shock, so that the $T_{p\perp}/T_{p\parallel}$ values touch the threshold values of both the ion cyclotron and mirror mode instabilities. Although the threshold values of the ion cyclotron instabilities are lower than the corresponding values of the ion mirror-mode instabilities, the presence of heavy ions in the solar wind ($n_{\alpha}/n_p \approx 5\%$ or even larger, see Figure 5.6 (g)) should depress the ion cyclotron wave growth rate, which favors the mirror mode growth (Price et al., 1986; Liu et al., 2006a). Therefore, the shocked plasma downstream of the IP shock is marginally unstable to the mirror mode. (2) Especially, the fluctuations denoted by the region between the two blue dashed vertical lines show mirror mode features, which is evidenced by the anti-correlated density and magnetic field magnitude fluctuations (Figure 5.6 (a); Hubert et al., 1989; Liu et al., 2006a; Zhao et al., 2019a) and the temperature anisotropy exceeding the mirror mode onset condition (Figure 5.6 (f)). Also, C_p is enhanced in the denoted large scale structures than in the ambient plasma. (3) Meanwhile, downstream of the IP shock, σ_c has both positive and negative values, and the ambient magnetic field is still generally sunward. Therefore, Alfvén waves in the shocked plasma can be separated into two parts with one propagating sunward ($\sigma_c < 0$) and the other propagating antisunward ($\sigma_c > 0$), which gives direct observational evidence for the simulation results (e.g., Lu et al., 2009).

This gives a similar picture that Alfvén waves striking the terrestrial bow shock should launch various disturbances into the magnetosheath, including both antisunward and sunward Alfvén fluctuations (e.g., Sibeck et al., 1997; Cable and Lin, 1998; Matsuoka et al., 2000). Furthermore, σ_c varies from positive to negative in the denoted large scale structures, which indicates that the sunward Alfvén waves may result from the interaction between the antisunward Alfvén waves and mirror mode waves. This is similar to the process that the antisunward Alfvén waves interacting with the fast and/or slow magnetosonic waves contributes to the growth of the sunward Alfvén waves (e.g., Schwartz, 1977; Lacombe and Mangeney, 1980).

We checked the ion distribution functions (Figure 5.7) from the PESA-High instrument onboard *Wind*/3DP to examine the ion dynamics at/around the IP shock interacting with Alfvén waves/fluctuations. The particle distributions have already been transformed into the solar wind bulk flow rest frame based on the proton bulk flow velocities measured by the PESA-Low/3DP instrument. The PESA particle detectors onboard the *Wind*/3DP suite were designed to make measurements of three-dimensional low energy (< 30 keV) ion distributions (Lin et al., 1995). The PESA-Low instrument measures ions from as low as 100 eV to as high as 10 keV with 14 different energy channels, which is designed primarily to provide solar wind bulk properties (i.e. ion density, velocity, and temperature). The PESA-High instrument measures ions of 80 eV to 30 keV at 15 different energies. The proton bulk velocity measurements by PESA-Low/3DP are in good agreements with those determined by *Wind*/SWE Faraday Cups (Ogilvie et al., 1995). As shown in Figure 5.7 (c), quite intense beam-like populations of gyrating ions (indicated by black arrows) are observed around the shock ramp with the velocities being about 450 km s^{-1} . The observed velocities of the gyrating ions are consistent with the theoretical values according to specular reflection theory (Gosling et al., 1982). The time range of Figure 5.7 (c) covers part of the shock foot/precursor, ramp and the overshoot structure (Figure 5.7 (a)). The gyrating ions are observed in association with the magnetic foot and overshoot structure, consistent with past theories/simulations (e.g., Paschmann et al., 1980; Leroy et al., 1982) and observations (e.g., Paschmann et al., 1982; Sckopke et al., 1983; Thomsen et al., 1985). Similarly, Figure 5.7 (d) gives evidence of gyrating ions behind the overshoot of the IP shock (indicated by black arrows). The velocity/density of the gyrating ions behind the overshoot of the IP shock is larger/smaller than the corresponding values at the shock ramp. This is similar to the ion dynamics at the IP shock propagating inside an ICME (Liu et al., 2018) and in the ambient solar wind (Wilson et al., 2012). Compared to another IP shock in the ambient solar wind ($M_f \sim 4.7$, $\theta_{Bn} = 82^\circ$; see Wilson et al., 2012), the present IP shock ($M_f \sim 2.1$, $\theta_{Bn} = 80^\circ$) which propagates within the terrestrial foreshock is weaker but associated with more intense beam-like gyrating-reflected ions (Figure 5.7 (c)).

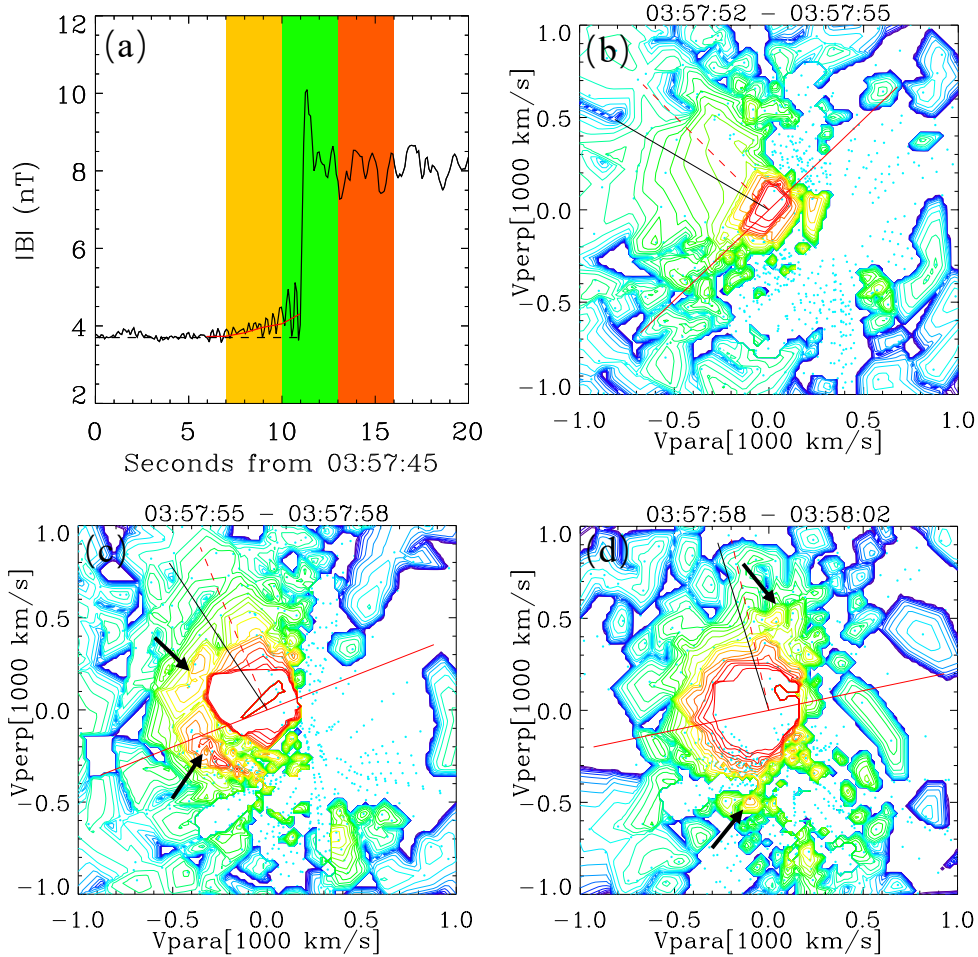


Figure 5.7 – Evolution of the ion distributions (in the solar wind frame) across the shock ramp obtained from the PESA-High/3DP instrument. The solar wind bulk flow velocities, which are used to transform particle distributions into the bulk flow rest frame, were determined from the measurements by the PESA-Low/3DP instrument. (a) Plot of a 20-second window of the magnetic field magnitude (11 samples/sec) around the IP shock. Foot-like magnetic enhancement (red curve) associated with precursor whistlers and magnetic overshoot can be clearly identified near the shock ramp. (b-d) Ion distributions corresponding to the time ranges of three color-coded shaded regions in panel (a). The contours show constant phase space density in the plane containing the ambient magnetic field (horizontal axis) and local solar wind velocity. Projected onto the planes are the following: shock normal direction (dashed red line), shock surface (solid red line), and solar wind velocity direction (solid black line). Gyration ions are indicated by the black arrows.

3 Summary and Discussions

This paper reports a comprehensive analysis of the properties of an IP shock magnetically connected to the terrestrial bow shock. Key findings are obtained concerning how the IP shock modifies the terrestrial foreshock.

1. As expected, intense Langmuir waves and $2f_{pe}$ emissions are generally detected when the terrestrial foreshock electron beams are observed. It is quite striking that intensive bursty Langmuir waves are detected downstream of the IP shock. They are likely driven by terrestrial foreshock electron beams penetrating the IP shock. Also, bursty Langmuir waves detected downstream of the IP shock are even more intense than those upstream of the IP shock. Based on the statistics on the waves at/around the IP shocks, Wilson et al. (2007) showed that Langmuir waves frequently occur at the ramp region, whereas are rarely detected downstream of the IP shocks. The present results indicate that Langmuir waves excited downstream of the IP shock depend on both the ambient upstream plasma (i.e. transient electron beams penetrating the IP shock) and the IP shock itself. We find that the intensity of the detected Langmuir waves is closely related to the energy of the electron beam and the corresponding ratio of the parallel to the perpendicular electron flux. Across the IP shock, the energy of the dominant electron beam is higher and the corresponding ratio of the parallel to the perpendicular electron flux is enhanced, which coincides with the more intensive Langmuir waves.
2. Oblique precursor whistlers are observed around the IP shock associated with the whistler heat flux instabilities. Whistler heat flux instabilities contribute to the pitch-angle scattering of the suprathermal electrons (both the terrestrial foreshock electrons and strahl electrons from the Sun) together with the normal betatron acceleration that occurs across the shock. This is similar to the picture of the disappearance of bi-directional electrons downstream of an IP shock inside an ICME (Liu et al., 2018).
3. The IP shock is interacting with the Alfvén waves/fluctuations detected in the terrestrial foreshock region. Upstream of the IP shock, Alfvén waves/fluctuations are incompressible and purely propagate antisunward. In contrast, downstream of the IP shock, the shocked plasma shows both Alfvénic and mirror-mode features. Alfvén waves/fluctuations are separated into two parts with one propagating sunward and the other propagating antisunward, which may be due to the interaction between the Alfvén waves/fluctuations and the mirror-mode waves.
4. Specularly-reflected gyrating ions are detected based on the particle distribution which covers the magnetic foot, ramp and overshoot structures. This is consistent with the specular reflection theory prediction, and provides evidence that the reflected ions may provide energy dissipation for a supercritical quasi-perpendicular IP Shock (Paschmann et al., 1980; Leroy et al., 1982). We note that more intense beam-like gyrating-reflected ions are associated with the present IP shock ($M_f \sim 2.1$, $\theta_{Bn} = 80^\circ$), compared to those reflected by another IP shock in the ambient solar wind ($M_f \sim 4.7$, $\theta_{Bn} = 82^\circ$; see Wilson et al., 2012). This may be partly explained by the interaction between the IP shock and

the upstream Alfvén waves/fluctuations (present within the terrestrial foreshock region), which can generate rippling of the IP shock front (e.g., Lu et al., 2009). This additional rippling can modify the dynamics of the gyrating ions reflected by the IP shock and lead to some diffusion. A detailed analysis of this interaction requires further investigation.

In summary, this work provides deeper insights on how an IP shock modifies the terrestrial foreshock region via wave analysis and particle distributions. Recent observations from Parker Solar Probe (Fox et al., 2016) show that the pristine solar wind in the inner heliosphere is highly-Alfvénic (e.g., Kasper et al., 2019; Bale et al., 2019; Huang et al., 2020; Zhao et al., 2021a). Also, quite a lot of Langmuir waves were detected in the free pristine solar wind (e.g., Bale et al., 2019; Jagarlamudi et al., 2021), which indicates the presence of the transient electron beams near the Sun. The Sun is becoming more and more active since 2021, and more IP shocks driven by solar eruptions are expected to be observed in the inner heliosphere. The IP shocks near the Sun will interact with Alfvén waves/fluctuations and the transient electron beams in the free pristine solar wind. Therefore, the present results may also provide some hints on the properties of IP shocks interacting with the Alfvén waves/fluctuations and the transient electron beams near the Sun.

Appendix 5.A Source of Transient Electron Beam

In section 2.1, Figure 5.2 (b–e) show that the transient electron flux enhancements around the IP shock mainly come from the direction parallel to the ambient magnetic field. In the present context, the ambient magnetic field in general directs sunward, therefore the parallel electron flux enhancements should come from the terrestrial bow shock. However, the ambient magnetic field is slightly rotating, which may change the situation. In Figure 5.8, we compare the parallel (antiparallel) electron flux with the sunward (antisunward) electron flux. The sunward electron flux is calculated based on the similar technique to calculate the electron pitch angle distributions. When calculating the parallel (and/or antiparallel) electron flux, the ambient magnetic field vectors are used to calculate the electron pitch angles. In contrast, sunward unit vector $[1, 0, 0]$ in the GSE coordinate is used to calculate the proxy electron pitch angles and then the sunward (antisunward) electron flux.

Specifically, both Figure 5.2 (b–e) and Figure 5.8 present the measurements derived by the EESA-Low/3DP instrument (Lin et al., 1995). The EESA particle detectors onboard the *Wind*/3DP were designed to make measurements of three-dimensional low energy (< 30 keV) electron distributions. The EESA-Low analyzer covers the energy range from 3 eV to 1.1 keV, whereas the EESA-High analyzer detects electrons of 300 eV to 30 keV. Both instruments have operational fields of view of $180^\circ \times 14^\circ$ and 15 logarithmically spaced energy channels. Each detector sweeps out $4 \times \pi$ steradians in space to give a full distribution in one spacecraft spin (with the spin period being 3 seconds). The data are combined onboard with 88 angular bins for both instruments.

We note that all particle data shown herein have been transformed from the spacecraft to the solar wind bulk flow rest reference frame using the proton bulk velocities measured by the PESA-

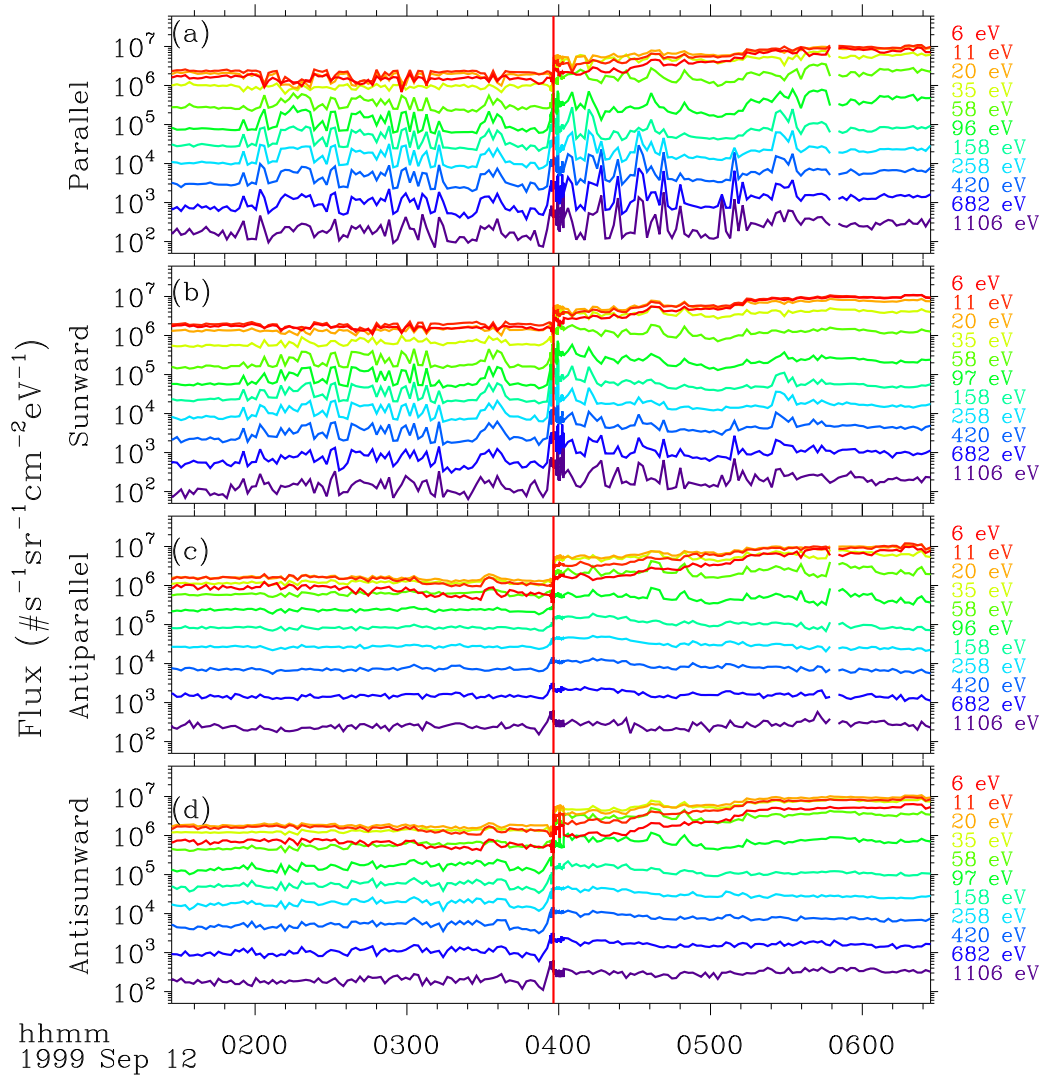


Figure 5.8 – Five-hour expanded view of electron flux measurements, from the EESA-Low instrument onboard *Wind*/3DP, around the IP shock. From top to bottom, the panels show electron flux (from about 6 eV to 1106 eV) at parallel, sunward, antiparallel, and antisunward directions, respectively. The labelled energies have been corrected by considering the spacecraft potential. The red vertical line marks the time when the IP shock was detected.

Low/3DP instrument. For each energy bin, eight pitch-angle (or the proxy ones) bins are defined to calculate the resulting distributions. For example, the mean values of eight defined pitch-angle bins are: $[14^\circ, 35^\circ, 57^\circ, 79^\circ, 101^\circ, 123^\circ, 145^\circ, 165^\circ]$. The derived distributions are summed and then averaged over each two consecutive defined pitch-angle bins. As a result, the parallel direction covers 14° – 35° , the perpendicular direction covers 79° – 101° , and the antiparallel direction covers 145° – 165° . The sunward and antisunward electron flux are defined in a similar way. Moreover, the EESA-Low measurements have been corrected by considering the effects of the spacecraft floating potential. We estimate the spacecraft potential following the procedures outlined in Salem et al. (2001). Only the measurements from the energy channels higher than the estimated spacecraft potential are shown. The labelled energies are the mean values of the corresponding energy channels after correcting the estimated spacecraft potential. Figure 5.8 (a–b) show a clear concurrence of the parallel electron flux enhancements and the sunward electron flux enhancements. Also, both the antiparallel and antisunward electron flux are relatively quiet (see Figure 5.8 (c–d)). Therefore, we confirm that the transient parallel electron flux enhancements should exclusively come from the terrestrial bow shock.

Appendix 5.B Exclusion of IP Shock as A Source

Past investigations (e.g., Bale et al., 1999; Pulupa and Bale, 2008) showed that the foreshock electrons of a quasi-perpendicular IP shock can cause increases in both the parallel and antiparallel electron flux in front of the shock surface. Furthermore, the timespan of such an IP electron foreshock region observed by the spacecraft is usually less than one minute. Therefore, such IP foreshock electrons are likely not contributing to the transient electron flux enhancements mentioned in Appendix 5.A. In spite of this, IP foreshock electrons may affect the analysis in section 2.2. As a result, we need to verify whether *Wind* detected such IP foreshock electrons. Based on burst-mode particle dataset, Figure 5.9 shows that no apparent increases are observed in electron flux in both the parallel (sunward) and antiparallel (antisunward) directions upstream of the IP shock. Therefore, we conclude that the IP foreshock electrons likely did not pass *Wind*.

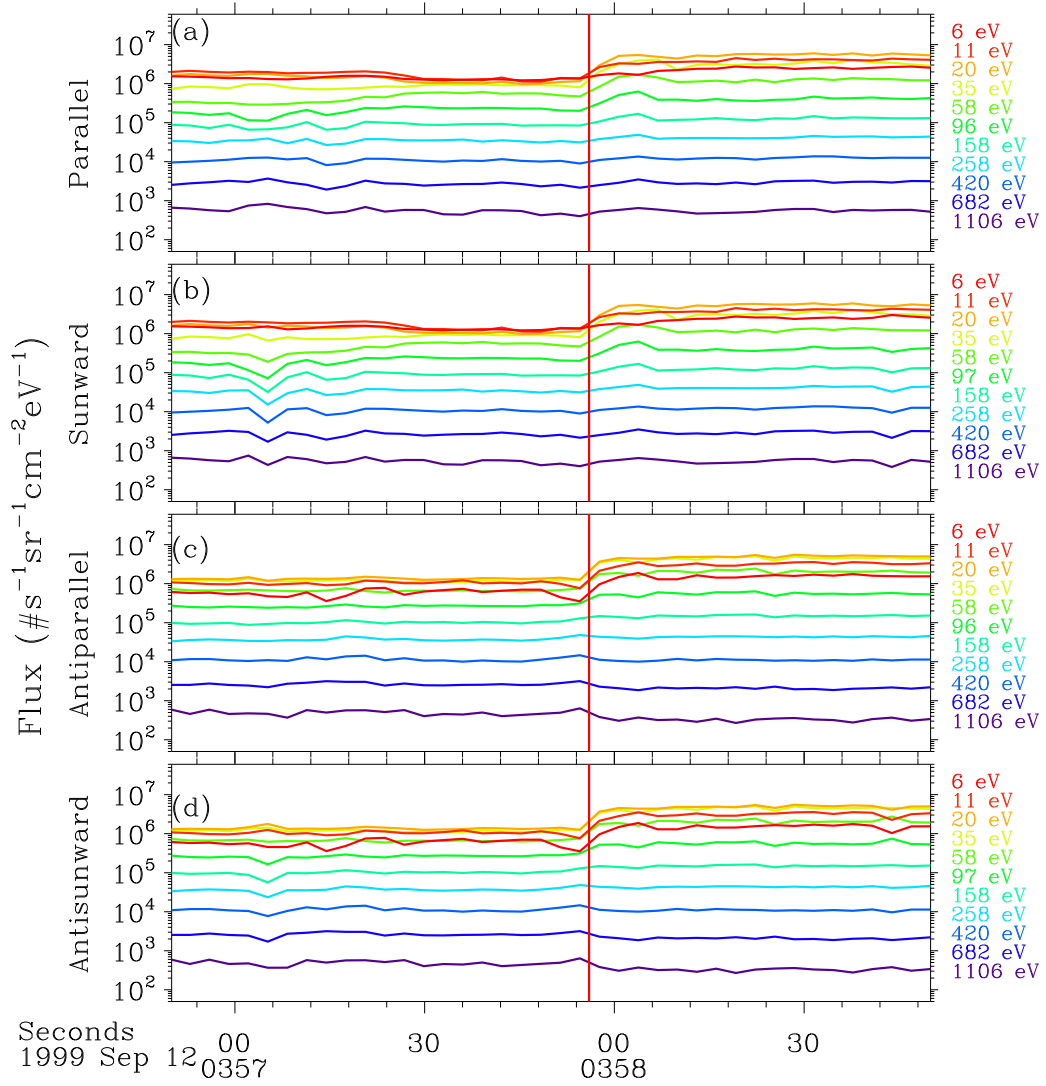


Figure 5.9 – Follows the same format as Figure 5.8 but for a 2-minute expanded view of electron flux measurements around the IP shock. Note that only the burst-mode particle dataset is considered in this plot.

Chapter 6

Quasi-Thermal Noise Spectroscopy: Application of Full Fittings on Parker Solar Probe Observations

Objectives

This chapter shows a work in progress to derive the electron properties with smaller uncertainties by fitting the whole quasi-thermal noise (QTN) spectrum. The basics of QTN spectroscopy are summarized and explained. A preliminary theoretical quasi-thermal noise (QTN) spectrum for PSP/FIELDS/RFS is shown, based on which the next steps to improve the current algorithms are given. Also, some caveats of performing full fittings on the QTN spectra are summarized.

Contents

1	Basics of Quasi-Thermal Noise Spectroscopy	97
2	Doppler-shifted Proton Thermal Noise	99
3	Antenna Impedance and Shot Noise	100
4	Gain Factor	101
5	Preliminary Numerical Results and Next Steps	101
6	Database of Spectra Affected by Langmuir Waves and/or Radio Emissions	103

1 Basics of Quasi-Thermal Noise Spectroscopy

With an electric antenna immersed in a plasma drifting with velocity \vec{V} , the electric voltage power spectrum density (at the angular frequency $\omega = 2\pi f$) at the antenna ports is

$$V_\omega^2 = \frac{2}{(2\pi)^3} \int \left| \frac{\vec{k} \cdot \vec{J}(\vec{k})}{k} \right|^2 E^2(\vec{k}, \omega - \vec{k} \cdot \vec{V}) d^3k \quad (6.1)$$

where the first term $\left(\left| \frac{\vec{k} \cdot \vec{J}(\vec{k})}{k} \right|^2 \right)$ in the integral characterizes the antenna response to electrostatic waves. $\vec{J}(\vec{k})$ is the current distribution along the antenna in Fourier space, and \vec{k} (k) denotes the wave vector (number) of the electrostatic waves. For a wire dipole antenna made of two aligned wires with length L and radius a ($a \ll L$), if each arm satisfy $L \ll \lambda$ (λ is the electrostatic wavelength) and $a \ll [L_D, L]$, the current distribution along the antenna can be assumed to be triangular (e.g., Meyer and Vernet, 1974; Meyer-Vernet et al., 2017),

$$\begin{aligned} \left| \vec{k} \cdot \vec{J}(\vec{k}) \right| &= \left| \frac{4 \sin^2(k_{\parallel} L/2)}{k_{\parallel} L} J_0(k_{\perp} a) \right| \\ &\simeq \left| \frac{4 \sin^2(k_{\parallel} L/2)}{k_{\parallel} L} \right| \end{aligned} \quad (6.2)$$

Here, k_{\parallel} (k_{\perp}) is the \vec{k} component parallel (perpendicular) to the antenna direction (Schiff, 1970; Couturier et al., 1981; Meyer-Vernet et al., 2017). J_0 is the zeroth order Bessel functions of the first kind (Abramowitz and Stegun, 1972). In the solar wind, the wave numbers k for the quasi-thermal noise (in the electrostatic limit $\omega/(kc) \ll 1$) are smaller than or of the order of the plasma Debye length (or the electron gyroradius if it is smaller), so that $ka \ll 1$ and $J_0(k_{\perp} a) \simeq 1$.

Now, let's make an assumption that the plasma fluctuations are isotropic in the antenna frame ($k_{\perp} = k_{\parallel}$), which holds true with $|\vec{V}| = 0$ and an isotropic velocity distribution $f(\vec{v})$ in a unmagnetized or weakly magnetized plasma ($\omega_{pe} \gg \omega_{ce}$). In the solar wind, $\omega_{pe} \gg \omega_{ce}$, so that the effects from the ambient static magnetic field in general can be neglected for the frequency range considered (near $\omega \approx \omega_{pe}$ or $\omega \gg \omega_{ce}$). The thermal velocity of electrons v_{the} is generally much higher than the plasma bulk velocity \vec{V} , so that the assumption that $|\vec{V}| = 0$ is reasonable in the case of solar wind electrons. The proton contribution to the electric voltage power spectrum given in Equation 6.1 has been extensively studied by Issautier et al. (1999b) and will be summarized in section 2. Then we can rewrite Equation 6.1 as

$$V_\omega^2 = \frac{8}{\pi^2} \int_0^\infty F(kL) E^2(\vec{k}, \omega) dk \quad (6.3)$$

with the so-called antenna response function as

$$\begin{aligned}
 F(x) &= \frac{1}{32\pi} \int |\vec{k} \cdot \vec{J}(\vec{k})|^2 d\Omega \\
 &= \frac{1}{x} [\text{Si}(x) - \frac{1}{2} \text{Si}(2x) - \frac{2}{x} \sin^4(\frac{x}{2})] J_0^2(\frac{xa}{L}) \\
 &\simeq \frac{1}{x} [\text{Si}(x) - \frac{1}{2} \text{Si}(2x) - \frac{2}{x} \sin^4(\frac{x}{2})]
 \end{aligned} \tag{6.4}$$

Here, $\text{Si}(x) = \int_0^x \sin(t)/t dt$ is the sine integral function. The second term in the integral of Equation 6.3 is the Fourier transform of the autocorrelation function of the electrostatic field fluctuations in the antenna frame after the isotropy assumption mentioned above, which is given as

$$E^2(\vec{k}, \omega) = 2\pi \frac{\sum_j q_j^2 \int f_j(\vec{v}) \delta(\omega - \vec{k} \cdot \vec{v}) d^3v}{k^2 \varepsilon_0^2 |\varepsilon_L(\vec{k}, \omega)|^2} \tag{6.5}$$

Here, $f_j(\vec{v})$ is the velocity distribution of the j th species of charge q_j and $\varepsilon_L(\vec{k}, \omega)$ is the plasma longitudinal dielectric permittivity. We point out that the term originating from transverse waves is negligible under the electrostatic limit ($\omega/(kc) \ll 1$). Again, if only the contribution of electrons are considered, after inserting Equation 6.5, we can rewrite Equation 6.3 as

$$V_\omega^2 = \frac{16m_e \omega_{pe}^2}{\pi \varepsilon_0} \int_0^\infty \frac{F(kL) B(k, \omega)}{k^2 |\varepsilon_L(k, \omega)|^2} dk \tag{6.6}$$

where $B(k, \omega)$, and $\varepsilon_L(k, \omega)$ are given as,

$$B(k, \omega) = \frac{2\pi}{k} \int_{\omega/k}^\infty v f(v) dv \tag{6.7}$$

$$\varepsilon_L(k, \omega) = 1 + \frac{2\pi \omega_{pe}^2}{k} \int_{-\infty}^{+\infty} \frac{v_{\parallel} f(v_{\parallel})}{k v_{\parallel} - \omega - i0} dv_{\parallel} \tag{6.8}$$

Here, v_{\parallel} is the \vec{v} component parallel to \vec{k} and the term $i0$ indicates an infinitesimal positive imaginary part.

Above all, the antenna response function $F(kL)$ depends on the current distribution along the antenna. Both $B(k, \omega)$ and $\varepsilon_L(k, \omega)$ depend on the plasma velocity distribution function (VDF). Therefore, improving the models to more accurately describe the current distribution along the antenna and the plasma velocity distribution functions are the two directions to extend the quasi-thermal noise (QTN) spectroscopy. Inserting the electron VDF $f(\vec{v})$ into Equation 6.6, the electron thermal noise $V_{electron}^2(\omega)$ is derived.

In the solar wind, the electron velocity distribution is typically assumed to be a superposition of two isotropic Maxwellian distributions: a thermal core (of density n_c and temperature T_c) and a suprathermal halo (of density n_h and temperature T_h) (e.g., Meyer-Vernet and Perche, 1989; Issautier et al., 1998). Then, the plasma longitudinal dielectric permittivity is rewritten

as

$$\varepsilon_L(k, \omega) = 1 + \sum_{P=c,h} \frac{1 - \Phi(z_P) + i\pi^{1/2} z_P e^{-z_P^2}}{k^2 L_{DP}^2} \quad (6.9)$$

$$\Phi(z) = 2ze^{-z^2} \int_0^z e^{x^2} dx \quad (6.10)$$

where n_c , T_c , n_h , T_h are the density and the temperature of respectively the thermal core (c) and suprathermal halo (h) components and $z_P = \omega/kv_{TP}$, $v_{TP} = (2k_B T_P/m_e)^{1/2}$, and $L_{DP} = (\varepsilon_0 k_B T_P / (n_P e^2))^{1/2}$, with $P = c, h$. Finally, the electron thermal noise $V_{electron}^2(\omega)$ is derived as,

$$V_{electron}^2(\omega) = \frac{16k_B}{\pi^{3/2} \varepsilon_0 \omega} \int_0^\infty \frac{F(kL)}{|\varepsilon_L(k, \omega)|^2} \sum_{P=c,h} \frac{T_P z_P}{k^2 L_{DP}^2} e^{-z_P^2} dk. \quad (6.11)$$

2 Doppler-shifted Proton Thermal Noise

In the plasma rest frame, the fluctuations induced by protons in the solar wind at the antenna terminals are expected to be observed around the proton plasma frequency $\omega_{pi} = \omega_{pe} \sqrt{m_e/m_p}$. However, unlike the electrons ($V_{sw} \ll v_{the}$), the solar wind speed is larger than the proton thermal speed ($V_{sw} \gg v_{thp}$), the proton thermal noise can be strongly Doppler-shifted towards higher frequencies in the electric antenna frame of reference and affect the low frequency part of the electron QTN spectrum. Therefore, the Doppler-shifted proton thermal noise should be considered when implementing the QTN spectroscopy. Starting from Equation 6.1, Issautier et al. (1999b) have extensively studied this noise and gave the ion contribution to the voltage power spectrum in cylindrical coordinates of axis parallel to \vec{V} :

$$\begin{aligned} V_{proton}^2(\omega) &= \frac{8}{\pi^2} \frac{n_p e^2}{\varepsilon_0^2} \left(\frac{m_e}{2\pi k_B T_e} \right)^{1/2} \mu \int_0^\infty \frac{dk}{k^3} \\ &\times \int_{-1}^{+1} \frac{\exp[-\mu^2(\omega - kVu)^2 / (v_{the}^2 k^2)]}{|\varepsilon_L(\vec{k}, \omega - kVu)|^2} du \\ &\times \int_0^{2\pi} \frac{\sin^4(\frac{kL}{2} \cos \gamma)}{(kL \cos \gamma)^2} d\Phi, \end{aligned} \quad (6.12)$$

Here, μ is the ratio between the electron and proton thermal speed, $u = \cos \theta$ with θ being the angle between \vec{k} and \vec{V} . γ is the angle between the antenna and \vec{k} , which is given by

$$\cos \gamma = u \cos \beta + \sqrt{1 - u^2} \sin \beta \cos \Phi,$$

where β is the angle between \vec{V} and the antenna, and Φ is the azimuthal angle of \vec{k} in a plane perpendicular to \vec{V} .

In order to deduce a formula for practical plasma diagnostic, two simple cases where the antenna is perpendicular or parallel to the velocity \vec{V} can be considered. It is pointed out that the first case is the most interesting in practice. The Doppler-shift effects for the proton thermal noise is maximum for \vec{k} parallel to \vec{V} . Furthermore, for a long dipole antenna ($kL \gg 1$), it is mainly sensitive to wave vectors roughly perpendicular to its proper direction. Therefore, Doppler-

shifted proton thermal noise is expected to be maximum when the antenna is perpendicular to \vec{V} . The simplified expression is given by,

$$V_{proton}^2(\omega) = \frac{(2m_e k_B)^{1/2} \sqrt{T_e}}{4\pi\epsilon_0 M} \int_0^\infty \frac{y F_\perp(yL/L_D)}{(y^2 + 1 + \Omega^2)(y^2 + 1 + \Omega^2 + t)} dy \quad (6.13)$$

where Ω , t , and M are given by

$$\Omega = \omega L_D/V, t = T_e/T_p, M = V/v_{the} \quad (6.14)$$

F_\perp is the antenna response to a wave field having a cylindrical symmetry (Meyer-Vernet et al., 1993b):

$$\begin{aligned} F_\perp(x) &= \frac{64}{\pi} \int_0^x \frac{\sin^4(s/2)}{s^2(x^2 - s^2)^{1/2}} ds \\ &= \frac{8}{x} [2 \int_0^x J_0(t) dt - \int_0^{2x} J_0(t) dt + J_1(2x) - 2J_1(x)] \end{aligned} \quad (6.15)$$

where J_0 and J_1 denote the Bessel functions of the first kind and L_D is the electron Debye length.

3 Antenna Impedance and Shot Noise

In section 1 and section 2, the electric antenna is assumed to be a "grid antenna", neglecting that the antenna can disturb the trajectories of the particles. In principle, the physical electric antenna immersed in a plasma like the solar wind can collect electrons and ions, and can also emit photoelectrons and/or secondary particles. As a result, an additional noise called shot noise should also be taken into account when implementing the QTN spectroscopy. This shot noise becomes important only for $f \ll f_{pe}$ and decreases as $1/f^2$. A good approximation for the shot noise at the antenna terminals below f_{pe} is given by Meyer-Vernet and Perche (1989),

$$V_{shot}^2(\omega) = 2e^2 N_e A |Z_A|^2 \quad (6.16)$$

where $N_e = (4\pi)^{1/2} n_e v_{the} S$ is the electron impact rate on one antenna arm with $S = 2\pi aL$ for a wire antenna. The factor $A \approx 1 + \frac{e\phi}{k_B T_e}$ comes from a first-order approximation of the shot noise (ϕ is the the DC potential). A practical expression of antenna impedance Z_A is given by,

$$Z_A(\omega) = \frac{4j}{\pi^2 \epsilon_0 \omega} \int_0^\infty \frac{F(kL) F_a(ka)}{\epsilon_L(k, \omega)} dk, \quad (6.17)$$

with the functions $F(kL)$ and $\epsilon_L(k, \omega)$ given in Equations 6.4 and 6.8, respectively. $F_a(ka)$ takes the finite radius a of the antenna into account as

$$F_a(x) = J_0^2(x). \quad (6.18)$$

As is discussed below in section 4, in the radio frequency range (at frequencies well above the kHz), the resistive part of the antenna impedance Z_A is negligible.

4 Gain Factor

In sections 1, 2, and 3, the electron thermal noise $V_{electron}^2$, the doppler-shifted proton thermal noise V_{proton}^2 , and the shot noise V_{shot}^2 are given at the antenna terminals. In practice, the antenna is electrically connected to an input receiver. Thus, the effective electric voltage power spectral density V_R^2 measured by the receiver is expressed as

$$V_R^2 = \Gamma_R^2(V_{electron}^2 + V_{proton}^2 + V_{shot}^2) + V_{noise}^2 + V_{galaxy}^2 \quad (6.19)$$

where the instrument noise V_{noise}^2 , and the galactic radio background noise V_{galaxy}^2 have been discussed in Chapter 4. In Equation 6.19, Γ_R^2 is the gain factor of the receiver, which is expressed as

$$\Gamma_R^2 \simeq \frac{Z_B^2}{(Z_A + Z_B)^2} \quad (6.20)$$

where $Z_A = R_A + \frac{1}{i\omega C_A}$ and $Z_B = R_B + \frac{1}{i\omega C_B}$ are the dipole antenna impedance and the (dipole) stray impedance determined by the spacecraft design, respectively. C_A and C_B are the dipole antenna capacitance and the (dipole) stray capacitance, respectively. R_A and R_B are the dipole antenna resistance and the (dipole) stray resistance, respectively. Since in the radio frequency range (at frequencies well above the kHz), the resistive part of these impedances is negligible (typically, at 1 MHz, $1/(\omega C_{A,B}) \sim 10 \text{ k}\Omega$ whereas $R_{A,B} \sim 1 \text{ }\Omega$) (e.g., Zaslavsky et al., 2011), the gain factor Γ_R^2 reduces to:

$$\Gamma_R^2 \simeq \frac{C_A^2}{(C_A + C_B)^2} \quad (6.21)$$

This shows the importance of minimizing the stray capacitance to increase the radio receiver sensitivity. For the PSP/FIELDS/RFS receiver, the value of the (dipole) stray capacitance is $C_B \simeq 18 \text{ pF}$ (Moncuquet et al., 2020). The value of the dipole antenna capacitance C_A is a function of frequency (Meyer-Vernet et al., 2017), of which the full expression can be derived from Equation 6.17. When considering the high and low frequencies separately, it can be approximated as,

$$C_A \simeq \begin{cases} \pi\epsilon_0 L / \ln(L_D/a), & f < f_{pe} \\ \pi\epsilon_0 L / [\ln(L/a) - 1], & f > f_{pe} \end{cases} \quad (6.22)$$

where, for PSP, $L \simeq 2 \text{ m}$ is the electric antenna physical length, $a \simeq 1.5 \text{ mm}$ is the wire radius, and L_D is the Debye length.

5 Preliminary Numerical Results and Next Steps

Figure 6.1 shows a preliminary theoretical quasi-thermal noise (QTN) spectrum calculated based on the solar wind parameters measured by PSP. A sum of two Maxwellian functions are used for modeling the electron velocity distributions (e.g., Meyer-Vernet and Perche, 1989;

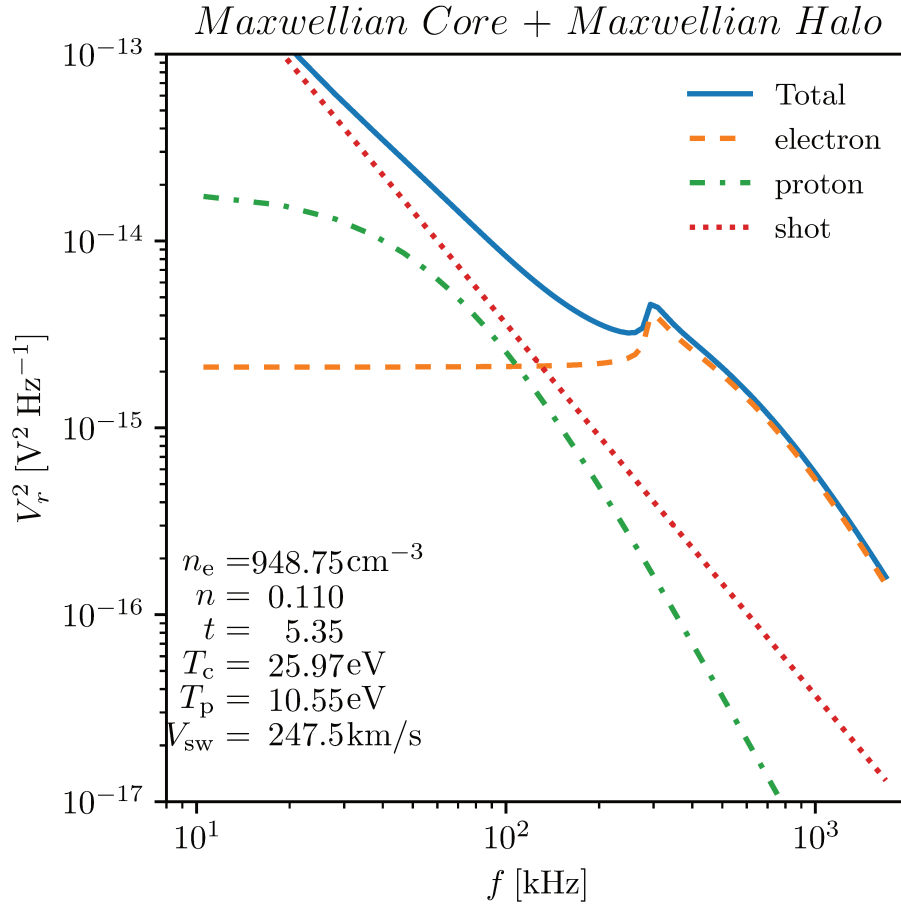


Figure 6.1 – A preliminary theoretical quasi-thermal noise (QTN) spectrum (blue line for the total noise) for the PSP/FIELDS/RFS. Three main different contributions are included: the electron QTN (yellow line), the doppler-shifted proton noise (green line), and the shot noise (red line). The electron QTN is calculated using a sum of two isotropic Maxwellians: a core and a halo. The solar wind parameters shown on the figure are: the total electron number density (n_e), the ratio of the halo to core electron number density ($n = \frac{n_h}{n_c}$), the ratio between the halo and core electron temperature ($t = \frac{T_h}{T_c}$), the core electron temperature (T_c), the proton temperature (T_p), and the proton bulk speed (V_{sw}).

Issautier et al., 1998). The doppler-shifted proton noise is calculated with Equation 6.13, and the shot noise is calculated with Equation 6.16. The electron parameters used herein are from the simplified QTN spectroscopy (Moncuquet et al., 2020), and proton parameters are from SPC/SWEAP (Case et al., 2020). The plasma parameters are obtained near the PSP orbit perihelion of E04, at around 30 solar radii. The plasma peak can be clearly shown. Below the plasma frequency (f_{pe}), the shot noise dominates, consistent with the theoretical calculations from Meyer-Vernet et al. (2017). This indicates that as PSP gets closer to the Sun, the proton noise will become negligible.

For PSP, the physical gap ($2d \simeq 3$ m) between the antenna arms is comparable to the electric antenna length ($L \simeq 2$ m). Therefore, an extension is needed to consider this physical gap when modelling the current distribution along the electric antenna ($F(kL)$ in Equation 6.4). This kind of extensions have been considered in the theoretical work of Meyer-Vernet and Perche (1989), who gave the antenna response function ($F(kL)$) considering the gap as,

$$F(k) = \frac{f[k(L + 2d)] + f(kL) - \frac{f[2k(L+d)]}{2} - \frac{f(2kd)}{2} - [\cos(k(L + d)) - \cos(kd)]^2}{(2k^2 L^2)} \quad (6.23)$$

where $f(x) = x\text{Si}(x)$. We note that in the limit $d \rightarrow 0$, Equation 6.23 will reduce to Equation 6.4. After inserting the Equation 6.23 into Equation 6.6, the algorithm herein will be ready for performing full fittings of the QTN spectra acquired by PSP/FIELDS/RFS. This is the next step for future work. And we can then compare this result with the study of Martinović et al. (2022), who took into account a non-triangular current distribution in addition to the gap formulae. In addition, we point out that another theoretical extension on the QTN technique is to consider the core electron anisotropy and the strahl electrons. In particular, considering the strahl electrons is especially necessary closer to the Sun (Meyer-Vernet et al., 2017).

6 Database of Spectra Affected by Langmuir Waves and/or Radio Emissions

As is discussed in Chapters 2 and 4, the quasi-thermal noise (QTN) spectra can be strongly contaminated by other signals which occur not so far from the electron plasma frequency (f_{pe}). These pollutions include: solar radio emissions ($f \geq f_{pe}$), bursty Langmuir waves (near f_{pe}), low-frequency (LF) plasma waves ($f < f_{pe}$), such as electron Bernstein waves and ion Acoustic waves, and dust impacts. With the purpose to implement the QTN Spectroscopy via performing full fittings (which means using a fast algorithm to fit in routine the radio spectra), these signals should be removed in advance in order to obtain clean QTN spectra. Figure 6.2 (a-d) show examples of typical clean QTN spectra and ones contaminated by other signals. These contaminations show bursty features with much higher intensities than those of QTN spectra at the corresponding frequencies. Thus, the contributions from the QTN can be considered as the baseline/background of the quiet time power for each electric field voltage spectrum. In each panel of Figure 6.2, as explained below, the black crosses denote the so-called background QTN

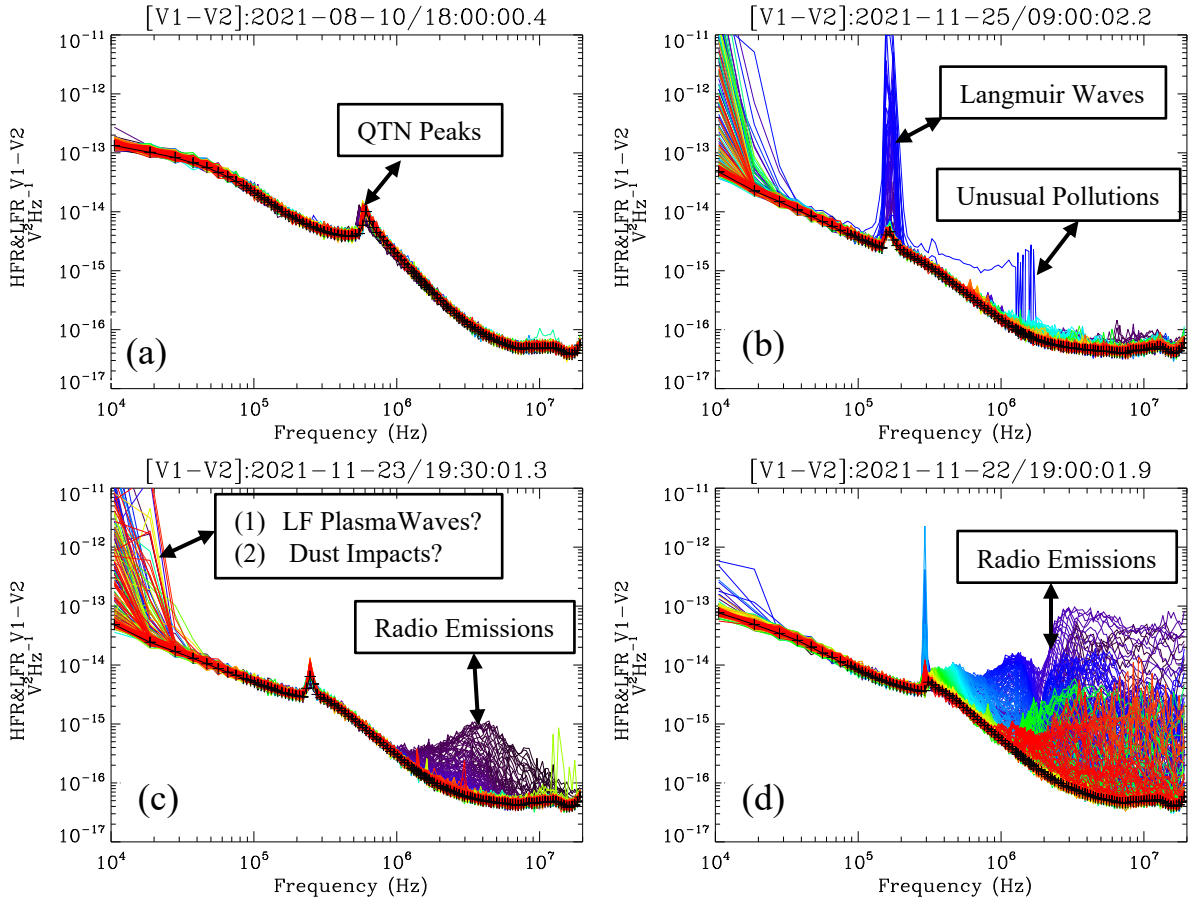


Figure 6.2 – Examples of electric field voltage spectra recorded by the PSP/FIELDS/RFS instrument. (a) A group of typical clean quasi-thermal noise (QTN) spectra with well-resolved plasma peaks. (b) A group of electric field voltage spectra affected by bursty Langmuir waves (near f_{pe}), unusual pollutions ($f \geq f_{pe}$), and LF plasma waves and/or dust impacts ($f < f_{pe}$). (c) A group of electric field voltage spectra affected by weak solar radio emissions ($f \gg f_{pe}$), and LF plasma waves and/or dust impacts ($f < f_{pe}$). (d) A group of electric field voltage spectra affected by strong solar radio emissions ($f \geq f_{pe}$), and LF plasma waves and/or dust impacts ($f < f_{pe}$).

spectrum at each frequency channel.

In order to automatically determine which spectra are contaminated by other signals, the detection algorithm compares the power at each frequency channel of the electric field voltage spectra with the baseline/background power of the QTN spectra. Specifically, we use a moving time window width of 10 minutes to calculate the background quantities (average of lowest 5% of the data for each frequency channel). Then, the ratios between the electric field voltage spectrum and the derived background QTN spectrum at each frequency channel is calculated. Based on the calculated ratios, we can further distinguish whether the electric field voltage spectra are contaminated:

1. We use the ratio of 5 as a preliminary threshold to distinguish whether the electric field voltage spectra are affected. For example, if the ratios at more than in total ten frequency channels (or at more than five consecutive frequency channels) exceed 5, then this spectrum

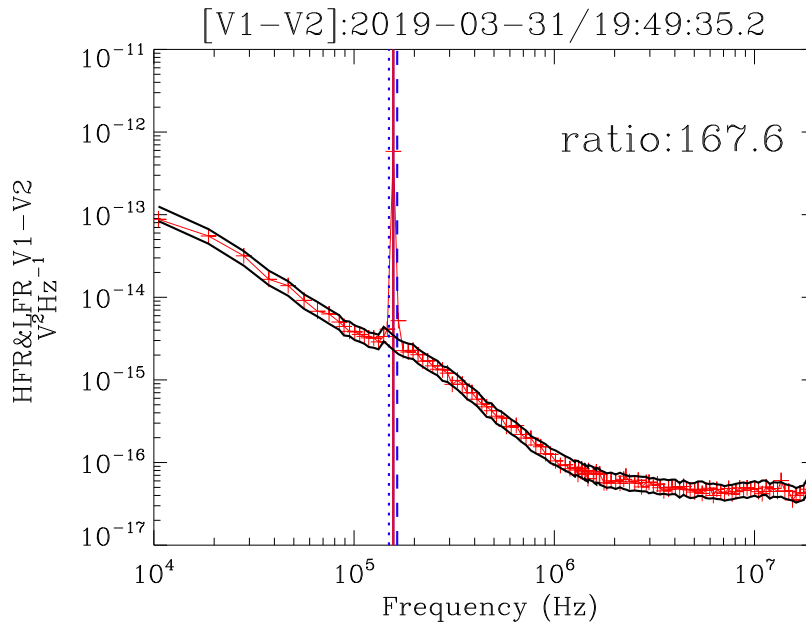


Figure 6.3 – A typical example of the identified spectrum disturbed by intensive Langmuir waves. The dataset is from PSP/FIELDS/RFS instrument.

is marked as a contaminated spectrum.

2. Then based on the electron number density (also f_{pe}) tracked by Moncuquet et al. (2020) and the corresponding uncertainty, the contaminated spectrum is divided into three areas: $f < f_{pe}$, $f \sim f_{pe}$, and $f > f_{pe}$.
3. Finally, we further check which area is contaminated. If the area $f < f_{pe}$ is contaminated, the spectrum is further marked as a spectrum affected by LF plasma waves and/or dust impacts. If the area $f \sim f_{pe}$ is contaminated, the spectrum is further marked as bursty Langmuir waves. If the area $f > f_{pe}$ is contaminated, the spectrum is further marked as a spectrum disturbed by solar radio emissions.

As is mentioned in Chapter 4, the two areas $f \sim f_{pe}$ and $f > f_{pe}$ have been processed to give two preliminary databases of bursty Langmuir waves and solar radio emissions, respectively. For the database of bursty Langmuir waves, the ratios of the maximum power spectrum density (in V^2/Hz) of bursty Langmuir waves to the background QTN plasma line power spectrum density are also given. Figure 6.3 shows a typical example of the identified spectrum disturbed by intense Langmuir waves, and the ratio is around 167.6. For the database of solar radio emissions, the upper bound and lower bound frequency of the solar radio emissions on each spectrum are also given. Figure 6.4 (left) gives the shape of an example Type III solar radio burst, by combining the identified lower bound and upper bound frequency. The shape is in general agreement with the spectrogram shown in Figure 6.4 (right).

We note that the database of bursty Langmuir waves is more accurate than that of the solar radio emissions. As is shown in Figure 6.2 (b), the unusual polluted signals may also be recognized as radio emissions. The time lengths of Type IIIs are usually less than 10 minutes. Therefore, the moving time window width of 10 minutes to calculate the background QTN

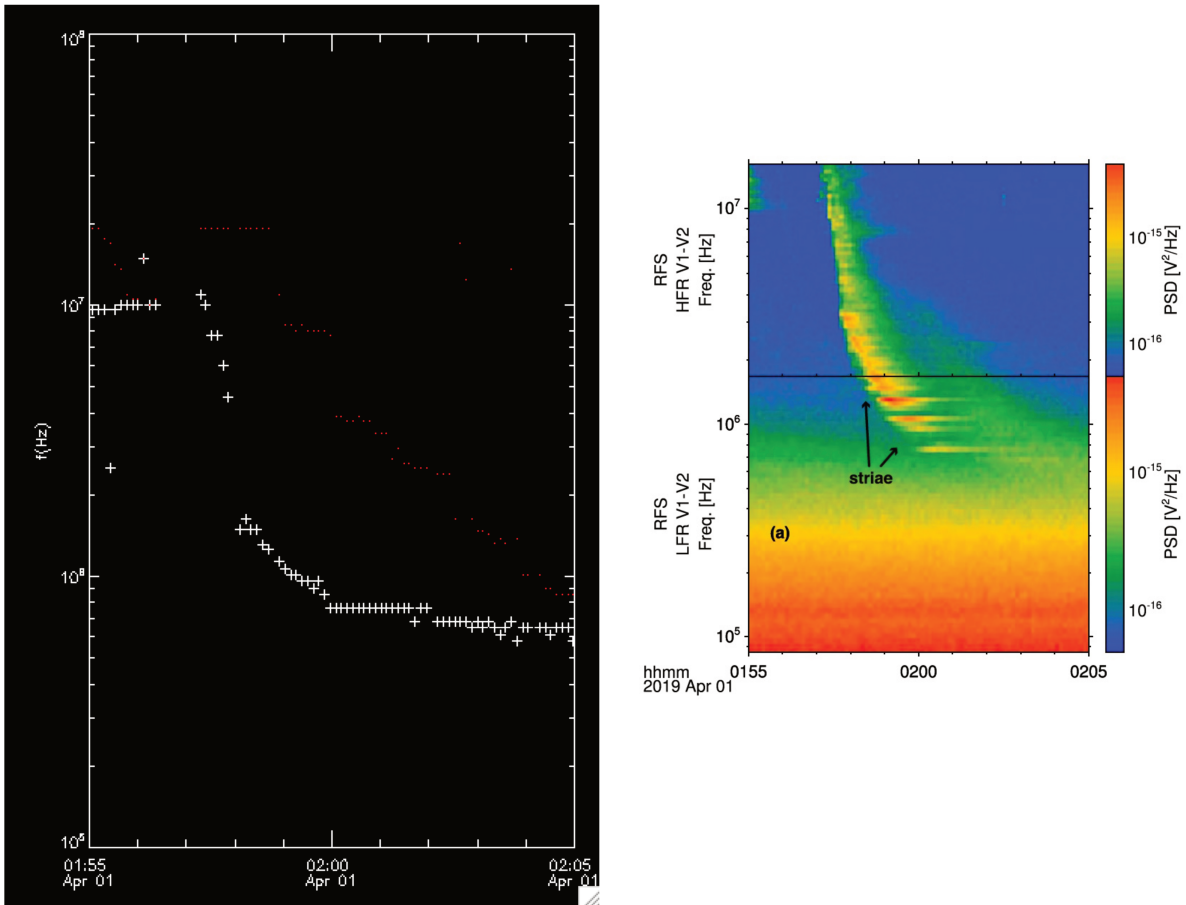


Figure 6.4 – (Left) Shape of an example Type III solar radio burst. The white crosses (red dots) are the lower bound (upper bound) frequency of the solar radio emissions on each spectrum. (Right) Radio spectrogram at the same time interval by combining all the frequency channels, which is adapted from Pulupa et al. (2020). The datasets are from PSP/FIELDS/RFS instrument.

spectrum is enough to cover the Type IIIs. However, one problem occurs if there are significant and rapid variations in the ambient plasma environments during the 10-minute time window. This is because the intensity and shape of the QTN spectrum are determined by the ambient electron parameters (i.e. density, temperature, and ratio of each electron component). When the electron density and temperature are very high, the intensity of the corresponding QTN spectrum will also be very high (Meyer-Vernet et al., 2017). In this way, the spectrum may also be considered as contaminated. This problem should be treated in a careful way by minimizing the time window width to derive the background QTN spectrum.

Chapter 7

Summary and Perspectives

Objectives

In this concluding chapter, the key results from Chapters 3, 4, 5, and 6 are reviewed and discussed in order, based on which perspectives for future work are pointed out. Specifically, based on Parker Solar Probe (PSP) observations, Chapter 3 examines the solar wind energy flux, Chapter 4 studies the radial evolution of the total electron temperature derived from the high frequency part of the quasi-thermal noise (QTN) spectra, and Chapter 6 is a work in progress to perform full fittings on the QTN Spectroscopy. In addition, Chapter 5 investigates the interaction between an interplanetary shock and the terrestrial foreshock via *Wind* measurements, combining particle distributions and wave analysis.

Contents

1	Solar Wind Energy Flux	109
2	Radial Evolution of the Total Electron Temperature	109
3	Shock Physics	111
4	Full Fittings of the QTN Spectroscopy	112

1 Solar Wind Energy Flux

The solar wind energy flux is an important quantity to understand the production and acceleration of the solar wind. Chapter 3 examines the solar wind energy flux (adding the flux equivalent to the energy necessary to move the wind out of the solar gravitational potential) as close to the Sun as $27.8 R_{\odot}$. We find that the average value of $W_{R_{\odot}}$, $\langle W_{R_{\odot}} \rangle$, is about 69.4 W m^{-2} with a total uncertainty of at most 20%, which is similar to previous results based on long-term observations at greater distances and various latitudes (eg., Schwenn and Marsch, 1990; Meyer-Vernet, 2006b; Le Chat et al., 2009; Le Chat et al., 2012; McComas et al., 2014). We confirm that this quantity appears as a global solar constant, which can be used to deduce a relation between the solar wind speed and density (Le Chat et al., 2012). The equation to formalize the anti-correlation between the solar wind speed and density is important for global heliospheric studies and modelling (eg., Shen et al., 2018; McComas et al., 2014; McComas et al., 2017; McComas et al., 2020; Krimigis et al., 2019; Wang et al., 2020). Furthermore, the normalized energy flux distributions are nearly symmetrical and well fitted by Gaussians, implying the limited interactions between the solar wind and transient plasma structures in the inner heliosphere. It is also interesting that this normalized energy flux represents a similar fraction of solar luminosity as observed for a large quantity of stars (Meyer-Vernet, 2006b; Le Chat et al., 2012). Since this quantity represents the energy flux to be supplied by the Sun for producing the wind (eg., Meyer-Vernet, 1999; Schwadron and McComas, 2003), this similarity may provide clues to the physical processes at the origin of stellar winds (eg., Johnstone et al., 2015).

As is discussed in Chapter 3, the heat flux is neglected when calculating the energy flux. When PSP gets much closer to the Sun, the contribution of the electron heat flux will become larger (see Halekas et al., 2020a; Halekas et al., 2020b). Furthermore, the solar wind protons often consist of two populations, a core and a beam drifting with respect to each other. The speed difference between them is typically of the order of the local Alfvén speed (Alterman et al., 2018). It is likely that the proton heat flux will also be more important closer to the Sun. Therefore, the heat flux will be considered in future work. Also, due to calibration issues with SPC measurements at that time, we deduce n_p and n_{α} based on n_e from QTN technique, and assume that $V_{\alpha} \approx V_p$. In fact, the differential speed between protons and alpha particles is also typically of the order of the local Alfvén speed (e.g. Steinberg et al., 1996; Ďurovcová et al., 2017; Alterman et al., 2018), so that it may affect the energy flux closer to the Sun. A long-term statistical analysis of the energy flux even closer to the Sun will be conducted with the well calibrated proton and alpha parameters.

2 Radial Evolution of the Total Electron Temperature

In Chapter 4, we derive the total electron temperature (T_e) from E01 to E10 (E08 not included), using the high frequency part of the QTN spectra recorded by RFS/FIELDS/PSP. Then, the radial evolution of the derived T_e is examined, with the heliocentric distance ranging from about 13 to $60 R_{\odot}$. We find that the total electron temperature decreases with the distance

as $\sim R^{-0.66}$, which is much slower than adiabatic. The radial T_e profile is flatter than that of the core electron temperature ($T_c \propto r^{-0.74}$, see Moncuquet et al., 2020), which is consistent with previous Helios and Ulysses observations farther out (e.g., Pilipp et al., 1990; Issautier et al., 1998; Le Chat et al., 2011). Based on the SPAN-E observations, there is no strong trend in variation of the strahl electron temperature with radial distance (Berčič et al., 2020). Therefore, the flatness of the radial T_e profile may mainly be due to the contribution of the strahl electrons. The extrapolated T_e based on PSP observations is consistent with the exospheric solar wind model prediction at $\sim 10 R_\odot$ assuming an electron velocity distribution with the Kappa index ranging between 4 and 6 (Zouganelis et al., 2004), Helios observations at ~ 0.3 AU (Maksimovic et al., 2005a) and Wind observations at 1 AU (Wilson et al., 2018). T_e extrapolated back to $10 R_\odot$ is almost the same as the solar corona strahl electron temperature (Berčič et al., 2020). This may confirm that the strahl electron temperature is closely related to or even almost equals to the coronal electron temperature. The extrapolated T_e based on the exospheric solar wind model is systematically higher (but still comparable to) than that derived from the power-law model fit.

The radial T_e profiles in the slower solar wind are relatively steeper than those in the faster solar wind, which is consistent with the long-term observations in the outer heliosphere (e.g., Maksimovic et al., 2005a; Štverák et al., 2015; Maksimovic et al., 2020). The radial T_e profile herein is generally steeper than that in the outer heliosphere (e.g., Pilipp et al., 1990; Issautier et al., 1998; Le Chat et al., 2011), which to some degree verify the exospheric model prediction in the inner heliosphere (Meyer-Vernet and Issautier, 1998). This indicates that the exospheric solar wind model explains partially the electron behaviour in the inner heliosphere. Furthermore, the solar wind mass flux derived from the in situ dataset in the inner heliosphere from PSP are in agreement with those even closer to the corona base (Bemporad, 2017) and further out in the interplanetary space (Issautier et al., 2008; Wang, 2010). Interestingly, the electron temperature cools down faster within flux tubes with larger mass flux. Given the solar wind mass flux conservation and the fact that the mass flux at the corona base increases with the footpoint field strength (Wang, 2010), it can be used as an effective physical quantity to distinguish the solar wind into different populations. This considers both the corona base conditions and the propagation effects in contrast to the proton bulk speed. Especially, the solar wind at distances of PSP orbit perihelia may be still accelerating, the speed should not be considered as the final speed.

With PSP observations from E01, E04, E05, E07 and E09, we find that the (V_p, T_e) anticorrelation is more pronounced when the solar wind is slower in the inner heliosphere. During the time period considered, most of the detected solar wind is slow wind, which on average is still being accelerated during the spherical expansion. Furthermore, the results may indicate that the slow solar wind acceleration during the expansion reduces/removes the strong (V_p, T_e) anticorrelation detected near the Sun. This is verified by the fact that the most pronounced anticorrelated V_p-T_e is observed close to the Sun, in agreement with Maksimovic et al. (2020). The solar wind V_p-T_e relation is still an interesting issue, which may depend on both the source region in the Sun (Griton et al., 2021) and the radial evolution during the expansion (Maksi-

movic et al., 2020; Pierrard et al., 2020). To comprehensively understand the V_p - T_e relation, more work is needed to distinguish and/or connect the effects from the source region, spherical expansion and the transient structures detected locally.

In future work, we will make systematic cross-checking between T_e herein and T_e from SPAN-E for all encounters. When the high-frequency part of the QTN spectra is strongly perturbed by the electromagnetic emissions (e.g., Type II and/or III radio emissions), they cannot be used for deriving T_e . As a byproduct, we therefore derive a database of spectra affected by bursty Langmuir waves and/or electromagnetic emissions (see Chapter 6), which will be useful for further analysis and routine full fittings on the QTN spectra. Currently, the database of the Langmuir waves are ready for direct use. It seems that more and more Langmuir waves are detected closer to the Sun. However, we need to combine the spectra affected by solar radio emissions to give a final database.

3 Shock Physics

The interaction between an interplanetary (IP) shock and the terrestrial foreshock is of great significance for both space weather predictions and fundamental plasma physics. Chapter 5 investigates the interaction between an interplanetary shock ($M_f = 2.1$, $\theta_{Bn} = 80^\circ$) and the terrestrial foreshock via *Wind* measurements, combining particle distributions and wave analysis. Some new features of wave activities and particle dynamics, resulting from the shock-foreshock interaction, are identified. These findings should raise questions and trigger further investigations regarding particle acceleration (i.e. through precursor whistlers) and the interaction between shocks and Alfvén waves. The key results and implications behind the new features are discussed below.

As expected, intense Langmuir waves and $2f_{pe}$ emissions are generally detected when terrestrial foreshock electron beams are observed. It is quite striking that intense bursty Langmuir waves are detected downstream of the IP shock. They are likely driven by terrestrial foreshock electron beams penetrating the IP shock. Also, bursty Langmuir waves detected downstream of the IP shock are even more intense than those upstream of the IP shock. We find that the intensity of the detected Langmuir waves is closely related to the energy of the electron beam and the corresponding ratio of the parallel to the perpendicular electron flux. Across the IP shock, the energy of the dominant electron beam is higher and the corresponding ratio of the parallel to the perpendicular electron flux is enhanced, which coincides with the more intense Langmuir waves. Previous investigations on the waves at/around IP shocks showed that Langmuir waves frequently occur at the ramp and/or upstream region (e.g., Wilson et al., 2007; Bale et al., 1999; Pulupa and Bale, 2008), whereas they are rarely detected downstream of IP shocks. The present results indicate that Langmuir waves excited downstream of the IP shock depend on both the ambient upstream plasma (i.e. transient electron beams penetrating the IP shock) and the IP shock itself. However, this also raises one question regarding how the penetrating terrestrial foreshock electron beams are accelerated parallel to the magnetic field toward downstream of the IP shock. Recent studies (e.g., Chen et al., 2018; Yu et al., 2022) showed that

precursor whistlers play a key role in the electron bulk acceleration toward the downstream at a quasi-perpendicular shock. This gives some hints for the identified features here, but still needs further investigations.

Specularly-reflected gyrating ions are detected based on the particle distribution which covers the magnetic foot, ramp and overshoot structures. This is consistent with the specular reflection theory prediction, and provides evidence that the reflected ions may provide energy dissipation for a supercritical quasi-perpendicular IP Shock (Paschmann et al., 1980; Leroy et al., 1982). We note that more intense beam-like gyrating-reflected ions are associated with the present IP shock ($M_f \sim 2.1$, $\theta_{Bn} = 80^\circ$), compared to those reflected by another IP shock in the ambient solar wind ($M_f \sim 4.7$, $\theta_{Bn} = 82^\circ$; see Wilson et al., 2012). This may be partly explained by the interaction between the IP shock and the upstream Alfvén waves/fluctuations (present within the terrestrial foreshock region), which can generate some rippling at the IP shock front (e.g., Lu et al., 2009). This additional rippling can modify the dynamics of the gyrating ions reflected by the IP shock and lead to some diffusion. A detailed analysis of this interaction requires further investigation.

Recent observations from Parker Solar Probe (Fox et al., 2016) showed that the pristine solar wind in the inner heliosphere is highly-Alfvénic (e.g., Kasper et al., 2019; Bale et al., 2019; Huang et al., 2020; Zhao et al., 2021a). Also, quite a lot of Langmuir waves were detected in the free pristine solar wind (e.g., Bale et al., 2019; Jagarlamudi et al., 2021), which indicates the presence of transient electron beams near the Sun. The Sun is becoming more and more active since 2021, and more IP shocks driven by solar eruptions are expected to be observed in the inner heliosphere. The IP shocks near the Sun will interact with Alfvén waves/fluctuations and the transient electron beams in the free pristine solar wind. Therefore, present results may also provide some hints on the properties of IP shocks interacting with the Alfvén waves/fluctuations and the transient electron beams near the Sun. Besides, another ongoing pioneering spacecraft mission called BepiColombo (Milillo et al., 2020) will reach Mercury end of 2025, and will provide a golden opportunity to study Mercury’s bow shock and its foreshock. At that time, electric antennas onboard BepiColombo will be deployed (Kasaba et al., 2020), and the analysis methods herein can be used to examine in particular Mercury’s electron foreshock.

4 Full Fittings of the QTN Spectroscopy

In Chapter 6, a work in progress to perform full fittings on the QTN Spectroscopy is described. Specifically, the basics of the QTN spectroscopy are explained together with a preliminary theoretical QTN spectrum for PSP/FIELDS/RFS. A sum of two Maxwellian functions are used to model the electron velocity distributions (e.g., Meyer-Vernet and Perche, 1989; Issautier et al., 1998). For PSP, the gap ($2d \simeq 3$ m) between the antenna arms is comparable to the electric antenna length ($L \simeq 2$ m). This gap should be considered to better model the current distribution along the electric antenna, based on which the specific next steps to improve the current algorithm are summarized. We expect to use this two-Maxwellian model to derive the electron properties (eg., n_e , T_c) with smaller uncertainties by fitting the whole QTN spectrum

in the future work. Besides, as is discussed in Chapter 2, the plasma peak of the QTN spectrum will become more and more prominent closer to the Sun. This makes it more practical to implement full fit on the QTN spectrum. In contrast, the effects of spacecraft charging will be stronger for SWEAP suite closer to the Sun (Ergun et al., 2010; Guillemant et al., 2012). Therefore, to validate the algorithm by considering the gap effects is important. We note the Sun is becoming more and more active since 2021, and more solar radio emissions will be driven by solar eruptions. This can contaminate more QTN spectra at $f \geq f_{pe}$, which should be dealt with in a careful way as is discussed in Chapter 6. Another ongoing work is to test algorithm (under development) to fit the whole electron QTN spectrum with the generalized Lorentzian (or so-called kappa) QTN model (e.g., Le Chat et al., 2009; Zouganelis, 2008), which enables to derive the electron properties (e.g., n_e , T_e , and kappa index). Finally, these extensions and algorithms discussed herein are also expected to be tested near Mercury (Milillo et al., 2020; Kasaba et al., 2020).

Appendix **A**

Other Results

Objectives

This appendix is complementary to the main chapters. Specifically, based on the results shown in Chapter 4, some further calculations are made to estimate and test the radial evolution of the Coulomb collisions and electron plasma beta (β_e).

Contents

A.1 Estimation of Coulomb Collisions and Electron Plasma Beta	115
---	------------

A.1 Estimation of Coulomb Collisions and Electron Plasma Beta

In Chapter 4, we derive the total electron temperature (T_e) from E01 to E10 (E08 not included), using the high frequency part of the QTN spectra recorded by RFS/FIELDS/PSP. Also, we obtain that T_e decreases with the distance as $\sim R^{-0.66}$, which is much slower than an adiabatic behavior. Based on the derived T_e and the power index of the radial T_e profile, some further calculations are made to estimate the Coulomb collisions and the electron plasma beta (β_e), which is useful for future work.

Coulomb collisions, which contribute to exchanging the internal kinetic and thermal energy between the plasma particles, can be estimated with both collision age A_e and temperature Knudsen number λ_{fp}/L_T (or density Knudsen number λ_{fp}/L_n). λ_{fp} is the mean free path and L_T (L_n) is the typical temperature (density) scale height of the ambient plasma. Following the procedures of Salem et al. (2003) and Štverák et al. (2008), A_e is expressed as:

$$A_e = 2.55\nu_{e\perp} \frac{R}{V_{sw}} \left(\frac{(R/r_0)^{1-1.5\alpha} - 1}{1 - 1.5\alpha} \right). \quad (\text{A.1})$$

Equation A.1 is derived, assuming that V_{sw} is constant and that n_e and T_e vary with the distance as r^{-2} and $r^{-\alpha}$, respectively. Here, $\nu_{e\perp}$ is the *in situ* transverse collision frequency of electrons. R and r_0 , in units of km, are the heliocentric distance of the spacecraft and the starting distance used to integrate/count the collisions. V_{sw} , in units of km/s, is the solar wind speed and α is the average total electron temperature power index. $\nu_{e\perp}$ is expressed as:

$$\nu_{e\perp} \simeq 7.7 \times 10^{-6} n_e T_e^{-3/2} \ln \Lambda, \quad (\text{A.2})$$

where T_e is in unit of eV, n_e is in unit of cm^{-3} , and $\ln \Lambda \simeq 25.5$ is the so-called Coulomb logarithm. We used V_p from SPC/SWEAP and/or SPAN-I/SWEAP. The parameters n_e , T_e , and α deduced from the QTN technique to calculate A_e . Here, we set $r_0=10.0 R_\odot$, which is a limit lower than the measurements. The collision age considers both the *in situ* plasma properties and to some degree the radial expansion of the solar wind from the solar corona (the initial distance $r_0=10.0 R_\odot$). However, the computation assumes that the electrons travel along open magnetic field lines with constant flow speeds. As a result, it is almost impossible to distinguish the electrons trapped by the closed magnetic field lines which have already spent more time in the expanding solar wind. Complementary to collision age A_e , we also computed temperature Knudsen number λ_{fp}/L_T as below:

$$K \simeq \lambda_{fp}/L_T = v_e \tau_e / \left(\frac{T_e}{\left| \frac{\partial T_e}{\partial r} \right|} \right) = \frac{v_e R}{\nu_{e\perp} \alpha}, \quad (\text{A.3})$$

where $\tau_e = 1/\nu_{e\perp}$ is the electron collision time, v_e is the electron thermal speed in unit of m/s, R is the heliocentric distance in unit of m, and α is the average total electron temperature power index.

Figure A.1 (a-d) summarizes the radial variation of the proton bulk speed (V_p), electron plasma beta (β_e), collision age (A_e), and Knudsen number (λ_{fp}/L_T), respectively. On average,

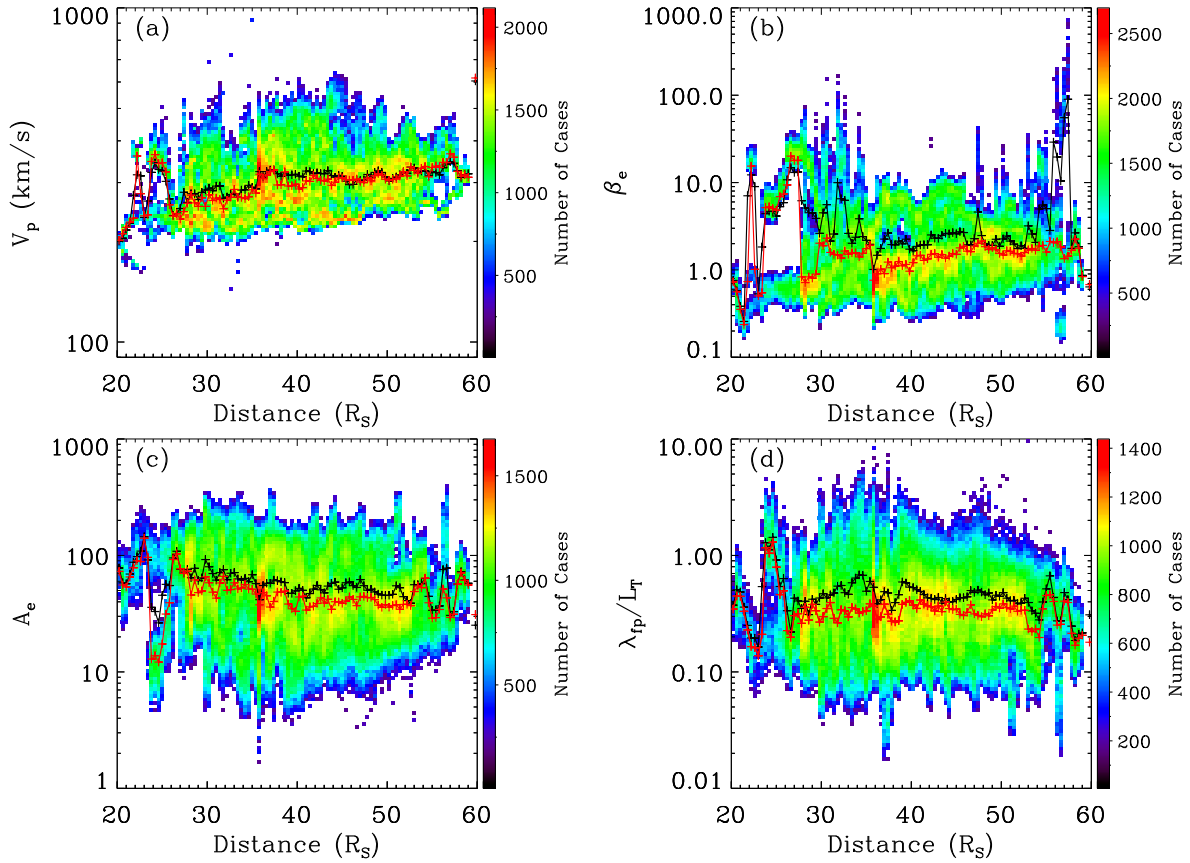


Figure A.1 – Radial variation of the proton bulk speed (V_p), electron plasma beta (β_e), collision age (A_e), and Knudsen number (λ_{fp}/L_T), combining 12-day Parker Solar Probe observations around each perihelion from E01 to E07. For each panel, both the mean (black crosses) and median (red crosses) values of each radial bin are superimposed for reference.

V_p increases with respect to the heliocentric distance, which indicates that the solar wind at distances of PSP orbit perihelia may be still accelerating, and the speed should not be considered as the final speed. There is no strong trend in variation of β_e with respect to the heliocentric distance. Also, there is a gap in $1 < \beta_e < 10$ when the heliocentric distance is lower than $\sim 28 R_\odot$. This may be due to that fewer data points are included below $\sim 28 R_\odot$, since the calculations herein stop at E07. The collision age A_e is the number of transverse collisions suffered by a thermal electron during the expansion of the solar wind over the scale of the density gradient. However, there is a weak trend that the collision age A_e is decreasing with respect to the heliocentric distance. This may be explained that PSP may not have collected enough solar wind flow states. As is discussed above, another issue is that the solar wind measured by PSP may be still under acceleration and have not reached its final speed. This means that a low speed (not the final speed) is used to make the calculations so that the corresponding A_e may be overestimated. This should be taken into account in the future work. As expected, the Knudsen number (λ_{fp}/L_T) is anticorrelated with A_e .

Appendix **B**

Publications

Contents

B.1	Solar Wind Energy Flux Observations in the Inner Heliosphere: First Results from Parker Solar Probe	122
B.2	Total Electron Temperature Derived from Quasi-Thermal Noise Spectroscopy In the Pristine Solar Wind : Parker Solar Probe Observations	130
B.3	Properties of A Supercritical Quasi-perpendicular Interplanetary Shock Propagating in Terrestrial Foreshock Region	141

Peer-reviewed articles

First-authored:

1. **Mingzhe Liu**, Karine Issautier, N. Meyer-Vernet, M. Moncuquet, M. Maksimovic, et al. "*Solar Wind Energy Flux Observations in the Inner Heliosphere: First Results from Parker Solar Probe*". *Astronomy & Astrophysics*.
DOI: [10.1051/0004-6361/202039615](https://doi.org/10.1051/0004-6361/202039615)
2. **Mingzhe Liu**, Karine Issautier, M. Moncuquet, N. Meyer-Vernet, M. Maksimovic, et al. "*Total Electron Temperature Derived from Quasi-Thermal Noise Spectroscopy In the Pristine Solar Wind : Parker Solar Probe Observations*". *Astronomy & Astrophysics* (Under Revision).
DOI: [AA/2022/45450](https://doi.org/AA/2022/45450)
3. **Mingzhe Liu**, Zhongwei Yang, Ying D. Liu, Bertrand Lembege, Karine Issautier, et al. "*Properties of A Supercritical Quasi-perpendicular Interplanetary Shock Propagating in Terrestrial Foreshock Region*". *The Astrophysical Journal Supplement Series*.
DOI: [10.3847/1538-4365/ac94c8](https://doi.org/10.3847/1538-4365/ac94c8)

Co-authored:

1. Zhongwei Yang, Ying D. Liu, Shuichi Matsukiyo, Quanming Lu, Fan Guo, **Mingzhe Liu**, Huasheng Xie, Xinliang Gao, Jun Guo. "*PIC simulations of microinstabilities and waves at near-Sun solar wind perpendicular shocks: Predictions for Parker Solar Probe and Solar*

-
- Orbiter*". The Astrophysical Journal Letters.
DOI: [10.3847/2041-8213/abaf59](https://doi.org/10.3847/2041-8213/abaf59)
2. Ying D. Liu, Chong Chen, Michael Stevens, **Mingzhe Liu**. "*Determination of Solar Wind Angular Momentum and Alfvén Radius from Parker Solar Probe Observations*". The Astrophysical Journal Letters.
DOI: [10.3847/2041-8213/abe38e](https://doi.org/10.3847/2041-8213/abe38e)
 3. Siqi Zhao, Huirong Yan, Terry Z. Liu, **Mingzhe Liu**, Mijie Shi. "*Analysis of Magnetohydrodynamic Perturbations in the Radial-field Solar Wind from Parker Solar Probe Observations*". The Astrophysical Journal.
DOI: [10.3847/1538-4357/ac2ffe](https://doi.org/10.3847/1538-4357/ac2ffe)
 4. Jiuqi Ma, Xinliang Gao, Zhongwei Yang, Bruce T. Tsurutani, **Mingzhe Liu**, Quanming Lu, and Shui Wang. "*Nonlinear Wave–Wave Coupling Related to Whistler-mode and Electron Bernstein Waves Observed by the Parker Solar Probe*". The Astrophysical Journal.
DOI: [10.3847/1538-4357/ac0ef4](https://doi.org/10.3847/1538-4357/ac0ef4)
 5. Mihailo M Martinović, Antonije Djordjevic, Kristopher Gregory Klein, Milan Maksimovic, Karine Issautier, **Mingzhe Liu**, Marc Pulupa, Stuart D. Bale, Jasper S. Halekas, Michael D. McManus. "*Plasma Parameters From Quasi-Thermal Noise Observed by Parker Solar Probe: A New Model for the Antenna Response*". Journal of Geophysical Research: Space Physics.
DOI: [10.1029/2021JA030182](https://doi.org/10.1029/2021JA030182)
 6. Siqi Zhao, Chijie Xiao, Terry Liu, Huayue Chen, Hui Zhang, Mijie Shi, Shangchun Teng, Heshou Zhang, Xiaogang Wang, Zuyin Pu, **Mingzhe Liu**. "*Observations of the beam-driven whistler mode waves in the magnetic reconnection region at the dayside magnetopause*". Journal of Geophysical Research: Space Physics.
DOI: [10.1029/2020JA028525](https://doi.org/10.1029/2020JA028525)
 7. Siqi Zhao, Hui Zhang, Terry Liu, Huirong Yan, Chijie Xiao, **Mingzhe Liu**, Qiugang Zong, Xiaogang Wang, Mijie Shi, Shangchun Teng, Huizi Wang, R. Rankin, Craig Pollock, Guan Le. "*Observations of an electron cold ion component reconnection embedded within an ion scale antiparallel reconnection at the dayside magnetopause*". Journal of Geophysical Research: Space Physics.
DOI: [10.1029/2021JA029390](https://doi.org/10.1029/2021JA029390)
 8. Siqi Zhao, Huirong Yan, Terry Z. Liu, **Mingzhe Liu**, Huizi Wang. "*Multi-spacecraft Analysis of the Properties of Magnetohydrodynamic Fluctuations in Sub-Alfvénic Solar Wind*". The Astrophysical Journal.
DOI: [10.3847/1538-4357/ac822e](https://doi.org/10.3847/1538-4357/ac822e)
 9. Wenwen Wei, Bin Zhuang, Jia Huang, Fang Shen, Lulu Zhao, **Mingzhe Liu**, Xiaoxin Zhang, Xueshang Feng. "*Energy Spectra Variations of Energetic Particles Associated with A Stream Interaction Region*". Journal of Geophysical Research: Space Physics.
DOI: [10.1029/2022JA030652](https://doi.org/10.1029/2022JA030652)
 10. Jia Huang, J. C. Kasper, Davin E. Larson, Michael McManus, Phyllis Whittlesey, Roberto Livi, Roberto Livi, Ali Rahmati, Orlando Romeo, K. G. Klein, Weijie Sun, Bart van der Holst, Zhenguang Huang, Lan K. Jian, Adam Szabo, C. H. K. Chen, B. Lavraud, **Mingzhe Liu**, Samuel T. Badman, Tatiana Niembro, Kristoff Paulson, M. Stevens, A. W. Case, Marc Pulupa, Stuart D. Bale, and J. S. Halekas. "*Parker Solar Probe Observations of High Plasma Beta Solar Wind from Streamer Belt*". The Astrophysical Journal Supplement

Series,2023.

DOI: [accepted](#)

11. Jia Huang, J. C. Kasper, L. A. Fisk, Davin E. Larson, Michael D. McManus, C. H. K. Chen, Mihailo M. Martinović, K. G. Klein, Luke Thomas, **Mingzhe Liu**, Bennett A. Maruca, Lingling Zhao, Yu Chen, Qiang Hu, Lan K. Jian, Marco Velli, Roberto Livi, P. Whittlesey, Ali Rahmati, Orlando Romeo, Tatiana Niembro, Kristoff Paulson, M. Stevens, A. W. Case, Marc Pulupa, Stuart D. Bale, and J. S. Halekas. "*The Structure and Origin of Switchbacks: Parker Solar Probe Observations*". *The Astrophysical Journal* (Submitted), 2023.
DOI: [10.48550/arXiv.2301.10374](#)

Articles/Reports in Preparation

1. **Mingzhe Liu**, Karine Issautier, M. Moncuquet, N. Meyer-Vernet, M. Maksimovic, FIELDS Team, SWEAP Team. "*Correlation of Solar Wind Bulk Parameters in the inner heliosphere: First Results from Parker Solar Probe*". Research Note (In Progress).
2. **Mingzhe Liu**, Karine Issautier, M. Moncuquet, N. Meyer-Vernet, M. Maksimovic, FIELDS Team, SWEAP Team. "*Calibration Suggestions on Parker Solar Probe Observations: Comparisons Between the SWEAP and QTN Results*". Research Note (In Progress).
3. **Mingzhe Liu**, Karine Issautier, M. Moncuquet, N. Meyer-Vernet, M. Maksimovic, FIELDS Team, SWEAP Team. "*Quasi-Thermal Noise Spectroscopy: Application of Full Fittings on Parker Solar Probe Observations*". Research Note (In Progress).
4. Haipeng An, Shuailiang Ge, Jia Liu, **Mingzhe Liu**. "*Dark Photon detection at Sun-related space probes*". Research Note (In Progress).
5. Jia Huang, J. C. Kasper, Davin E. Larson, Michael D. McManus, P. Whittlesey, Roberto Livi, Ali Rahmati, Orlando Romeo, **Mingzhe Liu**, Lan K. Jian, Marco Velli, Tatiana Niembro, Kristoff Paulson, M. Stevens, A. W. Case, Marc Pulupa, Stuart D. Bale, and J. S. Halekas. "*The Temperature, Electron and Pressure Characteristics of Switchbacks: Parker Solar Probe Observations*". *The Astrophysical Journal* (To be submitted).
6. Xiaowei Zhao, Jingsong Wang, Mingxian Zhao, Ying D. Liu, **Mingzhe Liu**, Xiaoying Sun, Tian Mao, and Qiugang Zong. "*Application of an Interplanetary Disturbance Index Based on the Solar Wind-Magnetosphere Energy Coupling Function and the Spectral Whitening Method*". *Space Weather* (To be submitted).

International Conferences (selected)

1. Karine Issautier, **Mingzhe Liu**, M. Moncuquet, N. Meyer-Vernet, M. Maksimovic, S. Bale, M. Pulupa. "*Large-scale electron solar wind parameters of the inner heliosphere with Parker Solar Probe/FIELDS*". EGU Conference, Online, May 7, 2020.
2. **Mingzhe Liu**, K. Issautier, N. Meyer-Vernet, M. Moncuquet, M. Maksimovic, et al. "*Solar Wind Energy Flux Observations in the Inner Heliosphere: First Results from Parker Solar Probe*". AGU Conference, Online, December 16, 2020.
3. **Mingzhe Liu**, K. Issautier, N. Meyer-Vernet, M. Moncuquet, M. Maksimovic, et al. "*Solar Wind Energy Flux Observations by Parker Solar Probe*". Solar Orbiter School, Online, April 6-9, 2021.

-
4. **Mingzhe Liu**, Zhongwei Yang, Ying D. Liu, Bertrand Lembège, Karine Issautier, et al. "*Properties of A Supercritical Quasi-perpendicular Interplanetary Shock Propagating in Super-Alfvénic Solar Wind: from MHD to Kinetic Scales*". EGU Conference, Online, April 19-31, 2021.
 5. **Mingzhe Liu**, K. Issautier, N. Meyer-Vernet, M. Moncuquet, M. Maksimovic, et al. "*Radial Evolution of the Electron Temperature and In-situ (T_e , V_p) Anticorrelation in the Pristine Solar Wind*". Parker One Conference, Online, June 14-18, 2021.
 6. **Mingzhe Liu**, K. Issautier, N. Meyer-Vernet, M. Moncuquet, M. Maksimovic, et al. "*Energy Flux and Heat Transport in the Pristine Solar Wind from Parker Solar Probe Observations*". Journées CNES Jeunes Chercheurs (JC2), Toulouse, France, October 6-8, 2021.
 7. **Mingzhe Liu**, K. Issautier, N. Meyer-Vernet, M. Moncuquet, M. Maksimovic, et al. "*Radial Evolution of the Electron Temperature Derived from the Quasi-Thermal Noise Spectroscopy in the Pristine Solar Wind: Parker Solar Probe Observations*". AGU Conference, Online, December 13-17, 2021.
 8. **Mingzhe Liu**, Zhongwei Yang, Ying D. Liu, Bertrand Lembège, Karine Issautier, et al. "*Properties of A Supercritical Quasi-perpendicular Interplanetary Shock Propagating in Terrestrial Electron Foreshock Region*". AGU Conference, Online, December 13-17, 2021.
 9. **Mingzhe Liu**, K. Issautier, M. Moncuquet, N. Meyer-Vernet, M. Maksimovic, et al. "*Total Electron Temperature Derived from the Quasi-Thermal Noise Spectroscopy in the Pristine Solar Wind: Parker Solar Probe Observations*". COSPAR Conference, Athens, Greece, July 16-24, 2022..
 10. **Mingzhe Liu**, K. Issautier, M. Moncuquet, N. Meyer-Vernet, M. Maksimovic, et al. "*Total Electron Temperature Derived from the Quasi-Thermal Noise Spectroscopy in the Pristine Solar Wind: Parker Solar Probe Observations*". AOGS Conference, Online, August 1-15, 2022.
 11. Jia Huang, Justin Christophe Kasper, **Mingzhe Liu**, Vamsee K Jagarlamudi, Davin E. Larson, et al. "*The Radial Evolution of Solar Wind Plasma in the Inner Heliosphere: PSP, Helios and Wind Observations*". AGU Conference, CHICAGO, USA, December 12-16, 2022.

B.1 Solar Wind Energy Flux Observations in the Inner Heliosphere: First Results from Parker Solar Probe

Mingzhe Liu, Karine Issautier, N. Meyer-Vernet, M. Moncuquet, M. Maksimovic, et al.
"*Solar Wind Energy Flux Observations in the Inner Heliosphere: First Results from Parker Solar Probe*". *Astronomy & Astrophysics*.
DOI: [10.1051/0004-6361/202039615](https://doi.org/10.1051/0004-6361/202039615)

Solar wind energy flux observations in the inner heliosphere: first results from Parker Solar Probe

M. Liu¹, K. Issautier¹, N. Meyer-Vernet¹, M. Moncuquet¹, M. Maksimovic¹, J. S. Halekas², J. Huang³, L. Griton⁴,
S. Bale^{5,6,7,8}, J. W. Bonnell⁵, A. W. Case⁹, K. Goetz¹⁰, P. R. Harvey⁵, J. C. Kasper^{3,9}, R. J. MacDowall¹¹,
D. M. Malaspina¹², M. Pulupa⁵, and M. L. Stevens⁹

¹ LESIA, Observatoire de Paris, Université PSL, CNRS, Sorbonne Université, Université de Paris, 5 place Jules Janssen,
92195 Meudon, France
e-mail: mingzhe.liu@obspm.fr

² Department of Physics and Astronomy, University of Iowa, IA 52242, USA

³ Climate and Space Sciences and Engineering, University of Michigan, Ann Arbor, MI 48109, USA

⁴ IRAP, Université Paul Sabatier, 9 Av du Colonel Roche, BP 4346, 31028, Toulouse Cedex 4, France

⁵ Space Sciences Laboratory, University of California, Berkeley, CA 94720-7450, USA

⁶ Physics Department, University of California, Berkeley, CA 94720-7300, USA

⁷ The Blackett Laboratory, Imperial College London, London, SW7 2AZ, UK

⁸ School of Physics and Astronomy, Queen Mary University of London, London E1 4NS, UK

⁹ Smithsonian Astrophysical Observatory, Cambridge, MA 02138, USA

¹⁰ School of Physics and Astronomy, University of Minnesota, Minneapolis, MN 55455, USA

¹¹ Solar System Exploration Division, NASA/Goddard Space Flight Center, Greenbelt, MD 20771, USA

¹² Laboratory for Atmospheric and Space Physics, University of Colorado, Boulder, CO 80303, USA

Received 8 October 2020 / Accepted 29 December 2020

ABSTRACT

Aims. We investigate the solar wind energy flux in the inner heliosphere using 12-day observations around each perihelion of Encounter One (E01), Two (E02), Four (E04), and Five (E05) of Parker Solar Probe (PSP), respectively, with a minimum heliocentric distance of 27.8 solar radii (R_{\odot}).

Methods. Energy flux was calculated based on electron parameters (density n_e , core electron temperature T_c , and suprathermal electron temperature T_h) obtained from the simplified analysis of the plasma quasi-thermal noise (QTN) spectrum measured by RFS/FIELDS and the bulk proton parameters (bulk speed V_p and temperature T_p) measured by the Faraday Cup onboard PSP, SPC/SWEAP.

Results. Combining observations from E01, E02, E04, and E05, the averaged energy flux value normalized to 1 R_{\odot} plus the energy necessary to overcome the solar gravitation ($W_{R_{\odot}}$) is about $70 \pm 14 \text{ W m}^{-2}$, which is similar to the average value ($79 \pm 18 \text{ W m}^{-2}$) derived by Le Chat, G., Issautier, K., & Meyer-Vernet, N. (2012, Sol. Phys., 279, 197) from 24-yr observations by Helios, Ulysses, and Wind at various distances and heliolatitudes. It is remarkable that the distributions of $W_{R_{\odot}}$ are nearly symmetrical and well fitted by Gaussians, much more so than at 1 AU, which may imply that the small heliocentric distance limits the interactions with transient plasma structures.

Key words. solar wind – Sun: heliosphere – Sun: corona – Sun: fundamental parameters – plasmas – acceleration of particles

1. Introduction

The question of how the solar wind is produced and accelerated is unsolved since its discovery about sixty years ago (Parker 1958; Neugebauer & Snyder 1962) and Parker (2001) showed that “we cannot state at the present time why the Sun is obliged by the basic laws of physics to produce the heliosphere”. An important property of the solar wind is its energy flux, which is similar in the whole heliosphere and in the fast and slow wind (e.g., Schwenn & Marsch 1990; Meyer-Vernet 2006; Le Chat et al. 2009, 2012), and much more so than the particle flux itself. As shown by Le Chat et al. (2009), the energy flux is of a similar fraction of the luminosity for Solar-like and cool giant stars, which suggests that stellar winds may share a basic process for their origin and acceleration. Investigations of the solar wind energy flux in the inner heliosphere are of significant importance for astrophysics, but there are still very few of them.

Meyer-Vernet (2006, 2007) showed that the average solar wind energy flux scaled to one solar radius of about 70 W m^{-2} from long-term Helios and Ulysses observations is close to 10^{-6} times the solar luminosity – a fraction similar to that of a number of other stars. With a much larger solar wind data set from several spacecraft at various distances and latitudes, Le Chat et al. (2012) found an average value of $79 \pm 18 \text{ W m}^{-2}$ between 1976 and 2012, whereas McComas et al. (2014) found an average value of about 60 W m^{-2} with OMNI data at 1 AU between 2011 and 2014. Helios 1 and 2 orbits ranged from 0.3 to 1 AU (Schwenn et al. 1975), whereas Ulysses operated between 1 and 4 AU (Wenzel et al. 1992). The ongoing, pioneering mission of Parker Solar Probe (PSP; Fox et al. 2016) orbits with perihelia of heliocentric distances decreasing from 35.7 solar radii (R_{\odot}) to 9.86 R_{\odot} within five years. Four instruments onboard PSP, including the Fields experiment (FIELDS; Bale et al. 2016), Solar Wind

Electrons Alphas and Protons investigation (SWEAP; Kasper et al. 2016), Integrated Science Investigation of the Sun (IS \odot IS; McComas et al. 2016), and Wide-field Imager for Solar PRobe (WISPR; Vourlidas et al. 2016), are working together to provide both in situ and remote observations. In situ field and plasma measurements of the inner heliosphere from FIELDS/PSP and SWEAP/PSP offer an opportunity to estimate the solar wind energy flux closer to the Sun than previously derived.

FIELDS/PSP provides accurate electron density and temperature measurements via quasi-thermal noise (QTN) spectroscopy. This technique has been used in a number of space missions (e.g., Meyer-Vernet 1979; Meyer-Vernet et al. 1986, 2017; Issautier et al. 1999, 2001, 2008; Maksimovic et al. 1995; Moncuquet et al. 2005, 2006), and it is an effective and efficient tool. Recently, Moncuquet et al. (2020) and Maksimovic et al. (2020) derived preliminary solar wind electron measurements from the plasma QTN spectra observed by the Radio Frequency Spectrometer (RFS/FIELDS; see Pulupa et al. 2017). SWEAP/PSP consists of the Solar Probe Cup (SPC) and the Solar Probe Analyzers (SPAN; Kasper et al. 2016; Case et al. 2020; Whittlesey et al. 2020). SPC is a fast Faraday cup designed to measure the one dimensional velocity distribution function (VDF) of ions and sometimes electrons and SPAN is a combination of three electrostatic analyzers operated to measure the three dimensional VDFs of ions and electrons. Due to the instrument design, the SPAN-Ai instrument cannot observe the complete core of the solar wind ions in the first several encounters and SPC can provide ion observations during SPAN's observational gaps by pointing at the Sun during the encounter phase of each orbit, although SPC sometimes cannot detect the whole distribution (Kasper et al. 2016; Whittlesey et al. 2020; Case et al. 2020).

Therefore, we calculated the solar wind energy flux with both the RFS/FIELDS/PSP (electron) and SPC/SWEAP/PSP (ion) observations during Encounters One (E01), Two (E02), Four (E04), and Five (E05) (Sect. 2). The minimum heliocentric distance is 35.66 R_{\odot} for E01 and E02 and around 27.8 R_{\odot} for E04 and E05. In Sect. 3, we analyze the relationship between the energy flux, the bulk speed, and the plasma density (Sect. 3.1). How the total energy flux and each component of it evolve with increasing heliocentric distance is studied in Sect. 3.2. In Sect. 4, the results are summarized and discussed.

2. Data analysis

The solar wind energy flux (W), which includes the kinetic energy (W_{kinetic}), the enthalpy (W_{enthalpy}), and the heat flux (Q), is expressed as

$$W = W_{\text{kinetic}} + W_{\text{enthalpy}} + W_{\text{g}} + Q \quad (1)$$

where we have neglected the wave energy flux and added the flux equivalent to the energy required to overcome the solar gravitation W_{g} (Schwenn & Marsch 1990); Q is the sum of the electron heat flux q_e and proton heat flux q_p . Halekas et al. (2021, 2020) found that q_e ranges from 10^{-4} to 10^{-3} W m $^{-2}$ during E01, E02, E04, and E05 of PSP orbits, which can be neglected (see Sect. 3). We note that at 1 AU, q_e measured with Helios is $q_e \approx 10^{-6}$ W m $^{-2}$ (Pilipp et al. 1990), while q_p ranges from about 10^{-7} (1 AU) to 10^{-5} (0.3 AU) W m $^{-2}$ (Hellinger et al. 2011). We therefore neglected both the electron and proton heat flux compared to the other components, so that

$$W = W_{\text{kinetic}} + W_{\text{enthalpy}} + W_{\text{g}} \quad (2)$$

where the expressions of the different components are given below. It is important to note that Le Chat et al. (2012) neglected the enthalpy at 1 AU. However, this contribution cannot be ignored closer to the Sun, where it contributes to about 5% of the total energy flux (see Sect. 3.2):

$$W_{\text{kinetic}} = n_p m_p V_p \frac{V_p^2}{2} + n_{\alpha} m_{\alpha} V_{\alpha} \frac{V_{\alpha}^2}{2} \quad (3)$$

$$\begin{aligned} W_{\text{enthalpy}} &= n_e V_p \frac{5k_B T_e}{2} + n_p V_p \frac{5k_B T_p}{2} + n_{\alpha} V_{\alpha} \frac{5k_B T_{\alpha}}{2} \\ &\approx n_e V_p \frac{5k_B T_e}{2} + n_p V_p \frac{5k_B T_p}{2} \end{aligned} \quad (4)$$

$$W_{\text{g}} = \left(n_p m_p V_p \frac{GM_{\odot}}{R_{\odot}} + n_{\alpha} m_{\alpha} V_{\alpha} \frac{GM_{\odot}}{R_{\odot}} \right) \left(1 - \frac{R_{\odot}}{r} \right). \quad (5)$$

Here, n_p , m_p , n_{α} , and m_{α} denote the proton number density, proton mass, α particle number density, and α particle mass, respectively. Furthermore, V_p (V_{α}) is the solar wind proton (α) bulk speed, n_e is the electron number density, k_B is the Boltzmann constant, T_p (T_e) is the proton (electron) temperature, G is the gravitational constant, M_{\odot} is the solar mass, R_{\odot} is the solar radius, and r is the heliocentric distance of PSP. We note that T_e was derived from the core electron temperature T_c and suprathermal electron temperature T_h with $T_e = T_c + (n_h/n_e)T_h$, where n_h denotes the suprathermal electron density and n_h/n_e is assumed to be 0.1 (see Moncuquet et al. 2020; Štverák et al. 2009). In Eqs. (3)–(5), we assume that $V_{\alpha} \approx V_p$ and ignore the enthalpy of the α particles since n_{α} is much smaller than n_e (and both V_{α} and T_{α} are not available). The energy flux was scaled to one solar radius as written below, yielding the total energy required at the base to produce the wind – a basic quantity for understanding the wind production and comparing the Sun to other wind-producing stars:

$$W_{R_{\odot}} = W(r) \frac{r^2}{R_{\odot}^2}. \quad (6)$$

We used the level-3 ion data (moments) from SPC/SWEAP (Kasper et al. 2016; Case et al. 2020) and the electron parameters deduced from the simplified QTN method with the observations from RFS/FIELDS (Moncuquet et al. 2020; Pulupa et al. 2017). For each encounter, only 12-day high-time-resolution observations near the perihelion were considered: SPC collects one sample or more every 0.874 s and the QTN datasets have a 7-s resolution. Since the resolution of the datasets from SPC is different from that of the QTN datasets, we interpolated them to the same resolution to carry out the calculations. Currently, α particle observations directly obtained from SPC/SWEAP cannot be used due to calibration issues. Also, n_p is too different from n_e (being smaller than n_e by more than 30% on average) with an estimation of $\langle n_{\alpha}/n_e \rangle = \langle (n_e - n_p)/(2 \times n_e) \rangle \approx 16.0\%$, which implies unrealistic values for n_{α} obtained based on plasma neutrality. Past studies (e.g., Kasper et al. 2007, 2012; Alterman & Kasper 2019; Alterman et al. 2021) show that the α particle abundance ($A_{\text{He}} = n_{\alpha}/n_p$) rarely exceeds $A_{\text{He}} \sim 5\%$, especially when the bulk speed of the solar wind is below $V_p = 400$ km s $^{-1}$. Alterman et al. (2021) show that at 1 AU, A_{He} ranges from 1 to 5% during Solar Cycle 23 and 24 and predict that $1\% < A_{\text{He}} < 4\%$ at the onset of Solar Cycle 25 (solar minimum). We assume that A_{He} (which is almost the same as n_{α}/n_e) of the solar wind remains the same when it propagates from the inner heliosphere to 1 AU (Viall & Borovsky 2020). As a result,

M. Liu et al.: Solar wind energy flux observations from PSP

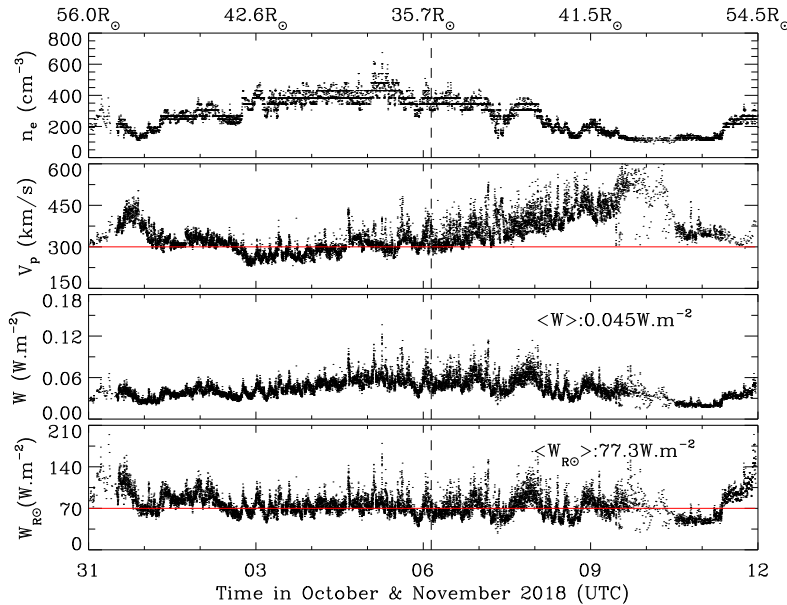


Fig. 1. Solar wind density, speed, and energy flux measurements by PSP during Encounter One (from October 31, 2018 00:00:00 to November 12, 2018 00:00:00 UTC). *First panel:* QTN electron density. *Second panel:* proton bulk speed. A red horizontal line ($V_p = 300 \text{ km s}^{-1}$) is plotted for reference. *Third panel:* solar wind energy flux W . *Fourth panel:* solar wind energy flux normalized to one solar radius W_{R_\odot} (black) with a red horizontal line ($W_{R_\odot} = 70 \text{ W m}^{-2}$) superimposed for reference. The heliocentric distance (in units of the Solar radius R_\odot) is indicated at the top of the first panel and the black vertical line denotes the perihelion of the PSP orbit.

we deduced n_α with n_e where n_α/n_e is a free parameter ranging from 1 to 4% (Alterman et al. 2021). This enabled us to determine n_p based on the plasma neutrality. The resulting values of n_α and n_p were used to calculate W and then W_{R_\odot} .

3. Observations and results

During the first and second encounter of PSP, it reached the perihelion of $35.66 R_\odot$ ($\sim 0.17 \text{ AU}$) on November 6, 2018 and April 5, 2019, respectively. For both E04 and E05, PSP arrived at the perihelion of $27.8 R_\odot$ ($\sim 0.13 \text{ AU}$) on January 29, 2020 and June 7, 2020, respectively. In Sect. 3.1, we give an overview of the PSP measurements of solar wind density, speed, and energy flux for all available encounters including E01, E02, E04, and E05. We note that E03 observations are not considered due to the lack of SPC observations near the perihelion. For each encounter, 12-day observations around the perihelion were used for calculations. The heliocentric distance for both E01 and E02 ranges from 35.66 to about $55 R_\odot$, and it ranges from 27.8 to about $57 R_\odot$ for both E04 and E05. In Sect. 3.2, we combine the observations from E01, E02, E04, and E05 to show the histogram distributions and the evolution of the energy flux as a function of heliocentric distance.

3.1. Overview of E01, E02, E04, and E05

Figure 1 shows an overview of the PSP measurements of solar wind density, speed, and energy flux during E01 (from October 31, 2018 00:00:00 to November 12, 2018 00:00:00 UTC). The top panel presents the electron number density (n_e) obtained by the QTN method. In the second panel, the proton bulk speed is shown. The third and fourth panels present the solar wind energy flux (W , from Eq. (2)) and its value scaled to one solar radius (W_{R_\odot} , from Eq. (6)), respectively. In Fig. 1, n_α and n_p were computed from n_e based on $n_\alpha/n_e = 2.5\%$ for calculating W and W_{R_\odot} . Most of the time, V_p varies around 300 km s^{-1} , and W_{R_\odot} varies around 70 W m^{-2} . The average values of W and W_{R_\odot} are 0.045 and 77.3 W m^{-2} , respectively. The average value of W_{R_\odot} of E01

is consistent with the long-term observations from Le Chat et al. (2012) (around 79 W m^{-2}). We note that W_{R_\odot} does not vary much with V_p when V_p increases abruptly (i.e., from November 8 to 10, 2018).

Figure 2, which follows the same format as Fig. 1, summarizes the PSP measurements of solar wind density, speed, and energy flux during E02 (from March 30, 2019 00:00:00 to April 11, 2019 00:00:00 UTC). We deduced n_p and n_α with the same method used for E01 to calculate both W and W_{R_\odot} . We note that n_e shows two successive low plateaus near the perihelion of E02 (from April 3 to 8, 2019 UT), as shown in the first panel of Fig. 2, whereas V_p shows two high peaks. This is in agreement with the well-known anticorrelation between the solar wind speed and density (e.g., Richardson et al. 1996; Le Chat et al. 2012). Both W_{R_\odot} and W also show two low plateaus near the perihelion of E02 (from April 3 to 8, 2019 UT), similar to the solar wind density. Elsewhere, V_p remains around 300 km s^{-1} and W_{R_\odot} varies around 70 W m^{-2} . The mean values of W and W_{R_\odot} during E02 are 0.032 and 59.4 W m^{-2} , respectively.

Similarly, Fig. 3 illustrates the PSP observations during E04 (from January 23, 2020 00:00:00 to February 4, 2020 00:00:00 UTC). We used n_p and n_α , which were deduced with the same method used for both E01 and E02, when calculating both W and W_{R_\odot} . The second panel of Fig. 3 shows that V_p varies around 375 km s^{-1} before January 29, 2020 and is predominantly 225 km s^{-1} afterward. Furthermore, W_{R_\odot} varies around 70 W m^{-2} and does not change significantly even when V_p decreases sharply from January 28 to 30, 2020. The average values of W and W_{R_\odot} for E04 are 0.054 and 67.2 W m^{-2} , respectively.

Figure 4 is similar to Figs. 1–3, but for E05 (from June 1, 2020 00:00:00 to June 13, 2020 00:00:00 UTC). We used the same method as previously explained for E01, E02, and E04 for calculating the energy flux. During this encounter, V_p usually stays at around 300 km s^{-1} except from June 7 to 12, 2020 during which V_p remains approximately at 225 km s^{-1} . For E05, W_{R_\odot} is predominantly about $W_{R_\odot} = 70 \text{ W m}^{-2}$. From June 7 to 10, 2020, both W and W_{R_\odot} experience sharp changes, which results

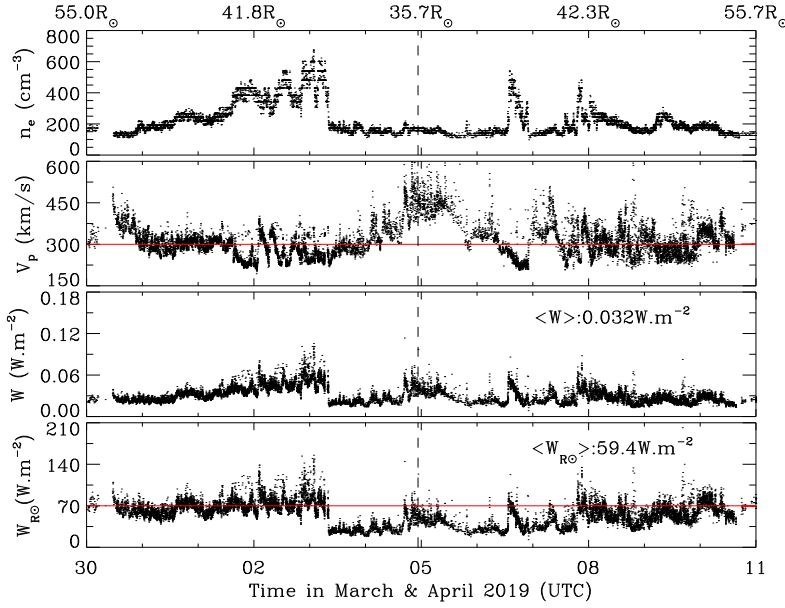


Fig. 2. Solar wind density, speed, and energy flux measurements by PSP for Encounter Two (March 30, 2019 00:00:00 to April 11, 2019 00:00:00 UTC). This figure follows the same format as that of Fig. 1.

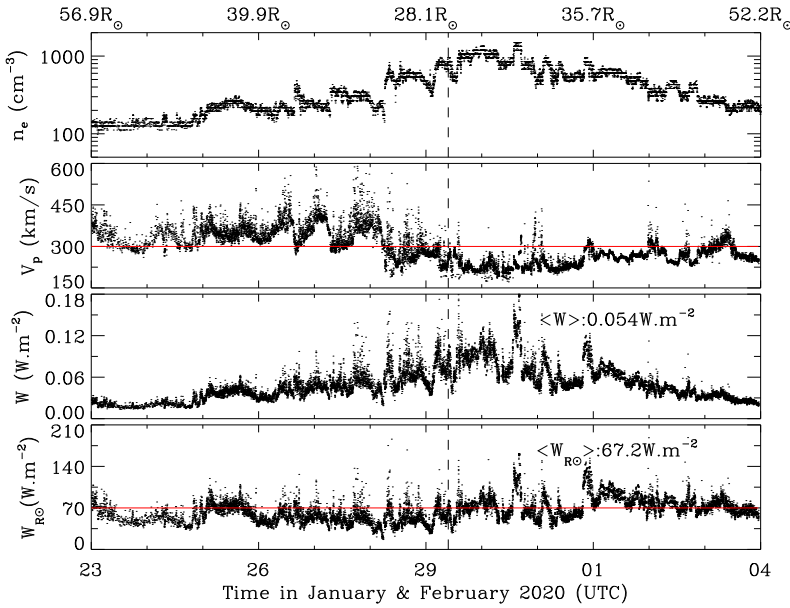


Fig. 3. Solar wind density, speed, and energy flux measurements by PSP for Encounter Four (from January 23, 2020 00:00:00 to February 4, 2020 00:00:00 UTC), which follows the same format as that of Fig. 1.

from a sharp variation in n_e . The corresponding values of both W and W_{R_o} are larger (smaller) than the ambient values at the beginning (in the end) of this time period. The average values of W and W_{R_o} for E05 are 0.057 and 73.6 $W m^{-2}$, respectively.

Table 1 summarizes the average values of the energy flux $\langle W \rangle$ and the values normalized to one solar radius $\langle W_{R_o} \rangle$ for the four PSP encounters mentioned above. We note that the sequence difference between $\langle W_{R_o} \rangle$ and $\langle W \rangle$ results from the r^{-2} normalization when deriving W_{R_o} , whereas the individual flux tubes vary differently. It is remarkable that these values of $\langle W_{R_o} \rangle$ are close to those found previously (Meyer-Vernet 2006; Le Chat et al. 2012) despite the smaller time durations and latitude extensions of PSP observations. We note the relatively low $\langle W_{R_o} \rangle$ of E02 and the low solar wind density near the

Table 1. Energy flux average value of each encounter.

Energy flux ($W m^{-2}$)	E01	E02	E04	E05
$\langle W \rangle$	0.045	0.032	0.054	0.057
$\langle W_{R_o} \rangle$	77.3	59.4	67.2	73.6

perihelion of PSP orbit (see Fig. 2). The dilute transient solar wind structure observed around the perihelion helps to explain this relatively low value compared to the long-term observations of Le Chat et al. (2012). The origins of the low plateaus of plasma density related to high peaks of bulk speed are discussed by

M. Liu et al.: Solar wind energy flux observations from PSP

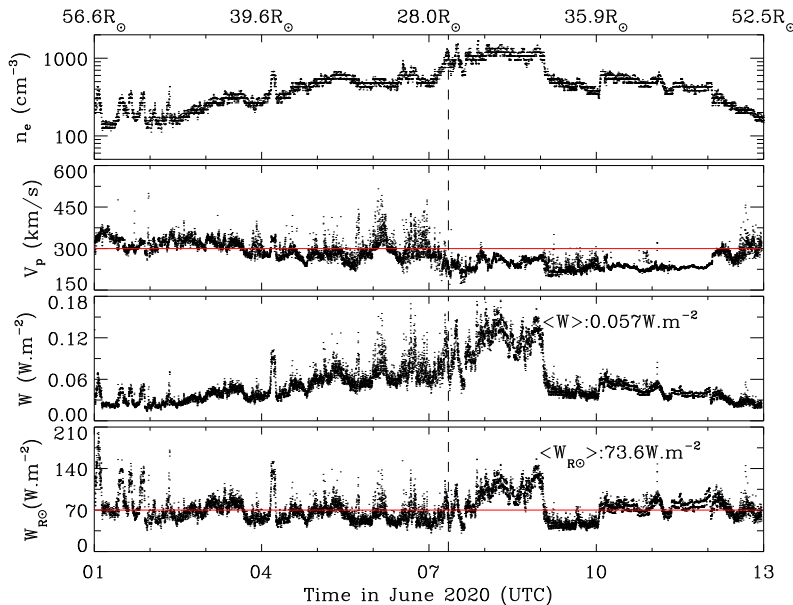


Fig. 4. Solar wind density, speed, and energy flux measurements by PSP for Encounter Five (from June 1, 2020 00:00:00 to June 13, 2020 00:00:00 UTC), which follows the same format as that of Fig. 1.

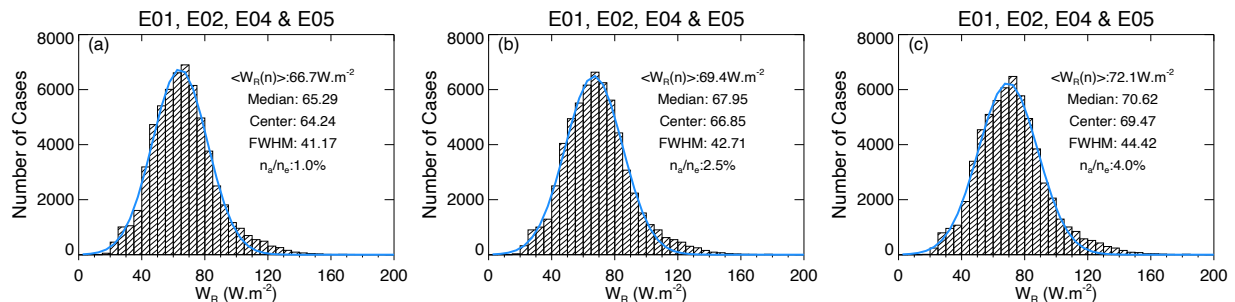


Fig. 5. Distributions of solar wind energy flux (W_R) normalized to one solar radius with a ratio between α particle number density (n_α) and electron number density (n_e) ranging from 1 to 4% for Encounters E01, E02, E04, and E05. (a)–(c): assume $n_\alpha/n_e = 1, 2.5,$ and 4% , respectively, to illustrate the uncertainty due to the absence of α measurements. Average and median values of each histogram are indicated with Gaussian fits superimposed in blue. Center value and standard deviation (full-width-half-maximum) of the Gaussian fit are also presented.

Rouillard et al. (2020) and they are outside the scope of this paper. Le Chat et al. (2012) averaged the values over a solar rotation (~ 27.2 days) to reduce the effect of transient events such as coronal mass ejections (CMEs) or corotating interaction regions (CIRs). Although CMEs or small-scale flux ropes are observed by PSP during E01 (e.g., Hess et al. 2020; Zhao et al. 2020; Korreck et al. 2020), $\langle W_{R_\odot} \rangle$ of E01 (77.3 W m^{-2}) is almost the same as the long-term averaged value found by Le Chat et al. (2012).

3.2. Distributions of energy flux and variation with distance

Figure 5 shows the distributions of W_{R_\odot} combining the observations from E01, E02, E04, and E05. Based on the assumption that n_α/n_e ranges from 1.0 to 4.0%, we calculated W_{R_\odot} with $n_\alpha/n_e = 1.0, 2.5,$ and 4.0% and the corresponding results are shown in Figs. 5a–c, respectively. Each histogram distribution was fitted with a Gaussian function (blue line), and the center value (the most probable value) and standard deviation (full-width-half-maximum which is short for FWHM) are shown together with the mean and median values. It is remarkable that the histograms

of W_{R_\odot} are very symmetrical and nearly Gaussian. The difference between the average, median, and most probable fit value of W_{R_\odot} is very small (less than 3%). With a fixed n_α/n_e ratio, the uncertainties of $\langle W_{R_\odot} \rangle$ resulting from the uncertainties of the plasma parameters $n_e, V_p, T_e,$ and T_p are 10.0, 4.1, 0.85, and 0.28%, respectively. We used the uncertainty of n_e provided by the QTN method, and Moncuquet et al. (2020) estimated that the uncertainty of T_e is around 20%. Case et al. (2020) shared that the estimated uncertainties of V_p and T_p are 3.0 and 19%, respectively. When n_α/n_e increases from 1.0 to 2.5% and then to 4.0%, $\langle W_{R_\odot} \rangle$ increases from 66.7 to 69.4 W m^{-2} and then to 72.1 W m^{-2} , and the values of FWHM increase from 41.2 to 42.7 W m^{-2} and then to 44.4 W m^{-2} . The uncertainty of W_{R_\odot} resulting from the variation of n_α/n_e is around 4%. Furthermore, $\langle W_{R_\odot} \rangle$ from the E01, E02, E04, and E05 observations is around 69.4 W m^{-2} with a total uncertainty that we estimate to be at most 20.0%, which is consistent with previous results (e.g., Schwenn & Marsch 1990; Meyer-Vernet 2006; Le Chat et al. 2009, 2012; McComas et al. 2014).

Figure 6 presents $W, W_{\text{kinetic}}/W, W_{\text{enthalpy}}/W,$ and W_g/W as a function of heliocentric distance in units of solar radius R_\odot ,

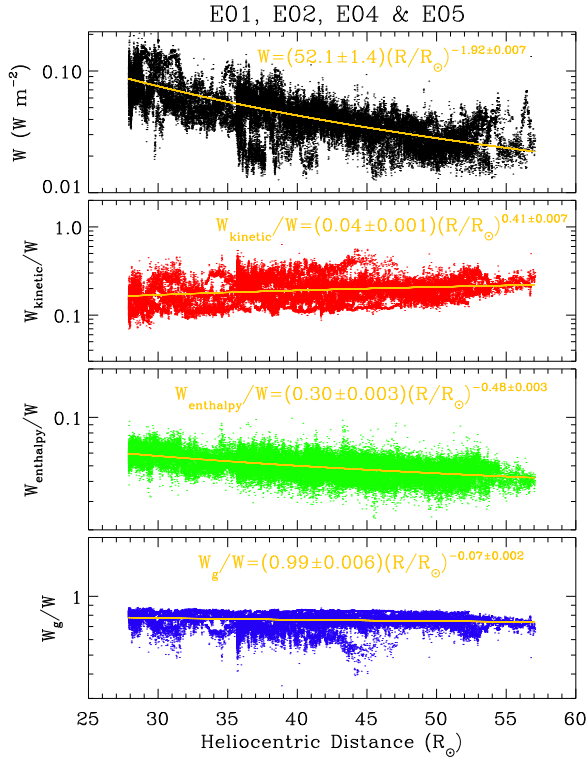


Fig. 6. Variation of W and its components with heliocentric distance combining observations from Encounter One (E01), Two (E02), Four (E04), and Five (E05). From top to bottom: evolution of W , W_{kinetic}/W , W_{enthalpy}/W , and W_g/W with heliocentric distance are shown, respectively. The fitted profile (yellow) is superimposed on each corresponding panel, respectively.

which includes the observations from E01, E02, E04, and E05. Levenberg-Marquardt least-squares fit was performed on each quantity and the fitted functions are shown in the figure. We note that the power index for W is -1.92 (near to -2.0), which is in agreement with Eq. (6) used to scale the solar wind energy flux to one R_\odot . When PSP moves from $57.1 R_\odot$ to $27.8 R_\odot$, W_{kinetic} , in order of magnitude, ranges from 10^{-3} to 10^{-2} W m^{-2} , while W_{enthalpy} and W_g range from 10^{-3} to 10^{-2} W m^{-2} and from 10^{-2} to 10^{-1} W m^{-2} , respectively. Further, as shown in Fig. 6, W_g is the dominant term for W , W_{kinetic} is the second most dominant one, and W_{enthalpy} is the least dominant term. Even though the contribution of W_{enthalpy} to W is still the least among the three components in the inner heliosphere, it reaches about 30% of the kinetic energy flux at the smallest distances and we cannot neglect it directly ($\langle W_{\text{enthalpy}} \rangle / \langle W \rangle \approx 5\%$). We note that since W_g exceeds W_{kinetic} by a factor of about four, most of the energy supplied by the Sun to generate the solar wind serves to overcome the solar gravity. As is shown in the first panel of Fig. 6, the energy flux can reach $W \approx 10^{-1} \text{ W m}^{-2}$ near the perihelia of PSP orbits, whereas the corresponding electron heat flux is $q_e \approx 10^{-3} \text{ W m}^{-2}$ (see Halekas et al. 2021, 2020). At most, q_e contributes to 1.0% of W , and proton heat flux q_p is usually much less than q_e . Therefore, neglecting the heat flux does not affect the conclusions made in this work.

A14, page 6 of 7

4. Discussion and conclusions

This paper presents the first analysis of the solar wind energy flux in the inner heliosphere (adding the flux equivalent to the energy necessary to move the wind out of the solar gravitational potential) with PSP observations. This covers heliocentric distances from 0.13 AU ($\sim 27.8 R_\odot$) to 0.27 AU ($\sim 57.1 R_\odot$) in combination of data during E01, E02, E04, and E05. This enables us to study the solar wind energy flux in the inner heliosphere, which is of great importance to understand the acceleration of the solar wind. We note that E03 is excluded due to the lack of SPC observations near perihelion.

We find that the average value of W_{R_\odot} , $\langle W_{R_\odot} \rangle$, is about 69.4 W m^{-2} with a total uncertainty of at most 20%, which is similar to previous results based on long-term observations at greater distances and various latitudes (e.g., Schwenn & Marsch 1990; Meyer-Vernet 2006; Le Chat et al. 2009, 2012; McComas et al. 2014). This result confirms that this quantity appears as a global solar constant, which is of importance since it is often used to deduce the solar wind density from the speed (or the reverse) in global heliospheric studies and modeling (e.g., Shen et al. 2018; McComas et al. 2014; McComas et al. 2017, 2020; Krimigis et al. 2019; Wang et al. 2020).

It is remarkable that the distributions of W_{R_\odot} are nearly symmetrical and well fitted by Gaussians. This may be explained by the limited interactions between solar wind and transient structures (e.g., CMEs and CIRs) in the inner heliosphere (below 0.27 AU).

Normalizing the solar wind energy flux as $1/r^2$ assumes a radial expansion of solar wind, which does not hold true for individual flux tubes, especially close to the Sun. However, this normalization holds true when integrating over a whole sphere surrounding the Sun, so that a large data set is necessary to obtain a reliable result. It is thus noteworthy that with only 12-day observations for each encounter (E01, E02, E04, and E05) and a limited latitude exploration, we find the same normalized energy flux as previous long-term studies at various latitudes. This is consistent with the fact that our dataset yields an energy flux varying with heliocentric distance with a power index close to -2 . It is also interesting that this normalized energy flux represents a similar fraction of solar luminosity as observed for a large quantity of stars (Meyer-Vernet 2006; Le Chat et al. 2012). Since this quantity represents the energy flux to be supplied by the Sun for producing the wind (e.g., Meyer-Vernet 1999; Schwadron & McComas 2003), this similarity may provide clues to the physical processes at the origin of stellar winds (e.g., Johnstone et al. 2015).

In this work, the heat flux was neglected when calculating the energy flux. When PSP gets much closer to the Sun, the contribution of the electron heat flux is larger (see Halekas et al. 2021, 2020). Furthermore, the solar wind protons often consist of two populations, that is to say core and beam drifting with respect to each other. The speed difference between them is typically on the order of the local Alfvén speed (Alterman et al. 2018). It is likely that the proton heat flux will also be more important closer to the Sun. Therefore, the heat flux will be considered in a future work. Due to the lack of alpha particle observations, we make an assumption that $V_\alpha \approx V_p$. In fact, the differential speed between protons and alpha particles is also typically on the order of the local Alfvén speed (e.g., Steinberg et al. 1996; Āurovcová et al. 2017; Alterman et al. 2018), so that it may affect the energy flux closer to the Sun. We await more data that are to come in the future PSP encounters, with the recovery of the well calibrated alpha parameters.

M. Liu et al.: Solar wind energy flux observations from PSP

Acknowledgements. The research was supported by the CNES and DIM ACAV+ PhD funding. Parker Solar Probe was designed, built, and is now operated by the Johns Hopkins Applied Physics Laboratory as part of NASA's Living with a Star (LWS) program (contract NNN06AA01C). Support from the LWS management and technical team has played a critical role in the success of the Parker Solar Probe mission. We acknowledge the use of data from FIELDS/PSP (<http://research.ssl.berkeley.edu/data/psp/data/sci/fields/12/>) and SWEAP/PSP (<http://sweap.cfa.harvard.edu/pub/data/sci/sweap/>).

References

- Alterman, B. L., & Kasper, J. C. 2019, *ApJ*, 879, L6
Alterman, B. L., Kasper, J. C., Stevens, M. L., & Koval, A. 2018, *ApJ*, 864, 112
Alterman, B. L., Kasper, J. C., Leamon, R. J., & McIntosh, S. W. 2021, *Sol. Phys.*, 296, 67
Bale, S. D., Goetz, K., Harvey, P. R., et al. 2016, *Space Sci. Rev.*, 204, 49
Case, A. W., Kasper, J. C., Stevens, M. L., et al. 2020, *ApJS*, 246, 43
Đurovcová, T., Šafránková, J., Němeček, Z., & Richardson, J. D. 2017, *ApJ*, 850, 164
Fox, N. J., Velli, M. C., Bale, S. D., et al. 2016, *Space Sci. Rev.*, 204, 7
Halekas, J. S., Whittlesey, P., Larson, D. E., et al. 2020, *ApJS*, 246, 22
Halekas, J. S., Whittlesey, P., Larson, D. E., et al. 2021, *A&A*, 650, A15 (PSP S1)
Hellinger, P., Matteini, L., Štverák, Š., Trávníček, P. M., & Marsch, E. 2011, *J. Geophys. Res. Space Phys.*, 116, A09105
Hess, P., Rouillard, A. P., Kouloumvakos, A., et al. 2020, *ApJS*, 246, 25
Issautier, K., Meyer-Vernet, N., Moncuquet, M., Hoang, S., & McComas, D. J. 1999, *J. Geophys. Res.*, 104, 6691
Issautier, K., Hoang, S., Moncuquet, M., & Meyer-Vernet, N. 2001, *Space Sci. Rev.*, 97, 105
Issautier, K., Le Chat, G., Meyer-Vernet, N., et al. 2008, *Geophys. Res. Lett.*, 35, L19101
Johnstone, C. P., Güdel, M., Lüftinger, T., Toth, G., & Brott, I. 2015, *A&A*, 577, A27
Kasper, J. C., Stevens, M. L., Lazarus, A. J., Steinberg, J. T., & Ogilvie, K. W. 2007, *ApJ*, 660, 901
Kasper, J. C., Stevens, M. L., Korreck, K. E., et al. 2012, *ApJ*, 745, 162
Kasper, J. C., Abiad, R., Austin, G., et al. 2016, *Space Sci. Rev.*, 204, 131
Korreck, K. E., Szabo, A., Nieves Chinchilla, T., et al. 2020, *ApJS*, 246, 69
Krimigis, S. M., Decker, R. B., Roelof, E. C., et al. 2019, *Nat. Astron.*, 3, 997
Le Chat, G., Meyer-Vernet, N., & Issautier, K. 2009, *AIP Conf. Ser.*, 1094, 365
Le Chat, G., Issautier, K., & Meyer-Vernet, N. 2012, *Sol. Phys.*, 279, 197
Maksimovic, M., Hoang, S., Meyer-Vernet, N., et al. 1995, *J. Geophys. Res.*, 100, 19881
Maksimovic, M., Bale, S. D., Berčić, L., et al. 2020, *ApJS*, 246, 62
McComas, D. J., Allegrini, F., Bzowski, M., et al. 2014, *ApJS*, 213, 20
McComas, D. J., Alexander, N., Angold, N., et al. 2016, *Space Sci. Rev.*, 204, 187
McComas, D. J., Zirnstein, E. J., Bzowski, M., et al. 2017, *ApJS*, 229, 41
McComas, D. J., Bzowski, M., Dayeh, M. A., et al. 2020, *ApJS*, 248, 26
Meyer-Vernet, N. 1979, *J. Geophys. Res.*, 84, 5373
Meyer-Vernet, N. 1999, *Eur. J. Phys.*, 20, 167
Meyer-Vernet, N. 2006, *IAU Symp.*, 233, 269
Meyer-Vernet, N. 2007, *Basics of the Solar Wind* (Cambridge: Cambridge University Press)
Meyer-Vernet, N., Couturier, P., Hoang, S., et al. 1986, *Science*, 232, 370
Meyer-Vernet, N., Issautier, K., & Moncuquet, M. 2017, *J. Geophys. Res.*, 122, 7925
Moncuquet, M., Lecacheux, A., Meyer-Vernet, N., Cecconi, B., & Kurth, W. S. 2005, *Geophys. Res. Lett.*, 32, L20S02
Moncuquet, M., Matsumoto, H., Bougeret, J. L., et al. 2006, *Adv. Space Res.*, 38, 680
Moncuquet, M., Meyer-Vernet, N., Issautier, K., et al. 2020, *ApJS*, 246, 44
Neugebauer, M., & Snyder, C. W. 1962, *Science*, 138, 1095
Parker, E. N. 1958, *ApJ*, 128, 664
Parker, E. N. 2001, *Ap&SS*, 277, 1
Pillipp, W. G., Muehlhaeuser, K. H., Miggenrieder, H., Rosenbauer, H., & Schwenn, R. 1990, *J. Geophys. Res.*, 95, 6305
Pulupa, M., Bale, S. D., Bonnell, J. W., et al. 2017, *J. Geophys. Res.*, 122, 2836
Richardson, J. D., Belcher, J. W., Lazarus, A. J., Paularena, K. I., & Gazis, P. R. 1996, *AIP Conf. Proc.*, 382, 483
Rouillard, A. P., Kouloumvakos, A., Vourlidas, A., et al. 2020, *ApJS*, 246, 37
Schwadron, N. A., & McComas, D. J. 2003, *ApJ*, 599, 1395
Schwenn, R., & Marsch, E. 1990, *Physics and Chemistry in Space* (Springer), 20
Schwenn, R., Rosenbauer, H., & Miggenrieder, H. 1975, *Raumfahrtforschung*, 19, 226
Shen, F., Yang, Z., Zhang, J., Wei, W., & Feng, X. 2018, *ApJ*, 866, 18
Steinberg, J. T., Lazarus, A. J., Ogilvie, K. W., Lepping, R., & Byrnes, J. 1996, *Geophys. Res. Lett.*, 23, 1183
Štverák, Š., Maksimovic, M., Trávníček, P. M., et al. 2009, *J. Geophys. Res.*, 114, A05104
Viall, N. M., & Borovsky, J. E. 2020, *J. Geophys. Res. Space Phys.*, 125, e26005
Vourlidas, A., Howard, R. A., Plunkett, S. P., et al. 2016, *Space Sci. Rev.*, 204, 83
Wang, Y. X., Guo, X. C., Wang, C., et al. 2020, *Space Weather*, 18, e02262
Wenzel, K. P., Marsden, R. G., Page, D. E., & Smith, E. J. 1992, *A&AS*, 92, 207
Whittlesey, P. L., Larson, D. E., Kasper, J. C., et al. 2020, *ApJS*, 246, 74
Zhao, L. L., Zank, G. P., Adhikari, L., et al. 2020, *ApJS*, 246, 26

B.2 Total Electron Temperature Derived from Quasi-Thermal Noise Spectroscopy In the Pristine Solar Wind : Parker Solar Probe Observations

Mingzhe Liu, Karine Issautier, M. Moncuquet, N. Meyer-Vernet, M. Maksimovic, et al. "*Total Electron Temperature Derived from Quasi-Thermal Noise Spectroscopy In the Pristine Solar Wind : Parker Solar Probe Observations*". Astronomy & Astrophysics (Under Revision). DOI: [AA/2022/45450](https://doi.org/10.1051/aa/2022/45450)

Total Electron Temperature Derived from Quasi-Thermal Noise Spectroscopy In the Pristine Solar Wind: Parker Solar Probe Observations

Mingzhe Liu¹, Karine Issautier¹, Michel Moncuquet¹, Nicole Meyer-Vernet¹, Milan Maksimovic¹, Jia Huang², Mihailo M. Martinovic^{3,1}, Léa Griton¹, Nicolina Chrysaphi¹, Vamsee Krishna Jagarlamudi⁴, Stuart D. Bale^{5,6}, Marc Pulupa⁵, Justin C. Kasper^{2,7}, and M. L. Stevens⁷

¹ LESIA, Observatoire de Paris, Université PSL, CNRS, Sorbonne Université, Université de Paris, 5 place Jules Janssen, 92195 Meudon, France

e-mail: mingzhe.liu@obspm.fr

² Climate and Space Sciences and Engineering, University of Michigan, Ann Arbor, MI 48109, USA

³ Lunar and Planetary Laboratory, University of Arizona, Tucson, AZ 85721, USA

⁴ Johns Hopkins University Applied Physics Laboratory, Laurel, MD, USA

⁵ Space Sciences Laboratory, University of California, Berkeley, CA 94720-7450, USA

⁶ Physics Department, University of California, Berkeley, CA 94720-7300, USA

⁷ Smithsonian Astrophysical Observatory, Cambridge, MA 02138 USA

Received #: Accepted #

ABSTRACT

Aims. We apply the Quasi-thermal noise (QTN) method on Parker Solar Probe (PSP) observations to derive the total electron temperature (T_e) and present a combination of 12-day observations around each perihelion from Encounter One (E01) to Ten (E10) (with E08 not included) with the heliocentric distance varying from about 13 to 60 solar radii (R_\odot).

Methods. The QTN technique is a reliable tool to yield accurate measurements of the electron parameters in the solar wind. We obtain T_e from the linear fit of the high-frequency part of the QTN spectra acquired by the RFS/FIELDS instrument. Then, we provide the mean radial electron temperature profile, and examine the electron temperature gradients for different solar wind populations (i.e. classified by the proton bulk speed (V_p), and the solar wind mass flux).

Results. We find that the total electron temperature decreases with the distance as $\sim R^{-0.66}$, which is much slower than adiabatic. The extrapolated T_e based on PSP observations is consistent with the exospheric solar wind model prediction at $\sim 10 R_\odot$, Helios observations at ~ 0.3 AU and Wind observations at 1 AU. Also, T_e , extrapolated back to $10 R_\odot$, is almost the same as the strahl electron temperature T_s (measured by SPAN-E) which is considered to be closely related to or even almost equal to the coronal electron temperature. Furthermore, the radial T_e profiles in the slower solar wind (or flux tube with larger mass flux) are steeper than those in the faster solar wind (or flux tube with smaller mass flux). More pronounced anticorrelated V_p-T_e is observed when the solar wind is slower and closer to the Sun.

Key words. (Sun:) solar wind—Sun: heliosphere—Sun: corona—methods: data analysis—plasmas—acceleration of particles

1. Introduction

Heat transport in the solar corona and wind, which is not completely understood, plays a key role in coronal heating and wind acceleration. Due to the large mass difference between ions and electrons, electrons mainly transport energy whereas ions transport momentum. Therefore, electrons are expected to play a key role in the thermally driven solar wind expansion. Furthermore, the accurately measured electron temperature radial profile is not only of prime interest to understand the energy transport in the solar wind but also an important ingredient to constrain the thermally driven solar wind models (e.g., Meyer-Vernet & Issautier 1998; Issautier et al. 1999a, 2001b; Maksimovic et al. 1997; Zouganelis et al. 2004). For simplicity, the electron temperature is generally assumed to be fitted with a power law of the distance to the Sun, assuming no large-scale temporal variations: $T_e = T_0 \times (R/R_\odot)^\beta$. β is observed to range between 0 (isothermal) and $-4/3$ (adiabatic), which indicates that electrons cool off with radial profiles spanning from nearly isothermal to

almost adiabatic (e.g., Marsch et al. 1989; Pilipp et al. 1990; Issautier et al. 1998; Le Chat et al. 2011; Maksimovic et al. 2000; Štverák et al. 2015; Moncuquet et al. 2020). The large scatter in the measurements of β is not surprising and may be due to several reasons: i) it is difficult to separate genuine variations along stream flux tubes from those across them; ii) transient structures such as coronal mass ejections, co-rotating interaction regions and interplanetary shocks can cause nongeneric effects; iii) the observations from different spacecraft have been carried out in different latitudinal and radial ranges and/or in different phases of the solar activity; iv) classification of data based on the solar wind speed, Coulomb collisions and plasma beta has not always been done. In contrast, the exospheric solar wind models give another theoretical radial profile of the total electron temperature with the expression $T_e = T_0 + T_1 \times (R/R_\odot)^{-4/3}$ for $(R/R_\odot)^2 \gg 1$ (e.g., Meyer-Vernet & Issautier 1998; Meyer-Vernet et al. 2003; Issautier et al. 2001b), which yields a profile that flattens at large distances, in agreement with Helios measurements (between 0.3

and 1 AU) (Marsch et al. 1989; Pilipp et al. 1990). Since this model has the same number of free parameters as the power-law model, it is difficult to distinguish both models from observations in a small radial range. Le Chat et al. (2011) has verified this fact with the Ulysses observations of high-speed solar wind during its first pole-to-pole latitude scan (from 1.5 to 2.3 AU).

Observations from Parker Solar Probe (PSP; Fox et al. 2016) indicate that there is an anticorrelation between the proton bulk speed V_p and the electron temperature T_e close to the Sun (e.g., Maksimovic et al. 2020; Halekas et al. 2020, 2022), whereas the correlation between the proton bulk speed V_p and the proton temperature T_p persists throughout the heliosphere (see Lopez & Freeman 1986; Totten et al. 1995; Matthaeus et al. 2006; Démoulin 2009, and references therein). Specifically, Maksimovic et al. (2020) found that the anticorrelation between V_p and T_e observed below 0.3 AU disappears as the wind expands, evolves and mixes with different electron temperature gradients for different wind speeds. The exospheric solar wind model (e.g., Maksimovic et al. 1997, 2001) showed that the fast wind from the polar coronal hole regions (low-temperature regions) might be produced by the non-thermal electron distributions in the corona, which might explain the anticorrelated (V_p, T_e) close to the Sun. Furthermore, the exospheric model predicted that the temperature profile is flatter in the fast wind as previously observed (Meyer-Vernet & Issautier 1998). However, exospheric models use simplified hypotheses and challenging questions remain about the heating and cooling mechanisms for electrons. The PSP observations close to the Sun therefore give us an opportunity to investigate the solar wind electron thermal dynamics in the inner heliosphere.

The Quasi-thermal noise (QTN) technique yields accurate electron density and temperature measurements in the solar wind. It has been used in a number of space missions (e.g., Meyer-Vernet 1979; Meyer-Vernet et al. 1986, 1993; Meyer-Vernet et al. 2017; Issautier et al. 1999b, 2001a,c, 2005, 2008; Maksimovic et al. 1995, 2005a; Moncuquet et al. 1995, 1997, 2005, 2006; Martinović et al. 2020; Le Chat et al. 2011; Salem et al. 2001; Lund et al. 1994; Schippers et al. 2013). Recent investigations (see Moncuquet et al. 2020; Maksimovic et al. 2020; Martinović et al. 2022) have already applied this technique on PSP based on electric voltage spectra acquired by the Radio Frequency Spectrometer (RFS/FIELDS) (Pulupa et al. 2017). Besides, SWEAP/PSP consists of the Solar Probe Cup (SPC) and the Solar Probe Analyzers (SPAN) (Kasper et al. 2016; Case et al. 2020; Whittlesey et al. 2020; Livi et al. 2022). SPC is a fast Faraday cup designed to measure the one dimensional velocity distribution function (VDF) of ions. SPAN is a combination of three electrostatic analyzers operated to measure the three dimensional ion and electron VDFs. Usually, traditional particle analyzers are affected by spacecraft photoelectrons and charging effects. Since the QTN electron density is deduced from a spectral peak, this measurement is independent of gain calibrations. Due to its reliability and accuracy, the electron number density derived from the QTN spectroscopy is called the gold standard density and serves routinely to calibrate other instruments (e.g., Maksimovic et al. 1995; Issautier et al. 2001c; Salem et al. 2001). Until now, on PSP, electron number density provided by the QTN technique has been playing an important role as a calibration standard for the scientific analysis (e.g., Kasper et al. 2021; Zhao et al. 2021; Liu et al. 2021a,b).

We derived the total electron temperature from the QTN spectroscopy in the so-called pristine or nascent solar wind observed by PSP. Specifically, a combination of 12-day observations around each perihelion from Encounter One (E01) to Ten

(E10) of PSP are presented with the heliocentric distance varying from about 13 to 60 R_\odot . Currently, observations from E08 are not considered due to the unusual biasing setting for the electric antenna at that time. In Section 2, we describe a simple but practical and effective way to deduce the total electron temperature with the high-frequency part of the quasi-thermal noise spectra provided by the dipole electric antenna onboard PSP. The corresponding results are compared to those from Maksimovic et al. (2020) (T_e from a different QTN technique), and Moncuquet et al. (2020) (T_c from a simplified QTN technique) for a preliminary cross-checking. In Section 3, we first provide the mean radial electron temperature profile, and then investigate the electron temperature gradients for different solar wind populations classified by the proton bulk speed and the solar wind mass flux, respectively. Also, we examine how the anticorrelation between V_p and T_e are affected by radial evolution. In Section 4, the results and their implications for the electron thermal dynamics are summarized and discussed.

2. Data analysis

The QTN spectroscopy technique provides in situ macroscopic plasma properties by analyzing the power spectrum of the electric field voltage induced on an electric antenna by the plasma particle quasi-thermal motions. The QTN spectra are determined by both the ambient plasma properties and the antenna configuration because of the strong coupling between the plasma particles and the electric field. For an ideal electric antenna configuration, the longer and thinner the electric antenna is set, the better the QTN technique performs. Specifically, the length of the electric antenna (L) should exceed the local Debye length L_D to ensure accurate temperature measurements. Fat antennas (with thick radius a) collect or emit more electrons so that the corresponding shot noise may exceed the quasi-thermal noise. Therefore, the electric antenna should be both long enough and thin enough ($a < L_D < L$) so that the QTN technique can work well. When the antenna is configured in a proper way (see Meyer-Vernet et al. 2017; Meyer-Vernet & Moncuquet 2020), the QTN spectra are completely determined by the particle velocity distributions of the ambient plasma.

The QTN spectrum around the electron plasma frequency (f_p) contains a wealth of information about the solar wind, whose basic shape can be explained based on simple plasma physics (Meyer-Vernet & Perche 1989). The quasi-thermal motion of the ambient plasma electrons passing by the antenna induces electric voltage pulses. At time scales exceeding $1/(2\pi f_p)$ (corresponding to frequencies $f < f_p$), the electrons are Debye shielded so that each ambient thermal electron passing closer than L_D produces on the antenna an electric voltage pulse with a duration (roughly equal to $1/(2\pi f_p)$) shorter than the inverse frequency of observation. Thus, the Fourier transform of such a pulse is a constant for $f < f_p$, producing a plateau whose amplitude is determined by the bulk of the thermal electrons. In contrast, at higher frequencies ($f > f_p$), the electron quasi-thermal motion excites Langmuir waves, thereby producing a spectral peak near f_p as well as a power spectrum proportional to the total electron pressure at high frequencies (Meyer-Vernet & Perche 1989; Meyer-Vernet et al. 2017). Furthermore, the height of the peak near f_p depends on the mean energy of suprathermal electrons, whereas the peak width depends on suprathermal electron concentration (Chateau & Meyer-Vernet 1991; Meyer-Vernet et al. 2017).

For the first several encounters, PSP is still not close enough to the Sun and therefore L_D generally exceeds the antenna length

B.2. Total Electron Temperature Derived from Quasi-Thermal Noise Spectroscopy In the Pristine Solar Wind : Parker Solar Probe Observations

Mingzhe Liu et al.: Radial Evolution of T_e Derived from QTN Technique

($L \approx 2$ m). Nevertheless, the plasma peak emerged because of the suprathermal electrons (Meyer-Vernet et al. 2022). Therefore, Moncuquet et al. (2020) gave the first results of QTN measurements on PSP based on a simplified QTN technique. The preliminary results include the electron number density n_e , the core electron temperature T_c and an estimation of the suprathermal electron temperature T_h (contribution of both the halo and strahl electron thermal pressure). Based on the derived n_e from Moncuquet et al. (2020), Maksimovic et al. (2020) yields the total electron temperature T_e during the first encounter of PSP by fitting the high-frequency part of the QTN spectra recorded by RFS/FIELDS. In this paper, we apply another simple, fast but effective method on PSP observations to derive T_e . In the next subsection, we provide details of the method that enables us to derive the total electron temperature from the high-frequency part of the electric field voltage spectra measured by RFS/FIELDS. Finally, we present the preliminary cross-checking between the total electron temperature derived in this work and those obtained via different QTN techniques.

2.1. Determination of T_e from QTN Spectroscopy

In practice, the measured electric field voltage power spectrum at the receiver ports is expressed as

$$V_R^2 = \Gamma_R^2(V_{electron}^2 + V_{proton}^2 + V_{shot}^2) + V_{noise}^2 + V_{galaxy}^2 \quad (1)$$

where $V_{electron}^2$, V_{proton}^2 , V_{shot}^2 , V_{noise}^2 , and V_{galaxy}^2 represent the electron QTN, the doppler-shifted proton thermal noise, the shot noise, the instrument noise, and the galactic radio background noise, respectively. In Equation 1, Γ_R^2 is the gain factor of the receiver, which is expressed as

$$\Gamma_R^2 \approx \frac{C_A^2}{(C_A + C_B)^2} \quad (2)$$

where C_A and C_B are the dipole antenna capacitance and the (dipole) stray capacitance, respectively. Since V_R^2 is the power spectrum at the receiver ports, Γ_R^2 is in factor of the first three terms. Note that Γ_R^2 has already been included in the expression of V_{galaxy}^2 (see below). For the frequencies satisfying $fL/(f_p L_D) \gg 1$, the electron QTN can be approximated as $V_{electron}^2 \approx \frac{f_p^2 k_B T_e}{\pi \epsilon_0 L'^3}$ (Meyer-Vernet & Perche 1989), where f_p is the local electron plasma frequency, L' equals to the physical length (L) of one boom (or arm) of the dipole antenna when it is long enough (i.e. $L \gg L_D$), k_B is the Boltzmann constant, and ϵ_0 is the permittivity of free space. PSP/FIELDS antennas are separated by the heat shield and the physical separation is ~ 3 meters for both |V1-V2| and |V3-V4| dipole antennas. Since the antenna physical length ($L \approx 2$ m) is not long enough, the gap should be considered for L' with $L' = 3.5$ m. The high-frequency electron QTN (above f_p) is proportional to the electron kinetic temperature whatever the shape of the velocity distribution is like. For the frequency ranges considered, $C_A \approx \pi \epsilon_0 L / [\ln(L/a) - 1]$ (Meyer-Vernet et al. 2017) and $C_B \approx 18$ pF (Moncuquet et al. 2020), where $L \approx 2$ m is the electric antenna physical length and $a \approx 1.5$ mm is the wire radius. Note that, when performing the fitting using the whole QTN spectra, the derived electron temperatures depend on the choice of the velocity distribution function for the electrons (Meyer-Vernet & Perche 1989). This is similar to the analysis to fit the velocity distribution functions observed

by the particle analyzer. However, in the present work, the derived total electron temperature is not model dependent. This is because, when deriving the expression of $V_{electron}^2 \approx \frac{f_p^2 k_B T_e}{\pi \epsilon_0 L'^3}$, T_e is defined directly from the second moment of the electron velocity distribution functions, and no models are assumed (Meyer-Vernet & Perche 1989; Chateau & Meyer-Vernet 1991; Meyer-Vernet et al. 2017).

When $fL/(f_p L_D) \gg 1$, the doppler-shifted proton thermal noise and the shot noise are negligible compared to the electron QTN (Meyer-Vernet et al. 2017). Note that the periodic antenna biasing performed for measuring the DC electric fields, which affect the shot noise, do not perturb our results, contrary to the perturbations these biasing bring to the QTN at smaller frequencies. In contrast, the contributions of the galactic radio background noise (Novaco & Brown 1978; Cane 1979; Zaslavsky et al. 2011) and the instrument noise become important and need to be subtracted to obtain the effective electron QTN spectrum at high frequency. The galaxy noise is almost constant in time and nearly isotropic in angular distribution with the modulation as a function of the observed solid angle being less than 20% in the considered frequency range (Manning & Dulk 2001). Therefore, it was frequently used to calibrate the antenna onboard previous spacecraft missions (e.g., Zaslavsky et al. 2011; Maksimovic et al. 2020). Specifically, the calibration is performed by relating the measured radio background radiation of the galaxy to the modelled flux of the source. The use of the empirical isotropic galaxy noise model from Novaco & Brown (1978) was justified by displaying a good agreement between the data and the model. Due to the high sensitivity of RFS/FIELDS/PSP (Pulupa et al. 2017), the galaxy noise lies within the RFS bandwidth and can be accurately measured. As a result, following the method outlined in Zaslavsky et al. (2011), Maksimovic et al. (2020) used an RFS spectrum measured when PSP was close to 1 AU to derive an accurate absolute value of the reduced effective length of |V1-V2| dipole antenna. Below, the galaxy noise measured by RFS/FIELDS/PSP is modelled based on the newly derived reduced effective length of |V1-V2| dipole antenna. The pre-deployment internal noise of RFS/FIELDS (after launch) in the considered frequency range was estimated to be $V_{noise}^2 \sim 2.2 \times 10^{-17} \text{ V}^2 \text{ Hz}^{-1}$ (Pulupa et al. 2020; Maksimovic et al. 2020). The background radio galactic noise is modelled following the procedures of Zaslavsky et al. (2011) and Maksimovic et al. (2020). The specific steps are summarized below.

The background radio galactic noise is modelled according to Equation (11) from Zaslavsky et al. (2011), $V_{galaxy}^2 = \frac{4\pi}{3} Z_0 \Gamma_R^2 L_{eff}^2 B_{model}$, where $Z_0 = \sqrt{\mu_0/\epsilon_0} \approx 120\pi$ is the impedance of vacuum, $\Gamma_R L_{eff} = 1.17$ is the reduced effective length (see Maksimovic et al. 2020), and B_{model} is the empirical model for the isotropic sky background brightness (Novaco & Brown 1978), expressed as

$$B_{model} = B_0 f_{MHz}^{-0.76} e^{-\tau} \quad (3)$$

where $B_0 = 1.38 \times 10^{-19} \text{ W/m}^2/\text{Hz}/\text{sr}$, f_{MHz} is the frequency expressed in MHz, and $\tau = 3.28 f_{MHz}^{-0.64}$.

Figure 1 presents a typical example of electric field voltage power spectrum plot ranging between 100 kHz and 10 MHz measured by the FIELDS |V1-V2| dipole antenna connected to the RFS receiver. We obtain the observations (crosses connected by the black curve) by merging the spectra measured by LFR/RFS and that by HFR/RFS. The dotted horizontal line represents pre-deployment internal noise of RFS/FIELDS as mentioned above. The black dashed line is the radio galaxy background noise calculated as described above. Both the instrument

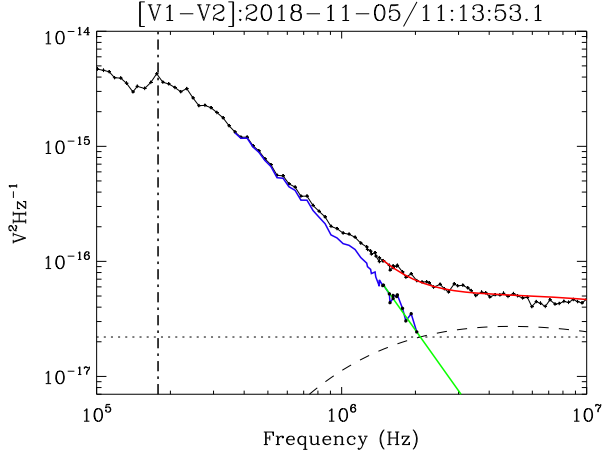


Fig. 1. Example of a voltage power spectrum (between 100 kHz and 10 MHz) recorded by the RFS receiver using the $|V1-V2|$ dipole electric antennas from FIELDS instrumentation (full black curve connected by crosses). The dot-dashed line gives the position of the local plasma peak (Moncuquet et al. 2020). The dotted horizontal line represents the pre-deployment RFS instrument noise (after launch) of $\sim 2.2 \times 10^{-17} \text{V}^2 \text{Hz}^{-1}$. The black dashed line shows the modelled radio galaxy noise. The blue and green lines represent the effective QTN signal and linear fit (f^{-3} variation that the QTN spectrum should follow when $f \gg f_p L_D/L$), respectively. The black dots on the blue line are used to derive the linear fit. The red line is the sum of the fitted QTN signal, the modelled radio galaxy noise and the instrument noise. The details are described in the text.

noise and radio galaxy noise are deducted from the observed electric field voltage spectrum so that the so-called pure QTN spectrum $\Gamma_R^2 V_{electron}^2 \simeq V_R^2 - V_{noise}^2 - V_{galaxy}^2$ (blue curve line) is derived following the similar requirement set by Maksimovic et al. (2020). Specifically, the data points are selected as: (1) the lower-frequency limit is set as $fL/(f_p L_D) \geq 2$ so that both the proton thermal noise and the shot noise can be neglected; (2) the derived so-called pure QTN spectrum should be larger than both the instrument noise and radio galaxy noise, which is used to set the higher-frequency limit. Then, we further select the dataset for the linear fitting to derive T_e following $fL/(f_p L_D) \geq 8$, which is a much more strict requirement. The green line represents the linear fitted results and there is only one free parameter which is the total electron temperature. The electron plasma frequency used for each fitted spectrum is derived from the plasma peak tracking technique (see Moncuquet et al. 2020). In Figure 1, the vertical black dashed-dotted line, which represents the location of the local electron plasma frequency, is plotted for reference. Specifically, we perform the numerical process by fitting the theoretical voltage spectral density $\log(V_R^2)$ to each measured spectrum via minimizing the χ^2 merit function with the implementation of a nonlinear least-squares Levenberg-Marquardt technique (Markwardt 2009). χ^2 is defined as $\chi^2 = \sum_{i=1}^N \frac{(O_i - E_i)^2}{O_i}$, where O_i is the value of the measured spectrum, and E_i is the corresponding expected value (theoretical one). All the electric field voltage spectra measured by the RFS/FIELDS are fitted following the same procedure mentioned above. The spectra fitted in this work usually comprise a number of frequency points ranging between ~ 5 and ~ 15 . We further quantify the quality of the fit with the overall standard deviation (σ_{fit}) of the numerical fitted values to the corresponding measurements. In general, $\sigma_{fit} < 2.5\%$ indi-

icates the goodness of the fittings. The physical uncertainty of T_e is estimated from the uncertainty of the plasma frequency, the uncertainty of the so-called pure QTN spectrum and the uncertainty of the numerical process. The uncertainty of the plasma frequency is about 4% ($\sim 8\%$ for f_p^2) (Moncuquet et al. 2020), which is the standard frequency resolution of the RFS/FIELDS. The uncertainty of the so-called pure QTN spectrum comes from the variations of the instrument noise and the empirical isotropic galaxy noise model, which is in total less than 20% (see Manning & Dulk 2001; Zaslavsky et al. 2011; Pulupa et al. 2017; Maksimovic et al. 2020). The uncertainty for the sum of the instrument noise and the empirical isotropic galaxy noise model mainly affect the pure QTN spectrum at the highest selected frequency, whereas it is negligible at the lowest selected frequency. For simplicity, the mean uncertainty of the so-called pure QTN spectrum is estimated to be about 10%. Therefore, the physical uncertainty of the derived T_e is at most 20%, which is almost the same as that of T_c (see Moncuquet et al. 2020; Liu et al. 2020, 2021a). This estimated physical uncertainty for T_e is consistent with the statistical uncertainty for T_e shown in Figure 4.

Note that the high-frequency part of the QTN spectrum can be strongly perturbed by the electromagnetic emissions (e.g., Type II and/or III radio emissions) and sometimes cannot be used for deriving T_e . Especially, such electromagnetic emissions were frequently detected during E02 (Pulupa et al. 2020) and should be carefully removed. In this work, when the QTN technique cannot be implemented in the presence of electromagnetic emissions, no T_e value is derived. The electric field voltage power spectrum below f_p in general remains unperturbed and both n_e and T_c can still be obtained (Moncuquet et al. 2020). As a byproduct, we managed to derive a database of spectra affected by bursty Langmuir waves and/or electromagnetic emissions.

2.2. Preliminary Cross Checking

Figure 2 shows an overview of the solar wind electron temperatures and the proton bulk speed measured by PSP during E01 (from October 31, 2018 to November 12, 2018 UTC). The electron temperatures derived from different techniques including T_e from QTN (this study) and T_c from QTN are compared for cross-checking. In the top panel, we present T_e (in black, labelled as $T_{e,QTN}(\text{Linear})$) derived from our linear fit QTN technique explained above and compare it to T_e (in blue, $T_{e,QTN}(\text{Kappa})$) derived from the generalized Lorentzian QTN model (Maksimovic et al. 2020). In general, they are in broad agreement with each other. Therefore, both the absolute values and variations of $T_{e,QTN}(\text{Linear})$ should be reliable. Similarly, T_c from QTN (Moncuquet et al. 2020) is displayed in blue in the bottom panel and are compared to $T_{e,QTN}(\text{Linear})$ (in black). The ratio T_e/T_c reflects the contribution of suprathermal electrons and should not be a constant. The median value of the $T_{e,QTN}(\text{Linear})/T_{c,QTN}$ is about 1.41, which is close to the median value of $T_{e,QTN}(\text{Kappa})/T_{c,SPAN-E}$ (~ 1.47) (see Maksimovic et al. 2020). $T_{c,SPAN-E}$ is the core electron temperature derived from SPAN-E (Halekas et al. 2021, 2020). Finally, the proton bulk speed from SPC/SWEAP is presented in the top panel for reference. The example time interval considered also shows an anticorrelation between V_p and T_e , which was previously reported in Maksimovic et al. (2020). We will further discuss this result in section 3.3.

We note that the ratio of T_e/T_c mentioned in this paper seems to disagree with that discussed by Halekas et al. (2020), especially near the perihelion (i.e. ≤ 0.2 AU). This may be due to a systematic discrepancy in measuring the suprather-

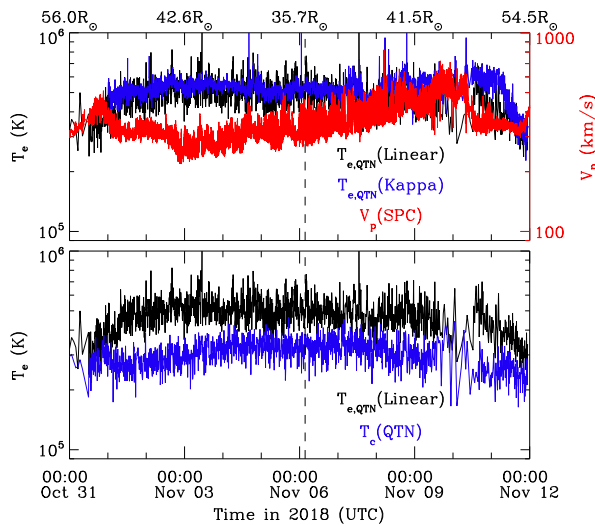


Fig. 2. Comparison of observations of solar wind electron temperatures derived from different methods on Parker Solar Probe (PSP). An example of 12-day period of measurements by PSP during Encounter One (from October 31, 2018 00:00:00 to November 12, 2018 00:00:00 UTC) is shown for reference. The heliocentric distance (in units of the solar radius R_{\odot}) is indicated at the top of the top panel and the black vertical line denotes the first perihelion of the PSP orbit. From the top to bottom panels, the total electron temperature derived from the linear fit QTN technique is displayed in black. In the top panel, the total electron temperature obtained by fitting the high-frequency part of the spectrum with the generalized Lorentzian QTN model (Maksimovic et al. 2020) is shown in blue for comparison. The bottom panel follows the same format as the first panel but for the core electron temperature derived from the simplified QTN technique (Moncuquet et al. 2020). The proton bulk speed from SPC/SWEAP is presented in the top panel for reference. An anticorrelation between V_p and T_e , which was also previously reported in Maksimovic et al. (2020), is visible during the time interval considered. Note that we have already smoothed $T_{e,QTN}(\text{Linear})$, $T_{c,QTN}$ and $T_{e,QTN}(\text{Kappa})$, so that the comparison between them is clear.

mal electrons between the QTN technique and the SPAN-E. For the SPAN-E instrument, measurements of suprathermal electrons are very difficult for essentially three reasons (see Whittlesey et al. 2020; Halekas et al. 2020, 2022). First, closer to the Sun, the temperature increase of thermal electrons means that, at the constant energy range, the number of energy bins of SPAN-E to characterize the halo electrons decreases as the radial distance decreases (see Maksimovic et al. 2021). Second, the strahl electrons, which contribute as much as the halo electrons to the total temperature, are more difficult to observe close to the Sun, when the magnetic field is more radial (Whittlesey et al. 2020; Berčič et al. 2020). These electrons can disappear from the SPAN-E field of view by being blocked by the heat shield. Finally, the geometrical factors of the SPAN-E instrument are not sufficient to properly characterize the halo electrons near the Sun (see for example Figure 1 of Halekas et al. (2022), where the halo electron VDF is clearly seen at the one count level of the instrument). Even though the low geometric factor of SPAN-E cannot explain the low total fractional supra-thermal density, but it indeed increases the difficulty to accurately measure the fractional halo and strahl density and their corresponding conversion process. These three effects combined make it more complicated to accurately measure the total electron tempera-

ture by SPAN-E than the core electron temperature. For the QTN spectroscopy, as is discussed in section 2.1, it is a passive method, thus the analysis of the additional contribution (instrument noise and galaxy noise) to the power level can lead to the uncertainty of the QTN electron temperature. All these factors may at least partly contribute to the systematic difference, but they cannot explain the magnitude of the difference. Therefore, an accurate and detailed comparison of the QTN total electron temperature with the one by SPAN-E should be made with more care and will be a future work. Similarly, an in-depth comparison between the core temperatures measured by the QTN (e.g., Moncuquet et al. 2020) and SPAN-E (e.g., Halekas et al. 2020, 2022) would also be useful, but is out of the scope of the present paper which is focused on the total electron temperature measurements from the high frequency part of the QTN spectra.

3. Observations and Results

PSP was designed to gradually shrink its orbit around the Sun and get closer step by step via seven Venus gravity assist flybys within about seven years. In this work, we focus on the 12-day period of observations around each perihelion from E01 to E10 (E08 not included) with the heliocentric distance varying from about 13.0 to 60.0 R_{\odot} . During its first three encounters, PSP followed similar trajectories and reached the perihelion of 35.66 R_{\odot} (~ 0.17 AU). In the following two orbits (from E04 to E05), PSP travelled closer to the Sun and reached perihelion of 27.8 R_{\odot} (~ 0.13 AU). The perihelia of PSP orbits became about 20.8 R_{\odot} for both E06 and E07 and about 16 R_{\odot} for both E08 and E09. During E10, PSP reached as close to the Sun as 13 R_{\odot} . In Section 3.1, we provide an overview of the radial evolution of the total electron temperature derived from the QTN technique, combining the datasets from E01 to E10 (E08 not included). In Section 3.2, we analyze and discuss the electron temperature gradients for different solar wind populations classified by the proton bulk speed and the solar wind mass flux, respectively. In Section 3.3, we investigate the radial evolution of anticorrelation between V_p and T_e .

3.1. Mean Radial Profiles of T_e

Figure 3 presents the total electron temperature derived from the QTN technique as a function of the heliocentric distance in units of solar radius R_{\odot} , combining 12-day period of observations near the perihelion of each encounter from E01 to E10 (E08 not included). Since PSP almost corotates with the Sun near the perihelion of each encounter, its observations only cover a very small heliographic latitude and longitude span (Kasper et al. 2019; Halekas et al. 2021). This means that, in each encounter, PSP detects the solar wind from only a limited number of sources. Therefore, a large data set from different encounters is necessary to remove/reduce the effects of transient structures such as CMEs or small-scale flux ropes (e.g., Hess et al. 2020; Zhao et al. 2020; Korreck et al. 2020; Chen et al. 2021), switchbacks (e.g., Bale et al. 2019; Dudok de Wit et al. 2020; Martinović et al. 2021; Fargette et al. 2021), magnetic holes associated with slow shock pairs (e.g., Chen et al. 2021; Zhou et al. 2022), and so on. As explained below, we fit the total electron temperature with respect to the heliocentric distance with both the power law model and the exospheric model to get their mean radial profiles.

Specifically, we perform the fittings for each model by minimizing the χ^2 value with the implementation of a nonlinear least-squares Levenberg-Marquardt technique (Markwardt

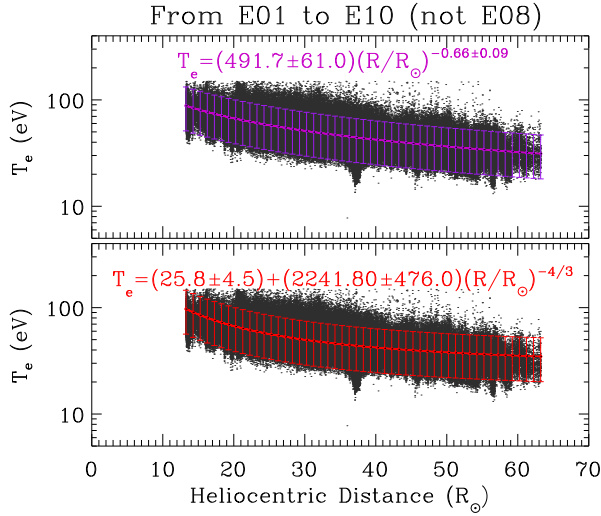


Fig. 3. Radial variation of the total electron temperature (T_e) combining observations from Encounter One (E01) to Ten (E10) with E08 excluded. From top to bottom, T_e was fitted with the power law expression $T_e = T_0 \times (R/R_\odot)^\beta$ (purple) and the expression given by the large distance exospheric solar wind model $T_e = T_0 + T_1 \times (R/R_\odot)^{-4/3}$ (red), respectively. The fitted profile and expression with corresponding color are superimposed for comparison. The variations of the free parameters in the fitted expressions are the corresponding 1-sigma ($1-\sigma$) fit uncertainties. The vertical error bars indicate the 2- σ fit uncertainties, which in total covers about 95% data points.

2009). This technique takes into account the heliocentric distance and all the data points, as is generally the case for previous studies (e.g., Issautier et al. 1998; Štverák et al. 2015; Hellinger et al. 2013; Moncuquet et al. 2020). In total, there are $N \sim 882,361$ data points and there are two adjustable free parameters for each model fit. Therefore, the degree of freedom is $DOF = N - 2 = 882,359$. χ^2 is defined as $\chi^2 = \sum_{i=1}^N \left(\frac{O_i - E_i}{\sigma_i}\right)^2$, where O_i is the value of the observations (T_e), E_i is the corresponding expected value (fit), and σ_i is the uncertainty of the measured T_e . As shown in section 2.1, we estimate that $\sigma \sim 0.2 \times T_e$. The power-law model is derived with $\chi^2 \approx 1178937$ and the so-called reduced/normalized $\chi^2_v = \chi^2/DOF \approx 1.34$. The exospheric model is derived with $\chi^2 \approx 1235002$ and the so-called reduced/normalized $\chi^2_v = \chi^2/DOF \approx 1.40$. Since χ^2_v for both model fits are close to unity and are comparable in the two cases, one can conclude that the exospheric temperature model of the form $T_e = T_0 + T_1 \times r^{(-4/3)}$ is as good as the power law approximation in fitting the observed total electron temperature gradient in the small radial range considered. The fitted profiles and expressions for both models are shown on Figure 3. Furthermore, both the mean and median values of $\overline{T_e}/T_e$ are very close to unity for both model fits, where $\overline{T_e}$ is the fitted value and T_e is the measured value. This again indicates the goodness of both model fittings. 1- σ value of $\overline{T_e}/T_e$ for both model fits is around 0.2, based on which the uncertainties of the two free parameters for each model fit are derived. 2- σ fit uncertainties are plotted in Figure 3 for reference, which in total covers about 95% data points.

The total electron temperature fitted by the power law model ($T_e \propto r^{-0.66}$, where r is the heliocentric distance in unit of solar radius) is displayed in purple. The derived total electron tem-

perature profile is flatter than that of the core electron temperature ($T_c \propto r^{-0.74}$, see Moncuquet et al. 2020), which is consistent with the results in the outer heliosphere (e.g., Issautier et al. 1998; Le Chat et al. 2011). The total electron temperature consists of the contribution of the core, halo and strahl electron thermal pressure. Therefore, the flatter radial profile of T_e may be explained by the nearly isothermal behaviour of suprathermal electrons (see Moncuquet et al. 2020). We note that in that study, the suprathermal temperature is the total contribution of both the halo and strahl electron thermal pressures. Based on the SPAN-E observations (Berčič et al. 2020), there is no strong trend in variation of the strahl electron temperature with radial distance. Also, the strahl electrons are more pronounced closer to the Sun while the density ratio between the halo and strahl electrons increases with the radial distance (Maksimovic et al. 2005b; Štverák et al. 2009), which suggests a conversion of some strahl electrons into halo ones. As a result, the fact that the T_e profile is flatter than the T_c one may mainly be due to the flatness of the strahl electron temperature profile. The recent results from PSP (see Abraham et al. 2022) suggest that the physical picture is somewhat different from a simple conversion of strahl to halo as discussed above. PSP results instead show that the overall suprathermal electron fraction (halo + strahl) increases with respect to the heliocentric distance below 0.25 AU, and that the halo and strahl relative density are quite small near perihelion. However, as is discussed in Section 2.2, close to the Sun, both the halo and strahl electrons may be missed by SPAN-E due to the instrument limitations. Therefore, since the overall suprathermal fraction (halo + strahl) closer to the Sun (e.g., Abraham et al. 2022; Maksimovic et al. 2021) may be underestimated, both of which should be treated with more care.

Then, based on the power-law fitted T_e profile ($T_e \propto r^{-0.66}$), we extrapolate T_e to $10 R_\odot$, 0.3 AU, and 1 AU, respectively. Figure 4 (a), (b), and (c) show the corresponding distributions of the scaled T_e combining the observations from E01 to E10 (E08 not included). A Gaussian function (blue line) was fitted on each histogram distribution and the corresponding center value (the most probable value) and 1- σ standard deviation of Gaussian fit are shown in comparison with the mean and median values. The histogram distributions of T_e are very symmetrical and almost Gaussian. Again, the difference between the mean, median, and the center value of Gaussian fit is quite small (less than 6%). This may be explained by the fact that we combine observations from several different encounters (different types of wind from different sources). The exospheric solar wind model indicates that for $r < 10 R_\odot$, the T_e radial profile becomes less steep (Zouganelis et al. 2004). So, when extrapolating T_e back to the Sun with a constant slope, we stop the extrapolation at about $10 R_\odot$. The value of T_e scaled to $10 R_\odot$ is around 100.6 ± 19.9 eV. The predicted absolute values here are somewhat larger than the predictions shown in Bale et al. (2016); however, they are similar to the strahl electron temperature measured by SPAN-E/SWEAP (Berčič et al. 2020; Maksimovic et al. 2021). The strahl electron temperature is considered to be closely related to or almost equal to the coronal electron temperature. At $10 R_\odot$, this extrapolated temperature is also consistent with the exospheric solar wind model prediction derived from an electron velocity distribution with a Kappa index ranging between 4 and 6 (Zouganelis et al. 2004), which indicates that the electron distribution has a suprathermal tail as measured by the QTN measurements (e.g., Maksimovic et al. 2020). That same model yields a solar wind bulk speed between 250 and 350 km s⁻¹. Note that the Kappa index mentioned here is based on one unique generalized Lorentzian or Kappa function that is an alternative to the

B.2. Total Electron Temperature Derived from Quasi-Thermal Noise Spectroscopy In the Pristine Solar Wind : Parker Solar Probe Observations

Mingzhe Liu et al.: Radial Evolution of T_e Derived from QTN Technique

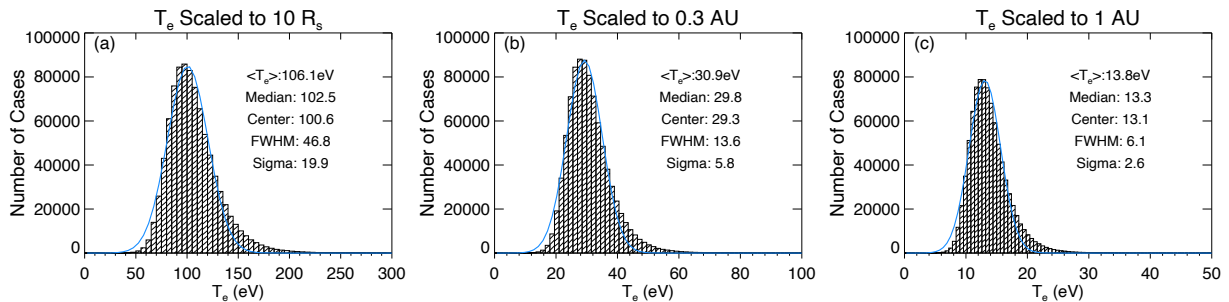


Fig. 4. (a–c): Histograms of the total electron temperature (T_e) scaled to 10 solar radii, 0.3 AU and 1 AU, based on observations displayed in Figure 3 and their corresponding power law modelling fit results. Gaussian fit is superimposed in blue on each histogram. The corresponding average and median values are also indicated together with the center value and 1- σ standard deviation of the Gaussian fit.

Maxwellian core plus Kappa/Maxwellian halo model. But the suprathermal tail itself may have a large kappa index, as found by SPAN-E near perihelion (e.g., Maksimovic et al. 2021; Abraham et al. 2022). Indeed, Zouganelis et al. (2004) showed that the acceleration provided by the exospheric model does not require specifically a Kappa function, but results more generally from nonthermal distributions. Our results show that the agreement between the extrapolated T_e based on PSP observations and the exospheric solar wind model prediction is quite good, given the simplifications made in both the T_e measurements and the solar wind model. Note that, T_e scaled to 0.3 AU is $\sim 29.3 \pm 5.8$ eV, which is consistent with the Helios observations at the same heliocentric distance (Maksimovic et al. 2005b). For T_e scaled to 1 AU, the value is $\sim 13.1 \pm 2.6$ eV, which is almost the same as the long-term (~ 10 years) Wind observations (Wilson et al. 2018). T_e scaled to 1 AU is also approximately the same as the mean/median value of the one-year statistical analysis based on STEREO observations (Martinović et al. 2016). Note also that the extrapolated electron temperatures from the exospheric model fit (not shown here) are always higher than but still comparable to those from the power law model fit.

3.2. Temperature gradients for different solar wind populations

As presented/discussed in previous investigations (e.g., Meyer-Vernet & Issautier 1998; Le Chat et al. 2011; Maksimovic et al. 2005b; Štverák et al. 2009, 2015; Maksimovic et al. 2020), solar wind classified based on the proton bulk speed may have different electron heating and cooling behaviours. Therefore, in order to do direct comparisons with the previous studies, we also separate solar wind populations based on the proton bulk speed. The dataset was split into four proton bulk speed bins as illustrated by Figure 5 (a). In this way, each proton bulk speed bin contains the same number of data points, which is $882,361/4 \sim 220590$. We used the total proton bulk speed (V_p) provided by SPC/SWEAP for E01 and E02 and those from SPAN-I/SWEAP after E02 (Kasper et al. 2016; Case et al. 2020). For each proton bulk speed bin, we fit the T_e radial profile with a power-law model using the method described in section 3.1. The derived power law indices are plotted against the corresponding proton bulk speed in Figure 5 (b). We use the proton bulk velocity measured in the RTN coordinate system. The radial component of the velocity (V_R) measured by SPC and SPAN-I are in good agreement, but there is a systematic discrepancy for the tangential component (V_T) (Woodham et al. 2021). However, V_R is the

main component of V_p (total proton bulk speed), and their absolute values are very close to each other. Furthermore, we use both V_R and V_p to cross-check the results below in this section and in section 3.3. We verify that the measurement uncertainty of V_p does not affect our conclusions.

The T_e radial gradients have a tendency (though weak) for the slower wind electrons to cool down with a steeper profile than the faster wind ones. It is noteworthy to mention that with only 12-day observations for each encounter (from E01 to E10, with E08 excluded) and a limited latitude exploration, we find similar behaviour for electrons in the inner heliosphere as previous long-term investigations (e.g., Maksimovic et al. 2005b; Štverák et al. 2015; Maksimovic et al. 2020) at various latitudes and longitudes and much larger span of heliocentric distances in the outer heliosphere. This is also consistent with the exospheric model predictions as shown in Meyer-Vernet & Issautier (1998). Also, we note that the T_e radial gradient within each proton bulk speed bin is steeper than that in the outer heliosphere based on Ulysses observations ($T_e \propto r^{-0.53}$, see Le Chat et al. (2011)). This may verify the exospheric model prediction that the electron temperature profile becomes steeper when getting closer to the Sun (Meyer-Vernet & Issautier 1998).

Moreover, since PSP is very close to the Sun during the encounter phase where the solar wind is still under acceleration, the proton bulk speed detected by PSP may not be the final speed. Therefore, because of the different types of winds coming from different source regions, we further use another basic physical quantity to partition the dataset based on almost constant streamline, i.e., the solar wind mass flux $F_w = n_e m_p V_p r^2$ (e.g., Wang & Sheeley 1990; Bemporad 2017). The resulting histogram distribution of F_w is shown in Figure 6 (a). The derived values ($F_w \sim 2 \times 10^{10} - 3 \times 10^{11} \text{ g s}^{-1}$) are in agreement with the remote-sensing observations from SOHO at altitudes higher than $3.5 R_\odot$ (Bemporad 2017), in situ measurements from ACE at 1 AU (Wang 2010), and in situ data by Ulysses from ~ 1.4 to ~ 1.8 AU (Issautier et al. 2008; Wang 2010). As expected, this indicates the conservation of the solar wind mass flux. Wang (2010) showed that the solar wind mass flux at the corona base increases roughly with the footpoint field strength. This indicates, to some degree, both the corona base conditions and the propagation effects are considered for F_w , in contrast to the proton bulk speed. Thus, as displayed in Figure 6 (a), we split the dataset into four solar wind mass flux tubes and check the corresponding electron temperature gradients. Figure 6 (b) shows that solar wind electrons within the flux tube with larger mass flux cool down faster.

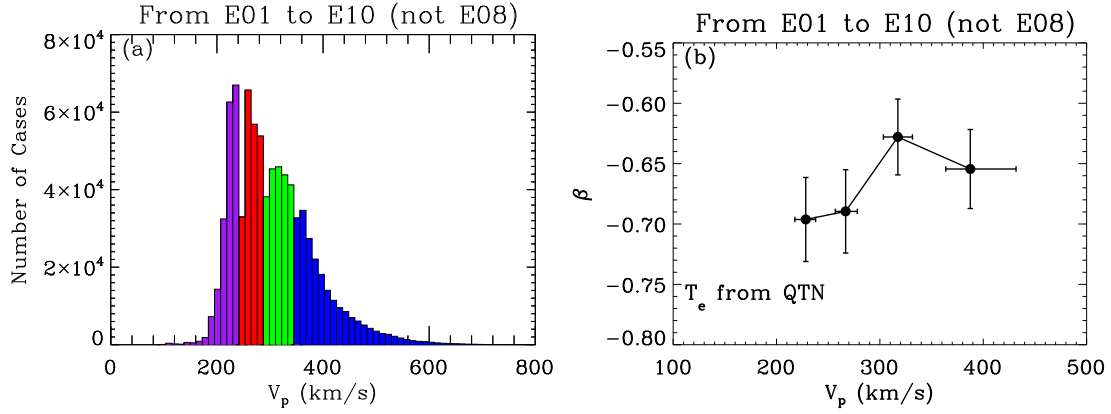


Fig. 5. (a) We define the four wind families based on the proton bulk speed histogram. Each colored histogram has the same number of observations. (b) Outcome of the power law modelling in the form $T_e = T_0 \times (R/R_\odot)^\beta$ for total electron temperature: β versus V_p . More details are described in the main text.

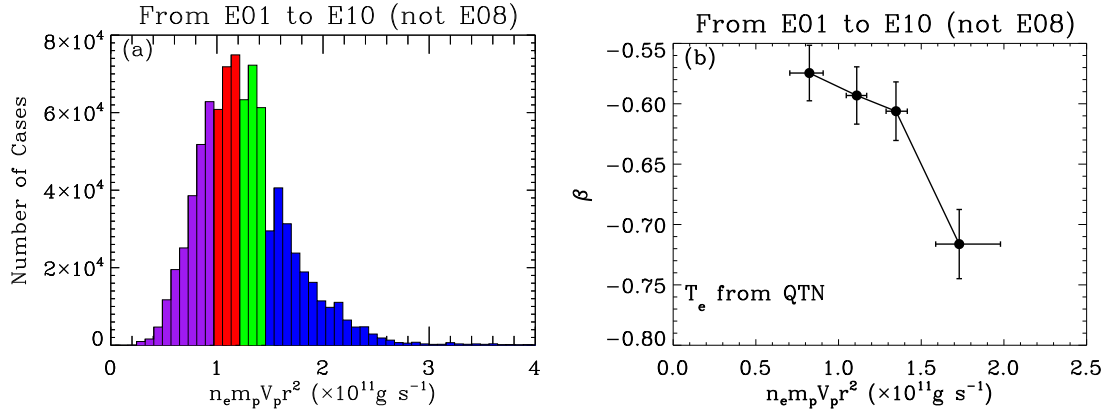


Fig. 6. Follows the same format as Figure 5 but for the solar wind mass flux.

3.3. Anticorrelated parameters: V_p and T_e

As shown in section 2.2, PSP observations display a clear anticorrelation between V_p and T_e during E01. A similar anticorrelation was observed during E04, E05, E07 and E09. During E02 and E10, frequent Type III radio emissions were detected by PSP and fewer effective data points of T_e derived from the QTN technique were obtained than during other encounters. This may affect the analysis of the relation between V_p and T_e . In contrast, slight correlated (V_p , T_e) were observed during E03 and E06 based on the QTN observations. The V_p - T_e relation measured in the solar wind may indeed depend on both the source region (Griton et al. 2021) and the radial evolution (Maksimovic et al. 2020; Pierrard et al. 2020; Halekas et al. 2022). The complexity of the electron temperature behaviours, especially the anticorrelation between V_p and T_e , contrasts with the correlation between the proton temperature and the wind speed that persists throughout the heliosphere (see Maksimovic et al. 2020, and references therein). We selected the data points from E01, E04, E05, E07 and E09, and further analyzed the effect of the radial evolution on the anticorrelation between V_p and T_e .

Figure 7 (a) compares T_e and V_p combining observations from E01, E04, E05, E07 and E09. A clear anticorrelated (V_p , T_e) is displayed. We also equally split the dataset into four ra-

dial distance bins as illustrated by Figure 7 (b). For each radial distance bin, the datasets are equally split into four proton bulk speed bins following the method mentioned in section 3.2. We then compute the median values of V_p and T_e for each proton bulk speed bin. The calculated median values of V_p and T_e belonging to each radial distance bin are presented in the same color in Figure 7 (c). For comparison, median values of V_p and T_e of the whole dataset equally divided into eight proton bulk speed bins are plotted in black.

We find that the (V_p , T_e) anticorrelation is stronger when the solar wind is slower (see black curve in Figure 7 (c)). For the solar wind considered, most of them are slow wind and on average they are being accelerated during the expansion. Therefore, the slower solar wind is detected closer to the Sun. This is consistent with the fact that the most pronounced anticorrelated V_p - T_e is observed close to the Sun (see purple curve in Figure 7 (c)). The results may also indicate that the (V_p , T_e) anticorrelation is reduced/removed during the acceleration process of the slow solar wind. Based on both the Helios and PSP measurements, Berčić et al. (2020) found a clear anticorrelation between the parallel strahl electron temperature $T_{s||}$ (proxy coronal electron temperature) and the local solar wind speed. Halekas et al. (2022) grouped the PSP observations by the asymptotic wind speed, and found that both the *in situ* electron temperature

B.2. Total Electron Temperature Derived from Quasi-Thermal Noise Spectroscopy In the Pristine Solar Wind : Parker Solar Probe Observations

Mingzhe Liu et al.: Radial Evolution of T_e Derived from QTN Technique

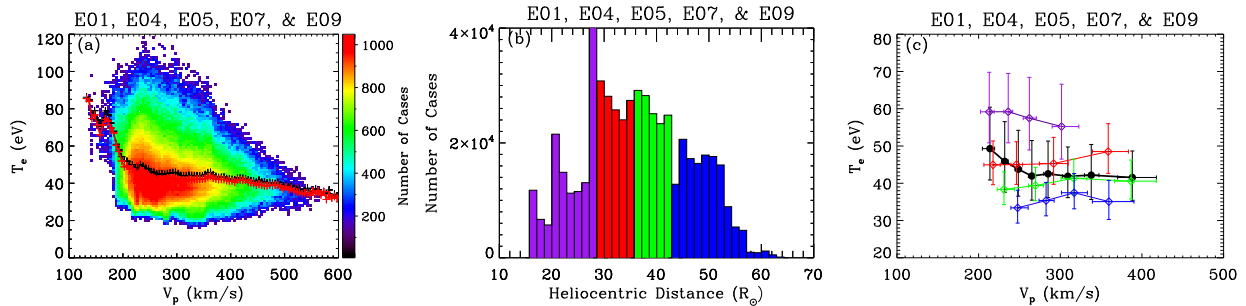


Fig. 7. (a) 2-D histogram distribution of T_e versus V_p with the color bar on the right side indicating the number of data points. Both the mean (red curve) and median values (black curve) are superimposed for reference. A clear anticorrelated (V_p, T_e) is displayed. (b) We define the four wind families based on the heliocentric distance histogram. Each colored histogram has the same number of observations. (c) Relation between V_p and T_e for each wind family, as defined in panel (b). The results are displayed in the same color as the corresponding heliocentric distance histogram in panel (b). More details are described in the main text.

(parallel core electron temperature $T_{c||}$) and the proxy coronal electron temperature ($T_{s||}$) are anticorrelated with the asymptotic wind speed. As a result, the anticorrelated (V_p, T_e) herein may be the remnants of the coronal conditions.

4. Summary and Discussion

In this work, we have implemented a simple, fast and effective method, based on the QTN spectroscopy, on PSP observations to derive the total electron temperature. To do so, we used the linear fit of the high frequency part of the QTN spectra observed by RFS/FIELDS. The derived total electron temperature is in broad agreement with T_e obtained from the QTN model with Lorentzian velocity distribution functions (Maksimovic et al. 2020). We present the radial evolution of the total electron temperature by combining 12-day observations around each perihelion from E01 to E10 (E08 not included) with the heliocentric distance ranging from about 13 to 60 R_\odot .

The radial profile of the total electron temperature ($T_e \propto r^{-0.66}$) in the inner heliosphere falls within the range between adiabatic and isothermal and is flatter than that of the electron core temperature ($T_c \propto r^{-0.74}$, see Moncuquet et al. 2020). This is consistent with previous Helios and Ulysses observations farther out (e.g., Pilipp et al. 1990; Issautier et al. 1998; Le Chat et al. 2011). The flatness of the radial profile of T_e may mainly be due to the contribution of the strahl electrons. The extrapolated T_e to 0.3 AU and 1 AU using the fitted power law are almost the same as the Helios and Wind observations at the same heliocentric distance (see Maksimovic et al. 2005b; Wilson et al. 2018), respectively. The total electron temperature extrapolated back to 10 R_\odot is almost the same as the solar corona strahl electron temperature (Berčić et al. 2020). This may confirm that the strahl electron temperature is closely related to or even almost equals to the coronal electron temperature. The temperature extrapolated back to 10 R_\odot is also consistent with the exospheric solar wind model prediction assuming an electron velocity distribution with the Kappa index ranging between 4 and 6 (Zouganelis et al. 2004). The extrapolated T_e based on the exospheric solar wind model is systematically higher (but still comparable to) than that derived from the power-law model fit.

The radial T_e profiles in the slower solar wind are relatively steeper than those in the faster solar wind. Stated in another way, electrons in the slower solar wind cool down more quickly than those in the faster wind. It is remarkable that with only 12-day observations for each encounter (from E01 to E10 with E08

excluded) and a limited latitude exploration, we find the same conclusions about electron cooling and heating behaviours in the inner heliosphere as previous long-term investigations (e.g., Maksimovic et al. 2005b; Štverák et al. 2015; Maksimovic et al. 2020) with a much larger span of the latitude, longitude and heliocentric distance explorations in the outer heliosphere. In general, the radial T_e profile observed in the pristine solar wind is steeper than that in the outer heliosphere, which to some degree verify the exospheric model prediction in the inner heliosphere (Meyer-Vernet & Issautier 1998). This indicates that the exospheric solar wind model explains partially the electron behaviours in the inner heliosphere. Furthermore, the solar wind mass flux derived from the in situ dataset in the inner heliosphere from PSP are in agreement with those even closer to the corona base (Bemporad 2017) and further out in the interplanetary space (Issautier et al. 2008; Wang 2010). Interestingly, the electron temperature cools down faster within the flux tube with larger mass flux. Given the solar wind mass flux conservation and the fact that the mass flux at the corona base increases with the footpoint field strength (Wang 2010), it can be used as an effective physical quantity to distinguish the solar wind into different populations. This considers both the corona base conditions and the propagation effects in contrast to the proton bulk speed. Especially, the solar wind at distances of PSP orbit perihelia may be still accelerating, the speed should not be considered as the final speed.

With PSP observations from E01, E04, E05, E07 and E09, we find that the (V_p, T_e) anticorrelation is more pronounced when the solar wind is slower in the inner heliosphere. During the time period considered, most of the detected solar wind is slow wind, which on average is still being accelerated during the spherical expansion. Furthermore, the results may indicate that the slow solar wind acceleration during the expansion reduces/removes the strong (V_p, T_e) anticorrelation detected near the Sun. This is verified by the fact that the most pronounced anticorrelated V_p-T_e is observed close to the Sun, in agreement with Maksimovic et al. (2020). The solar wind V_p-T_e relation is still an interesting issue, which may depend on both the source region in the Sun (Griton et al. 2021) and the radial evolution during the expansion (Maksimovic et al. 2020; Pierrard et al. 2020). To comprehensively understand the V_p-T_e relation, more work is needed to distinguish and/or connect the effects from the source region, spherical expansion and the transient structures detected locally.

Based on the Helios and preliminary PSP observations (e.g., Maksimovic et al. 2005b; Štverák et al. 2009; Halekas et al. 2021, 2020; Berčič et al. 2020), the strahl electrons will become more pronounced when PSP gets closer to the Sun. However, the QTN technique currently cannot resolve the strahl electrons well, which needs further theoretical/model extensions. When PSP gets closer to the Sun, L/L_D is expected to become larger. This will enable us to derive the electron properties (e.g., n_e , T_e , and kappa index) with smaller uncertainties by fitting the whole QTN spectrum with the generalized Lorentzian (or so-called kappa) QTN model. Also, we await for well calibrated fixed T_e from SPAN-E for all encounters to make systematic cross-checking with T_e provided by the QTN technique, which should benefit to both methods.

Acknowledgements. The research was supported by the CNES and DIM ACAV+ PhD funding. Parker Solar Probe was designed, built, and is now operated by the Johns Hopkins Applied Physics Laboratory as part of NASAs Living with a Star (LWS) program (contract NNN06AA01C). Support from the LWS management and technical team has played a critical role in the success of the Parker Solar Probe mission. We acknowledge the use of data from FIELDS/PSP (<http://research.ssl.berkeley.edu/data/psp/data/sci/fields/l2/>) and SWEAP/PSP (<http://sweap.cfa.harvard.edu/pub/data/sci/sweap/>). We thank the CDDP (Centre de Données de la Physique des Plasmas) and CNES (Centre National d'Etudes Spatiales) for their archiving and provision of SQTN data (<https://cdpp-archivage.cnes.fr/>).

References

Abraham, J. B., Owen, C. J., Verscharen, D., et al. 2022, *ApJ*, 931, 118
 Bale, S. D., Badman, S. T., Bonnell, J. W., et al. 2019, *Nature*, 576, 237
 Bale, S. D., Goetz, K., Harvey, P. R., et al. 2016, *Space Sci. Rev.*, 204, 49
 Bemporad, A. 2017, *ApJ*, 846, 86
 Berčič, L., Larson, D., Whittlesey, P., et al. 2020, *ApJ*, 892, 88
 Cane, H. V. 1979, *MNRAS*, 189, 465
 Case, A. W., Kasper, J. C., Stevens, M. L., et al. 2020, *ApJS*, 246, 43
 Chateau, Y. F. & Meyer-Vernet, N. 1991, *J. Geophys. Res.*, 96, 5825
 Chen, Y., Hu, Q., Zhao, L., Kasper, J. C., & Huang, J. 2021, *ApJ*, 914, 108
 Démoulin, P. 2009, *Sol. Phys.*, 257, 169
 Dudok de Wit, T., Krasnoselskikh, V. V., Bale, S. D., et al. 2020, *ApJS*, 246, 39
 Fargette, N., Lavraud, B., Rouillard, A. P., et al. 2021, *ApJ*, 919, 96
 Fox, N. J., Velli, M. C., Bale, S. D., et al. 2016, *Space Sci. Rev.*, 204, 7
 Gritton, L., Rouillard, A. P., Poirier, N., et al. 2021, *ApJ*, 910, 63
 Halekas, J. S., Whittlesey, P., Larson, D. E., et al. 2022, *ApJ*, 936, 53
 Halekas, J. S., Whittlesey, P., Larson, D. E., et al. 2020, *ApJS*, 246, 22
 Halekas, J. S., Whittlesey, P. L., Larson, D. E., et al. 2021, *A&A*, 650, A15
 Hellinger, P., Trávníček, P. M., Štverák, Š., Matteini, L., & Velli, M. 2013, *Journal of Geophysical Research (Space Physics)*, 118, 1351
 Hess, P., Rouillard, A. P., Kouloumvakos, A., et al. 2020, *ApJS*, 246, 25
 Issautier, K., Hoang, S., Moncuquet, M., & Meyer-Vernet, N. 2001a, *Space Sci. Rev.*, 97, 105
 Issautier, K., Le Chat, G., Meyer-Vernet, N., et al. 2008, *Geophys. Res. Lett.*, 35, L19101
 Issautier, K., Meyer-Vernet, N., Moncuquet, M., & Hoang, S. 1998, *J. Geophys. Res.*, 103, 1969
 Issautier, K., Meyer-Vernet, N., Moncuquet, M., & Hoang, S. 1999a, in *American Institute of Physics Conference Series*, Vol. 471, Solar Wind Nine, ed. S. R. Habbal, R. Esser, J. V. Hollweg, & P. A. Isenberg, 581–584
 Issautier, K., Meyer-Vernet, N., Moncuquet, M., Hoang, S., & McComas, D. J. 1999b, *J. Geophys. Res.*, 104, 6691
 Issautier, K., Meyer-Vernet, N., Pierrard, V., & Lemaire, J. 2001b, *Ap&SS*, 277, 189
 Issautier, K., Perche, C., Hoang, S., et al. 2005, *Advances in Space Research*, 35, 2141
 Issautier, K., Skoug, R. M., Gosling, J. T., Gary, S. P., & McComas, D. J. 2001c, *J. Geophys. Res.*, 106, 15665
 Kasper, J. C., Abiad, R., Austin, G., et al. 2016, *Space Sci. Rev.*, 204, 131
 Kasper, J. C., Bale, S. D., Belcher, J. W., et al. 2019, *Nature*, 576, 228
 Kasper, J. C., Klein, K. G., Lichko, E., et al. 2021, *Phys. Rev. Lett.*, 127, 255101
 Korreck, K. E., Szabo, A., Nieves Chinchilla, T., et al. 2020, *ApJS*, 246, 69
 Le Chat, G., Issautier, K., Meyer-Vernet, N., & Hoang, S. 2011, *Sol. Phys.*, 271, 141
 Liu, M., Issautier, K., Meyer-Vernet, N., et al. 2021a, *A&A*, 650, A14

Liu, M., Issautier, K., Meyer-Vernet, N., et al. 2020, in *AGU Fall Meeting Abstracts*, Vol. 2020, SH052–04
 Liu, Y. D., Chen, C., Stevens, M. L., & Liu, M. 2021b, *ApJ*, 908, L41
 Livi, R., Larson, D. E., Kasper, J. C., et al. 2022, *ApJ*, 938, 138
 Lopez, R. E. & Freeman, J. W. 1986, *J. Geophys. Res.*, 91, 1701
 Lund, E. J., Labelle, J., & Treumann, R. A. 1994, *J. Geophys. Res.*, 99, 23651
 Maksimovic, M., Bale, S. D., Berčič, L., et al. 2020, *ApJS*, 246, 62
 Maksimovic, M., Gary, S. P., & Skoug, R. M. 2000, *J. Geophys. Res.*, 105, 18337
 Maksimovic, M., Hoang, S., Meyer-Vernet, N., et al. 1995, *J. Geophys. Res.*, 100, 19881
 Maksimovic, M., Issautier, K., Meyer-Vernet, N., et al. 2005a, *Advances in Space Research*, 36, 1471
 Maksimovic, M., Pierrard, V., & Lemaire, J. 2001, *Ap&SS*, 277, 181
 Maksimovic, M., Pierrard, V., & Lemaire, J. F. 1997, *A&A*, 324, 725
 Maksimovic, M., Walsh, A. P., Pierrard, V., Štverák, Š., & Zouganelis, I. 2021, *Electron Kappa Distributions in the Solar Wind: Cause of the Acceleration or Consequence of the Expansion?*, ed. M. Lazar & H. Fichtner (Cham: Springer International Publishing), 39–51
 Maksimovic, M., Zouganelis, I., Chaufray, J. Y., et al. 2005b, *Journal of Geophysical Research (Space Physics)*, 110, A09104
 Manning, R. & Dulk, G. A. 2001, *A&A*, 372, 663
 Markwardt, C. B. 2009, in *Astronomical Society of the Pacific Conference Series*, Vol. 411, *Astronomical Data Analysis Software and Systems XVIII*, ed. D. A. Bohlender, D. Durand, & P. Dowler, 251
 Marsch, E., Pilipp, W. G., Thieme, K. M., & Rosenbauer, H. 1989, *J. Geophys. Res.*, 94, 6893
 Martinović, M. M., Dordević, A. R., Klein, K. G., et al. 2022, *Journal of Geophysical Research (Space Physics)*, 127, e30182
 Martinović, M. M., Klein, K. G., Gramze, S. R., et al. 2020, *Journal of Geophysical Research (Space Physics)*, 125, e28113
 Martinović, M. M., Klein, K. G., Huang, J., et al. 2021, *ApJ*, 912, 28
 Martinović, M. M., Zaslavsky, A., Maksimovic, M., et al. 2016, *Journal of Geophysical Research (Space Physics)*, 121, 129
 Matthaeus, W. H., Elliott, H. A., & McComas, D. J. 2006, *Journal of Geophysical Research (Space Physics)*, 111, A10103
 Meyer-Vernet, N. 1979, *J. Geophys. Res.*, 84, 5373
 Meyer-Vernet, N., Couturier, P., Hoang, S., et al. 1986, *Science*, 232, 370
 Meyer-Vernet, N., Hoang, S., & Moncuquet, M. 1993, *J. Geophys. Res.*, 98, 21163
 Meyer-Vernet, N. & Issautier, K. 1998, *J. Geophys. Res.*, 103, 29705
 Meyer-Vernet, N., Issautier, K., & Moncuquet, M. 2017, *J. Geophys. Res.*, 122, 7925
 Meyer-Vernet, N., Lecacheux, A., Issautier, K., & Moncuquet, M. 2022, *A&A*, 658, L12
 Meyer-Vernet, N., Mangeney, A., Maksimovic, M., Pantellini, F., & Issautier, K. 2003, in *American Institute of Physics Conference Series*, Vol. 679, *Solar Wind Ten*, ed. M. Velli, R. Bruno, F. Malara, & B. Bucci, 263–266
 Meyer-Vernet, N. & Moncuquet, M. 2020, *Journal of Geophysical Research (Space Physics)*, 125, e27723
 Meyer-Vernet, N. & Perche, C. 1989, *J. Geophys. Res.*, 94, 2405
 Moncuquet, M., Lecacheux, A., Meyer-Vernet, N., Ceconi, B., & Kurth, W. S. 2005, *Geophys. Res. Lett.*, 32, L20S02
 Moncuquet, M., Matsumoto, H., Bougeret, J. L., et al. 2006, *Advances in Space Research*, 38, 680
 Moncuquet, M., Meyer-Vernet, N., & Hoang, S. 1995, *J. Geophys. Res.*, 100, 21697
 Moncuquet, M., Meyer-Vernet, N., Hoang, S., Forsyth, R. J., & Canu, P. 1997, *J. Geophys. Res.*, 102, 2373
 Moncuquet, M., Meyer-Vernet, N., Issautier, K., et al. 2020, *ApJS*, 246, 44
 Novaco, J. C. & Brown, L. W. 1978, *ApJ*, 221, 114
 Pierrard, V., Lazar, M., & Štverák, Š. 2020, *Sol. Phys.*, 295, 151
 Pilipp, W. G., Muehlhaeuser, K. H., Miggendorfer, H., Rosenbauer, H., & Schwenn, R. 1990, *J. Geophys. Res.*, 95, 6305
 Pulupa, M., Bale, S. D., Badman, S. T., et al. 2020, *ApJS*, 246, 49
 Pulupa, M., Bale, S. D., Bonnell, J. W., et al. 2017, *J. Geophys. Res.*, 122, 2836
 Salem, C., Bosqued, J. M., Larson, D. E., et al. 2001, *J. Geophys. Res.*, 106, 21701
 Schippers, P., Moncuquet, M., Meyer-Vernet, N., & Lecacheux, A. 2013, *Journal of Geophysical Research (Space Physics)*, 118, 7170
 Totten, T. L., Freeman, J. W., & Arya, S. 1995, *J. Geophys. Res.*, 100, 13
 Štverák, Š., Maksimovic, M., Trávníček, P. M., et al. 2009, *J. Geophys. Res.*, 114, A05104
 Štverák, Š., Trávníček, P. M., & Hellinger, P. 2015, *Journal of Geophysical Research (Space Physics)*, 120, 8177
 Wang, Y. M. 2010, *ApJ*, 715, L121
 Wang, Y. M. & Sheeley, N. R., Jr. 1990, *ApJ*, 355, 726
 Whittlesey, P. L., Larson, D. E., Kasper, J. C., et al. 2020, *ApJS*, 246, 74
 Wilson, Lynn B., Stevens, M. L., Kasper, J. C., et al. 2018, *ApJS*, 236, 41
 Woodham, L. D., Horbury, T. S., Matteini, L., et al. 2021, *A&A*, 650, L1
 Zaslavsky, A., Meyer-Vernet, N., Hoang, S., Maksimovic, M., & Bale, S. D. 2011, *Radio Science*, 46, RS2008
 Zhao, L. L., Zank, G. P., Adhikari, L., et al. 2020, *ApJS*, 246, 26
 Zhao, S. Q., Yan, H., Liu, T. Z., Liu, M., & Shi, M. 2021, *ApJ*, 923, 253
 Zhou, Z., Xu, X., Zuo, P., et al. 2022, *Geophys. Res. Lett.*, 49, e97564
 Zouganelis, I., Maksimovic, M., Meyer-Vernet, N., Lamy, H., & Issautier, K. 2004, *ApJ*, 606, 542

B.3 Properties of A Supercritical Quasi-perpendicular Interplanetary Shock Propagating in Terrestrial Foreshock Region

Mingzhe Liu, Zhongwei Yang, Ying D. Liu, Bertrand Lembège, Karine Issautier, et al. "*Properties of A Supercritical Quasi-perpendicular Interplanetary Shock Propagating in Terrestrial Foreshock Region*". The Astrophysical Journal Supplement Series.

DOI: [10.3847/1538-4365/ac94c8](https://doi.org/10.3847/1538-4365/ac94c8)



Properties of a Supercritical Quasi-perpendicular Interplanetary Shock Propagating in the Terrestrial Foreshock Region

Mingzhe Liu^{1,2,3}, Zhongwei Yang^{2,4}, Ying D. Liu^{2,4}, Bertrand Lembège³, Karine Issautier¹, L. B. Wilson, III⁵, Siqi Zhao⁶, Vamsee Krishna Jagarlamudi⁷, Xiaowei Zhao^{8,9}, Jia Huang¹⁰, and Nicolina Chrysaphi¹

¹ LESIA, Observatoire de Paris, Université PSL, CNRS, Sorbonne Université, Université de Paris, 5 place Jules Janssen, F-92195 Meudon, France
mingzhe.liu@obspm.fr

² State Key Laboratory of Space Weather, National Space Science Center, Chinese Academy of Sciences, Beijing 100190, People's Republic of China

³ LATMOS / IPSL, UVSQ Paris-Saclay University, Sorbonne University, CNRS, Guyancourt, France

⁴ University of Chinese Academy of Sciences, Beijing 100049, People's Republic of China

⁵ NASA Goddard Space Flight Center, Code 672, Greenbelt, Maryland, MD20707, USA

⁶ Deutsches Elektronen Synchrotron, Platanenallee 6, D-15738 Zeuthen, Germany

⁷ Johns Hopkins University Applied Physics Laboratory, Laurel, MD, USA

⁸ Key Laboratory of Space Weather, National Satellite Meteorological Center (National Center for Space Weather), China Meteorological Administration, Beijing 100081, People's Republic of China

⁹ School of Earth and Space Sciences, Peking University, Beijing 100871, People's Republic of China

¹⁰ Climate and Space Sciences and Engineering, University of Michigan, Ann Arbor, MI 48109, USA

Received 2022 May 11; revised 2022 September 6; accepted 2022 September 22; published 2022 November 9

Abstract

We investigate the properties of an interplanetary (IP) shock ($M_f = 2.1$, $\theta = 80^\circ$) that was detected by Wind on 1999 September 12 and was magnetically connected to the terrestrial bow shock. Key results are obtained concerning how the IP shock modifies the terrestrial foreshock electron and ion dynamics: (1) Intensive Langmuir waves were detected downstream of the IP shock due to the enhanced penetrating terrestrial foreshock electron beams. (2) Whistler heat flux instabilities associated with the oblique precursor whistler pitch-angle scatter the suprathermal electrons, together with the normal betatron acceleration that occurs across the IP shock. (3) The IP shock interacts with the antisunward propagating Alfvén waves/fluctuations, and the shocked plasma shows both Alfvénic and mirror-mode features where Alfvén waves were separated into two parts propagating in opposite directions. (4) Intense specularly reflected gyrating ions were detected around the IP shock, which indicates that the energy dissipation effects at the IP shock depend on both reflected ions and the waves intrinsic to the shock. These results provide new insights into the interaction between an IP shock and the terrestrial foreshock.


Unified Astronomy Thesaurus concepts: Solar wind (1534); Interplanetary shocks (829); Alfvén waves (23); Shocks (2086); Planetary bow shocks (1246)

1. Introduction

Collisionless shocks are important plasma structures, and appear ubiquitously in the solar wind and around the planets. From the Sun to the Earth, interplanetary (IP) shocks are typically driven by coronal mass ejections (CMEs) or by the fast solar wind (e.g., Liu et al. 2012, 2014a, 2014b; Möstl et al. 2012; Lugaz et al. 2015; Zhao et al. 2019b). Near the Earth, the bow shock forms in front of the Earth due to the interaction between the solar wind and the Earth's magnetosphere. Upstream of the terrestrial bow shock, the region that is magnetically connected to the shock is called the terrestrial foreshock. It is well-known and has long been investigated that the terrestrial foreshock region is dominated by waves and backstreaming particles (Wilson 2016; Parks et al. 2017). When IP shocks are Earth directed, they may interact with the terrestrial foreshock region, which is of great significance for both space weather predictions and fundamental plasma physics (e.g., Přeč et al. 2009; Šafránková et al. 2007a, 2007b; Goncharov et al. 2018). Previous studies mainly focused on how the mutual interaction modifies the geometry, propagation, and strength of the IP shock. There are still very

few studies of how an IP shock modifies terrestrial foreshock electron and ion dynamics and associated waves, however.

Terrestrial foreshocks are identified by the enhanced flux of backstreaming particles. Due to the $\mathbf{E} \times \mathbf{B}$ drift and high mass ratio between the ions and electrons, a clear separation appears between the ion and electron foreshock boundaries (see Parks et al. 2017). In the region between the ion and electron foreshock boundaries, only backstreaming electrons are detected. In contrast, in the ion foreshock region, both backstreaming ions and electrons are observed. The backstreaming electrons can exhibit a bump on tail electron velocity distribution function that is unstable to the growth of Langmuir waves via Landau resonance (see Savoini & Lembège 2001; Pulupa et al. 2011, 2012, and references therein). Savoini & Lembège (2001) showed that local backstreaming-electron distributions consist of two components: (i) a high-energy component characterized by a field-aligned bump on tail or beam signature, and/or (ii) a low-energy component characterized by a loss-cone signature. Also, electrons that are locally accelerated in the deep downstream region may escape back into the upstream region (Savoini & Lembège 2009). Furthermore, in the leading edge of the electron foreshock region, the most intense Langmuir waves around the local electron plasma frequency (f_{pe}) are generally observed, associated with more energetic backstreaming-electron beams above 1 keV (e.g., Kasaba et al. 2000; Bale et al. 2000; Pulupa et al. 2012). In addition, in the deeper region of the

 Original content from this work may be used under the terms of the [Creative Commons Attribution 4.0 licence](https://creativecommons.org/licenses/by/4.0/). Any further distribution of this work must maintain attribution to the author(s) and the title of the work, journal citation and DOI.

terrestrial foreshock, weaker Langmuir waves are detected in association with less energetic backstreaming electrons below 1 keV (e.g., Matsumoto et al. 1997; Kasaba et al. 2000; Pulupa et al. 2011). The $2f_{pe}$ emissions, frequently detected in the terrestrial foreshock, are considered to be generated by backstreaming-electron-driven Langmuir waves and correlated with the amplitude of Langmuir waves. Then, the $2f_{pe}$ emission source region is confirmed to be the leading region of the electron foreshock (e.g., Yoon et al. 1994; Reiner et al. 1996; Kasaba et al. 2000). Above all, when backstreaming electrons and associated electrostatic Langmuir waves/fluctuations are detected upstream of the terrestrial bow shock, the spacecraft is considered to be magnetically connected to the terrestrial bow shock. Thus, an interesting question arises regarding how an IP shock modifies the terrestrial foreshock electron dynamics when the IP shock is magnetically connected to the terrestrial bow shock.

The backstreaming ions near the ion foreshock boundary are field aligned and become more diffuse and isotropic when they travel deeper into the foreshock and/or approach the quasi-parallel shock region (Wilson 2016). Due to the interaction between the incoming and backstreaming ions, numerous large-amplitude waves/fluctuations that fall in a broad frequency range were detected in the quasi-parallel foreshock region (e.g., low-frequency Alfvén/ion cyclotron waves, and fast magnetosonic or magnetosonic-whistler waves). Alfvén waves and/or Alfvén-like oscillations were frequently detected in the quasi-parallel terrestrial foreshock region in association with the left-hand resonant ion/ion instability (e.g., Wang et al. 2015; Wilson 2016, and references therein). In particular, when a quasi-perpendicular IP shock is Earth directed, it may interact with Alfvén waves/fluctuations in the quasi-parallel terrestrial foreshock. In the past, many theoretical and simulation investigations focused on the interaction of Alfvén waves with shocks (e.g., McKenzie & Westphal 1969; Lu et al. 2009). The amplitude of the Alfvén waves is enhanced by the shock (e.g., McKenzie & Westphal 1969; Lu et al. 2009), and Alfvén waves detected in the shocked plasma are separated into two branches propagating in the opposite directions (Lu et al. 2009). Furthermore, clear ripples were identified at the front of the perpendicular shock due to the interaction with the upstream Alfvén waves based on two-dimensional hybrid simulations (Lu et al. 2009). The ripples at the shock front can affect both reflected ion and electron dynamics (e.g., Lembège & Savoini 2002; Lembege et al. 2004; Saito & Umeda 2011; Yang et al. 2012, 2018). Interactions between the Alfvén waves/fluctuations and a quasi-perpendicular shock are still an interesting issue that is far from completely understood. Examination of the features of the particle populations and waves around the IP shock interacting with Alfvén waves/fluctuations may provide new insights.

In this work, we report properties of an IP shock propagating in the quasi-parallel terrestrial foreshock region, which was observed by Wind (Wilson et al. 2021) at 03:57:56 UT on 1999 September 12. Specifically, in situ measurements of the solar wind from Wind/MFI (Lepping et al. 1995), Wind/3DP (Lin et al. 1995) and the thermal noise receiver (TNR) on board Wind/WAVES (Bougeret et al. 1995) have been used for the analysis. In Section 2.1, we confirm that the IP shock is magnetically connected to the terrestrial bow shock via a comprehensive analysis of magnetic field measurements, electron pitch-angle distributions (PADs), and wave observations. Then, with high-cadence magnetic field data (11 samples

per second) and the burst-mode particle data (a full distribution per three seconds), we investigate how the IP shock modifies the electron dynamics of the terrestrial foreshock at kinetic scales in Section 2.2. Furthermore, the interactions between the IP shock and the Alfvén waves/fluctuations detected in the terrestrial foreshock region are reported in Section 2.3, including the properties of Alfvén waves/fluctuations around the IP shock and the IP shock-reflected ion dynamics. In the end, the main results are summarized and discussed in Section 3.

2. Observations and Data Analysis

2.1. Magnetic Connection between IP Shock and Terrestrial Bow Shock

Figure 1 (left) shows the Wind spacecraft trajectory (solid black curve) projected in the XY-GSE plane, which covers the time period from 00:00:00 on 1999 September 10, UTC, to 12:00:00 on 1999 September 12, UTC. Projections of the model terrestrial bow shock (solid red curve; see Peredo et al. 1995) and magnetopause (solid blue curve; see Roelof & Sibeck 1993) locations are also plotted for reference. The model bow shock parameters are adjusted to match the average location of the observed crossings by the spacecraft. During the time period considered, the spacecraft traveled across the quasi-parallel side of the terrestrial bow shock from the downstream (magnetosheath) to the upstream and then detected an IP shock (yellow asterisk). The projection of the average magnetic field vector was determined by averaging the magnetic field during the time period between the last crossing of the terrestrial bow shock and detection of the IP shock. As a result, Wind may generally be magnetically connected to the terrestrial bow shock along the trajectory between the terrestrial bow shock and the IP shock. For the basic information of the IP shock, it passed the Wind spacecraft at 03:57:56 UT on 1999 September 12. The IP shock that is in the supercritical regime with a fast magnetosonic Mach number $M_f \sim 2.1$ and an Alfvén Mach number $M_A \sim 3.0$ propagates in the proton plasma beta $\beta_p \approx 1$ environment. It is a fast-mode, quasi-perpendicular shock, with a shock normal angle $\theta_{Bn} = 80^\circ$ and a shock speed $V_{shn} = 532.8 \pm 3.3 \text{ km s}^{-1}$. The basic parameters of the IP shock are obtained by the shock discontinuity analysis tool (Vinas & Scudder 1986). They are consistent with those from the shock database maintained by J. C. Kasper.¹¹

Figure 1 (right) presents an overview plot of the Wind observations along the spacecraft trajectory mentioned above. Figures 1(b)–(c) give the magnetic field magnitude and GSE components of the magnetic field, respectively. From the terrestrial bow shock (dashed vertical red line) to the IP shock (dashed vertical yellow line), the magnetic field magnitude decreases in general. Furthermore, the X-GSE component (in red) of the magnetic field is positive in general ($\langle B_x \rangle \sim 2.1 \text{ nT}$) and the Y-GSE component (in green) of the magnetic field is usually negative ($\langle B_y \rangle \sim -3.0 \text{ nT}$). This implies that the observed ambient magnetic field is generally directed sunward. Therefore, electrons with pitch angles close to 0° are traveling toward the Sun and may be backstreaming from the bow shock. In contrast, electrons with pitch angles close to 180° are traveling antisunward and may be incident to the bow shock. Figure 1(d) presents the PAD of 265 eV electrons measured by EESA-Low/

¹¹ <https://www.cfa.harvard.edu/shocks/>

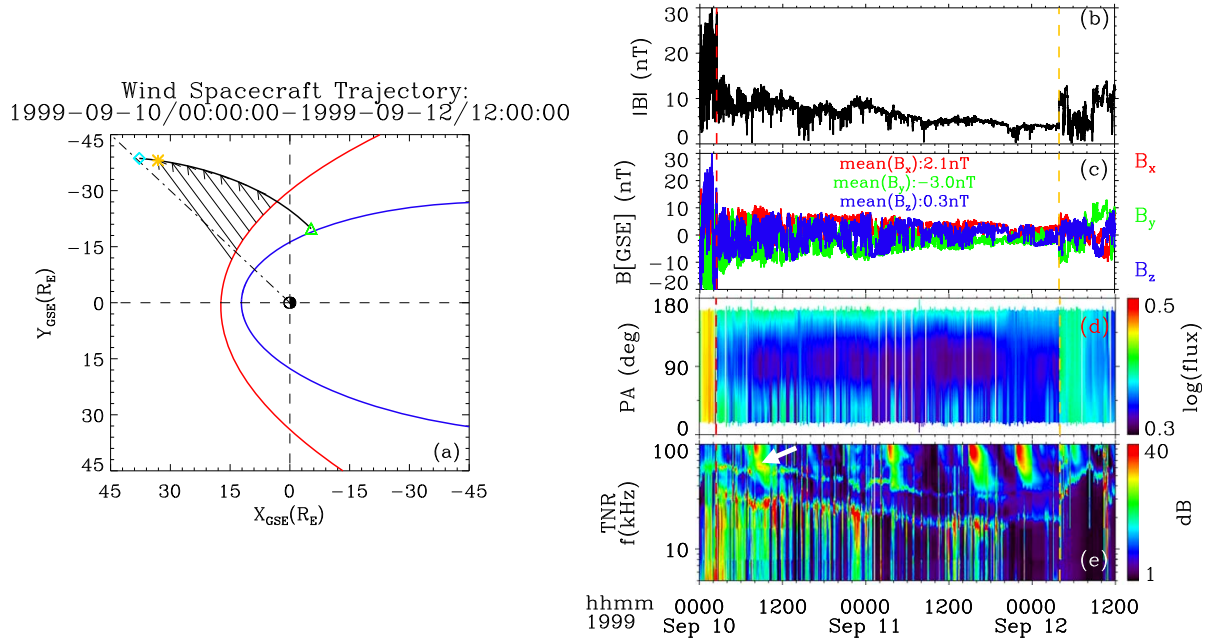


Figure 1. (Left) The Wind satellite orbits in the XY plane of geocentric solar ecliptic (GSE) coordinate reference frame from 00:00:00 on 1999 September 10, UTC, to 12:00:00 on 1999 September 12, UTC. The solid black line denotes the spacecraft trajectory. The empirical model bow shock (solid red line; see Peredo et al. 1995) and magnetopause (solid blue line; see Roelof & Sibeck 1993) are plotted for reference. The triangle and diamond mark the start and end of the Wind trajectory, respectively. The asterisk denotes the position where an IP shock was detected by Wind. The black arrows represents the projection of the average magnetic field vectors between the terrestrial bow shock and the IP shock. (Right) The Wind observations that correspond to the trajectory shown on the left. From top to bottom, the panels show the magnetic field magnitude, magnetic field components in GSE coordinates, the PAD of 265 eV electrons obtained from the EESA-Low instrument on board Wind/3DP, and the electric field voltage dynamic spectrum from TNR on board Wind/WAVES. The dashed vertical red and yellow lines mark the crossing of the terrestrial bow shock and the IP shock, respectively.

3DP for reference. Typically, the relevant electron populations of this energy are the halo and/or strahl in the quiet solar wind or bidirectional streams of suprathermal electrons within CMEs (Gosling et al. 1987). Here, the strahl electrons from the Sun are apparent in the direction antiparallel to the magnetic field, whereas terrestrial foreshock electron beams (backstreaming electrons from the bow shock) are clearly identified as evident enhancements when pitch angles are smaller than 90° . Figure 1(e) shows the electric field voltage dynamic spectrum measured by TNR on board Wind/WAVES. The TNR radio receiver on board Wind/WAVES, which is connected to the 2×50 m thin wire electric dipole antennas (before it was broken by dust impacts), measures electric fields (from 4 to 256 kHz) by combining five logarithmically spaced (overlapping) frequency bands (with the standard frequency resolution being $\Delta f/f = 4.3\%$). The TNR radio receiver is especially designed to measure electrostatic fluctuations produced by the quasi-thermal noise due to the thermal motion of the ambient electrons and ions. The quasi-thermal plasma line is clearly visible (between 20 and 40 kHz before and after the IP shock) and can be used to straightforwardly determine the local electron density (e.g., Meyer-Vernet & Perche 1989; Meyer-Vernet et al. 2017). The Langmuir wave activity can be identified as the intense enhancement near the plasma line. As expected, intense Langmuir waves are associated with transient enhancements of the electron flux in parallel direction. Also, $2f_{pe}$ emissions are clearly detected during the time period considered. Again, observations of the terrestrial foreshock electron beams along the magnetic field and the associated Langmuir wave activity indicate that Wind may in

general be magnetically connected to the terrestrial bow shock along the trajectory between the terrestrial bow shock and the IP shock. In addition, the timespan of the electron foreshock region of a quasi-perpendicular IP shock observed by the spacecraft is usually shorter than one minute (e.g., Bale et al. 1999; Hoang et al. 2007; Pulupa & Bale 2008). Therefore, we exclude the possibility that the terrestrial foreshock electrons and strahl electrons are disturbed by the IP foreshock electrons. More details are described in Appendices A and B.

We note that the terrestrial foreshock electron beams are observed intermittently, whereas the strahl electrons from the Sun are observed constantly. This may be due to the dynamic nature of the terrestrial bow shock, especially the large-scale bow shock expansion (i.e., back and forth movements) due to the solar wind compression. For the time period considered, Wind crossed the bow shock three times due to the expansion from 02:00:00 to 03:00:00 on 1999 September 10, UTC. In addition, the ambient magnetic field rotates slightly. As a result, it may connect to different regions on the bow shock and/or disconnect to the bow shock. In contrast, in Figure 1(a), both the model bow shock and the projected upstream magnetic field lines are assumed to be static. Therefore, Wind may not always be magnetically connected to the bow shock (although it was for most of the time considered), which may be the main reason for the intermittent features of the terrestrial foreshock electron beams. Furthermore, when Wind is magnetically connected to the quasi-perpendicular terrestrial bow shock, Lembège & Savoini (2002) showed that electrons may not be reflected uniformly by the bow shock based on two-

dimensional full particle electromagnetic simulation. Instead, packs of reflected electrons may be formed along the rippled shock front. This may also contribute to the intermittent features of the terrestrial foreshock electron beams. Also, a few weak Type III radio bursts were observed with a cutoff frequency much higher than local f_{pe} (except for the one indicated by the white arrow in Figure 1(e)). This indicates that most Langmuir waves detected between the terrestrial bow shock and the IP shock are not associated with the energetic electrons from the Sun, but are driven by the terrestrial foreshock electron beams.

An expanded view of 5 hr observations around the IP shock (indicated by the vertical red line) is shown in Figure 2. The plasma line is apparent, and both local f_{pe} and $2f_{pe}$ are overplotted as white dots in Figure 2(a) for reference. Accurate measurements of local f_{pe} are derived by tracking the plasma peaks based on the neural network method, whose accuracy is verified by the full fit of the quasi-thermal noise spectrum (see Salem et al. 2001; Issautier et al. 2005, and references therein). Moreover, Figures 2(b)–(e) show that the transient electron flux enhancements around the IP shock mainly come from the direction parallel to the ambient magnetic field. More details about the detectors and specific definition of the directions are given in Appendix A. Thereby, we verified that the transient parallel electron flux enhancements exclusively come from the terrestrial bow shock and therefore correspond to the terrestrial foreshock electrons. Indeed, intermittent Langmuir waves (Figure 2(a)) driven by transient terrestrial foreshock electron beams are observed around the IP shock. We note that a weak Type III burst was observed around the IP shock. The cutoff frequency of the Type III burst is much higher than local f_{pe} , which means that the corresponding flare-accelerated energetic electrons did not reach the spacecraft. We further checked the EESA-High/3DP ($\sim 300 \text{ eV} \leq E \leq 30 \text{ keV}$) and SST-Foil/3DP ($\sim 20 \text{ keV} \leq E \leq 500 \text{ keV}$) measurements and indeed found no apparent enhancements of the antisunward energetic electron flux (not shown here). Therefore, we confirm that the Langmuir waves detected around the IP shock were exclusively driven by the terrestrial foreshock electrons and not associated with the energetic electrons from the Sun. Thus, it is quite striking to mention that the intensity of the bursty Langmuir waves detected downstream of the IP shock is much higher than those upstream of the IP shock. Figures 2(a) and (f) show that the detected Langmuir wave intensity is closely related to the ratio of the parallel to perpendicular electron flux. When the terrestrial foreshock electrons and the associated Langmuir waves are detected, the ratio of the parallel to the perpendicular electron flux is higher than the ambient values in the free solar wind. Upstream of the IP shock, the ratio of the parallel to the perpendicular electron flux is highest for the terrestrial foreshock electrons with an energy from 96 to 258 eV (see the green lines in Figure 2(f)). In contrast, downstream of the IP shock, the energy of the dominant terrestrial foreshock electrons (with a higher ratio of the parallel to perpendicular electron flux) is higher than 420 eV (see the dark blue and/or purple lines in Figure 2(f)). Across the IP shock, the energy of the dominant terrestrial foreshock electrons and the corresponding ratio of the parallel to perpendicular electron flux are greatly enhanced. This coincides with the enhanced Langmuir wave activity downstream of the IP shock. The possible driving mechanisms are explained in Section 2.2.

2.2. Electron Dynamics at Kinetic Scales

In this section, we investigate how the electron features are modified across the IP shock at kinetic scales, which are associated with the mechanisms of wave generations/enhancements. Full electron PADs around the IP shock are plotted in Figure 3. The labeled energies in Figure 3 are the mean values of the nine highest energy channels of EESA-Low/3DP after correcting the estimated spacecraft potential (Salem et al. 2001). Figures 3(a)–(b) present the observations upstream of the IP shock. Figure 3(c) covers the foot, ramp, and overshoot structures of the IP shock. Figures 3(d)–(f) give the observations downstream of the IP shock. The foot, ramp, and overshoot structures are clearly displayed in both Figures 4(a) and 7 (a). In Figures 3(a)–(b), both the electron (with an energy higher than 35 eV) number flux and the energy flux along the magnetic field (including both parallel, $PA < 45^\circ$, and antiparallel, $PA > 135^\circ$) are higher than those perpendicular ($PA = 90^\circ$) to the magnetic field. We confirm that IP foreshock electrons were not detected by Wind in Appendix B. Therefore, suprathermal electrons flowing parallel (antiparallel) to the ambient magnetic field correspond to the terrestrial foreshock electron beams (strahl electrons from the Sun). This gives further confirmation that the IP shock is indeed magnetically connected to the terrestrial bow shock.

We note that both the suprathermal electron number flux and the energy flux perpendicular to the ambient magnetic field (i.e., $PA = 90^\circ$) increase from upstream to the shock ramp position (see Figures 3 (a)–(c)). This enhancement may be explained by the pitch-angle scattering by the whistler heat flux instabilities observed near the shock ramp, together with the normal betatron acceleration of electrons (see below). Downstream of the IP shock, the parallel suprathermal (especially with an energy higher than 258 eV) electron flux ($PA < 45^\circ$) is in general higher than those antiparallel ($PA > 135^\circ$) and perpendicular ($PA = 90^\circ$) to the ambient magnetic field. This is consistent with the enhanced ratio of the parallel to perpendicular suprathermal electron flux across the IP shock mentioned in Section 2.1 (see Figure 2(f)). This may account for the generation and/or enhancement of intensive Langmuir wave activity downstream of the IP shock. When the transient terrestrial foreshock electrons penetrate the IP shock, the parallel terrestrial foreshock electron flux is enhanced accordingly. Stated in another way, the transient electron flux enhancements upstream of the IP shock are further enhanced when penetrating the IP shock (e.g., Figure 2). Downstream of the IP shock, the further enhanced terrestrial foreshock electron beams may contribute to create a larger bump on tail distributions. In Figure 2(f), the higher energy parallel electron fluxes can sometimes reach the lower energy parallel fluxes (higher than 258 eV) when terrestrial foreshock electrons are detected, which may be remnants of positive slopes. Indeed, even though the parallel electron fluxes at higher energies are enhanced (see both Figures 2(f) and 3), they are not high enough to produce positive slopes on the tail of the electron distributions. There are two possible explanations: (i) the bump (the region with a positive slope) on the tail of the distribution function has already been relaxed to generate and/or enhance the Langmuir waves, or (ii) the bump still exists, but the EESA instruments on board Wind/3DP have an insufficient energy resolution to resolve it. Based on the quasilinear theory of beam relaxation (e.g., Groggnard 1975; Pulupa et al. 2012; Zhao et al. 2021b, and references therein), positive slopes on the bump on

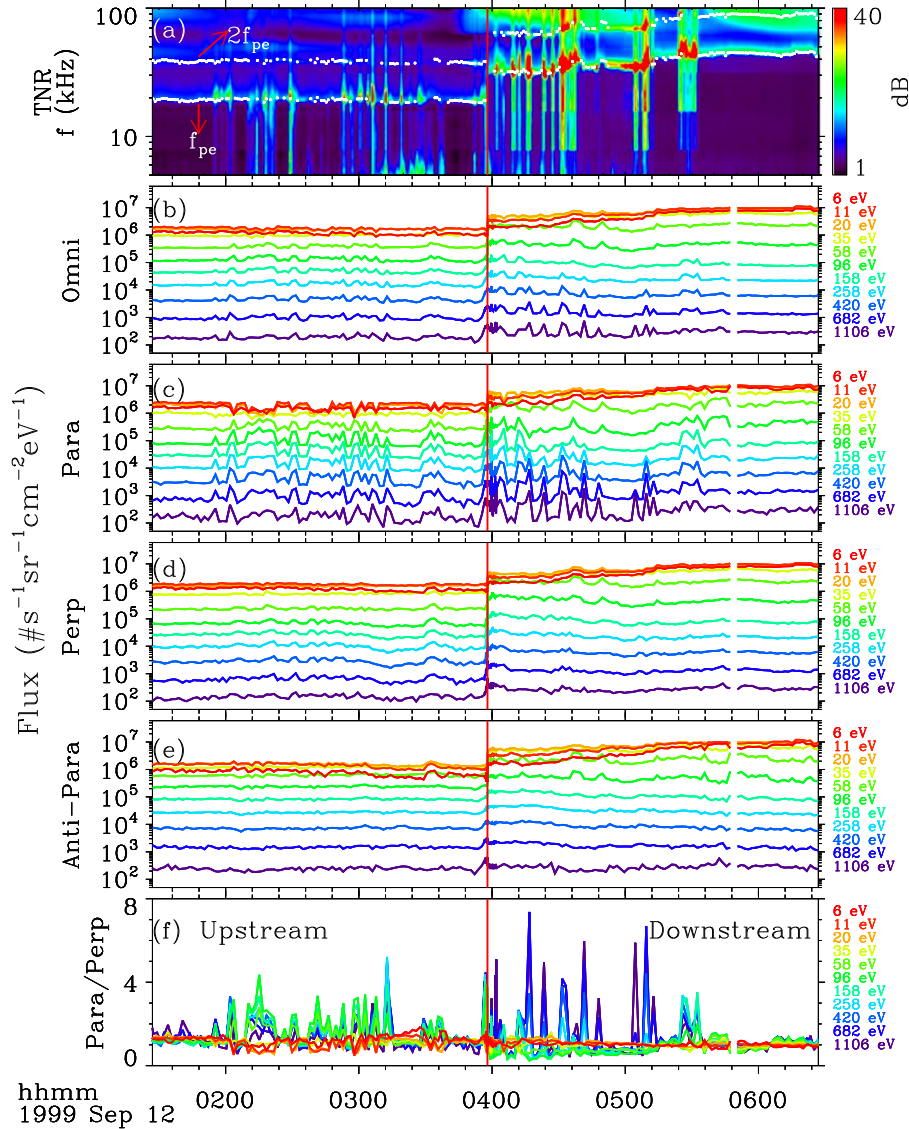


Figure 2. Five-hour expanded view of measurements from Wind around the IP shock detected at 03:57:56 on 1999 September 12, UT. From top to bottom, the panels show the electron field voltage power spectrum from TNR on board Wind/WAVES, omnidirectional electron flux, electron flux at different pitch angles including those parallel, perpendicular, and antiparallel to the ambient magnetic field, and the ratio of the parallel to perpendicular flux. For electron fluxes at different pitch angles, they are derived from the measurements by the EESA-Low instrument on board Wind/3DP, and electrons from about 6 to 1106 eV are considered. The labeled energies have been corrected by considering the spacecraft potential. The vertical red line marks the time when the IP shock was detected.

tail electron velocity distributions can be mediated by Landau resonance and then further generate/enhance Langmuir waves. The intensity of the Langmuir waves depends on both the energy of the electron beam and the height of the bump on tail distribution, which could explain the more intensive Langmuir waves downstream of the IP shock well.

Figure 4 gives the wavelet analysis of the magnetic field at a high cadence of $11 \text{ samples s}^{-1}$ around the IP shock with a 2-minute time interval considered. The magnetic foot associated with the precursor whistlers and the magnetic overshoot are indicated by two arrows in Figure 4(a), respectively. A detailed view of the magnetic foot and overshoot is shown in

Figure 7(a). Across the IP shock, the magnetic field magnitude is enhanced. This field jump (at the foot and ramp of the shock) lasts for about 5 s, much longer than the electron cyclotron period T_{ce} ($0.0038 \text{ s} < T_{ce} < 0.0086 \text{ s}$). Therefore, the first adiabatic invariant $\mu = E_{\perp}/B$ should be conserved during the compression, which means that normal betatron acceleration of electrons may exist. Normal betatron acceleration of electrons mainly occurs before and at the IP shock (at the foot and ramp of the shock), as the variation of the magnetic field magnitude almost remains relatively small downstream of the IP shock. The normal betatron acceleration of electrons may contribute to the change of the pitch angle of electrons (Liu et al. 2018).

B.3. Properties of A Supercritical Quasi-perpendicular Interplanetary Shock Propagating in Terrestrial Foreshock Region

THE ASTROPHYSICAL JOURNAL SUPPLEMENT SERIES, 263:11 (15pp), 2022 November

Liu et al.

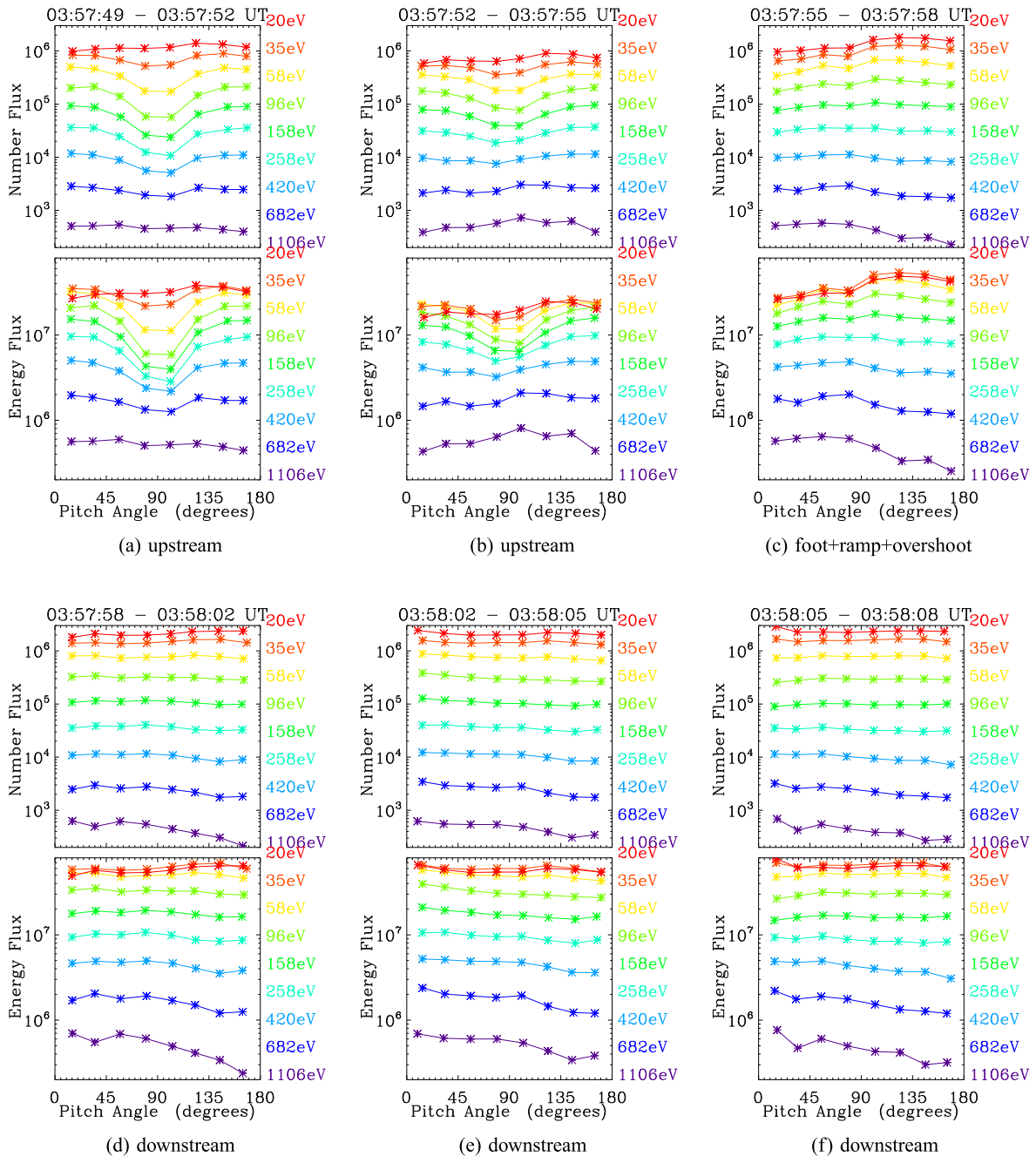


Figure 3. Evolution of the stacked line plot of the PADs at the nine highest energies (after correcting the spacecraft potential) from the EESA-Low instrument on board Wind/3DP. The top/bottom panel of each figure shows the electron PAD of number/energy flux. The physics units are the number flux ($\#s^{-1}sr^{-1}cm^{-2}eV^{-1}$) and the energy flux ($eVs^{-1}sr^{-1}cm^{-2}eV^{-1}$).

Precursor whistlers (indicated by the white arrows in Figures 4(c)–(f)) are observed at $2.0\text{ Hz} < f < 4.0\text{ Hz}$ (in spacecraft frame) near the shock ramp. Figure 5 shows an example of a minimum variance (MV) analysis (Khrabrov & Sonnerup 1998) of the magnetic fluctuations at $2.0\text{ Hz} < f < 4.0\text{ Hz}$ (in spacecraft frame) at the foot/precursor region of

the IP shock. The hodograms in GSE and MV coordinates are shown in the left and right panels, respectively. The wave event is right-handed polarized with respect to the local magnetic field, which is consistent with the whistler properties. The wave event is also right-handed polarized with respect to the wavevector \hat{K}_{GSE} . However, there is an ambiguity of the sign

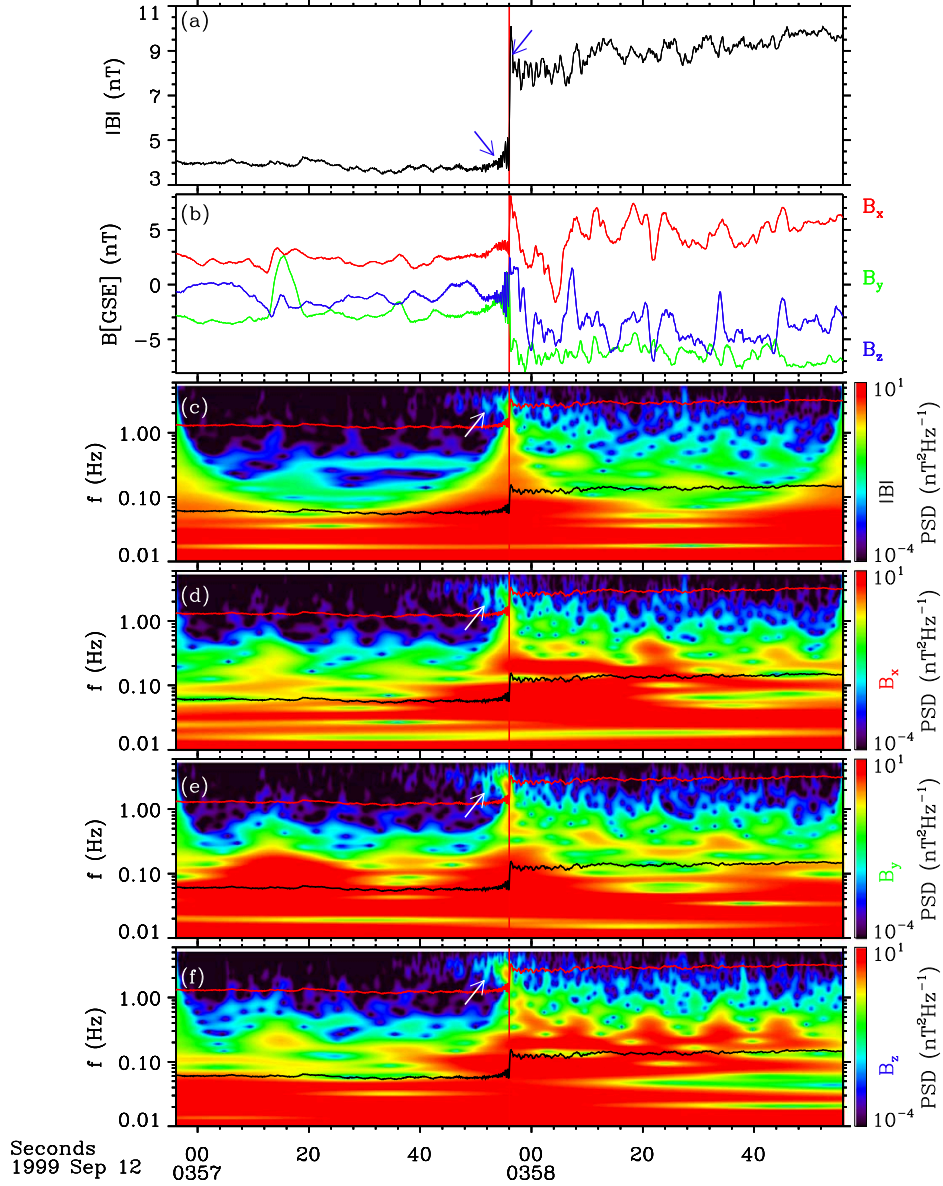


Figure 4. Wavelet analysis of the magnetic field measurements around the IP shock. From top to bottom, the panels show the magnetic field magnitude, the GSE components of the magnetic field, the wavelet analysis of the magnetic field magnitude $|B|$, and components including B_x , B_y , and B_z , respectively. The frequency range of the wavelet analysis is from 0.01 to 5.5 Hz. The two blue arrows in panel (a) indicate the foot (left) and overshoot (right) structures. The white arrows in panels (c)–(f) indicate the precursor whistlers. The vertical red line marks the IP shock. In panels (c)–(f), the local proton cyclotron frequency (horizontal black line) and 1/2 lower hybrid frequency (horizontal red line) are plotted for reference.

of \hat{K}_{GSE} due to projection effects, which results from using only single-spacecraft magnetic field measurements (Khrabrov & Sonnerup 1998; Wilson et al. 2017). Since $\theta_{\text{kB}} > 0^\circ$, the whistlers observed around the shock are oblique whistler waves. The shock angle $\theta_{\text{kn}} > 0^\circ$, so they are not likely to be phase standing (Mellott & Greenstadt 1984).

Precursor whistlers are generated through dispersive radiation from the shock ramp or indirectly due to instabilities that are excited by reflected particles (see Wilson et al. 2012, 2017, and references therein). In addition, precursor whistlers can be

generated (and/or enhanced) by whistler heat flux instabilities and/or whistler anisotropy instabilities (Wilson et al. 2009; Liu et al. 2018), which are discussed below. Gary et al. (1999) demonstrated that the heat-flux-driven whistler mode is always unstable when the temperature anisotropy of halo electrons $T_{\perp h}/T_{\parallel h} > 1.01$ and always stable when the parallel beta of core electrons $\beta_{\parallel c} \leq 0.25$. The primary influence of whistler heat flux instabilities is to pitch-angle-scatter halo electrons through cyclotron resonance. Table 1 shows the electron parameters derived from the 3DP/EESA-Low data around the

B.3. Properties of A Supercritical Quasi-perpendicular Interplanetary Shock Propagating in Terrestrial Foreshock Region

THE ASTROPHYSICAL JOURNAL SUPPLEMENT SERIES, 263:11 (15pp), 2022 November

Liu et al.

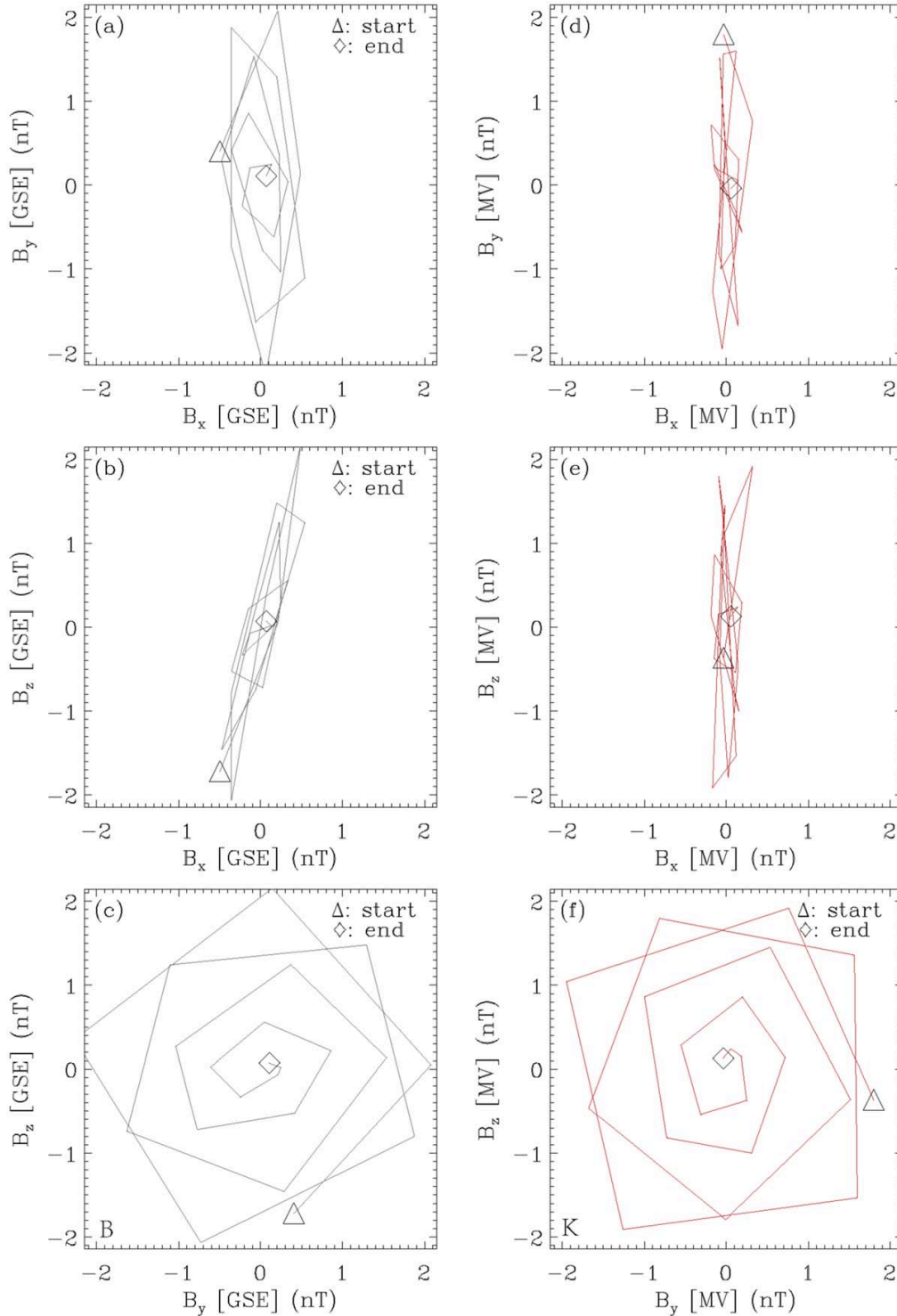


Figure 5. An example of an MV analysis of the waves during the time period of 03:57:55 UT ~ 03:57:57 UT ($2.0 \text{ Hz} < f < 4.0 \text{ Hz}$ in the spacecraft frame, ratio of the intermediate to minimum eigenvalues $\lambda_2/\lambda_3 = 59.71$, and ratio of the maximum to intermediate eigenvalues $\lambda_1/\lambda_2 = 1.110$, $\hat{K}_{\text{GSE}} = [0.96715, 0.06149, -0.24665]$, $\theta_{kB} = 53^\circ.7$ (or $126^\circ.3$), $\theta_{kv} = 14^\circ.2$ (or $165^\circ.8$), $\theta_{kV} = 12^\circ.4$ (or $167^\circ.6$)). The hodograms in GSE and MV coordinates are shown. The $[X, Y, Z]$ -MV coordinates represent the directions parallel to the minimum, intermediate, and maximum variance eigenvectors, respectively. The projections of the magnetic field (B) and wavevector (K) point outward.

Table 1
Wind/3DP Electron Parameters from EESA-Low Burst Mode Data

Time(UT)	$T_{\perp c}/T_{\parallel c}$	$T_{\perp h}/T_{\parallel h}$	$T_{\parallel h}/T_{\parallel c}$	$\beta_{\parallel c}$	$n_{ce}(\text{cm}^{-3})$	$n_{he}(\text{cm}^{-3})$	n_{he}/n_{ce}
03:57:49–03:57:52	0.71	0.65	9.85	1.61	3.61	0.27	0.075
03:57:52–03:57:55	0.72	0.89	6.90	1.67	2.27	0.20	0.087
03:57:55–03:57:58	1.10	1.09	7.56	0.84	4.27	0.27	0.063
03:57:58–03:58:02	1.03	1.10	10.31	1.10	7.35	0.10	0.014
03:58:02–03:58:05	0.98	1.07	10.31	1.23	7.20	0.10	0.015

IP shock. Electron parameters were derived by fitting core electrons to bi-Maxwellian distributions and halo electrons to bi-Kappa distributions (Mace & Sydora 2010). For more details about the fitting algorithm, we refer to Wilson et al. (2009) and Liu et al. (2018). From 03:57:55 UT to 03:58:05 UT, whistler heat flux instabilities can be excited, which is a possible driver of the whistler waves. In Table 1, a clear increase in $T_{\perp h}/T_{\parallel h}$ is seen across the shock (03:57:5503:57:58 UT), which may result from the normal cyclotron resonance that can increase the transverse energy of the suprathermal electrons and the normal betatron acceleration of electrons mentioned above. These results illustrate that (when passing through the IP shock) whistler heat flux instabilities may contribute to the increase in perpendicular suprathermal number flux and energy flux (see Figure 3) through pitch-angle scattering together with the normal betatron acceleration of electrons.

2.3. Interactions between IP Shock and Alfvén Waves/Fluctuations

Figure 6 presents the in situ solar wind observations around the IP shock from Wind, including the magnetic field and the plasma measurements. Figures 6(b)–(d) show that the magnetic field components are in phase with the proton bulk velocity components, indicating signatures of Alfvén waves/fluctuations both upstream and downstream of the IP shock. This means that the IP shock is interacting with the ambient Alfvén waves/fluctuations. We further analyze the features of Alfvén fluctuations with the corresponding compressibility C_p (Figure 6(g)), and cross helicity σ_c (Figure 6(h)). The compressibility C_p is defined as $C_p(t) = \frac{\langle \delta N_p^2 \rangle}{\bar{N}_p^2} \frac{\bar{B}^2}{\langle \delta B \cdot \delta B \rangle}$ (Gary 1986; Yao et al. 2013; Zhao et al. 2021a), where \bar{N}_p is the mean proton density, \bar{B} is the mean magnetic field magnitude, δN_p is the fluctuation of the ambient proton density, and δB is the ambient magnetic field fluctuation. The cross helicity σ_c is defined as $\sigma_c(t) = \frac{2\langle \delta V \cdot \delta V_A \rangle}{\langle \delta V^2 + \delta V_A^2 \rangle}$ (Matthaeus & Goldstein 1982; Yao et al. 2013), where δV is the proton bulk velocity fluctuation and δV_A is the fluctuation of the ambient Alfvén velocity. Following similar procedures to those of Yao et al. (2013), we used a moving-time window width of 10 minutes to calculate the background quantities (mean values) and then the corresponding fluctuating quantities. Also, a moving-time step of 3 s was used for the calculations, so that C_p and σ_c were obtained for each 3 s time interval.

Upstream of the IP shock, for most of the time, σ_c is close to one, whereas C_p is close to zero, which indicates signatures of shear Alfvén waves. Since $\sigma_c > 0$ and the ambient magnetic field is in general sunward, the detected Alfvén waves purely propagate antisunward. Also, Figure 6(f) shows that the upstream plasma ($T_{\perp}/T_{\parallel} \sim 1.0$) inhibits ion mirror-mode and cyclotron instabilities. Downstream of the IP shock, (1) the IP shock shows evidence for preferentially perpendicular ion heating by the enhanced T_{\perp}/T_{\parallel} across the shock, so that the

T_{\perp}/T_{\parallel} values touch the threshold values of both the ion cyclotron and mirror-mode instabilities. Although the threshold values of the ion cyclotron instabilities are lower than the corresponding values of the ion mirror-mode instabilities, the presence of heavy ions in the solar wind ($n_{\alpha}/n_p \approx 5\%$ or even larger; see Figure 6(g)) should depress the ion cyclotron wave growth rate, which favors the mirror-mode growth (Price et al. 1986; Liu et al. 2006). Therefore, the shocked plasma downstream of the IP shock is marginally unstable to the mirror mode. (2) Especially, the fluctuations denoted by the region between the two dashed vertical blue lines show mirror-mode features, which is evidenced by the anticorrelated density and magnetic field magnitude fluctuations (Figure 6(a); Hubert et al. 1989; Liu et al. 2006; Zhao et al. 2019a) and the temperature anisotropy exceeding the mirror-mode onset condition (Figure 6(f)). Also, C_p is enhanced in the denoted large-scale structures than in the ambient plasma. (3) Meanwhile, downstream of the IP shock, σ_c has both positive and negative values, and the ambient magnetic field is still generally sunward. Therefore, Alfvén waves in the shocked plasma can be separated into two parts, one propagating sunward ($\sigma_c < 0$), and the other propagating antisunward ($\sigma_c > 0$), which gives direct observational evidence for the simulation results (e.g., Lu et al. 2009). This gives a similar picture that Alfvén waves striking the terrestrial bow shock should launch various disturbances into the magnetosheath, including both antisunward and sunward Alfvén fluctuations (e.g., Sibeck et al. 1997; Cable & Lin 1998; Matsuoka et al. 2000). Furthermore, σ_c varies from positive to negative in the denoted large-scale structures, which indicates that the sunward Alfvén waves may result from the interaction between the antisunward Alfvén waves and mirror-mode waves. This is similar to the process that the antisunward Alfvén waves interacting with the fast and/or slow magnetosonic waves contributes to the growth of the sunward Alfvén waves (e.g., Schwartz 1977; Lacombe & Mangeney 1980).

We checked the ion distribution functions (Figure 7) from the PESA-High instrument on board Wind/3DP to examine the ion dynamics at/around the IP shock interacting with Alfvén waves/fluctuations. The particle distributions have already been transformed into the solar wind bulk flow rest frame based on the proton bulk flow velocities measured by the PESA-Low/3DP instrument. The PESA particle detectors on board the Wind/3DP suite were designed to make measurements of three-dimensional low-energy (<30 keV) ion distributions (Lin et al. 1995). The PESA-Low instrument measures ions from as low as 100 eV to as high as 10 keV with 14 different energy channels, which is designed primarily to provide solar wind bulk properties (i.e., ion density, velocity, and temperature). The PESA-High instrument measures ions of 80 eV–30 keV at 15 different energies. The proton bulk velocity measurements by PESA-Low/3DP agree well with those determined by Wind/SWE Faraday Cups (Ogilvie et al. 1995). As shown in

B.3. Properties of A Supercritical Quasi-perpendicular Interplanetary Shock Propagating in Terrestrial Foreshock Region

THE ASTROPHYSICAL JOURNAL SUPPLEMENT SERIES, 263:11 (15pp), 2022 November

Liu et al.

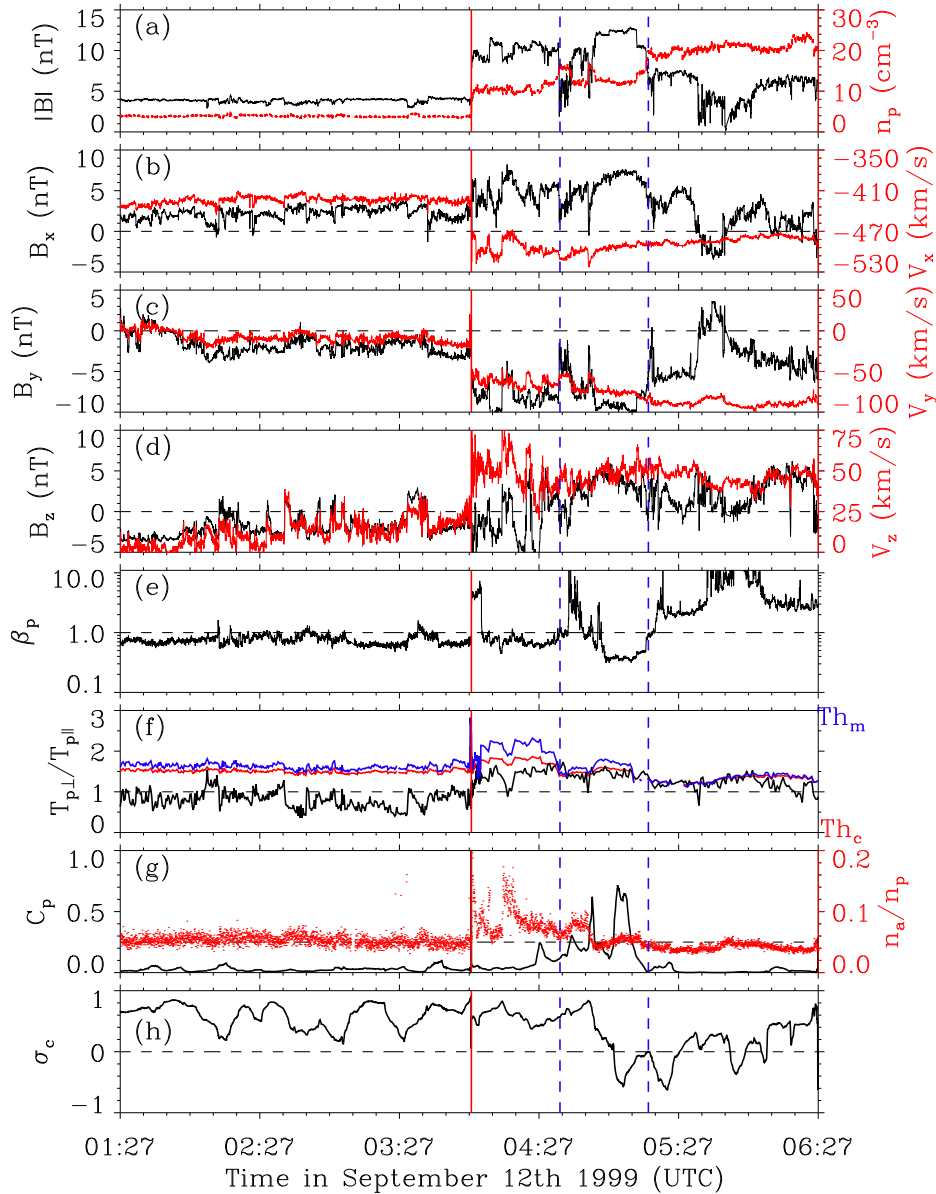


Figure 6. From top to bottom, the panels show (a) the comparison between the magnetic field strength and the proton number density, (b)–(d) the comparison between X (Y , Z) component of magnetic field and proton bulk velocity in the GSE coordinate, (e) the proton plasma β_p , (f) the proton temperature anisotropy (black) with thresholds of ion cyclotron (red) and mirror-mode (blue) instabilities for comparison, (g) the compressibility (black) and alpha abundance (red), and (h) the cross helicity, respectively. The vertical red line marks the IP shock propagating in the terrestrial foreshock region. The region denoted by the two dashed vertical blue lines downstream of the IP shock shows mirror-mode features. For the calculations of thresholds of ion cyclotron and mirror-mode instabilities, we refer to Liu et al. (2006) and references therein.

Figure 7(c), quite intense beam-like populations of gyrating ions (indicated by black arrows) are observed around the shock ramp, with velocities of about 450 km s^{-1} . The observed velocities of the gyrating ions are consistent with the theoretical values according to specular reflection theory (Gosling et al. 1982). The time range of Figure 7(c) covers part of the shock foot/precursor, ramp, and the overshoot structure (Figure 7(a)). The gyrating ions are observed in association with the magnetic foot and overshoot structure, consistent with previous theories/

simulations (e.g., Paschmann et al. 1980; Leroy et al. 1982) and observations (e.g., Paschmann et al. 1982; Sckopke et al. 1983; Thomsen et al. 1985). Similarly, Figure 7(d) gives evidence of gyrating ions behind the overshoot of the IP shock (indicated by black arrows). The velocity/density of the gyrating ions behind the overshoot of the IP shock is higher/lower than the corresponding values at the shock ramp. This is similar to the ion dynamics of the IP shock propagating inside an ICME (Liu et al. 2018) and in the ambient solar wind (Wilson et al. 2012).

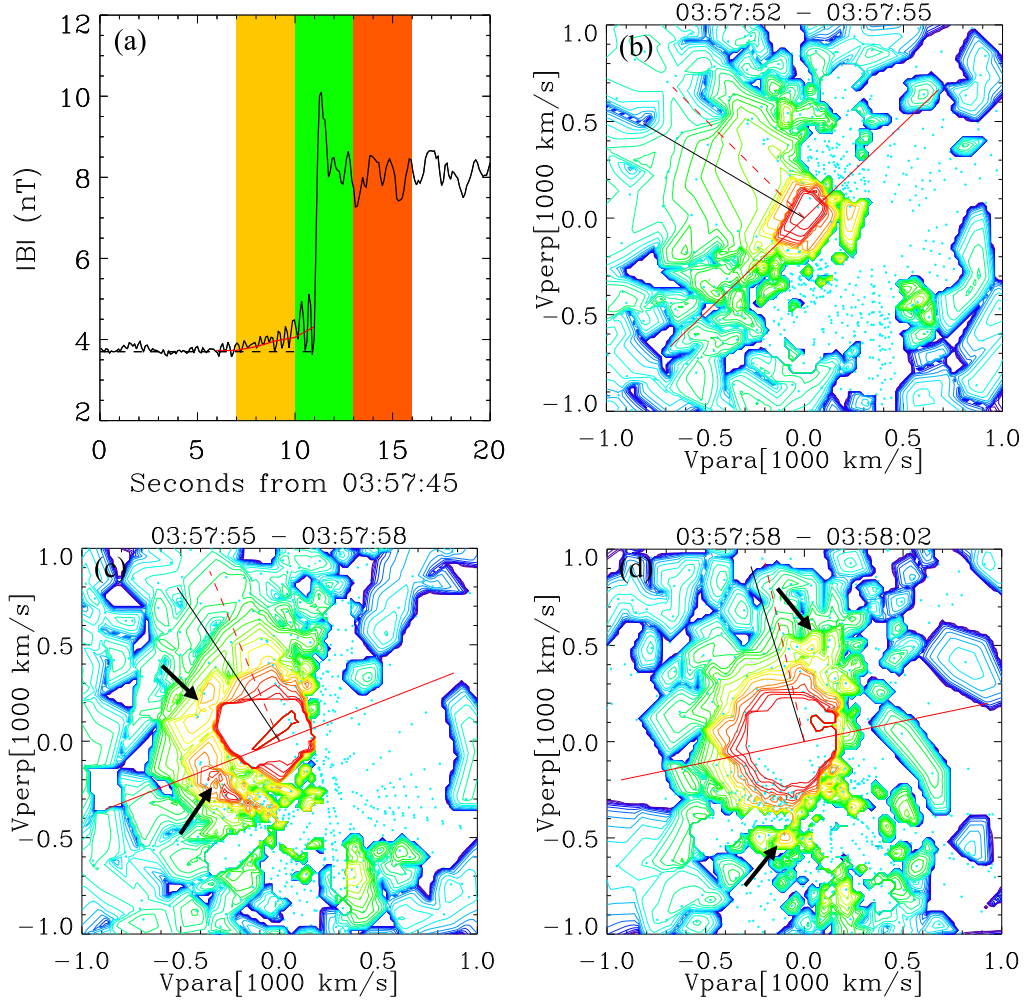


Figure 7. Evolution of the ion distributions (in the solar wind frame) across the shock ramp obtained from the PESA-High/3DP instrument. The solar wind bulk flow velocities, which are used to transform particle distributions into the bulk flow rest frame, were determined from the measurements by the PESA-Low/3DP instrument. (a) Plot of a 20 s window of the magnetic field magnitude (11 samples s^{-1}) around the IP shock. Foot-like magnetic enhancement (red curve) associated with precursor whistlers and magnetic overshoot can be clearly identified near the shock ramp. (b)–(d) Ion distributions corresponding to the time ranges of three color-coded shaded regions in panel (a). The contours show constant phase space density in the plane containing the ambient magnetic field (horizontal axis) and the local solar wind velocity. Projected onto the planes are the shock normal direction (dashed red line), the shock surface (solid red line), and the solar wind velocity direction (solid black line). Gyration ions are indicated by the black arrows.

Compared to another IP shock in the ambient solar wind ($M_f \sim 4.7$, $\theta_{Bn} = 82^\circ$; see Wilson et al. 2012), the current IP shock ($M_f \sim 2.1$, $\theta_{Bn} = 80^\circ$), which propagates within the terrestrial foreshock, is weaker but associated with more intense beam-like gyrating-reflected ions (Figure 7(c)).

3. Summary and Discussions

This paper reports a comprehensive analysis of the properties of an IP shock magnetically connected to the terrestrial bow shock. Key findings are obtained concerning how the IP shock modifies the terrestrial foreshock.

1. As expected, intense Langmuir waves and $2f_{pe}$ emissions are generally detected when the terrestrial foreshock electron beams are observed. It is quite striking that intensive bursty Langmuir waves are detected downstream

of the IP shock. They are likely driven by terrestrial foreshock electron beams penetrating the IP shock. Also, bursty Langmuir waves detected downstream of the IP shock are even more intensive than those upstream of the IP shock. Based on the statistics on the waves at/around the IP shocks, Wilson et al. (2007) showed that Langmuir waves frequently occur in the ramp region, whereas they are rarely detected downstream of the IP shocks. Our results indicate that Langmuir waves excited downstream of the IP shock depend on both the ambient upstream plasma (i.e., transient electron beams penetrating the IP shock) and the IP shock itself. We find that the intensity of the detected Langmuir waves is closely related to the energy of the electron beam and the corresponding ratio of the parallel to perpendicular electron flux. Across the IP shock, the energy of the dominant electron beam is higher

and the corresponding ratio of the parallel to perpendicular electron flux is enhanced, which coincides with the more intensive Langmuir waves.

2. Oblique precursor whistlers are observed around the IP shock, associated with the whistler heat flux instabilities. Whistler heat flux instabilities contribute to the pitch-angle scattering of the suprathermal electrons (both the terrestrial foreshock electrons and strahl electrons from the Sun), together with the normal betatron acceleration that occurs across the shock. This is similar to the picture of the disappearance of bidirectional electrons downstream of an IP shock inside an ICME (Liu et al. 2018).
3. The IP shock is interacting with the Alfvén waves/fluctuations detected in the terrestrial foreshock region. Upstream of the IP shock, Alfvén waves/fluctuations are incompressible and purely propagate antisunward. In contrast, downstream of the IP shock, the shocked plasma shows both Alfvénic and mirror-mode features. Alfvén waves/fluctuations are separated into two parts, one part that propagates sunward, and the other that propagates antisunward, which may be due to the interaction between the Alfvén waves/fluctuations and the mirror-mode waves.
4. Specularly reflected gyrating ions are detected based on the particle distribution, which covers the magnetic foot, ramp, and overshoot structures. This is consistent with the specular reflection theory prediction, and provides evidence that the reflected ions may provide energy dissipation for a supercritical quasi-perpendicular IP Shock (Paschmann et al. 1980; Leroy et al. 1982). We note that more intense beam-like gyrating-reflected ions are associated with the present IP shock ($M_f \sim 2.1$, $\theta_{Bn} = 80^\circ$), compared to those reflected by another IP shock in the ambient solar wind ($M_f \sim 4.7$, $\theta_{Bn} = 82^\circ$; see Wilson et al. 2012). This may be partly explained by the interaction between the IP shock and the upstream Alfvén waves/fluctuations (present within the terrestrial foreshock region), which can generate some rippling at the IP shock front (e.g., Lu et al. 2009). This additional rippling can modify the dynamics of the gyrating ions reflected by the IP shock and lead to some diffusion. A detailed analysis of this interaction requires further investigation.

In summary, this work provides deeper insights into how an IP shock modifies the terrestrial foreshock region via wave analysis and particle distributions. Recent observations from the Parker Solar Probe (Fox et al. 2016) show that the pristine solar wind in the inner heliosphere is highly Alfvénic (e.g., Kasper et al. 2019; Bale et al. 2019; Huang et al. 2020; Zhao et al. 2021a). Also, very many Langmuir waves were detected in the free pristine solar wind (e.g., Bale et al. 2019; Jagarlamudi et al. 2021), which indicates the presence of the transient electron beams near the Sun. The Sun has become more and more active since 2021, and more IP shocks driven by solar eruptions are expected to be observed in the inner heliosphere. The IP shocks near the Sun will interact with Alfvén waves/fluctuations and the transient electron beams in the free pristine solar wind. Therefore, present results may also provide some hints on the properties of IP shocks interacting with Alfvén waves/fluctuations and transient electron beams near the Sun.

M.L. acknowledges Milan Maksimovic, Karl-Ludwig Klein, and Carine Briand for helpful discussions. The research was supported by the CNES and DIM ACAV+ PhD funding in France. Z.Y. was supported by the project of Civil Aerospace “13th Five Year Plan” Preliminary Research in Space Science (Nos. D020301 and D030202) and NSFC under grants 42274210 and 42188101. Y.D.L. was supported by NSFC under grants 41774179 and 42274201, the Specialized Research Fund for State Key Laboratories of China, the CAS Strategic Priority Program on Space Science (XDA15018500), and National Key R&D Program of China (No. 2021YFA0718600). We acknowledge the use of data from Wind/MFI (<https://spdf.gsfc.nasa.gov/pub/data/wind/mfi/>) and Wind/3DP (<http://sprg.ssl.berkeley.edu/wind3dp/>). The authors acknowledge CNES (Centre National d’Études Spatiales), CNRS (Centre National de la Recherche Scientifique), and Observatoire de Paris for support to the Wind/WAVES team and the CDPP (Centre de Données de la Physique des Plasmas) for the provision of the Wind/WAVES data.

Appendix A Source of the Transient Electron Beam

In Section 2.1, Figures 2(b)–(e) show that the transient electron flux enhancements around the IP shock mainly come from the direction parallel to the ambient magnetic field. In this context, the ambient magnetic field is in general directed sunward, therefore the parallel electron flux enhancements should come from the terrestrial bow shock. However, the ambient magnetic field rotates slightly, which may change the situation. In Figure 8, we compare the parallel (antiparallel) electron flux with the sunward (antisunward) electron flux. The sunward electron flux is calculated based on the similar technique to calculate the electron PADs. When calculating the parallel (and/or antiparallel) electron flux, the ambient magnetic field vectors are used to calculate the electron pitch angles. In contrast, the sunward unit vector $[1, 0, 0]$ in the GSE coordinate is used to calculate the proxy electron pitch angles and then the sunward (antisunward) electron flux.

Specifically, both Figures 2(b)–(e) and Figure 8 present the measurements derived by the EESA-Low/3DP instrument (Lin et al. 1995). The EESA particle detectors on board the Wind/3DP were designed to make measurements of three-dimensional low-energy (<30 keV) electron distributions. The EESA-Low analyzer covers the energy range from 3 eV to 1.1 keV, whereas the EESA-High analyzer detects electrons of 300 eV to 30 keV. Both instruments have operational fields of view of $180^\circ \times 14^\circ$ and 15 logarithmically spaced energy channels. Each detector sweeps out $4 \times \pi$ steradians in space to give a full distribution in one spacecraft spin (with the spin period being 3 s). The data are combined on board with 88 angular bins for both instruments.

We note that all particle data shown herein have been transformed from the spacecraft into the solar wind bulk flow rest reference frame using the proton bulk velocities measured by the PESA-Low/3DP instrument. For each energy bin, eight pitch-angle (or the proxy ones) bins are defined to calculate the resulting distributions. For example, the mean values of eight defined pitch-angle bins are $[14^\circ, 35^\circ, 57^\circ, 79^\circ, 101^\circ, 123^\circ, 145^\circ, \text{ and } 165^\circ]$. The derived distributions are summed and then averaged over each two consecutive defined pitch-angle bins. As a result, the parallel direction covers 14° – 35° , the perpendicular direction covers 79° – 101° ,

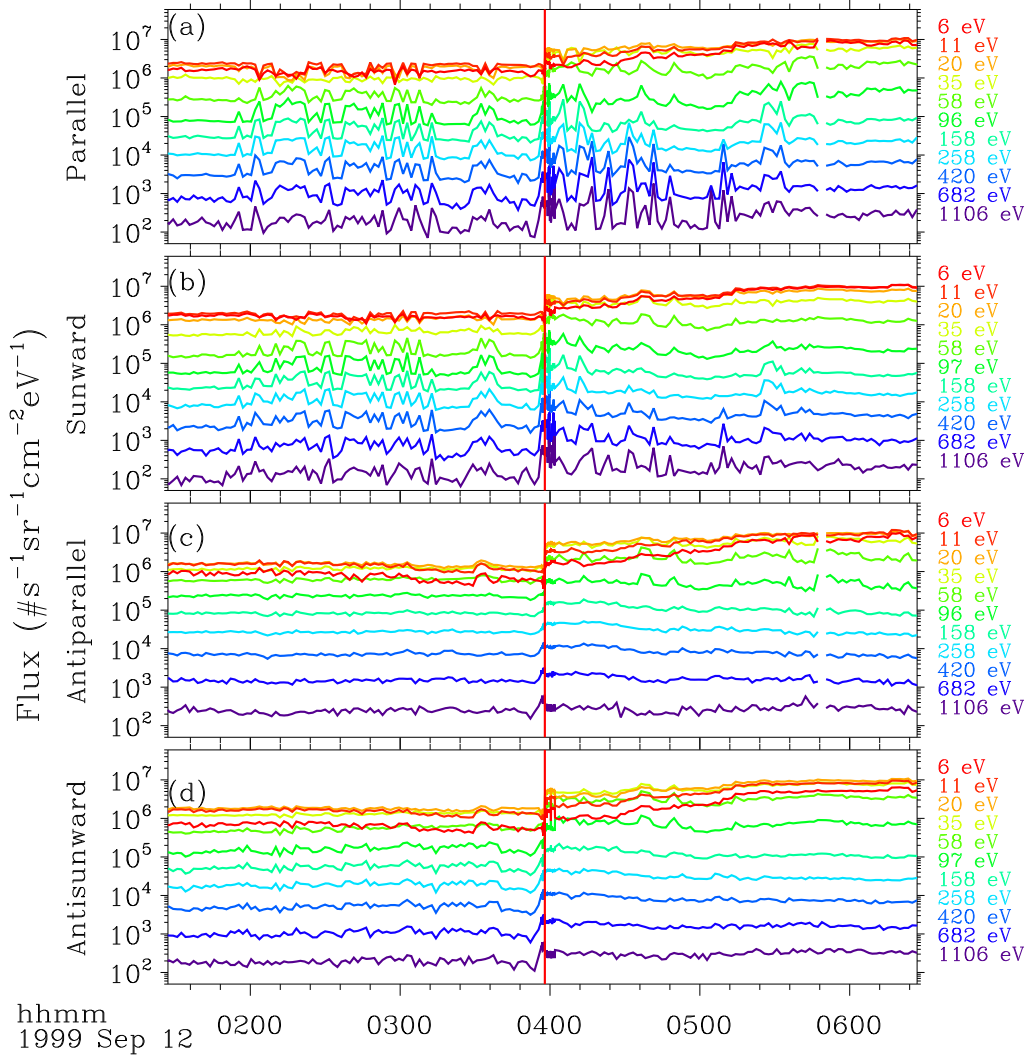


Figure 8. Five-hour expanded view of electron flux measurements from the EESA-Low instrument on board Wind/3DP around the IP shock. From top to bottom, the panels show electron flux (from about 6 to 1106 eV) in parallel, sunward, antiparallel, and antisunward directions, respectively. The labeled energies have been corrected by considering the spacecraft potential. The vertical red line marks the time when the IP shock was detected.

and the antiparallel direction covers 145° – 165° . The sunward and antisunward electron flux are defined in a similar way. Moreover, the EESA-Low measurements have been corrected by considering the effects of the spacecraft floating potential. We estimate the spacecraft potential following the previous methods/procedures outlined in Salem et al. (2001). Only measurements from the energy channels higher than the estimated spacecraft potential are shown. The labeled energies are the mean values of the corresponding energy channels after correcting the estimated spacecraft potential. Figures 8(a)–(b) show a clear concurrence of the parallel electron flux enhancements and the sunward electron flux enhancements. Also, both the antiparallel and antisunward electron flux are relatively quiet (see Figures 8(c)–(d)). Therefore, we confirm that the transient parallel electron flux enhancements should exclusively come from the terrestrial bow shock.

Appendix B Exclusion of IP Shock as a Source

Previous investigations (e.g., Bale et al. 1999; Pulupa & Bale 2008) showed that the foreshock electrons of a quasi-perpendicular IP shock can cause increases in both the parallel and antiparallel electron flux in front of the shock surface. Furthermore, the timespan of such an IP electron foreshock region observed by the spacecraft is usually shorter than one minute. Therefore, such IP foreshock electrons likely do not contribute to the transient electron flux enhancements mentioned in Appendix A. IP foreshock electrons may nevertheless affect the analysis in Section 2.2. As a result, we need to verify whether Wind detected such IP foreshock electrons. Based on the burst-mode particle data set, Figure 9 shows that no apparent increases are observed in electron flux in either the parallel (sunward) or antiparallel (antisunward) directions

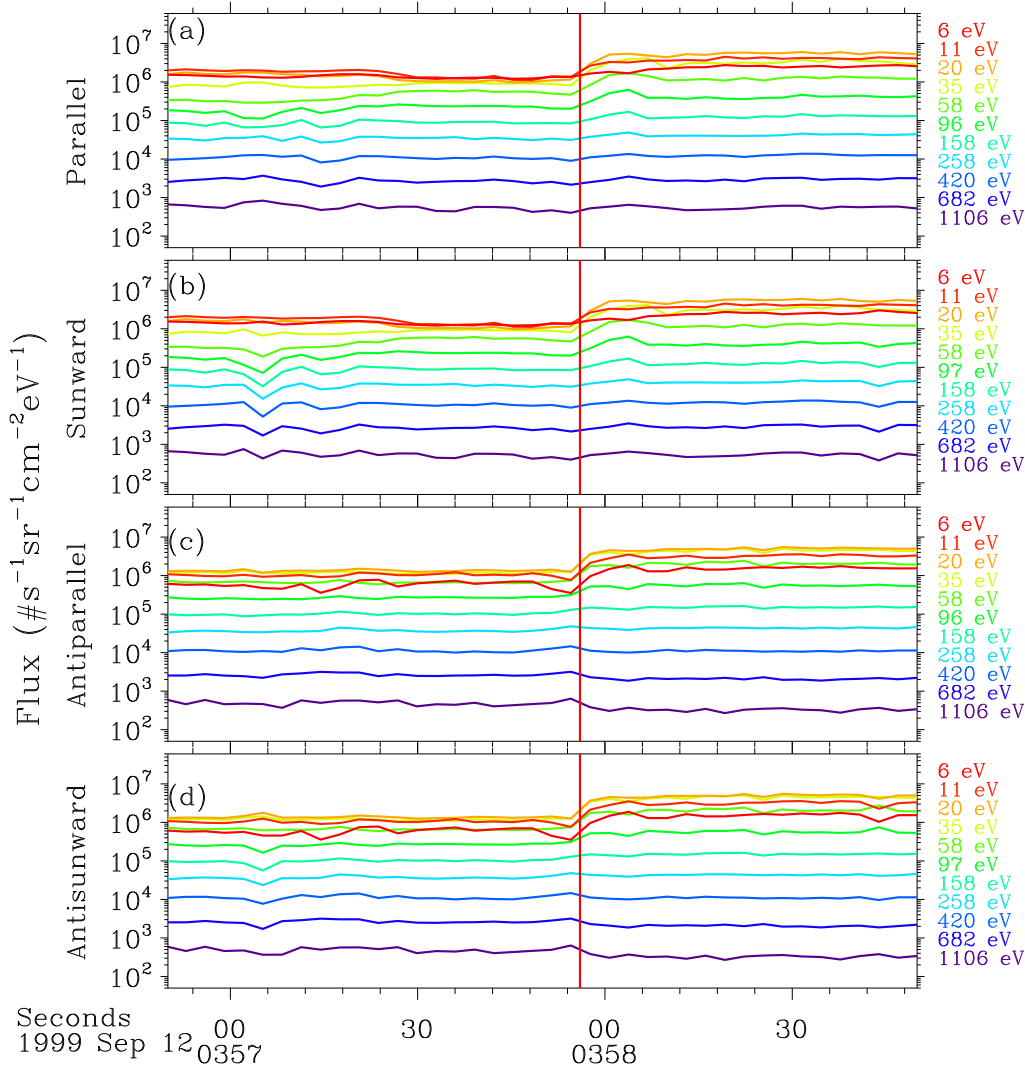


Figure 9. Same as Figure 8, but for a 2-minute expanded view of electron flux measurements around the IP shock. Note that only the burst-mode particle data set is considered in this plot.

upstream of the IP shock. Therefore, we conclude that the IP foreshock electrons likely did not pass Wind.

ORCID iDs

Mingzhe Liu <https://orcid.org/0000-0003-2981-0544>
 Zhongwei Yang <https://orcid.org/0000-0002-1509-1529>
 Ying D. Liu <https://orcid.org/0000-0002-3483-5909>
 Bertrand Lembège <https://orcid.org/0000-0002-5528-0228>
 Karine Issautier <https://orcid.org/0000-0002-2757-101X>
 L. B. Wilson III <https://orcid.org/0000-0002-4313-1970>
 Siqi Zhao <https://orcid.org/0000-0003-4268-7763>
 Vamsee Krishna Jagarlamudi <https://orcid.org/0000-0002-4313-1970>
 Xiaowei Zhao <https://orcid.org/0000-0002-4016-5710>
 Jia Huang <https://orcid.org/0000-0002-9954-4707>
 Nicolina Chrysaphi <https://orcid.org/0000-0002-4389-5540>

References

- Bale, S. D., Badman, S. T., Bonnell, J. W., et al. 2019, *Natur*, 576, 237
 Bale, S. D., Larson, D. E., Lin, R. P., et al. 2000, *JGR*, 105, 27353
 Bale, S. D., Reiner, M. J., Bougeret, J. L., et al. 1999, *GeoRL*, 26, 1573
 Bougeret, J. L., Kaiser, M. L., Kellogg, P. J., et al. 1995, *SSRv*, 71, 231
 Cable, S., & Lin, Y. 1998, *GeoRL*, 25, 1821
 Fox, N. J., Velli, M. C., Bale, S. D., et al. 2016, *SSRv*, 204, 7
 Gary, S. P. 1986, *JPIPh*, 35, 431
 Gary, S. P., Skoug, R. M., & Daughton, W. 1999, *PhPI*, 6, 2607
 Goncharov, O., Koval, A. Á., Afránková, J., et al. 2018, *JGRA*, 123, 3822
 Gosling, J. T., Baker, D. N., Bame, S. J., et al. 1987, *JGR*, 92, 8519
 Gosling, J. T., Thomsen, M. F., Bame, S. J., et al. 1982, *GeoRL*, 9, 1333
 Grogard, R. J. M. 1975, *AuJPh*, 28, 731
 Hoang, S., Lacombe, C., MacDowall, R. J., & Thejappa, G. 2007, *JGRA*, 112, A09102
 Huang, J., Kasper, J. C., Stevens, M., et al. 2020, arXiv:2005.12372
 Hubert, D., Perche, C., Harvey, C. C., Lacombe, C., & Russell, C. T. 1989, *GeoRL*, 16, 159
 Issautier, K., Perche, C., Hoang, S., et al. 2005, *AdSpR*, 35, 2141

- Jagarlamudi, V. K., Dudok de Wit, T., Froment, C., et al. 2021, *A&A*, **650**, A9
- Kasaba, Y., Matsumoto, H., Omura, Y., et al. 2000, *JGR*, **105**, 79
- Kasper, J. C., Bale, S. D., Belcher, J. W., et al. 2019, *Natur*, **576**, 228
- Khrabrov, A. V., & Sonnerup, B. U. Ö. 1998, *JGR*, **103**, 6641
- Lacombe, C., & Mangeney, A. 1980, *A&A*, **88**, 277
- Lembege, B., Giacalone, J., Scholer, M., et al. 2004, *SSRv*, **110**, 161
- Lembège, B., & Savoini, P. 2002, *JGRA*, **107**, 1037
- Lepping, R. P., Acuña, M. H., Burlaga, L. F., et al. 1995, *SSRv*, **71**, 207
- Leroy, M. M., Winske, D., Goodrich, C. C., Wu, C. S., & Papadopoulos, K. 1982, *JGR*, **87**, 5081
- Lin, R. P., Anderson, K. A., Ashford, S., et al. 1995, *SSRv*, **71**, 125
- Liu, M., Liu, Y. D., Yang, Z., Wilson, L. B., III, & Hu, H. 2018, *ApJL*, **859**, L4
- Liu, Y., Richardson, J. D., Belcher, J. W., Kasper, J. C., & Skoug, R. M. 2006, *JGR*, **111**, A09108
- Liu, Y. D., Luhmann, J. G., Kajdič, P., et al. 2014b, *NatCo*, **5**, 3481
- Liu, Y. D., Luhmann, J. G., Möstl, C., et al. 2012, *ApJL*, **746**, L15
- Liu, Y. D., Yang, Z., Wang, R., et al. 2014a, *ApJL*, **793**, L41
- Lu, Q., Hu, Q., & Zank, G. P. 2009, *ApJ*, **706**, 687
- Lugaz, N., Farrugia, C. J., Smith, C. W., & Paulson, K. 2015, *JGRA*, **120**, 2409
- Mace, R. L., & Sydora, R. D. 2010, *JGR*, **115**, A07206
- Matsumoto, H., Kojima, H., Kasaba, Y., et al. 1997, *AdSpR*, **20**, 683
- Matsuoka, A., Southwood, D. J., Kokubun, S., & Mukai, T. 2000, *JGR*, **105**, 18,361
- Matthaeus, W. H., & Goldstein, M. L. 1982, *JGR*, **87**, 6011
- McKenzie, J. F., & Westphal, K. O. 1969, *P&SS*, **17**, 1029
- Mellott, M. M., & Greenstadt, E. W. 1984, *JGR*, **89**, 2151
- Meyer-Vernet, N., Issautier, K., & Moncuquet, M. 2017, *JGRA*, **122**, 7925
- Meyer-Vernet, N., & Perche, C. 1989, *JGR*, **94**, 2405
- Möstl, C., Farrugia, C. J., Kilpua, E. K. J., et al. 2012, *ApJ*, **758**, 10
- Ogilvie, K. W., Chornay, D. J., Fritzenreiter, R. J., et al. 1995, *SSRv*, **71**, 55
- Parks, G. K., Lee, E., Fu, S. Y., et al. 2017, *RvMPP*, **1**, 1
- Paschmann, G., Scokopke, N., Asbridge, J. R., Bame, S. J., & Gosling, J. T. 1980, *JGR*, **85**, 4689
- Paschmann, G., Scokopke, N., Bame, S. J., & Gosling, J. T. 1982, *GeoRL*, **9**, 881
- Peredo, M., Slavin, J. A., Mazur, E., & Curtis, S. A. 1995, *JGR*, **100**, 7907
- Price, C. P., Swift, D. W., & Lee, L. C. 1986, *JGR*, **91**, 101
- Pulupa, M., & Bale, S. D. 2008, *ApJ*, **676**, 1330
- Pulupa, M., Bale, S. D., Opitz, A., et al. 2012, arXiv:1202.3678
- Pulupa, M. P., Bale, S. D., & Salem, C. 2011, *GeoRL*, **38**, L14105
- Přech, L., Němeček, Z., & Šafránková, J. 2009, *EP&S*, **61**, 610
- Reiner, M. J., Kaiser, M. L., Fainberg, J., Desch, M. D., & Stone, R. G. 1996, *GeoRL*, **23**, 1247
- Roelof, E. C., & Sibeck, D. G. 1993, *JGR*, **98**, 21421
- Šafránková, J., Němeček, Z., Přech, L., et al. 2007a, *P&SS*, **55**, 2324
- Šafránková, J., Němeček, Z., Přech, L., et al. 2007b, *JGRA*, **112**, A08212
- Saito, S., & Umeda, T. 2011, *ApJ*, **736**, 35
- Salem, C., Bosqued, J. M., Larson, D. E., et al. 2001, *JGR*, **106**, 21701
- Savoini, P., & Lembège, B. 2001, *JGR*, **106**, 12975
- Savoini, P., & Lembège, B. 2009, AGUFM, SH31A–1470
- Schwartz, S. J. 1977, *MNRAS*, **178**, 399
- Scokopke, N., Paschmann, G., Bame, S. J., Gosling, J. T., & Russell, C. T. 1983, *JGR*, **88**, 6121
- Sibeck, D. G., Takahashi, K., Kokubun, S., et al. 1997, *GeoRL*, **24**, 3133
- Thomsen, M. F., Gosling, J. T., Bame, S. J., & Russell, C. T. 1985, *JGR*, **90**, 267
- Vinas, A. F., & Scudder, J. D. 1986, *JGR*, **91**, 39
- Wang, X., Tu, C., Wang, L., He, J., & Marsch, E. 2015, *GeoRL*, **42**, 3654
- Wilson, L. B. 2016, *GMS*, **216**, 269
- Wilson, L. B. I., Brosius, A. L., Gopalswamy, N., et al. 2021, *RvGeo*, **59**, e2020RG000714
- Wilson, L. B., III, Cattell, C., Kellogg, P. J., et al. 2007, *PhRvL*, **99**, 041101
- Wilson, L. B., III, Cattell, C. A., Kellogg, P. J., et al. 2009, *JGRA*, **114**, A10106
- Wilson, L. B., III, Koval, A., Szabo, A., et al. 2012, *GeoRL*, **39**, L08109
- Wilson, L. B., III, Koval, A., Szabo, A., et al. 2017, *JGRA*, **122**, 9115
- Yang, Z., Lu, Q., Liu, Y. D., & Wang, R. 2018, *ApJ*, **857**, 36
- Yang, Z. W., Lembège, B., & Lu, Q. M. 2012, *JGRA*, **117**, A07222
- Yao, S., He, J. S., Tu, C. Y., Wang, L. H., & Marsch, E. 2013, *ApJ*, **774**, 59
- Yoon, P. H., Wu, C. S., Vinas, A. F., et al. 1994, *JGR*, **99**, 481
- Zhao, S. Q., Xiao, C. J., Liu, T. Z., et al. 2021b, *JGRA*, **126**, e28525
- Zhao, S. Q., Xiao, C. J., Wang, X. G., et al. 2019a, *JGRA*, **124**, 200
- Zhao, S. Q., Yan, H., Liu, T. Z., Liu, M., & Shi, M. 2021a, *ApJ*, **923**, 253
- Zhao, X., Liu, Y. D., Hu, H., & Wang, R. 2019b, *ApJ*, **882**, 122

Bibliography

- Abhyankar, K. D. (1977). « A Survey of the Solar Atmospheric Models ». *Bulletin of the Astronomical Society of India* 5, p. 40 (cit. on p. 2).
- Abraham, Joel B. et al. (2022). « Radial Evolution of Thermal and Suprathermal Electron Populations in the Slow Solar Wind from 0.13 to 0.5 au: Parker Solar Probe Observations ». *ApJ* 931.2, 118, p. 118. DOI: [10.3847/1538-4357/ac6605](https://doi.org/10.3847/1538-4357/ac6605). arXiv: [2204.05001](https://arxiv.org/abs/2204.05001) [astro-ph.SR] (cit. on pp. 66, 67).
- Abramowitz, M. and Stegun, I. A. (1972). *Handbook of Mathematical Functions* (cit. on p. 97).
- Alfvén, H. (1947). « Magneto hydrodynamic waves, and the heating of the solar corona ». *MNRAS* 107, p. 211. DOI: [10.1093/mnras/107.2.211](https://doi.org/10.1093/mnras/107.2.211) (cit. on p. 11).
- Alterman, B. L. and Kasper, Justin C. (2019). « Helium Variation across Two Solar Cycles Reveals a Speed-dependent Phase Lag ». *ApJL* 879.1, L6, p. L6. DOI: [10.3847/2041-8213/ab2391](https://doi.org/10.3847/2041-8213/ab2391). arXiv: [1906.12273](https://arxiv.org/abs/1906.12273) [physics.space-ph] (cit. on p. 44).
- Alterman, B. L. et al. (2018). « A Comparison of Alpha Particle and Proton Beam Differential Flows in Collisionally Young Solar Wind ». *ApJ* 864.2, 112, p. 112. DOI: [10.3847/1538-4357/aad23f](https://doi.org/10.3847/1538-4357/aad23f). arXiv: [1809.01693](https://arxiv.org/abs/1809.01693) [astro-ph.SR] (cit. on pp. 6, 53, 54, 109).
- Alterman, B. L. et al. (2020). « Helium Abundance Heralds the Onset of Solar Cycle 25 ». *arXiv e-prints*, arXiv:2006.04669, arXiv:2006.04669. arXiv: [2006.04669](https://arxiv.org/abs/2006.04669) [astro-ph.SR] (cit. on pp. 11, 12, 44, 45).
- Andreopoulos, Yiannis, Agui, Juan H., and Briassulis, George (2000). « Shock Wave – Turbulence Interactions ». *Annual Review of Fluid Mechanics* 32, pp. 309–345. DOI: [10.1146/annurev.fluid.32.1.309](https://doi.org/10.1146/annurev.fluid.32.1.309) (cit. on p. 14).
- Aptekar, R. L. et al. (1995). « Konus-W Gamma-Ray Burst Experiment for the GGS Wind Spacecraft ». *SSRv* 71, pp. 265–272. DOI: [10.1007/BF00751332](https://doi.org/10.1007/BF00751332) (cit. on p. 39).
- Asbridge, J. R., Bame, S. J., and Feldman, W. C. (1974). « Abundance Differences in Solar Wind Double Streams ». *SoPh* 37.2, pp. 451–467. DOI: [10.1007/BF00152503](https://doi.org/10.1007/BF00152503) (cit. on p. 6).
- Bale, S. D. et al. (1996). « Phase coupling in Langmuir wave packets: Possible evidence of three-wave interactions in the upstream solar wind ». *Geophys. Res. Lett.* 23.1, pp. 109–112. DOI: [10.1029/95GL03595](https://doi.org/10.1029/95GL03595) (cit. on pp. 20, 39).
- Bale, S. D. et al. (1998). « Transverse z-mode waves in the terrestrial electron foreshock ». *Geophys. Res. Lett.* 25.1, pp. 9–12. DOI: [10.1029/97GL03493](https://doi.org/10.1029/97GL03493) (cit. on pp. 20, 39).
- Bale, S. D. et al. (1999). « The source region of an interplanetary type II radio burst ». *Geophys. Res. Lett.* 26.11, pp. 1573–1576. DOI: [10.1029/1999GL900293](https://doi.org/10.1029/1999GL900293) (cit. on pp. 20, 35, 39, 79, 94, 111).
- Bale, S. D. et al. (2000). « On the beam speed and wavenumber of intense electron plasma waves near the foreshock edge ». *J. Geophys. Res.* 105.A12, pp. 27353–27368. DOI: [10.1029/2000JA900042](https://doi.org/10.1029/2000JA900042) (cit. on pp. 22, 75).
- Bale, S. D. et al. (2002). « Electrostatic Turbulence and Debye-Scale Structures Associated with Electron Thermalization at Collisionless Shocks ». *ApJL* 575.1, pp. L25–L28. DOI: [10.1086/342609](https://doi.org/10.1086/342609) (cit. on pp. 20, 39).
- Bale, S. D. et al. (2005). « Measurement of the Electric Fluctuation Spectrum of Magnetohydrodynamic Turbulence ». *PhRvL* 94.21, 215002, p. 215002. DOI: [10.1103/PhysRevLett.94.215002](https://doi.org/10.1103/PhysRevLett.94.215002). arXiv: [physics/0503103](https://arxiv.org/abs/physics/0503103) [physics.space-ph] (cit. on p. 14).
- Bale, S. D. et al. (2008). « The Electric Antennas for the STEREO/WAVES Experiment ». *SSRv* 136.1-4, pp. 529–547. DOI: [10.1007/s11214-007-9251-x](https://doi.org/10.1007/s11214-007-9251-x) (cit. on pp. 25, 34).
- Bale, S. D. et al. (2016). « The FIELDS Instrument Suite for Solar Probe Plus. Measuring the Coronal Plasma and Magnetic Field, Plasma Waves and Turbulence, and Radio Signatures of Solar Transients ». *SSRv* 204.1-4, pp. 49–82. DOI: [10.1007/s11214-016-0244-5](https://doi.org/10.1007/s11214-016-0244-5) (cit. on pp. 29–31, 33, 42, 67).

- Bale, S. D. et al. (2019). « Highly structured slow solar wind emerging from an equatorial coronal hole ». *Nature* 576.7786, pp. 237–242. DOI: [10.1038/s41586-019-1818-7](https://doi.org/10.1038/s41586-019-1818-7) (cit. on pp. 25, 33, 36, 65, 92, 112).
- Balikhin, Michael and Gedalin, Michael (2022). « Collisionless Shocks in the Heliosphere: Foot Width Revisited ». *ApJ* 925.1, 90, p. 90. DOI: [10.3847/1538-4357/ac3bb3](https://doi.org/10.3847/1538-4357/ac3bb3) (cit. on p. 16).
- Bemporad, A. (2017). « Exploring the Inner Acceleration Region of Solar Wind: A Study Based on Coronagraphic UV and Visible Light Data ». *ApJ* 846.1, 86, p. 86. DOI: [10.3847/1538-4357/aa7de4](https://doi.org/10.3847/1538-4357/aa7de4) (cit. on pp. 69, 72, 110).
- Berčić, L. et al. (2019). « Scattering of strahl electrons in the solar wind between 0.3 and 1 au: Helios observations ». *MNRAS* 486.3, pp. 3404–3414. DOI: [10.1093/mnras/stz1007](https://doi.org/10.1093/mnras/stz1007). arXiv: [1904.08272](https://arxiv.org/abs/1904.08272) [physics.space-ph] (cit. on pp. 8, 9).
- Berčić, Laura et al. (2020). « Coronal Electron Temperature Inferred from the Strahl Electrons in the Inner Heliosphere: Parker Solar Probe and Helios Observations ». *ApJ* 892.2, 88, p. 88. DOI: [10.3847/1538-4357/ab7b7a](https://doi.org/10.3847/1538-4357/ab7b7a). arXiv: [2003.04016](https://arxiv.org/abs/2003.04016) [astro-ph.SR] (cit. on pp. 8, 9, 64, 66, 67, 71, 72, 110).
- Bessho, N. et al. (2019). « Magnetic Reconnection in a Quasi-Parallel Shock: Two-Dimensional Local Particle-in-Cell Simulation ». *Geophys. Res. Lett.* 46.16, pp. 9352–9361. DOI: [10.1029/2019GL083397](https://doi.org/10.1029/2019GL083397) (cit. on p. 14).
- Birmingham, T. J. et al. (1981). « Observations of electron gyroharmonic waves and the structure of the 10 torus ». *J. Geophys. Res.* 86.A10, pp. 8497–8507. DOI: [10.1029/JA086iA10p08497](https://doi.org/10.1029/JA086iA10p08497) (cit. on p. 24).
- Bordoni, F. (1971). « Channel electron multiplier efficiency for 10-1000 eV electrons ». *Nuclear Instruments and Methods* 97.2, pp. 405–408. DOI: [10.1016/0029-554X\(71\)90300-4](https://doi.org/10.1016/0029-554X(71)90300-4) (cit. on p. 31).
- Bougeret, J. -L. et al. (1995). « Waves: The Radio and Plasma Wave Investigation on the Wind Spacecraft ». *SSRv* 71.1-4, pp. 231–263. DOI: [10.1007/BF00751331](https://doi.org/10.1007/BF00751331) (cit. on pp. 34, 38–40, 76).
- Bougeret, J. L. et al. (2008). « S/WAVES: The Radio and Plasma Wave Investigation on the STEREO Mission ». *SSRv* 136.1-4, pp. 487–528. DOI: [10.1007/s11214-007-9298-8](https://doi.org/10.1007/s11214-007-9298-8) (cit. on pp. 25, 34).
- Bowen, T. A. et al. (2020). « A Merged Search-Coil and Fluxgate Magnetometer Data Product for Parker Solar Probe FIELDS ». *Journal of Geophysical Research (Space Physics)* 125.5, e27813, e27813. DOI: [10.1029/2020JA027813](https://doi.org/10.1029/2020JA027813). arXiv: [2001.04587](https://arxiv.org/abs/2001.04587) [astro-ph.IM] (cit. on p. 30).
- Briand, C. (2015). « Langmuir waves across the heliosphere ». *Journal of Plasma Physics* 81.2, 325810204, p. 325810204. DOI: [10.1017/S0022377815000112](https://doi.org/10.1017/S0022377815000112) (cit. on p. 25).
- Broggini, Carlo (2003). « Nuclear Processes at Solar Energy ». *Physics in Collision*. Ed. by I. Antoniou, V. A. Sadovnichy, and H. Walther, p. 21. arXiv: [astro-ph/0308537](https://arxiv.org/abs/astro-ph/0308537) [astro-ph] (cit. on p. 2).
- Brown, Larry W. (1973). « The Galactic Radio Spectrum Between 130 and 2600kHz ». *ApJ* 180, pp. 359–370. DOI: [10.1086/151968](https://doi.org/10.1086/151968) (cit. on p. 24).
- Burch, J. L. et al. (2016). « Electron-scale measurements of magnetic reconnection in space ». *Science* 352, aaf2939, aaf2939. DOI: [10.1126/science.aaf2939](https://doi.org/10.1126/science.aaf2939) (cit. on p. 14).
- Burlaga, L. F. (1971). « Hydromagnetic Waves and Discontinuities in the Solar Wind ». *SSRv* 12.5, pp. 600–657. DOI: [10.1007/BF00173345](https://doi.org/10.1007/BF00173345) (cit. on p. 16).
- Burlaga, L. F. et al. (2005). « Crossing the Termination Shock into the Heliosheath: Magnetic Fields ». *Science* 309.5743, pp. 2027–2029. DOI: [10.1126/science.1117542](https://doi.org/10.1126/science.1117542) (cit. on pp. 4, 17).
- Burlaga, L. F. et al. (2008). « Magnetic fields at the solar wind termination shock ». *Nature* 454.7200, pp. 75–77. DOI: [10.1038/nature07029](https://doi.org/10.1038/nature07029) (cit. on pp. 4, 17).
- Cable, S. and Lin, Y. (1998). « MHD simulations of oppositely propagating Alfvén waves in the magnetosheath and solar wind ». *Geophys. Res. Lett.* 25.11, pp. 1821–1824. DOI: [10.1029/98GL01397](https://doi.org/10.1029/98GL01397) (cit. on p. 89).
- Cane, H. V. (1979). « Spectra of the non-thermal radio radiation from the galactic polar regions. » *MNRAS* 189, pp. 465–478. DOI: [10.1093/mnras/189.3.465](https://doi.org/10.1093/mnras/189.3.465) (cit. on p. 59).
- Case, A. W. et al. (2020). « The Solar Probe Cup on the Parker Solar Probe ». *ApJS* 246.2, 43, p. 43. DOI: [10.3847/1538-4365/ab5a7b](https://doi.org/10.3847/1538-4365/ab5a7b). arXiv: [1912.02581](https://arxiv.org/abs/1912.02581) [astro-ph.IM] (cit. on pp. 30, 42–44, 51, 57, 68, 103).
- Chandran, Benjamin D. G. and Hollweg, Joseph V. (2009). « Alfvén Wave Reflection and Turbulent Heating in the Solar Wind from 1 Solar Radius to 1 AU: An Analytical Treatment ». *ApJ* 707.2, pp. 1659–1667. DOI: [10.1088/0004-637X/707/2/1659](https://doi.org/10.1088/0004-637X/707/2/1659). arXiv: [0911.1068](https://arxiv.org/abs/0911.1068) [astro-ph.SR] (cit. on p. 4).
- Chao, J. K. et al. (1993). « Observations of an intermediate shock in interplanetary space ». *J. Geophys. Res.* 98.A10, pp. 17443–17450. DOI: [10.1029/93JA01609](https://doi.org/10.1029/93JA01609) (cit. on pp. 16–18).
- Chateau, Yves F. and Meyer-Vernet, Nicole (1991). « Electrostatic noise in non-maxwellian plasmas: Generic properties and “kappa” distributions ». *J. Geophys. Res.* 96.A4, pp. 5825–5836. DOI: [10.1029/90JA02565](https://doi.org/10.1029/90JA02565) (cit. on pp. 25, 59).

- Chen, L. -J. et al. (2018). « Electron Bulk Acceleration and Thermalization at Earth's Quasiperpendicular Bow Shock ». *PhRvL* 120.22, 225101, p. 225101. DOI: [10.1103/PhysRevLett.120.225101](https://doi.org/10.1103/PhysRevLett.120.225101) (cit. on p. 111).
- Chen, Yu et al. (2021). « Small-scale Magnetic Flux Ropes with Field-aligned Flows via the PSP In Situ Observations ». *ApJ* 914.2, 108, p. 108. DOI: [10.3847/1538-4357/abfd30](https://doi.org/10.3847/1538-4357/abfd30). arXiv: 2105.06550 [astro-ph.SR] (cit. on p. 65).
- Chéret, R. (1992). « The life and work of Pierre-Henri Hugoniot ». *Shock Waves* 2.1, pp. 1–4. DOI: [10.1007/BF01414415](https://doi.org/10.1007/BF01414415) (cit. on p. 16).
- Couturier, P. et al. (1981). « Quasi-thermal noise in a stable plasma at rest: theory and observations from ISEE 3 ». *J. Geophys. Res.* 86.A13, pp. 11127–11138. DOI: [10.1029/JA086iA13p11127](https://doi.org/10.1029/JA086iA13p11127) (cit. on p. 97).
- Cravens, T. E. and Gombosi, T. I. (2004). « Cometary magnetospheres: a tutorial ». *Advances in Space Research* 33.11, pp. 1968–1976. DOI: [10.1016/j.asr.2003.07.053](https://doi.org/10.1016/j.asr.2003.07.053) (cit. on p. 17).
- Croswell, Ken (2021). « News Feature: Voyager still breaking barriers decades after launch ». *Proceedings of the National Academy of Science* 118.17, e2106371118, e2106371118. DOI: [10.1073/pnas.2106371118](https://doi.org/10.1073/pnas.2106371118) (cit. on p. 6).
- Curtis, D. W. et al. (1989). « On-board data analysis techniques for space plasma particle instruments ». *Review of Scientific Instruments* 60.3, pp. 372–380. DOI: [10.1063/1.1140441](https://doi.org/10.1063/1.1140441) (cit. on p. 31).
- de Pazzis, O. (1969). « Shot Noise in Antennas ». *Radio Science* 4.1, pp. 91–92. DOI: [10.1029/RS004i001p00091](https://doi.org/10.1029/RS004i001p00091) (cit. on p. 24).
- De Pontieu, B. et al. (2007). « Chromospheric Alfvénic Waves Strong Enough to Power the Solar Wind ». *Science* 318.5856, p. 1574. DOI: [10.1126/science.1151747](https://doi.org/10.1126/science.1151747) (cit. on p. 4).
- Decker, R. B. et al. (2005). « Voyager 1 in the Foreshock, Termination Shock, and Heliosheath ». *Science* 309.5743, pp. 2020–2024. DOI: [10.1126/science.1117569](https://doi.org/10.1126/science.1117569) (cit. on p. 4, 17).
- Démoulin, P. (2009). « Why Do Temperature and Velocity Have Different Relationships in the Solar Wind and in Interplanetary Coronal Mass Ejections? » *SoPh* 257.1, pp. 169–184. DOI: [10.1007/s11207-009-9338-5](https://doi.org/10.1007/s11207-009-9338-5) (cit. on p. 56).
- Deng, X. H. and Matsumoto, H. (2001). « Rapid magnetic reconnection in the Earth's magnetosphere mediated by whistler waves ». *Nature* 410.6828, pp. 557–560. DOI: [10.1038/410557A0](https://doi.org/10.1038/410557A0) (cit. on p. 14).
- Donzis, Diego A. (2012). « Shock structure in shock-turbulence interactions ». *Physics of Fluids* 24.12, 126101-126101-18, pp. 126101-126101-18. DOI: [10.1063/1.4772064](https://doi.org/10.1063/1.4772064) (cit. on p. 14).
- Dudok de Wit, T. et al. (2022). « First Results From the SCM Search-Coil Magnetometer on Parker Solar Probe ». *Journal of Geophysical Research (Space Physics)* 127.4, e30018, e30018. DOI: [10.1029/2021JA030018](https://doi.org/10.1029/2021JA030018) (cit. on p. 30).
- Dudok de Wit, Thierry et al. (2020). « Switchbacks in the Near-Sun Magnetic Field: Long Memory and Impact on the Turbulence Cascade ». *ApJS* 246.2, 39, p. 39. DOI: [10.3847/1538-4365/ab5853](https://doi.org/10.3847/1538-4365/ab5853). arXiv: 1912.02856 [astro-ph.SR] (cit. on p. 65).
- Dulk, G. A. (1985). « Radio emission from the sun and stars. » *ARA&A* 23, pp. 169–224. DOI: [10.1146/annurev.aa.23.090185.001125](https://doi.org/10.1146/annurev.aa.23.090185.001125) (cit. on p. 35).
- Dulk, George A. (2000). « Type III Solar Radio Bursts at Long Wavelengths ». *Geophysical Monograph Series* 119, p. 115. DOI: [10.1029/GM119p0115](https://doi.org/10.1029/GM119p0115) (cit. on p. 35).
- Dungey, J. W. (1961). « Interplanetary Magnetic Field and the Auroral Zones ». *PhRvL* 6.2, pp. 47–48. DOI: [10.1103/PhysRevLett.6.47](https://doi.org/10.1103/PhysRevLett.6.47) (cit. on p. 14).
- Đurovcová, T. et al. (2017). « Evolution of Proton and Alpha Particle Velocities through the Solar Cycle ». *ApJ* 850.2, 164, p. 164. DOI: [10.3847/1538-4357/aa9618](https://doi.org/10.3847/1538-4357/aa9618) (cit. on pp. 54, 109).
- Dwivedi, B. N. and Parker, Foreword by E. N. (2003). *Dynamic Sun* (cit. on p. 4).
- Eastwood, J. P. et al. (2009). « Observations of Turbulence Generated by Magnetic Reconnection ». *PhRvL* 102.3, 035001, p. 035001. DOI: [10.1103/PhysRevLett.102.035001](https://doi.org/10.1103/PhysRevLett.102.035001) (cit. on pp. 14, 34).
- Edlén, B. (1945). « The identification of the coronal lines (George Darwin Lecture) ». *MNRAS* 105, p. 323. DOI: [10.1093/mnras/105.6.323](https://doi.org/10.1093/mnras/105.6.323) (cit. on p. 2).
- Edmiston, J. P. and Kennel, C. F. (1984). « A parametric survey of the first critical Mach number for a fast MHD shock ». *Journal of Plasma Physics* 32.3, pp. 429–441. DOI: [10.1017/S002237780000218X](https://doi.org/10.1017/S002237780000218X) (cit. on pp. 16, 18).
- Edmondson, J. K. et al. (2009). « Reconnection-Driven Dynamics of Coronal-Hole Boundaries ». *ApJ* 707.2, pp. 1427–1437. DOI: [10.1088/0004-637X/707/2/1427](https://doi.org/10.1088/0004-637X/707/2/1427) (cit. on p. 4).

- Emslie, A. G. and Miller, J. A. (2003). « Particle acceleration ». *Dynamic Sun*. Ed. by B. N. Dwivedi and Foreword by E. N. Parker, pp. 262–287 (cit. on p. 4).
- Erdélyi, R. and Ballai, I. (2007). « Heating of the solar and stellar coronae: a review ». *Astronomische Nachrichten* 328.8, pp. 726–733. DOI: [10.1002/asna.200710803](https://doi.org/10.1002/asna.200710803) (cit. on pp. 2, 4, 11, 14).
- Ergun, R. E. et al. (2010). « Spacecraft charging and ion wake formation in the near-Sun environment ». *Physics of Plasmas* 17.7, 072903, p. 072903. DOI: [10.1063/1.3457484](https://doi.org/10.1063/1.3457484). arXiv: [1006.0760](https://arxiv.org/abs/1006.0760) [physics.space-ph] (cit. on pp. 36, 113).
- Fargette, Nais et al. (2021). « Characteristic Scales of Magnetic Switchback Patches Near the Sun and Their Possible Association With Solar Supergranulation and Granulation ». *ApJ* 919.2, 96, p. 96. DOI: [10.3847/1538-4357/ac1112](https://doi.org/10.3847/1538-4357/ac1112). arXiv: [2109.01519](https://arxiv.org/abs/2109.01519) [astro-ph.SR] (cit. on p. 65).
- Fejer, J. A. and Kan, J. R. (1969). « Noise Spectrum Received by an Antenna in a Plasma ». *Radio Science* 4.8, pp. 721–728. DOI: [10.1029/RS004i008p00721](https://doi.org/10.1029/RS004i008p00721) (cit. on p. 24).
- Feldman, W. C. et al. (1974). « Interpenetrating solar wind streams. » *Reviews of Geophysics and Space Physics* 12, pp. 715–723. DOI: [10.1029/RG012i004p00715](https://doi.org/10.1029/RG012i004p00715) (cit. on p. 6).
- Feldman, W. C. et al. (1975). « Solar wind electrons ». *J. Geophys. Res.* 80.31, p. 4181. DOI: [10.1029/JA080i031p04181](https://doi.org/10.1029/JA080i031p04181) (cit. on pp. 7–9).
- Feng, Hengqiang and Wang, J. M. (2008). « Observations of a 2→3 Type Interplanetary Intermediate Shock ». *SoPh* 247.1, pp. 195–201. DOI: [10.1007/s11207-007-9087-2](https://doi.org/10.1007/s11207-007-9087-2) (cit. on pp. 16–18).
- Fomin, N. A. (2016). « How the Term “Shock Waves” Came Into Being ». *Journal of Engineering Physics and Thermophysics* 89.4, pp. 1047–1065. DOI: [10.1007/s10891-016-1467-8](https://doi.org/10.1007/s10891-016-1467-8) (cit. on p. 16).
- Fox, N. J. et al. (2016). « The Solar Probe Plus Mission: Humanity’s First Visit to Our Star ». *SSRv* 204.1-4, pp. 7–48. DOI: [10.1007/s11214-015-0211-6](https://doi.org/10.1007/s11214-015-0211-6) (cit. on pp. 29, 42, 56, 92, 112).
- García, Rafael A. et al. (2007). « Tracking Solar Gravity Modes: The Dynamics of the Solar Core ». *Science* 316.5831, p. 1591. DOI: [10.1126/science.1140598](https://doi.org/10.1126/science.1140598) (cit. on p. 2).
- Gary, S. P. (1981). « Microinstabilities upstream of the earth’s bow shock: A brief review ». *J. Geophys. Res.* 86.A6, pp. 4331–4336. DOI: [10.1029/JA086iA06p04331](https://doi.org/10.1029/JA086iA06p04331) (cit. on p. 16).
- (1985). « Electromagnetic ion beam instabilities - Hot beams at interplanetary shocks ». *ApJ* 288, pp. 342–352. DOI: [10.1086/162797](https://doi.org/10.1086/162797) (cit. on p. 16).
- (1986). « Low-frequency waves in a high-beta collisionless plasma: polarization, compressibility and helicity ». *Journal of Plasma Physics* 35.3, pp. 431–447. DOI: [10.1017/S0022377800011442](https://doi.org/10.1017/S0022377800011442) (cit. on p. 86).
- Gary, S. P., Gosling, J. T., and Forslund, D. W. (1981). « The electromagnetic ion beam instability upstream of the earth’s bow shock ». *J. Geophys. Res.* 86.A8, pp. 6691–6696. DOI: [10.1029/JA086iA08p06691](https://doi.org/10.1029/JA086iA08p06691) (cit. on p. 16).
- Gary, S. P. and Lee, M. A. (1994). « The ion cyclotron anisotropy instability and the inverse correlation between proton anisotropy and proton beta ». *J. Geophys. Res.* 99, pp. 11297–11302. DOI: [10.1029/94JA00253](https://doi.org/10.1029/94JA00253) (cit. on pp. 6, 88).
- Gary, S. P. and Mellott, M. M. (1985). « Whistler damping at oblique propagation: Laminar shock precursors ». *J. Geophys. Res.* 90.A1, pp. 99–104. DOI: [10.1029/JA090iA01p00099](https://doi.org/10.1029/JA090iA01p00099) (cit. on p. 16).
- Gary, S. P., Skoug, R. M., and Daughton, W. (1999). « Electron heat flux constraints in the solar wind ». *Physics of Plasmas* 6, pp. 2607–2612. DOI: [10.1063/1.873532](https://doi.org/10.1063/1.873532) (cit. on p. 86).
- Gary, S. P. et al. (1997). « Proton temperature anisotropy upper bound ». *J. Geophys. Res.* 102, pp. 27159–27170. DOI: [10.1029/97JA01726](https://doi.org/10.1029/97JA01726) (cit. on pp. 6, 88).
- Gary, S. Peter (1970). « Longitudinal waves in a perpendicular collisionless plasma shock: II. Vlasov ions ». *Journal of Plasma Physics* 4.4, pp. 753–760. DOI: [10.1017/S0022377800005407](https://doi.org/10.1017/S0022377800005407) (cit. on p. 16).
- (1972). « Longitudinal waves in a perpendicular collisionless plasma shock Part 4. Gradient B ». *Journal of Plasma Physics* 7.3, pp. 417–425. DOI: [10.1017/S0022377800006747](https://doi.org/10.1017/S0022377800006747) (cit. on p. 16).
- Gary, S. Peter and Sanderson, J. J. (1970). « Longitudinal waves in a perpendicular collisionless plasma shock: I. Cold ions ». *Journal of Plasma Physics* 4.4, pp. 739–751. DOI: [10.1017/S0022377800005390](https://doi.org/10.1017/S0022377800005390) (cit. on p. 16).
- Giacalone, Joe (2005). « Particle Acceleration at Shocks Moving through an Irregular Magnetic Field ». *ApJ* 624.2, pp. 765–772. DOI: [10.1086/429265](https://doi.org/10.1086/429265) (cit. on p. 14).
- Gloeckler, G. et al. (1995). « The Solar Wind and Suprathermal Ion Composition Investigation on the Wind Spacecraft ». *SSRv* 71, pp. 79–124. DOI: [10.1007/BF00751327](https://doi.org/10.1007/BF00751327) (cit. on p. 38).

- Goetz, K. et al. (2018). « The Time Domain Sampler instrument onboard the Parker Solar Probe ». *AGU Fall Meeting Abstracts*. Vol. 2018, SH51B–2818 (cit. on p. 30).
- Gas dynamics of cosmic clouds; proceedings from IAU symposium no. 2 held at Cambridge, England, July 6-11, 1953*. (1955). Vol. 2 (cit. on pp. 15, 16).
- Gold, T. (1962). « Magnetic Storms ». *SSRv* 1.1, pp. 100–114. DOI: [10.1007/BF00174637](https://doi.org/10.1007/BF00174637) (cit. on pp. 15, 16).
- Goldreich, P. and Sridhar, S. (1995). « Toward a Theory of Interstellar Turbulence. II. Strong Alfvénic Turbulence ». *ApJ* 438, p. 763. DOI: [10.1086/175121](https://doi.org/10.1086/175121) (cit. on p. 14).
- Goldstein, Bruce E. et al. (2000). « Observed constraint on proton-proton relative velocities in the solar wind ». *Geophys. Res. Lett.* 27.1, pp. 53–56. DOI: [10.1029/1999GL003637](https://doi.org/10.1029/1999GL003637) (cit. on p. 6).
- Goncharov, O. et al. (2018). « Interaction of the Interplanetary Shock and IMF Directional Discontinuity in the Solar Wind ». *Journal of Geophysical Research (Space Physics)* 123.5, pp. 3822–3835. DOI: [10.1029/2018JA025195](https://doi.org/10.1029/2018JA025195) (cit. on p. 75).
- Gopalswamy, N. (2004). « Recent advances in the long-wavelength radio physics of the Sun ». *Planet. Space Sci.* 52.15, pp. 1399–1413. DOI: [10.1016/j.pss.2004.09.016](https://doi.org/10.1016/j.pss.2004.09.016) (cit. on p. 35).
- Goruganthu, R. R. and Wilson, W. G. (1984). « Relative electron detection efficiency of microchannel plates from 0-3 keV ». *Review of Scientific Instruments* 55.12, pp. 2030–2033. DOI: [10.1063/1.1137709](https://doi.org/10.1063/1.1137709) (cit. on p. 31).
- Gosling, J. T. and Pizzo, V. J. (1999). « Formation and Evolution of Corotating Interaction Regions and their Three Dimensional Structure ». *SSRv* 89, pp. 21–52. DOI: [10.1023/A:1005291711900](https://doi.org/10.1023/A:1005291711900) (cit. on p. 17).
- Gosling, J. T., Skoug, R. M., and Feldman, W. C. (2001). « Solar wind electron halo depletions at 90° pitch angle ». *Geophys. Res. Lett.* 28.22, pp. 4155–4158. DOI: [10.1029/2001GL013758](https://doi.org/10.1029/2001GL013758) (cit. on pp. 7, 8).
- Gosling, J. T. et al. (1982). « Evidence for specularly reflected ions upstream from the quasi-parallel bow shock ». *Geophys. Res. Lett.* 9, pp. 1333–1336. DOI: [10.1029/GL009i012p01333](https://doi.org/10.1029/GL009i012p01333) (cit. on pp. 21, 89).
- Gosling, J. T. et al. (1987). « Bidirectional solar wind electron heat flux events ». *J. Geophys. Res.* 92.A8, pp. 8519–8535. DOI: [10.1029/JA092iA08p08519](https://doi.org/10.1029/JA092iA08p08519) (cit. on p. 78).
- Graham, G. A. et al. (2017). « The evolution of solar wind strahl with heliospheric distance ». *Journal of Geophysical Research (Space Physics)* 122.4, pp. 3858–3874. DOI: [10.1002/2016JA023656](https://doi.org/10.1002/2016JA023656) (cit. on p. 9).
- Griton, Léa et al. (2021). « Source-dependent Properties of Two Slow Solar Wind States ». *ApJ* 910.1, 63, p. 63. DOI: [10.3847/1538-4357/abe309](https://doi.org/10.3847/1538-4357/abe309). arXiv: [2102.06568](https://arxiv.org/abs/2102.06568) [astro-ph.SR] (cit. on pp. 70, 72, 110).
- Grognard, R. J. -M. (1975). « Deficiencies of the asymptotic solutions commonly found in the quasilinear relaxation theory ». *Australian Journal of Physics* 28, p. 731. DOI: [10.1071/PH750731](https://doi.org/10.1071/PH750731) (cit. on p. 83).
- Guillemant, S. et al. (2012). « Solar wind plasma interaction with solar probe plus spacecraft ». *Annales Geophysicae* 30.7, pp. 1075–1092. DOI: [10.5194/angeo-30-1075-2012](https://doi.org/10.5194/angeo-30-1075-2012) (cit. on pp. 36, 113).
- Guo, Fan and Giacalone, Joe (2010). « The Effect of Large-scale Magnetic Turbulence on the Acceleration of Electrons by Perpendicular Collisionless Shocks ». *ApJ* 715.1, pp. 406–411. DOI: [10.1088/0004-637X/715/1/406](https://doi.org/10.1088/0004-637X/715/1/406). arXiv: [1003.5946](https://arxiv.org/abs/1003.5946) [astro-ph.SR] (cit. on p. 16).
- Gurnett, D. A. and Bhattacharjee, A. (2005). *Introduction to Plasma Physics* (cit. on p. 15).
- Halekas, J. S. et al. (2020a). « Electron heat flux in the near-Sun environment ». *A&A* accepted, same series, same series. DOI: [10.3847/1538-4365/ab4cec](https://doi.org/10.3847/1538-4365/ab4cec). arXiv: [1912.02216](https://arxiv.org/abs/1912.02216) [astro-ph.SR] (cit. on pp. 43, 51, 53, 63, 65, 72, 109).
- Halekas, J. S. et al. (2020b). « Electrons in the Young Solar Wind: First Results from the Parker Solar Probe ». *ApJS* 246.2, 22, p. 22. DOI: [10.3847/1538-4365/ab4cec](https://doi.org/10.3847/1538-4365/ab4cec). arXiv: [1912.02216](https://arxiv.org/abs/1912.02216) [astro-ph.SR] (cit. on pp. 8, 9, 43, 51, 53, 56, 63, 64, 72, 109).
- Halekas, J. S. et al. (2022). « The Radial Evolution of the Solar Wind as Organized by Electron Distribution Parameters ». *ApJ* 936.1, 53, p. 53. DOI: [10.3847/1538-4357/ac85b8](https://doi.org/10.3847/1538-4357/ac85b8). arXiv: [2207.06563](https://arxiv.org/abs/2207.06563) [astro-ph.SR] (cit. on pp. 56, 64, 70, 71).
- Hammond, C. M. et al. (1996). « Variation of electron-strahl width in the high-speed solar wind: ULYSSES observations. » *A&A* 316, pp. 350–354 (cit. on pp. 8, 9).
- Hansen, Carl J., Kawaler, Steven D., and Trimble, Virginia (2004). *Stellar interiors : physical principles, structure, and evolution* (cit. on p. 2).
- Hansteen, Viggo H. (2009). « Stellar winds and magnetic fields ». *Heliophysics: Plasma Physics of the Local Cosmos*. Ed. by Carolus J. Schrijver and George L. Siscoe, pp. 225–255 (cit. on p. 9).

- Harten, Ronald and Clark, Kenn (1995). « The Design Features of the GGS Wind and Polar Spacecraft ». *SSRv* 71.1-4, pp. 23–40. DOI: [10.1007/BF00751324](https://doi.org/10.1007/BF00751324) (cit. on p. 38).
- Harvey, C. C., Etcheto, J., and Mangeney, A. (1979). « Early Results from the ISEE Electron Density Experiment [Article published in the Special issues: Advances in Magnetospheric Physics with GEOS- 1 and ISEE - 1 and 2. (Proceedings of the 13th ESLAB Symposium, innsbruck, 1978. - pp. 3-133)] ». *SSRv* 23.1, pp. 39–58. DOI: [10.1007/BF00174110](https://doi.org/10.1007/BF00174110) (cit. on p. 24).
- Hathaway, David H. (2010). « The Solar Cycle ». *Living Reviews in Solar Physics* 7.1, 1, p. 1. DOI: [10.12942/lrsp-2010-1](https://doi.org/10.12942/lrsp-2010-1) (cit. on p. 9).
- (2015). « The Solar Cycle ». *Living Reviews in Solar Physics* 12.1, 4, p. 4. DOI: [10.1007/lrsp-2015-4](https://doi.org/10.1007/lrsp-2015-4). arXiv: [1502.07020](https://arxiv.org/abs/1502.07020) [[astro-ph.SR](#)] (cit. on p. 9).
- Hellinger, Petr et al. (2006). « Solar wind proton temperature anisotropy: Linear theory and WIND/SWE observations ». *Geophys. Res. Lett.* 33.9, L09101, p. L09101. DOI: [10.1029/2006GL025925](https://doi.org/10.1029/2006GL025925) (cit. on p. 7).
- Hellinger, Petr et al. (2011). « Heating and cooling of protons in the fast solar wind between 0.3 and 1 AU: Helios revisited ». *Journal of Geophysical Research (Space Physics)* 116.A9, A09105, A09105. DOI: [10.1029/2011JA016674](https://doi.org/10.1029/2011JA016674) (cit. on p. 43).
- Hellinger, Petr et al. (2013). « Proton thermal energetics in the solar wind: Helios reloaded ». *Journal of Geophysical Research (Space Physics)* 118.4, pp. 1351–1365. DOI: [10.1002/jgra.50107](https://doi.org/10.1002/jgra.50107) (cit. on p. 66).
- Hess, Phillip et al. (2020). « WISPR Imaging of a Pristine CME ». *ApJS* 246.2, 25, p. 25. DOI: [10.3847/1538-4365/ab4ff0](https://doi.org/10.3847/1538-4365/ab4ff0). arXiv: [1912.02255](https://arxiv.org/abs/1912.02255) [[astro-ph.SR](#)] (cit. on pp. 50, 65).
- Hillan, D. S. et al. (2010). « Prediction of background levels for the Wind WAVES instrument and implications for the galactic background radiation ». *J. Geophys. Res.* 115.A6, A06102, A06102. DOI: [10.1029/2009JA014714](https://doi.org/10.1029/2009JA014714) (cit. on p. 34).
- Hoang, S. et al. (2007). « Radio tracking of the interplanetary coronal mass ejection driven shock crossed by Ulysses on 10 May 2001 ». *Journal of Geophysical Research (Space Physics)* 112.A9, A09102, A09102. DOI: [10.1029/2006JA011906](https://doi.org/10.1029/2006JA011906) (cit. on pp. 20, 79).
- Horaites, Konstantinos et al. (2018). « Kinetic Theory and Fast Wind Observations of the Electron Strahl ». *MNRAS* 474.1, pp. 115–127. DOI: [10.1093/mnras/stx2555](https://doi.org/10.1093/mnras/stx2555). arXiv: [1706.03464](https://arxiv.org/abs/1706.03464) [[physics.space-ph](#)] (cit. on p. 8).
- Huang, Jia et al. (2020). « Proton Temperature Anisotropy Variations in Inner Heliosphere Estimated with the First Parker Solar Probe Observations ». *ApJS* 246.2, 70, p. 70. DOI: [10.3847/1538-4365/ab74e0](https://doi.org/10.3847/1538-4365/ab74e0). arXiv: [1912.03871](https://arxiv.org/abs/1912.03871) [[physics.space-ph](#)] (cit. on pp. 7, 92, 112).
- Hubert, D. et al. (1989). « Observation of mirror waves downstream of a quasi-perpendicular shock ». *Geophys. Res. Lett.* 16.2, pp. 159–162. DOI: [10.1029/GL016i002p00159](https://doi.org/10.1029/GL016i002p00159) (cit. on p. 88).
- Issautier, K. et al. (2005). « Solar wind electron density and temperature over solar cycle 23: Thermal noise measurements on Wind ». *Advances in Space Research* 35.12, pp. 2141–2146. DOI: [10.1016/j.asr.2005.04.085](https://doi.org/10.1016/j.asr.2005.04.085) (cit. on pp. 57, 79).
- Issautier, K. et al. (2008). « Electron properties of high-speed solar wind from polar coronal holes obtained by Ulysses thermal noise spectroscopy: Not so dense, not so hot ». *Geophys. Res. Lett.* 35.19, L19101, p. L19101. DOI: [10.1029/2008GL034912](https://doi.org/10.1029/2008GL034912) (cit. on pp. 9, 42, 57, 69, 72, 110).
- Issautier, Karine et al. (1996). « A novel method to measure the solar wind speed ». *Geophys. Res. Lett.* 23.13, pp. 1649–1652. DOI: [10.1029/96GL01070](https://doi.org/10.1029/96GL01070) (cit. on pp. 24, 36).
- (1998). « Solar wind radial and latitudinal structure: Electron density and core temperature from Ulysses thermal noise spectroscopy ». *J. Geophys. Res.* 103.A2, pp. 1969–1980. DOI: [10.1029/97JA02661](https://doi.org/10.1029/97JA02661) (cit. on pp. 56, 66, 71, 98, 103, 110, 112).
- (1999a). « High-speed solar wind from Ulysses measurements and comparison with exospheric models ». *Solar Wind Nine*. Ed. by Shadia Rifai Habbal et al. Vol. 471. American Institute of Physics Conference Series, pp. 581–584. DOI: [10.1063/1.58699](https://doi.org/10.1063/1.58699) (cit. on pp. 4, 56).
- Issautier, Karine et al. (1999b). « Quasi-thermal noise in a drifting plasma: Theory and application to solar wind diagnostic on Ulysses ». *J. Geophys. Res.* 104.A4, pp. 6691–6704. DOI: [10.1029/1998JA900165](https://doi.org/10.1029/1998JA900165) (cit. on pp. 24, 36, 42, 57, 97, 99).
- Issautier, Karine et al. (2001a). « Electron Temperature in the Solar Wind From a Kinetic Collisionless Model: Application to High-Latitude Ulysses Observations ». *Ap&SS* 277, pp. 189–193. DOI: [10.1023/A:1012206230015](https://doi.org/10.1023/A:1012206230015) (cit. on pp. 4, 56).

- Issautier, Karine et al. (2001b). « Solar Wind Electron Observations Near Solar Maximum at High Latitudes From Thermal Noise Spectroscopy ». *SSRv* 97, pp. 105–108. DOI: [10.1023/A:1011878228168](https://doi.org/10.1023/A:1011878228168) (cit. on pp. 42, 57).
- Issautier, Karine et al. (2001c). « Solar wind plasma parameters on Ulysses: Detailed comparison between the URAP and SWOOPS experiments ». *J. Geophys. Res.* 106.A8, pp. 15665–15676. DOI: [10.1029/2000JA000412](https://doi.org/10.1029/2000JA000412) (cit. on pp. 24, 57).
- Izmodenov, Vladislav V. (2004). « The Heliospheric Interface: Models and Observations ». *The Sun and the Heliosphere as an Integrated System*. Ed. by G. Poletto and S. T. Suess. Vol. 317. Astrophysics and Space Science Library, p. 23. DOI: [10.1007/978-1-4020-2831-9_2](https://doi.org/10.1007/978-1-4020-2831-9_2) (cit. on pp. 4, 5).
- Jagarlamudi, V. K. et al. (2021). « Whistler wave occurrence and the interaction with strahl electrons during the first encounter of Parker Solar Probe ». *A&A* 650, A9, A9. DOI: [10.1051/0004-6361/202039808](https://doi.org/10.1051/0004-6361/202039808). arXiv: [2101.06723](https://arxiv.org/abs/2101.06723) [physics.space-ph] (cit. on pp. 25, 33, 36, 92, 112).
- Jian, L. et al. (2006). « Properties of Stream Interactions at One AU During 1995–2004 ». *SoPh* 239.1-2, pp. 337–392. DOI: [10.1007/s11207-006-0132-3](https://doi.org/10.1007/s11207-006-0132-3) (cit. on p. 17).
- Johnstone, C. P. et al. (2015). « Stellar winds on the main-sequence. I. Wind model ». *A&A* 577, A27, A27. DOI: [10.1051/0004-6361/201425300](https://doi.org/10.1051/0004-6361/201425300). arXiv: [1503.06669](https://arxiv.org/abs/1503.06669) [astro-ph.SR] (cit. on pp. 53, 109).
- Karimabadi, H. et al. (2014). « The link between shocks, turbulence, and magnetic reconnection in collisionless plasmas ». *Physics of Plasmas* 21.6, 062308, p. 062308. DOI: [10.1063/1.4882875](https://doi.org/10.1063/1.4882875) (cit. on p. 14).
- Kasaba, Y. et al. (2000). « Statistical studies of plasma waves and backstreaming electrons in the terrestrial electron foreshock observed by Geotail ». *J. Geophys. Res.* 105.A1, pp. 79–104. DOI: [10.1029/1999JA900408](https://doi.org/10.1029/1999JA900408) (cit. on pp. 22, 75).
- Kasaba, Yasumasa et al. (2020). « Plasma Wave Investigation (PWI) Aboard BepiColombo Mio on the Trip to the First Measurement of Electric Fields, Electromagnetic Waves, and Radio Waves Around Mercury ». *SSRv* 216.4, 65, p. 65. DOI: [10.1007/s11214-020-00692-9](https://doi.org/10.1007/s11214-020-00692-9) (cit. on pp. 112, 113).
- Kasper, J. C. et al. (2012). « EVOLUTION OF THE RELATIONSHIPS BETWEEN HELIUM ABUNDANCE, MINOR ION CHARGE STATE, AND SOLAR WIND SPEED OVER THE SOLAR CYCLE ». *ApJ* 745.2, p. 162. DOI: [10.1088/0004-637x/745/2/162](https://doi.org/10.1088/0004-637x/745/2/162) (cit. on p. 44).
- Kasper, J. C. et al. (2019). « Alfvénic velocity spikes and rotational flows in the near-Sun solar wind ». *Nature* 576.7786, pp. 228–231. DOI: [10.1038/s41586-019-1813-z](https://doi.org/10.1038/s41586-019-1813-z) (cit. on pp. 65, 92, 112).
- Kasper, J. C. et al. (2021). « Parker Solar Probe Enters the Magnetically Dominated Solar Corona ». *PhRvL* 127.25, 255101, p. 255101. DOI: [10.1103/PhysRevLett.127.255101](https://doi.org/10.1103/PhysRevLett.127.255101) (cit. on pp. 4, 36, 57).
- Kasper, Justin C., Lazarus, Alan J., and Gary, S. Peter (2002). « Wind/SWE observations of firehose constraint on solar wind proton temperature anisotropy ». *Geophys. Res. Lett.* 29.17, 1839, p. 1839. DOI: [10.1029/2002GL015128](https://doi.org/10.1029/2002GL015128) (cit. on p. 6).
- Kasper, Justin C. et al. (2007). « Solar Wind Helium Abundance as a Function of Speed and Heliographic Latitude: Variation through a Solar Cycle ». *ApJ* 660.1, pp. 901–910. DOI: [10.1086/510842](https://doi.org/10.1086/510842) (cit. on pp. 11, 44).
- Kasper, Justin C. et al. (2016). « Solar Wind Electrons Alphas and Protons (SWEAP) Investigation: Design of the Solar Wind and Coronal Plasma Instrument Suite for Solar Probe Plus ». *SSRv* 204.1-4, pp. 131–186. DOI: [10.1007/s11214-015-0206-3](https://doi.org/10.1007/s11214-015-0206-3) (cit. on pp. 29, 30, 42–44, 57, 68).
- Kellogg, P. J. (1962). « Flow of Plasma around the Earth ». *J. Geophys. Res.* 67.10, pp. 3805–3811. DOI: [10.1029/JZ067i010p03805](https://doi.org/10.1029/JZ067i010p03805) (cit. on pp. 15, 16).
- Kellogg, Paul J. (2003). « Langmuir waves associated with collisionless shocks; a review ». *Planet. Space Sci.* 51.11, pp. 681–691. DOI: [10.1016/j.pss.2003.05.001](https://doi.org/10.1016/j.pss.2003.05.001) (cit. on pp. 20, 39).
- Kellogg, Paul J. et al. (1996). « Early Wind observations of bow shock and foreshock waves ». *Geophys. Res. Lett.* 23.10, pp. 1243–1246. DOI: [10.1029/96GL01067](https://doi.org/10.1029/96GL01067) (cit. on pp. 20, 39).
- Kellogg, Paul J. et al. (1999). « A search for Langmuir solitons in the Earth’s foreshock ». *J. Geophys. Res.* 104.A4, pp. 6751–6758. DOI: [10.1029/1999JA900021](https://doi.org/10.1029/1999JA900021) (cit. on pp. 20, 39).
- Kennel, Charles F. (1987). « Critical Mach numbers in classical magnetohydrodynamics ». *J. Geophys. Res.* 92.A12, pp. 13427–13437. DOI: [10.1029/JA092iA12p13427](https://doi.org/10.1029/JA092iA12p13427) (cit. on pp. 16, 18).
- Khrabrov, A. V. and Sonnerup, B. U. Ö. (1998). « Error estimates for minimum variance analysis ». *J. Geophys. Res.* 103, pp. 6641–6652. DOI: [10.1029/97JA03731](https://doi.org/10.1029/97JA03731) (cit. on pp. 83, 84).
- Korreck, Kelly E. et al. (2020). « Source and Propagation of a Streamer Blowout Coronal Mass Ejection Observed by the Parker Solar Probe ». *ApJS* 246.2, 69, p. 69. DOI: [10.3847/1538-4365/ab6ff9](https://doi.org/10.3847/1538-4365/ab6ff9) (cit. on pp. 50, 65).

- Krimigis, Stamatios M. et al. (2019). « Energetic charged particle measurements from Voyager 2 at the heliopause and beyond ». *Nature Astronomy* 3, pp. 997–1006. DOI: [10.1038/s41550-019-0927-4](https://doi.org/10.1038/s41550-019-0927-4) (cit. on pp. 53, 109).
- Krupar, V. et al. (2014). « Statistical Survey of Type III Radio Bursts at Long Wavelengths Observed by the Solar TERrestrial RELations Observatory (STEREO)/ Waves Instruments: Radio Flux Density Variations with Frequency ». *SoPh* 289.8, pp. 3121–3135. DOI: [10.1007/s11207-014-0522-x](https://doi.org/10.1007/s11207-014-0522-x). arXiv: [1410.2053](https://arxiv.org/abs/1410.2053) [astro-ph.SR] (cit. on p. 35).
- Lacombe, C. and Mangeney, A. (1980). « Non-Linear Interaction of Alfvén Waves with Compressive Fast Magnetosonic Waves ». *A&A* 88, p. 277 (cit. on p. 89).
- Langmuir, Irving (1928). « Oscillations in Ionized Gases ». *Proceedings of the National Academy of Science* 14.8, pp. 627–637. DOI: [10.1073/pnas.14.8.627](https://doi.org/10.1073/pnas.14.8.627) (cit. on p. 25).
- Lavraud, B. et al. (2006). « Evidence for newly closed magnetosheath field lines at the dayside magnetopause under northward IMF ». *Journal of Geophysical Research (Space Physics)* 111.A5, A05211, A05211. DOI: [10.1029/2005JA011266](https://doi.org/10.1029/2005JA011266) (cit. on p. 14).
- Lavraud, B. et al. (2020). « The Heliospheric Current Sheet and Plasma Sheet during Parker Solar Probe’s First Orbit ». *ApJL* 894.2, L19, p. L19. DOI: [10.3847/2041-8213/ab8d2d](https://doi.org/10.3847/2041-8213/ab8d2d) (cit. on p. 50).
- Lavraud, B. et al. (2021). « Magnetic reconnection as a mechanism to produce multiple thermal proton populations and beams locally in the solar wind ». *A&A* 656, A37, A37. DOI: [10.1051/0004-6361/202141149](https://doi.org/10.1051/0004-6361/202141149). arXiv: [2109.11232](https://arxiv.org/abs/2109.11232) [astro-ph.SR] (cit. on p. 14).
- Le Chat, G., Issautier, K., and Meyer-Vernet, N. (2012). « The Solar Wind Energy Flux ». *SoPh* 279.1, pp. 197–205. DOI: [10.1007/s11207-012-9967-y](https://doi.org/10.1007/s11207-012-9967-y). arXiv: [1203.1316](https://arxiv.org/abs/1203.1316) [astro-ph.SR] (cit. on pp. 11, 13, 41–43, 47, 50, 51, 53, 109).
- Le Chat, G., Meyer-Vernet, N., and Issautier, K. (2009). « Study of stellar wind energy flux: from the Sun to Beltegeuse ». *15th Cambridge Workshop on Cool Stars, Stellar Systems, and the Sun*. Ed. by Eric Stempels. Vol. 1094. American Institute of Physics Conference Series, pp. 365–368. DOI: [10.1063/1.3099121](https://doi.org/10.1063/1.3099121) (cit. on pp. 11, 42, 51, 53, 109, 113).
- Le Chat, G. et al. (2011). « Large-Scale Variation of Solar Wind Electron Properties from Quasi-Thermal Noise Spectroscopy: Ulysses Measurements ». *SoPh* 271.1-2, pp. 141–148. DOI: [10.1007/s11207-011-9797-3](https://doi.org/10.1007/s11207-011-9797-3) (cit. on pp. 56, 57, 66, 68, 69, 71, 110).
- Le, G. and Russell, C. T. (1992a). « A study of ULF wave foreshock morphology - I: ULF foreshock boundary ». *Planet. Space Sci.* 40.9, pp. 1203–1213. DOI: [10.1016/0032-0633\(92\)90077-2](https://doi.org/10.1016/0032-0633(92)90077-2) (cit. on p. 21).
- (1992b). « A study of ULF wave foreshock morphology - II: spatial variation of ULF waves ». *Planet. Space Sci.* 40.9, pp. 1215–1225. DOI: [10.1016/0032-0633\(92\)90078-3](https://doi.org/10.1016/0032-0633(92)90078-3) (cit. on p. 21).
- Le, Guan (1991). « Generation of upstream ULF waves in the Earth’s foreshock ». PhD thesis. University of California, Los Angeles (cit. on p. 21).
- Leblanc, Yolande, Dulk, George A., and Bougeret, Jean-Louis (1998). « Tracing the Electron Density from the Corona to 1 au ». *SoPh* 183.1, pp. 165–180. DOI: [10.1023/A:1005049730506](https://doi.org/10.1023/A:1005049730506) (cit. on p. 35).
- Lembège, B. and Savoini, P. (2002). « Formation of reflected electron bursts by the nonstationarity and nonuniformity of a collisionless shock front ». *J. Geophys. Res.* 107.A3, 1037, p. 1037. DOI: [10.1029/2001JA900128](https://doi.org/10.1029/2001JA900128) (cit. on pp. 76, 79).
- Lembege, B. et al. (2004). « Selected Problems in Collisionless-Shock Physics ». *SSRv* 110.3, pp. 161–226. DOI: [10.1023/B:SPAC.0000023372.12232.b7](https://doi.org/10.1023/B:SPAC.0000023372.12232.b7) (cit. on p. 76).
- Lembège, Bertrand and Yang, Zhongwei (2016). « Physical Roles of Interstellar-origin Pickup Ions at the Heliospheric Termination Shock: Impact on the Shock Front Microstructures and Nonstationarity ». *ApJ* 827.1, 73, p. 73. DOI: [10.3847/0004-637X/827/1/73](https://doi.org/10.3847/0004-637X/827/1/73) (cit. on p. 17).
- (2018). « Physical Roles of Interstellar-origin Pickup Ions at Heliospheric Termination Shock. II. Impact of the Front Nonstationary on the Energy Partition and Particle Velocity Distribution ». *ApJ* 860.1, 84, p. 84. DOI: [10.3847/1538-4357/aabe85](https://doi.org/10.3847/1538-4357/aabe85) (cit. on p. 17).
- Lepping, R. P. et al. (1995). « The Wind Magnetic Field Investigation ». *SSRv* 71, pp. 207–229. DOI: [10.1007/BF00751330](https://doi.org/10.1007/BF00751330) (cit. on pp. 38, 40, 76).
- Leroy, M. M. et al. (1982). « The structure of perpendicular bow shocks ». *J. Geophys. Res.* 87.A7, pp. 5081–5094. DOI: [10.1029/JA087iA07p05081](https://doi.org/10.1029/JA087iA07p05081) (cit. on pp. 16, 18, 21, 89, 91, 112).
- Lin, R. P. (1980). « Energetic Particles in Space ». *SoPh* 67.2, pp. 393–399. DOI: [10.1007/BF00149816](https://doi.org/10.1007/BF00149816) (cit. on p. 9).

- (1998). « WIND Observations of Suprathermal Electrons in the Interplanetary Medium ». *SSRv* 86, pp. 61–78. DOI: [10.1023/A:1005048428480](https://doi.org/10.1023/A:1005048428480) (cit. on pp. 7, 8).
- Lin, R. P. et al. (1995). « A Three-Dimensional Plasma and Energetic Particle Investigation for the Wind Spacecraft ». *SSRv* 71, pp. 125–153. DOI: [10.1007/BF00751328](https://doi.org/10.1007/BF00751328) (cit. on pp. 38, 39, 76, 89, 92).
- Liu, M. et al. (2018). « Kinetic Properties of an Interplanetary Shock Propagating inside a Coronal Mass Ejection ». *ApJL* 859, L4, p. L4. DOI: [10.3847/2041-8213/aac269](https://doi.org/10.3847/2041-8213/aac269) (cit. on pp. 7, 20, 39, 83, 86, 88, 89, 91).
- Liu, M. et al. (2020). « Solar Wind Energy Flux Observations in the Inner Heliosphere: First Results from Parker Solar Probe ». *AGU Fall Meeting Abstracts*. Vol. 2020, SH052–04 (cit. on p. 61).
- Liu, M. et al. (2021a). « Solar wind energy flux observations in the inner heliosphere: first results from Parker Solar Probe ». *A&A* 650, A14, A14. DOI: [10.1051/0004-6361/202039615](https://doi.org/10.1051/0004-6361/202039615). arXiv: [2101.03121](https://arxiv.org/abs/2101.03121) [[astro-ph.SR](#)] (cit. on pp. 36, 57, 61).
- Liu, Mingzhe (2018). « Studies of the Kinetic Properties of Interplanetary Shocks ». MA thesis. National Space Science Center, Chinese Academy of Sciences (cit. on pp. 16, 17, 20, 39).
- Liu, Mingzhe et al. (2022). « Radial Evolution of the Electron Temperature Derived from the Quasi-Thermal Noise Spectroscopy in the Pristine Solar Wind: Parker Solar Probe Observations ». *44th COSPAR Scientific Assembly. Held 16-24 July*. Vol. 44, p. 1462 (cit. on p. 36).
- Liu, Y. D. et al. (2012). « Interactions between Coronal Mass Ejections Viewed in Coordinated Imaging and in situ Observations ». *ApJL* 746, L15, p. L15. DOI: [10.1088/2041-8205/746/2/L15](https://doi.org/10.1088/2041-8205/746/2/L15). arXiv: [1201.2968](https://arxiv.org/abs/1201.2968) [[astro-ph.SR](#)] (cit. on pp. 17, 75).
- Liu, Y. D. et al. (2014a). « Observations of an extreme storm in interplanetary space caused by successive coronal mass ejections ». *Nat. Commun* 5, 3481, p. 3481. DOI: [10.1038/ncomms4481](https://doi.org/10.1038/ncomms4481). arXiv: [1405.6088](https://arxiv.org/abs/1405.6088) [[physics.space-ph](#)] (cit. on p. 75).
- Liu, Y. D. et al. (2014b). « Sun-to-Earth Characteristics of Two Coronal Mass Ejections Interacting Near 1 AU: Formation of a Complex Ejecta and Generation of a Two-step Geomagnetic Storm ». *ApJL* 793, L41, p. L41. DOI: [10.1088/2041-8205/793/2/L41](https://doi.org/10.1088/2041-8205/793/2/L41). arXiv: [1409.2954](https://arxiv.org/abs/1409.2954) [[physics.space-ph](#)] (cit. on p. 75).
- Liu, Y. et al. (2006a). « Plasma depletion and mirror waves ahead of interplanetary coronal mass ejections ». *J. Geophys. Res.* 111, A09108, A09108. DOI: [10.1029/2006JA011723](https://doi.org/10.1029/2006JA011723). eprint: [physics/0602164](https://arxiv.org/abs/physics/0602164) (cit. on pp. 7, 39, 88).
- Liu, Y. et al. (2006b). « Thermodynamic structure of collision-dominated expanding plasma: Heating of interplanetary coronal mass ejections ». *Journal of Geophysical Research (Space Physics)* 111.A1, A01102, A01102. DOI: [10.1029/2005JA011329](https://doi.org/10.1029/2005JA011329) (cit. on p. 7).
- Liu, Y. et al. (2007). « Temperature Anisotropy in a Shocked Plasma: Mirror-Mode Instabilities in the Heliosheath ». *ApJL* 659, pp. L65–L68. DOI: [10.1086/516568](https://doi.org/10.1086/516568). eprint: [astro-ph/0702599](https://arxiv.org/abs/astro-ph/0702599) (cit. on pp. 7, 88).
- Liu, Y. et al. (2009). « Relationship Between a Coronal Mass Ejection-Driven Shock and a Coronal Metric Type II Burst ». *ApJL* 691.2, pp. L151–L155. DOI: [10.1088/0004-637X/691/2/L151](https://doi.org/10.1088/0004-637X/691/2/L151) (cit. on p. 35).
- Liu, Ying D., Zhao, Xiaowei, and Zhu, Bei (2017). « Propagation and Interaction Properties of Successive Coronal Mass Ejections in Relation to a Complex Type II Radio Burst ». *ApJ* 849.2, 112, p. 112. DOI: [10.3847/1538-4357/aa9075](https://doi.org/10.3847/1538-4357/aa9075). arXiv: [1709.10263](https://arxiv.org/abs/1709.10263) [[physics.space-ph](#)] (cit. on p. 35).
- Liu, Ying D. et al. (2021b). « Determination of Solar Wind Angular Momentum and Alfvén Radius from Parker Solar Probe Observations ». *ApJL* 908.2, L41, p. L41. DOI: [10.3847/2041-8213/abe38e](https://doi.org/10.3847/2041-8213/abe38e). arXiv: [2102.03376](https://arxiv.org/abs/2102.03376) [[astro-ph.SR](#)] (cit. on pp. 4, 36, 57).
- Liu, Ying David (2007). « Evolution of Coronal Mass Ejections through the Heliosphere ». PhD thesis. MIT (cit. on pp. 7, 88).
- Livi, Roberto et al. (2018). « Solar Probe ANalyzer for Ions - Laboratory Performance ». *Solar Heliospheric and Interplanetary Environment (SHINE 2018)*, p. 184 (cit. on pp. 30, 31).
- Livi, Roberto et al. (2022). « The Solar Probe ANalyzer-Ions on the Parker Solar Probe ». *ApJ* 938.2, 138, p. 138. DOI: [10.3847/1538-4357/ac93f5](https://doi.org/10.3847/1538-4357/ac93f5) (cit. on p. 57).
- Livi, S., Marsch, E., and Rosenbauer, H. (1986). « Coulomb collisional domains in solar wind ». *J. Geophys. Res.* 91.A7, pp. 8045–8050. DOI: [10.1029/JA091iA07p08045](https://doi.org/10.1029/JA091iA07p08045) (cit. on p. 16).
- Lockwood, Mike (2016). « Jim Dungey, The Open Magnetosphere, and Space Weather ». *Space Weather* 14.6, pp. 380–383. DOI: [10.1002/2016SW001438](https://doi.org/10.1002/2016SW001438) (cit. on p. 14).
- Lodders, Katharina (2003). « Solar System Abundances and Condensation Temperatures of the Elements ». *ApJ* 591.2, pp. 1220–1247. DOI: [10.1086/375492](https://doi.org/10.1086/375492) (cit. on p. 2).

- Lopez, R. E. and Freeman, J. W. (1986). « Solar wind proton temperature-velocity relationship ». *J. Geophys. Res.* 91.A2, pp. 1701–1705. DOI: [10.1029/JA091iA02p01701](https://doi.org/10.1029/JA091iA02p01701) (cit. on p. 56).
- Loureiro, Nuno F. and Boldyrev, Stanislav (2017). « Role of Magnetic Reconnection in Magnetohydrodynamic Turbulence ». *PhRvL* 118.24, 245101, p. 245101. DOI: [10.1103/PhysRevLett.118.245101](https://doi.org/10.1103/PhysRevLett.118.245101). arXiv: [1612.07266](https://arxiv.org/abs/1612.07266) [[physics.plasm-ph](https://arxiv.org/archive/physics)] (cit. on p. 14).
- Lu, Quanming, Hu, Qiang, and Zank, G. P. (2009). « The Interaction of Alfvén Waves with Perpendicular Shocks ». *ApJ* 706.1, pp. 687–692. DOI: [10.1088/0004-637X/706/1/687](https://doi.org/10.1088/0004-637X/706/1/687) (cit. on pp. 14, 76, 88, 92, 112).
- Lu, Quanming et al. (2021). « Two-dimensional Particle-in-cell Simulation of Magnetic Reconnection in the Downstream of a Quasi-perpendicular Shock ». *ApJ* 919.1, 28, p. 28. DOI: [10.3847/1538-4357/ac18c0](https://doi.org/10.3847/1538-4357/ac18c0). arXiv: [2108.11036](https://arxiv.org/abs/2108.11036) [[physics.space-ph](https://arxiv.org/archive/physics)] (cit. on p. 14).
- Lugaz, N. et al. (2015). « Shocks inside CMEs: A survey of properties from 1997 to 2006 ». *J. Geophys. Res.* 120, pp. 2409–2427. DOI: [10.1002/2014JA020848](https://doi.org/10.1002/2014JA020848). arXiv: [1503.04141](https://arxiv.org/abs/1503.04141) [[physics.space-ph](https://arxiv.org/archive/physics)] (cit. on pp. 17, 75).
- Luhmann, J. G. (1986). « The Solar Wind Interaction with Venus ». *SSRv* 44.3-4, pp. 241–306. DOI: [10.1007/BF00200818](https://doi.org/10.1007/BF00200818) (cit. on p. 17).
- Lund, E. J., Labelle, J., and Treumann, R. A. (1994). « On quasi-thermal fluctuations near the plasma frequency in the outer plasmasphere: A case study ». *J. Geophys. Res.* 99.A12, pp. 23651–23660. DOI: [10.1029/94JA02134](https://doi.org/10.1029/94JA02134) (cit. on p. 57).
- Ma, Bing et al. (2021a). « Statistics of Low Frequency Cutoffs for Type III Radio Bursts Observed by Parker Solar Probe during Its Encounters 1-5 ». *ApJL* 913.1, L1, p. L1. DOI: [10.3847/2041-8213/abfb77](https://doi.org/10.3847/2041-8213/abfb77) (cit. on pp. 35, 36).
- Ma, Bing et al. (2022). « Discrepancy between the Low-frequency Cutoffs of Type III Radio Bursts Based on Simultaneous Observations by WIND and PSP ». *ApJL* 932.2, L26, p. L26. DOI: [10.3847/2041-8213/ac7525](https://doi.org/10.3847/2041-8213/ac7525) (cit. on pp. 35, 36).
- Ma, Jiuqi et al. (2021b). « Nonlinear Wave-Wave Coupling Related to Whistler-mode and Electron Bernstein Waves Observed by the Parker Solar Probe ». *ApJ* 918.1, 26, p. 26. DOI: [10.3847/1538-4357/ac0ef4](https://doi.org/10.3847/1538-4357/ac0ef4) (cit. on pp. 33, 36).
- Mace, R. L. and Sydora, R. D. (2010). « Parallel whistler instability in a plasma with an anisotropic bi-kappa distribution ». *J. Geophys. Res.* 115, A07206, A07206. DOI: [10.1029/2009JA015064](https://doi.org/10.1029/2009JA015064) (cit. on p. 86).
- Macquorn Rankine, W. J. (1870). « On the Thermodynamic Theory of Waves of Finite Longitudinal Disturbance ». *Philosophical Transactions of the Royal Society of London Series I* 160, pp. 277–288 (cit. on p. 16).
- Maksimovic, M., Pierrard, V., and Lemaire, J. F. (1997). « A kinetic model of the solar wind with Kappa distribution functions in the corona. » *A&A* 324, pp. 725–734 (cit. on pp. 4, 56).
- Maksimovic, M. et al. (1995). « Solar wind electron parameters from quasi-thermal noise spectroscopy and comparison with other measurements on Ulysses ». *J. Geophys. Res.* 100.A10, pp. 19881–19892. DOI: [10.1029/95JA01550](https://doi.org/10.1029/95JA01550) (cit. on pp. 24, 42, 57).
- Maksimovic, M. et al. (2005a). « Radial evolution of the electron distribution functions in the fast solar wind between 0.3 and 1.5 AU ». *Journal of Geophysical Research (Space Physics)* 110.A9, A09104, A09104. DOI: [10.1029/2005JA011119](https://doi.org/10.1029/2005JA011119) (cit. on pp. 7–9, 66–68, 71, 72, 110).
- Maksimovic, M. et al. (2005b). « Solar wind electron temperature and density measurements on the Solar Orbiter with thermal noise spectroscopy ». *Advances in Space Research* 36.8, pp. 1471–1473. DOI: [10.1016/j.asr.2005.01.088](https://doi.org/10.1016/j.asr.2005.01.088) (cit. on p. 57).
- Maksimovic, M. et al. (2020). « Anticorrelation between the Bulk Speed and the Electron Temperature in the Pristine Solar Wind: First Results from the Parker Solar Probe and Comparison with Helios ». *ApJS* 246.2, 62, p. 62. DOI: [10.3847/1538-4365/ab61fc](https://doi.org/10.3847/1538-4365/ab61fc) (cit. on pp. 34, 36, 42, 56–61, 63, 67, 68, 70–72, 110).
- Maksimovic, Milan, Gary, S. Peter, and Skoug, Ruth M. (2000). « Solar wind electron suprathermal strength and temperature gradients: Ulysses observations ». *J. Geophys. Res.* 105.A8, pp. 18337–18350. DOI: [10.1029/2000JA900039](https://doi.org/10.1029/2000JA900039) (cit. on pp. 7, 8, 56).
- Maksimovic, Milan, Pierrard, Viviane, and Lemaire, Joseph (2001). « On the Exospheric Approach for the Solar Wind Acceleration ». *Ap&SS* 277, pp. 181–187. DOI: [10.1023/A:1012250027289](https://doi.org/10.1023/A:1012250027289) (cit. on p. 56).
- Maksimovic, Milan et al. (2021). « Electron Kappa Distributions in the Solar Wind: Cause of the Acceleration or Consequence of the Expansion? » *Kappa Distributions: From Observational Evidences via Controversial Predictions to a Consistent Theory of Nonequilibrium Plasmas*. Ed. by Marian Lazar and Horst Fichtner. Cham: Springer International Publishing, pp. 39–51. DOI: [10.1007/978-3-030-82623-9_3](https://doi.org/10.1007/978-3-030-82623-9_3) (cit. on pp. 64, 67).

- Makwana, K. D. and Yan, Huirong (2020). « Properties of Magnetohydrodynamic Modes in Compressively Driven Plasma Turbulence ». *Physical Review X* 10.3, 031021, p. 031021. DOI: [10.1103/PhysRevX.10.031021](https://doi.org/10.1103/PhysRevX.10.031021). arXiv: [1907.01853](https://arxiv.org/abs/1907.01853) [[physics.plasm-ph](#)] (cit. on p. 14).
- Malaspina, David M. et al. (2016). « The Digital Fields Board for the FIELDS instrument suite on the Solar Probe Plus mission: Analog and digital signal processing ». *Journal of Geophysical Research (Space Physics)* 121.6, pp. 5088–5096. DOI: [10.1002/2016JA022344](https://doi.org/10.1002/2016JA022344) (cit. on pp. 30, 32, 36).
- Malaspina, David M. et al. (2020). « Plasma Waves near the Electron Cyclotron Frequency in the Near-Sun Solar Wind ». *ApJS* 246.2, 21, p. 21. DOI: [10.3847/1538-4365/ab4c3b](https://doi.org/10.3847/1538-4365/ab4c3b). arXiv: [1912.06793](https://arxiv.org/abs/1912.06793) [[physics.space-ph](#)] (cit. on pp. 33, 36).
- Manning, R. and Dulk, G. A. (2001). « The Galactic background radiation from 0.2 to 13.8 MHz ». *A&A* 372, pp. 663–666. DOI: [10.1051/0004-6361:20010516](https://doi.org/10.1051/0004-6361:20010516) (cit. on pp. 34, 59, 61).
- Markwardt, C. B. (2009). « Non-linear Least-squares Fitting in IDL with MPFIT ». *Astronomical Data Analysis Software and Systems XVIII*. Ed. by D. A. Bohlender, D. Durand, and P. Dowler. Vol. 411. Astronomical Society of the Pacific Conference Series, p. 251. arXiv: [0902.2850](https://arxiv.org/abs/0902.2850) [[astro-ph.IM](#)] (cit. on pp. 61, 66).
- Marsch, E. et al. (1982). « Solar wind protons: Three-dimensional velocity distributions and derived plasma parameters measured between 0.3 and 1 AU ». *J. Geophys. Res.* 87.A1, pp. 52–72. DOI: [10.1029/JA087iA01p00052](https://doi.org/10.1029/JA087iA01p00052) (cit. on p. 6).
- Marsch, E. et al. (1989). « Cooling of solar wind electrons inside 0.3 AU ». *J. Geophys. Res.* 94.A6, pp. 6893–6898. DOI: [10.1029/JA094iA06p06893](https://doi.org/10.1029/JA094iA06p06893) (cit. on p. 56).
- Marsch, Eckart (2006). « Kinetic Physics of the Solar Corona and Solar Wind ». *Living Reviews in Solar Physics* 3.1, 1, p. 1. DOI: [10.12942/lrsp-2006-1](https://doi.org/10.12942/lrsp-2006-1) (cit. on p. 9).
- Martinović, M. M. et al. (2016). « Quasi-thermal noise measurements on STEREO: Kinetic temperature deduction using electron shot noise model ». *Journal of Geophysical Research (Space Physics)* 121.1, pp. 129–139. DOI: [10.1002/2015JA021710](https://doi.org/10.1002/2015JA021710) (cit. on p. 67).
- Martinović, Mihailo M. et al. (2020). « Solar Wind Electron Parameters Determination on Wind Spacecraft Using Quasi-Thermal Noise Spectroscopy ». *Journal of Geophysical Research (Space Physics)* 125.8, e28113, e28113. DOI: [10.1029/2020JA028113](https://doi.org/10.1029/2020JA028113) (cit. on p. 57).
- Martinović, Mihailo M. et al. (2021). « Multiscale Solar Wind Turbulence Properties inside and near Switchbacks Measured by the Parker Solar Probe ». *ApJ* 912.1, 28, p. 28. DOI: [10.3847/1538-4357/abebe5](https://doi.org/10.3847/1538-4357/abebe5). arXiv: [2103.00374](https://arxiv.org/abs/2103.00374) [[astro-ph.SR](#)] (cit. on p. 65).
- Martinović, Mihailo M. et al. (2022). « Plasma Parameters From Quasi-Thermal Noise Observed by Parker Solar Probe: A New Model for the Antenna Response ». *Journal of Geophysical Research (Space Physics)* 127.4, e30182, e30182. DOI: [10.1029/2021JA030182](https://doi.org/10.1029/2021JA030182) (cit. on pp. 24, 36, 57, 103).
- Matsumoto, H. et al. (1997). « Plasma waves in the upstream and bow shock regions observed by geotail ». *Advances in Space Research* 20.4-5, pp. 683–693. DOI: [10.1016/S0273-1177\(97\)00456-0](https://doi.org/10.1016/S0273-1177(97)00456-0) (cit. on pp. 22, 75).
- Matsuoka, Ayako et al. (2000). « Propagation sense of low-frequency MHD waves in the magnetosheath observed by Geotail ». *J. Geophys. Res.* 105.A8, pp. 18, 361–18, 376. DOI: [10.1029/2000JA900014](https://doi.org/10.1029/2000JA900014) (cit. on p. 89).
- Matthaeus, W. H., Elliott, H. A., and McComas, D. J. (2006). « Correlation of speed and temperature in the solar wind ». *Journal of Geophysical Research (Space Physics)* 111.A10, A10103, A10103. DOI: [10.1029/2006JA011636](https://doi.org/10.1029/2006JA011636) (cit. on p. 56).
- Matthaeus, W. H. and Goldstein, M. L. (1982). « Measurement of the rugged invariants of magnetohydrodynamic turbulence in the solar wind ». *J. Geophys. Res.* 87.A8, pp. 6011–6028. DOI: [10.1029/JA087iA08p06011](https://doi.org/10.1029/JA087iA08p06011) (cit. on p. 86).
- Matthaeus, W. H. and Lamkin, S. L. (1986). « Turbulent magnetic reconnection ». *Physics of Fluids* 29.8, pp. 2513–2534. DOI: [10.1063/1.866004](https://doi.org/10.1063/1.866004) (cit. on p. 14).
- Mazelle, C. et al. (2004). « Bow Shock and Upstream Phenomena at Mars ». *SSRv* 111.1, pp. 115–181. DOI: [10.1023/B:SPAC.0000032717.98679.d0](https://doi.org/10.1023/B:SPAC.0000032717.98679.d0) (cit. on p. 17).
- McComas, D. J. et al. (2008). « Weaker solar wind from the polar coronal holes and the whole Sun ». *Geophys. Res. Lett.* 35.18, L18103, p. L18103. DOI: [10.1029/2008GL034896](https://doi.org/10.1029/2008GL034896) (cit. on pp. 9, 10).
- McComas, D. J. et al. (2014). « IBEX: The First Five Years (2009–2013) ». *ApJS* 213.2, 20, p. 20. DOI: [10.1088/0067-0049/213/2/20](https://doi.org/10.1088/0067-0049/213/2/20) (cit. on pp. 42, 51, 53, 109).
- McComas, D. J. et al. (2016). « Integrated Science Investigation of the Sun (ISIS): Design of the Energetic Particle Investigation ». *SSRv* 204.1-4, pp. 187–256. DOI: [10.1007/s11214-014-0059-1](https://doi.org/10.1007/s11214-014-0059-1) (cit. on pp. 29, 42).

- McComas, D. J. et al. (2017). « Seven Years of Imaging the Global Heliosphere with IBEX ». *ApJS* 229.2, 41, p. 41. DOI: [10.3847/1538-4365/aa66d8](https://doi.org/10.3847/1538-4365/aa66d8). arXiv: [1704.06316](https://arxiv.org/abs/1704.06316) [[physics.space-ph](#)] (cit. on pp. 53, 109).
- McComas, D. J. et al. (2020). « Solar Cycle of Imaging the Global Heliosphere: Interstellar Boundary Explorer (IBEX) Observations from 2009-2019 ». *ApJS* 248.2, 26, p. 26. DOI: [10.3847/1538-4365/ab8dc2](https://doi.org/10.3847/1538-4365/ab8dc2) (cit. on pp. 53, 109).
- McKenzie, James F. and Westphal, Karl O. (1969). « Transmission of Alfvén waves through the Earth's bow shock ». *Planet. Space Sci.* 17.5, pp. 1029–1037. DOI: [10.1016/0032-0633\(69\)90107-X](https://doi.org/10.1016/0032-0633(69)90107-X) (cit. on p. 76).
- Meeks, Craig and Siegel, P. B. (2008). « Dead time correction via the time series ». *American Journal of Physics* 76.6, pp. 589–590. DOI: [10.1119/1.2870432](https://doi.org/10.1119/1.2870432) (cit. on p. 31).
- Mellott, M. M. and Greenstadt, E. W. (1984). « The structure of oblique subcritical bow shocks - ISEE 1 and 2 observations ». *J. Geophys. Res.* 89, pp. 2151–2161. DOI: [10.1029/JA089iA04p02151](https://doi.org/10.1029/JA089iA04p02151) (cit. on pp. 16, 18, 85).
- Meyer-Vernet, N. (1979). « On natural noises detected by antennas in plasmas ». *J. Geophys. Res.* 84.A9, pp. 5373–5373. DOI: [10.1029/JA084iA09p05373](https://doi.org/10.1029/JA084iA09p05373) (cit. on pp. 24, 42, 57).
- Meyer-Vernet, N., Issautier, K., and Moncuquet, M. (2017). « Quasi-thermal noise spectroscopy: The art and the practice ». *J. Geophys. Res.* 122.8, pp. 7925–7945. DOI: [10.1002/2017JA024449](https://doi.org/10.1002/2017JA024449) (cit. on pp. 24, 25, 35, 42, 57–59, 78, 97, 101, 103, 107).
- Meyer-Vernet, N. et al. (1986). « Plasma Diagnosis from Thermal Noise and Limits on Dust Flux or Mass in Comet Giacobini-Zinner ». *Science* 232.4748, pp. 370–374. DOI: [10.1126/science.232.4748.370](https://doi.org/10.1126/science.232.4748.370) (cit. on pp. 24, 42, 57).
- Meyer-Vernet, N. et al. (2009). « Dust Detection by the Wave Instrument on STEREO: Nanoparticles Picked up by the Solar Wind? » *SoPh* 256.1-2, pp. 463–474. DOI: [10.1007/s11207-009-9349-2](https://doi.org/10.1007/s11207-009-9349-2). arXiv: [0903.4141](https://arxiv.org/abs/0903.4141) [[astro-ph.SR](#)] (cit. on p. 36).
- Meyer-Vernet, N. et al. (2022). « Weak line discovered by Voyager 1 in the interstellar medium: Quasi-thermal noise produced by very few fast electrons ». *A&A* 658, L12, p. L12. DOI: [10.1051/0004-6361/202243030](https://doi.org/10.1051/0004-6361/202243030). arXiv: [2202.04684](https://arxiv.org/abs/2202.04684) [[astro-ph.SR](#)] (cit. on pp. 36, 58).
- Meyer-Vernet, Nicole (1999). « How does the solar wind blow? A simple kinetic model ». *European Journal of Physics* 20.3, pp. 167–176. DOI: [10.1088/0143-0807/20/3/006](https://doi.org/10.1088/0143-0807/20/3/006) (cit. on pp. 53, 109).
- (2006a). « How does the solar wind blow? Some basic aspects ». *Solar Activity and its Magnetic Origin*. Ed. by Volker Bothmer and Ahmed Abdel Hady. Vol. 233. IAU Symposium, pp. 269–276. DOI: [10.1017/S1743921306001992](https://doi.org/10.1017/S1743921306001992) (cit. on p. 11).
- (2006b). « How does the solar wind blow? Some basic aspects ». *Solar Activity and its Magnetic Origin*. Ed. by Volker Bothmer and Ahmed Abdel Hady. Vol. 233. IAU Symposium, pp. 269–276. DOI: [10.1017/S1743921306001992](https://doi.org/10.1017/S1743921306001992) (cit. on pp. 42, 50, 51, 53, 109).
- (2007). *Basics of the Solar Wind* (cit. on pp. 6, 11, 15, 42).
- Meyer-Vernet, Nicole, Hoang, Sang, and Moncuquet, Michel (1993a). « Bernstein waves in the Io plasma torus: A novel kind of electron temperature sensor ». *J. Geophys. Res.* 98.A12, pp. 21163–21176. DOI: [10.1029/93JA02587](https://doi.org/10.1029/93JA02587) (cit. on p. 57).
- (1993b). « Bernstein waves in the Io plasma torus: A novel kind of electron temperature sensor ». *J. Geophys. Res.* 98.A12, pp. 21163–21176. DOI: [10.1029/93JA02587](https://doi.org/10.1029/93JA02587) (cit. on p. 100).
- Meyer-Vernet, Nicole and Issautier, Karine (1998). « Electron temperature in the solar wind: Generic radial variation from kinetic collisionless models ». *J. Geophys. Res.* 103.A12, pp. 29705–29718. DOI: [10.1029/98JA02853](https://doi.org/10.1029/98JA02853) (cit. on pp. 4, 56, 57, 68, 69, 72, 110).
- Meyer-Vernet, Nicole and Moncuquet, Michel (2020). « Plasma Waves in Space: The Importance of Properly Accounting for the Measuring Device ». *Journal of Geophysical Research (Space Physics)* 125.3, e27723, e27723. DOI: [10.1029/2019JA027723](https://doi.org/10.1029/2019JA027723) (cit. on pp. 24, 35, 58).
- Meyer-Vernet, Nicole and Perche, Claude (1989). « Tool kit for antennae and thermal noise near the plasma frequency ». *J. Geophys. Res.* 94, pp. 2405–2415. DOI: [10.1029/JA094iA03p02405](https://doi.org/10.1029/JA094iA03p02405) (cit. on pp. 24, 25, 35, 59, 78, 98, 100, 101, 103, 112).
- Meyer-Vernet, Nicole et al. (2003). « Some Basic Aspects of Solar Wind Acceleration ». *Solar Wind Ten*. Ed. by Marco Velli et al. Vol. 679. American Institute of Physics Conference Series, pp. 263–266. DOI: [10.1063/1.1618591](https://doi.org/10.1063/1.1618591) (cit. on p. 56).
- Meyer, P. and Vernet, N. (1974). « Impedance of a short antenna in a warm magnetoplasma ». *Radio Science* 9.3, pp. 409–416. DOI: [10.1029/RS009i003p00409](https://doi.org/10.1029/RS009i003p00409) (cit. on p. 97).

- Miles, John W. (1978). « Linear and Nonlinear Waves. By G. B. WHITHAM . Wiley-Interscience, 1974. 636 pp. \$625.75 ». *Journal of Fluid Mechanics* 87.2, p. 395. DOI: [10.1017/S0022112078211676](https://doi.org/10.1017/S0022112078211676) (cit. on p. 15).
- Milillo, A. et al. (2020). « Investigating Mercury’s Environment with the Two-Spacecraft BepiColombo Mission ». *SSRv* 216.5, 93, p. 93. DOI: [10.1007/s11214-020-00712-8](https://doi.org/10.1007/s11214-020-00712-8). arXiv: [2202.13243](https://arxiv.org/abs/2202.13243) [astro-ph.EP] (cit. on pp. 112, 113).
- Moncuquet, M., Meyer-Vernet, N., and Hoang, S. (1995). « Dispersion of electrostatic waves in the Io plasma torus and derived electron temperature ». *J. Geophys. Res.* 100.A11, pp. 21697–21708. DOI: [10.1029/95JA02299](https://doi.org/10.1029/95JA02299) (cit. on p. 57).
- Moncuquet, M. et al. (2006). « The radio waves and thermal electrostatic noise spectroscopy (SORBET) experiment on BEPICOLOMBO/MMO/PWI: Scientific objectives and performance ». *Advances in Space Research* 38.4, pp. 680–685. DOI: [10.1016/j.asr.2006.01.020](https://doi.org/10.1016/j.asr.2006.01.020) (cit. on pp. 42, 57).
- Moncuquet, Michel et al. (1997). « Detection of Bernstein wave forbidden bands in the Jovian magnetosphere: A new way to measure the electron density ». *J. Geophys. Res.* 102.A2, pp. 2373–2380. DOI: [10.1029/96JA03313](https://doi.org/10.1029/96JA03313) (cit. on p. 57).
- Moncuquet, Michel et al. (2005). « Quasi thermal noise spectroscopy in the inner magnetosphere of Saturn with Cassini/RPWS: Electron temperatures and density ». *Geophys. Res. Lett.* 32.20, L20S02, L20S02. DOI: [10.1029/2005GL022508](https://doi.org/10.1029/2005GL022508) (cit. on pp. 42, 57).
- Moncuquet, Michel et al. (2020). « First In Situ Measurements of Electron Density and Temperature from Quasi-thermal Noise Spectroscopy with Parker Solar Probe/FIELDS ». *ApJS* 246.2, 44, p. 44. DOI: [10.3847/1538-4365/ab5a84](https://doi.org/10.3847/1538-4365/ab5a84). arXiv: [1912.02518](https://arxiv.org/abs/1912.02518) [astro-ph.SR] (cit. on pp. 24, 26, 30, 36, 42, 44, 51, 56–64, 66, 71, 101, 103, 105, 110).
- Monin, A. S. (1980). *The solar cycle*. (Cit. on p. 9).
- Möstl, C. et al. (2012). « Multi-point Shock and Flux Rope Analysis of Multiple Interplanetary Coronal Mass Ejections around 2010 August 1 in the Inner Heliosphere ». *ApJ* 758, 10, p. 10. DOI: [10.1088/0004-637X/758/1/10](https://doi.org/10.1088/0004-637X/758/1/10). arXiv: [1209.2866](https://arxiv.org/abs/1209.2866) [astro-ph.SR] (cit. on pp. 17, 75).
- Mozer, F. S. et al. (2020). « Large-amplitude, Wideband, Doppler-shifted, Ion Acoustic Waves Observed on the Parker Solar Probe ». *ApJ* 901.2, 107, p. 107. DOI: [10.3847/1538-4357/abafb4](https://doi.org/10.3847/1538-4357/abafb4) (cit. on p. 36).
- Němeček, Zdeněk et al. (2021). « Spectra of Temperature Fluctuations in the Solar Wind ». *Atmosphere* 12.10, p. 1277. DOI: [10.3390/atmos12101277](https://doi.org/10.3390/atmos12101277) (cit. on pp. 6, 7).
- Ness, Norman F., Scarce, Clell S., and Seek, Joseph B. (1964). « Initial Results of the Imp 1 Magnetic Field Experiment ». *J. Geophys. Res.* 69.17, pp. 3531–3569. DOI: [10.1029/JZ069i017p03531](https://doi.org/10.1029/JZ069i017p03531) (cit. on p. 16).
- Neugebauer, Marcia and Snyder, Conway W. (1962). « Solar Plasma Experiment ». *Science* 138.3545, pp. 1095–1097. DOI: [10.1126/science.138.3545.1095-a](https://doi.org/10.1126/science.138.3545.1095-a) (cit. on pp. 4, 6, 11, 42).
- (1966). « Mariner 2 Observations of the Solar Wind, 1, Average Properties ». *J. Geophys. Res.* 71, p. 4469. DOI: [10.1029/JZ071i019p04469](https://doi.org/10.1029/JZ071i019p04469) (cit. on pp. 4, 6, 11).
- Newbury, J. A., Russell, C. T., and Gedalin, M. (1998). « The ramp widths of high-Mach-number, quasi-perpendicular collisionless shocks ». *J. Geophys. Res.* 103.A12, pp. 29581–29594. DOI: [10.1029/1998JA900024](https://doi.org/10.1029/1998JA900024) (cit. on p. 16).
- Nishikawa, Kyoji and Wakatani, Masahiro (1994). *Plasma Physics* (cit. on p. 15).
- Novaco, J. C. and Brown, L. W. (1978). « Nonthermal galactic emission below 10 megahertz. » *ApJ* 221, pp. 114–123. DOI: [10.1086/156009](https://doi.org/10.1086/156009) (cit. on pp. 59, 60).
- Ocker, Stella Koch et al. (2021). « Persistent plasma waves in interstellar space detected by Voyager 1 ». *Nature Astronomy* 5, pp. 761–765. DOI: [10.1038/s41550-021-01363-7](https://doi.org/10.1038/s41550-021-01363-7). arXiv: [2105.04000](https://arxiv.org/abs/2105.04000) [astro-ph.GA] (cit. on p. 6).
- Ogilvie, K. W. et al. (1995). « SWE, A Comprehensive Plasma Instrument for the Wind Spacecraft ». *SSRv* 71, pp. 55–77. DOI: [10.1007/BF00751326](https://doi.org/10.1007/BF00751326) (cit. on pp. 38, 89).
- Ogilvie, K. W. et al. (1999). « Sources of the solar wind electron strahl in 1995 ». *J. Geophys. Res.* 104.A10, pp. 22389–22394. DOI: [10.1029/1999JA900294](https://doi.org/10.1029/1999JA900294) (cit. on p. 8).
- Ossendrijver, M. and Hoyng, P. (2002). « Solar Cycle ». *Encyclopedia of Astronomy and Astrophysics*. Ed. by P. Murdin, E1980. DOI: [10.1888/0333750888/1980](https://doi.org/10.1888/0333750888/1980) (cit. on p. 9).
- Owens, A. et al. (1995). « A High-Resolution GE Spectrometer for Gamma-Ray Burst Astronomy ». *SSRv* 71, pp. 273–296. DOI: [10.1007/BF00751333](https://doi.org/10.1007/BF00751333) (cit. on p. 39).

- Parker, E. N. (1958a). « Dynamical Instability in an Anisotropic Ionized Gas of Low Density ». *Physical Review* 109.6, pp. 1874–1876. DOI: [10.1103/PhysRev.109.1874](https://doi.org/10.1103/PhysRev.109.1874) (cit. on pp. 4, 6, 42, 88).
- (1958b). « Dynamics of the Interplanetary Gas and Magnetic Fields. » *ApJ* 128, p. 664. DOI: [10.1086/146579](https://doi.org/10.1086/146579) (cit. on pp. 4, 6).
- (1965). « Dynamical Theory of the Solar Wind ». *SSRv* 4.5-6, pp. 666–708. DOI: [10.1007/BF00216273](https://doi.org/10.1007/BF00216273) (cit. on pp. 4, 6).
- (1988). « Nanoflares and the Solar X-Ray Corona ». *ApJ* 330, p. 474. DOI: [10.1086/166485](https://doi.org/10.1086/166485) (cit. on pp. 11, 14).
- (2001). « A Critical Review of Sun-Space Physics ». *Ap&SS* 277.1-2, pp. 1–11. DOI: [10.1023/A:1012243600572](https://doi.org/10.1023/A:1012243600572) (cit. on p. 42).
- Parks, G. K. et al. (2017). « Shocks in collisionless plasmas ». *Reviews of Modern Plasma Physics* 1, 1, p. 1. DOI: [10.1007/s41614-017-0003-4](https://doi.org/10.1007/s41614-017-0003-4) (cit. on pp. 16–18, 20, 22, 23, 27, 75).
- Parks, George K. (2004). « Why space physics needs to go beyond the MHD box ». *SSRv* 113.1, pp. 97–121. DOI: [10.1023/B:SPAC.0000042941.14372.9b](https://doi.org/10.1023/B:SPAC.0000042941.14372.9b) (cit. on p. 16).
- Paschmann, G. et al. (1980). « Energization of solar wind ions by reflection from the earth’s bow shock ». *J. Geophys. Res.* 85, pp. 4689–4693. DOI: [10.1029/JA085iA09p04689](https://doi.org/10.1029/JA085iA09p04689) (cit. on pp. 16, 18, 21, 89, 91, 112).
- Paschmann, G. et al. (1982). « Observations of gyrating ions in the foot of the nearly perpendicular bow shock ». *Geophys. Res. Lett.* 9, pp. 881–884. DOI: [10.1029/GL009i008p00881](https://doi.org/10.1029/GL009i008p00881) (cit. on p. 89).
- Paschmann, Götz and Daly, Patrick W. (1998). « Analysis Methods for Multi-Spacecraft Data. ISSI Scientific Reports Series SR-001, ESA/ISSI, Vol. 1. ISBN 1608-280X, 1998 ». *ISSI Scientific Reports Series* 1 (cit. on p. 31).
- Peredo, M. et al. (1995). « Three-dimensional position and shape of the bow shock and their variation with Alfvénic, sonic, and magnetosonic Mach numbers and interplanetary magnetic field orientation ». *J. Geophys. Res.* 100.A5, pp. 7907–7916. DOI: [10.1029/94JA02545](https://doi.org/10.1029/94JA02545) (cit. on p. 77).
- Phan, T. D., Gosling, J. T., and Davis, M. S. (2009). « Prevalence of extended reconnection X-lines in the solar wind at 1 AU ». *Geophys. Res. Lett.* 36.9, L09108, p. L09108. DOI: [10.1029/2009GL037713](https://doi.org/10.1029/2009GL037713) (cit. on p. 14).
- Phan, T. D. et al. (2000). « Extended magnetic reconnection at the Earth’s magnetopause from detection of bi-directional jets ». *Nature* 404.6780, pp. 848–850. DOI: [10.1038/35009050](https://doi.org/10.1038/35009050) (cit. on p. 14).
- Phan, T. D. et al. (2006). « A magnetic reconnection X-line extending more than 390 Earth radii in the solar wind ». *Nature* 439.7073, pp. 175–178. DOI: [10.1038/nature04393](https://doi.org/10.1038/nature04393) (cit. on p. 14).
- Phan, T. D. et al. (2018). « Electron magnetic reconnection without ion coupling in Earth’s turbulent magnetosheath ». *Nature* 557.7704, pp. 202–206. DOI: [10.1038/s41586-018-0091-5](https://doi.org/10.1038/s41586-018-0091-5) (cit. on p. 14).
- Phan, T. D. et al. (2021). « Prevalence of magnetic reconnection in the near-Sun heliospheric current sheet ». *A&A* 650, A13, A13. DOI: [10.1051/0004-6361/202039863](https://doi.org/10.1051/0004-6361/202039863) (cit. on p. 14).
- Phan, T. D. et al. (2022). « Parker Solar Probe Observations of Solar Wind Energetic Proton Beams Produced by Magnetic Reconnection in the Near-Sun Heliospheric Current Sheet ». *Geophys. Res. Lett.* 49.9, e96986, e96986. DOI: [10.1029/2021GL096986](https://doi.org/10.1029/2021GL096986) (cit. on p. 14).
- Pierrard, V. and Pieters, M. (2014). « Coronal heating and solar wind acceleration for electrons, protons, and minor ions obtained from kinetic models based on kappa distributions ». *Journal of Geophysical Research (Space Physics)* 119.12, pp. 9441–9455. DOI: [10.1002/2014JA020678](https://doi.org/10.1002/2014JA020678) (cit. on p. 4).
- Pierrard, Viviane, Lazar, Marian, and Štverák, Stepan (2020). « Solar Wind Plasma Particles Organized by the Flow Speed ». *SoPh* 295.11, 151, p. 151. DOI: [10.1007/s11207-020-01730-z](https://doi.org/10.1007/s11207-020-01730-z) (cit. on pp. 70, 72, 111).
- Pierrard, Viviane, Maksimovic, Milan, and Lemaire, Joseph (2001). « Core, Halo and Strahl Electrons in the Solar Wind ». *Ap&SS* 277, pp. 195–200. DOI: [10.1023/A:1012218600882](https://doi.org/10.1023/A:1012218600882) (cit. on pp. 4, 7, 9).
- Pilipp, W. G. et al. (1987). « Characteristics of electron velocity distribution functions in the solar wind derived from the helios plasma experiment ». *J. Geophys. Res.* 92.A2, pp. 1075–1092. DOI: [10.1029/JA092iA02p01075](https://doi.org/10.1029/JA092iA02p01075) (cit. on pp. 7, 8).
- Pilipp, W. G. et al. (1990). « Large-scale variations of thermal electron parameters in the solar wind between 0.3 and 1 AU. » *J. Geophys. Res.* 95, pp. 6305–6329. DOI: [10.1029/JA095iA05p06305](https://doi.org/10.1029/JA095iA05p06305) (cit. on pp. 43, 56, 71, 110).
- Podesta, J. J. (2009). « Dependence of Solar-Wind Power Spectra on the Direction of the Local Mean Magnetic Field ». *ApJ* 698.2, pp. 986–999. DOI: [10.1088/0004-637X/698/2/986](https://doi.org/10.1088/0004-637X/698/2/986). arXiv: [0901.4940](https://arxiv.org/abs/0901.4940) [astro-ph.EP] (cit. on p. 14).

- Přech, Lubomír, Němeček, Zdeněk, and Šafránková, Jana (2009). « Influence of the foreshock of the Earth's bow shock on the interplanetary shock propagation during their mutual interaction ». *Earth, Planets and Space* 61, p. 610. DOI: [10.1186/BF03352933](https://doi.org/10.1186/BF03352933) (cit. on p. 75).
- Price, C. P., Swift, D. W., and Lee, L. -C. (1986). « Numerical simulation of nonoscillatory mirror waves at the Earth's magnetosheath ». *J. Geophys. Res.* 91.A1, pp. 101–112. DOI: [10.1029/JA091iA01p00101](https://doi.org/10.1029/JA091iA01p00101) (cit. on p. 88).
- Pulupa, M. P., Bale, S. D., and Salem, C. (2011). « An asymmetry of the electron foreshock due to the strahl ». *Geophys. Res. Lett.* 38.14, L14105, p. L14105. DOI: [10.1029/2011GL048029](https://doi.org/10.1029/2011GL048029) (cit. on pp. 21, 22, 39, 75).
- Pulupa, M. P. et al. (2014a). « Core Electron Heating in Solar Wind Reconnection Exhausts ». *ApJL* 791.1, L17, p. L17. DOI: [10.1088/2041-8205/791/1/L17](https://doi.org/10.1088/2041-8205/791/1/L17) (cit. on p. 14).
- Pulupa, M. P. et al. (2014b). « Spin-modulated spacecraft floating potential: Observations and effects on electron moments ». *Journal of Geophysical Research (Space Physics)* 119.2, pp. 647–657. DOI: [10.1002/2013JA019359](https://doi.org/10.1002/2013JA019359) (cit. on p. 9).
- Pulupa, M. and Bale, S. D. (2008). « Structure on Interplanetary Shock Fronts: Type II Radio Burst Source Regions ». *ApJ* 676.2, pp. 1330–1337. DOI: [10.1086/526405](https://doi.org/10.1086/526405). arXiv: [0711.1028](https://arxiv.org/abs/0711.1028) [physics.space-ph] (cit. on pp. 20, 35, 39, 79, 94, 111).
- Pulupa, M. et al. (2017). « The Solar Probe Plus Radio Frequency Spectrometer: Measurement requirements, analog design, and digital signal processing ». *J. Geophys. Res.* 122.3, pp. 2836–2854. DOI: [10.1002/2016JA023345](https://doi.org/10.1002/2016JA023345) (cit. on pp. 30–34, 42, 44, 57, 60, 61).
- Pulupa, Marc Peter (2010). « Langmuir waves and electron acceleration at heliospheric shocks ». PhD thesis. University of California, Berkeley (cit. on pp. 16, 17).
- Pulupa, Marc et al. (2012). « STEREO measurements of electron acceleration beyond fast Fermi at the bow shock ». *arXiv e-prints*, arXiv:1202.3678, arXiv:1202.3678. arXiv: [1202.3678](https://arxiv.org/abs/1202.3678) [physics.space-ph] (cit. on pp. 21, 22, 75, 83).
- Pulupa, Marc et al. (2020). « Statistics and Polarization of Type III Radio Bursts Observed in the Inner Heliosphere ». *ApJS* 246.2, 49, p. 49. DOI: [10.3847/1538-4365/ab5dc0](https://doi.org/10.3847/1538-4365/ab5dc0). arXiv: [1912.03371](https://arxiv.org/abs/1912.03371) [astro-ph.SR] (cit. on pp. 25, 33, 35, 36, 60, 61, 106).
- Reid, Hamish Andrew Sinclair and Ratcliffe, Heather (2014). « A review of solar type III radio bursts ». *Research in Astronomy and Astrophysics* 14.7, pp. 773–804. DOI: [10.1088/1674-4527/14/7/003](https://doi.org/10.1088/1674-4527/14/7/003). arXiv: [1404.6117](https://arxiv.org/abs/1404.6117) [astro-ph.SR] (cit. on p. 35).
- Reiner, M. J. and MacDowall, R. J. (2015). « Electron Exciter Speeds Associated with Interplanetary Type III Solar Radio Bursts ». *SoPh* 290.10, pp. 2975–3004. DOI: [10.1007/s11207-015-0779-8](https://doi.org/10.1007/s11207-015-0779-8) (cit. on p. 35).
- Reiner, M. J. et al. (1996). « $2f_p$ radio emission from the vicinity of the Earth's foreshock: WIND observations ». *Geophys. Res. Lett.* 23.10, pp. 1247–1250. DOI: [10.1029/96GL00841](https://doi.org/10.1029/96GL00841) (cit. on pp. 22, 75).
- Reiner, M. J. et al. (2009). « Multipoint Observations of Solar Type III Radio Bursts from STEREO and Wind ». *SoPh* 259.1-2, 255, p. 255. DOI: [10.1007/s11207-009-9404-z](https://doi.org/10.1007/s11207-009-9404-z) (cit. on p. 35).
- Richardson, J. D. et al. (1996). « Statistical properties of the solar wind ». *AIP Conference Proceedings* 382.1, pp. 483–486. DOI: [10.1063/1.51433](https://doi.org/10.1063/1.51433). eprint: <https://aip.scitation.org/doi/pdf/10.1063/1.51433> (cit. on p. 47).
- Richardson, John D. (2013). « Voyager observations of the interaction of the heliosphere with the interstellar medium ». *Journal of Advanced Research* 4.3, pp. 229–233. DOI: [10.1016/j.jare.2012.09.002](https://doi.org/10.1016/j.jare.2012.09.002) (cit. on p. 6).
- Roelof, Edmond C. and Sibeck, David G. (1993). « Magnetopause shape as a bivariate function of interplanetary magnetic field B_z and solar wind dynamic pressure ». *J. Geophys. Res.* 98.A12, pp. 21421–21450. DOI: [10.1029/93JA02362](https://doi.org/10.1029/93JA02362) (cit. on p. 77).
- Rosenbauer, H. et al. (1977). « A survey on initial results of the HELIOS plasma experiment ». *Journal of Geophysics Zeitschrift Geophysik* 42.6, pp. 561–580 (cit. on pp. 7, 8).
- Rouillard, Alexis P. et al. (2020). « Relating Streamer Flows to Density and Magnetic Structures at the Parker Solar Probe ». *ApJS* 246.2, 37, p. 37. DOI: [10.3847/1538-4365/ab579a](https://doi.org/10.3847/1538-4365/ab579a). arXiv: [2001.01993](https://arxiv.org/abs/2001.01993) [astro-ph.SR] (cit. on p. 50).
- Russell, C. T. (2001). « Solar wind and interplanetary magnetic field: A tutorial ». *Washington DC American Geophysical Union Geophysical Monograph Series* 125, pp. 73–89. DOI: [10.1029/GM125p0073](https://doi.org/10.1029/GM125p0073) (cit. on p. 4).
- Šafránková, J. et al. (2007a). « Interaction of interplanetary shocks with the bow shock ». *Planet. Space Sci.* 55.15, pp. 2324–2329. DOI: [10.1016/j.pss.2007.05.012](https://doi.org/10.1016/j.pss.2007.05.012) (cit. on p. 75).

- Šafránková, J. et al. (2007b). « Modification of interplanetary shocks near the bow shock and through the magnetosheath ». *Journal of Geophysical Research (Space Physics)* 112.A8, A08212, A08212. DOI: [10.1029/2007JA012503](https://doi.org/10.1029/2007JA012503) (cit. on p. 75).
- Saito, S. and Umeda, T. (2011). « Suppression of Reflected Electrons by Kinetic Alfvén Turbulence in a Quasi-perpendicular Shock: Particle-in-cell Simulations ». *ApJ* 736.1, 35, p. 35. DOI: [10.1088/0004-637X/736/1/35](https://doi.org/10.1088/0004-637X/736/1/35) (cit. on p. 76).
- Salem, C. et al. (2001). « Determination of accurate solar wind electron parameters using particle detectors and radio wave receivers ». *J. Geophys. Res.* 106.A10, pp. 21701–21717. DOI: [10.1029/2001JA900031](https://doi.org/10.1029/2001JA900031) (cit. on pp. 24, 57, 79, 81, 94).
- Salem, C. et al. (2003). « Electron Properties and Coulomb Collisions in the Solar Wind at 1 AU: Wind Observations ». *ApJ* 585.2, pp. 1147–1157. DOI: [10.1086/346185](https://doi.org/10.1086/346185) (cit. on pp. 7–9, 16, 115).
- Salem, Chadi S. et al. (2021). « Precision Electron Measurements in the Solar Wind at 1 au from NASA’s Wind Spacecraft ». *arXiv e-prints*, arXiv:2107.08125, arXiv:2107.08125. arXiv: [2107.08125](https://arxiv.org/abs/2107.08125) [[physics.space-ph](https://arxiv.org/abs/2107.08125)] (cit. on pp. 9, 57).
- Savoini, P. and Lembege, B. (2009). « Sources of energetic backstreaming particles in the electron foreshock: 2D PIC simulation of a curved supercritical shock ». *AGU Fall Meeting Abstracts*. Vol. 2009, SH31A–1470 (cit. on pp. 21, 75).
- Savoini, Philippe and Lembège, Bertrand (2001). « Two-dimensional simulations of a curved shock: Self-consistent formation of the electron foreshock ». *J. Geophys. Res.* 106.A7, pp. 12975–12992. DOI: [10.1029/2001JA900007](https://doi.org/10.1029/2001JA900007) (cit. on pp. 21, 75).
- Schiff, M. L. (1970). « Impedance of a Short Dipole Antenna in a Warm Isotropic Plasma ». *Radio Science* 5.12, pp. 1489–1496. DOI: [10.1029/RS005i012p01489](https://doi.org/10.1029/RS005i012p01489) (cit. on p. 97).
- Schippers, P. et al. (2013). « Core electron temperature and density in the innermost Saturn’s magnetosphere from HF power spectra analysis on Cassini ». *Journal of Geophysical Research (Space Physics)* 118.11, pp. 7170–7180. DOI: [10.1002/2013JA019199](https://doi.org/10.1002/2013JA019199) (cit. on p. 57).
- Schubert, G. and Lichtenstein, B. R. (1974). « Observations of moon-plasma interactions by orbital and surface experiments. » *Reviews of Geophysics and Space Physics* 12, pp. 592–626. DOI: [10.1029/RG012i004p00592](https://doi.org/10.1029/RG012i004p00592) (cit. on p. 17).
- Schwadron, N. A. and McComas, D. J. (2003). « Solar Wind Scaling Law ». *ApJ* 599.2, pp. 1395–1403. DOI: [10.1086/379541](https://doi.org/10.1086/379541) (cit. on pp. 53, 109).
- Schwartz, S. J. (1977). « Cosmic ray generated anisotropic magnetohydrodynamic turbulence. » *MNRAS* 178, pp. 399–408. DOI: [10.1093/mnras/178.3.399](https://doi.org/10.1093/mnras/178.3.399) (cit. on p. 89).
- Schwenn, R. and Marsch, E. (1990). « Physics of the inner heliosphere. 1. Large-scale phenomena. » *Physics and Chemistry in Space* 20 (cit. on pp. 11, 42, 43, 51, 53, 109).
- Schwenn, R., Rosenbauer, H., and Miggenrieder, H. (1975). « Das Plasmaexperiment auf Helios (E1). » *Raumfahrtforschung* 19, pp. 226–232 (cit. on pp. 6, 42).
- Scokopke, N. et al. (1983). « Evolution of ion distributions across the nearly perpendicular bow shock - Specularly and non-specularly reflected-gyrating ions ». *J. Geophys. Res.* 88, pp. 6121–6136. DOI: [10.1029/JA088iA08p06121](https://doi.org/10.1029/JA088iA08p06121) (cit. on pp. 16, 89).
- Scudder, Jack D. (1992). « Why All Stars Should Possess Circumstellar Temperature Inversions ». *ApJ* 398, p. 319. DOI: [10.1086/171859](https://doi.org/10.1086/171859) (cit. on p. 4).
- Servidio, S. et al. (2009). « Magnetic Reconnection in Two-Dimensional Magnetohydrodynamic Turbulence ». *PhRvL* 102.11, 115003, p. 115003. DOI: [10.1103/PhysRevLett.102.115003](https://doi.org/10.1103/PhysRevLett.102.115003) (cit. on p. 14).
- Shaw, R. R. and Gurnett, D. A. (1975). « Electrostatic noise bands associated with the electron gyrofrequency and plasma frequency in the outer magnetosphere ». *J. Geophys. Res.* 80.31, p. 4259. DOI: [10.1029/JA080i031p04259](https://doi.org/10.1029/JA080i031p04259) (cit. on p. 24).
- Shen, Fang et al. (2018). « Three-dimensional MHD Simulation of Solar Wind Using a New Boundary Treatment: Comparison with In Situ Data at Earth ». *ApJ* 866.1, 18, p. 18. DOI: [10.3847/1538-4357/aad806](https://doi.org/10.3847/1538-4357/aad806) (cit. on pp. 53, 109).
- Shu, Frank H. (1992). *Physics of Astrophysics, Vol. II* (cit. on p. 15).
- Sibeck, D. G. et al. (1997). « A case study of oppositely propagating Alfvénic fluctuations in the solar wind and magnetosheath ». *Geophys. Res. Lett.* 24.24, pp. 3133–3136. DOI: [10.1029/97GL03263](https://doi.org/10.1029/97GL03263) (cit. on p. 89).

- Smith, E. J. and Wolfe, J. H. (1976). « Observations of interaction regions and corotating shocks between one and five AU: Pioneers 10 and 11 ». *Geophys. Res. Lett.* 3.3, pp. 137–140. DOI: [10.1029/GL003i003p00137](https://doi.org/10.1029/GL003i003p00137) (cit. on p. 16).
- Solanki, S. K., Livingston, W., and Ayres, T. (1994). « New Light on the Heart of Darkness of the Solar Chromosphere ». *Science* 263.5143, pp. 64–66. DOI: [10.1126/science.263.5143.64](https://doi.org/10.1126/science.263.5143.64) (cit. on p. 2).
- Sreenivasan, Katepalli R. (1999). « Fluid turbulence ». *Reviews of Modern Physics Supplement* 71.2, S383–S395. DOI: [10.1103/RevModPhys.71.S383](https://doi.org/10.1103/RevModPhys.71.S383) (cit. on p. 11).
- Steinberg, J. T. et al. (1996). « Differential flow between solar wind protons and alpha particles: First WIND observations ». *Geophys. Res. Lett.* 23.10, pp. 1183–1186. DOI: [10.1029/96GL00628](https://doi.org/10.1029/96GL00628) (cit. on pp. 54, 109).
- Stone, R. G. et al. (1992). « The Unified Radio and Plasma wave investigation ». *AGUAS* 92.2, pp. 291–316 (cit. on p. 34).
- Stone, Robert G. and Tsurutani, Bruce T. (1985). « Collisionless shocks in the heliosphere. A tutorial review. » *Washington DC American Geophysical Union Geophysical Monograph Series* 34. DOI: [10.1029/GM034](https://doi.org/10.1029/GM034) (cit. on p. 16).
- Sturrock, P. A. and Uchida, Y. (1981). « Coronal heating by stochastic magnetic pumping ». *ApJ* 246, pp. 331–336. DOI: [10.1086/158926](https://doi.org/10.1086/158926) (cit. on p. 11).
- Štverák, Štěpán., Trávníček, Pavel M., and Hellinger, Petr (2015). « Electron energetics in the expanding solar wind via Helios observations ». *Journal of Geophysical Research (Space Physics)* 120.10, pp. 8177–8193. DOI: [10.1002/2015JA021368](https://doi.org/10.1002/2015JA021368) (cit. on pp. 9, 56, 66, 68, 72, 110).
- Štverák, Štěpán et al. (2008). « Electron temperature anisotropy constraints in the solar wind ». *Journal of Geophysical Research (Space Physics)* 113.A3, A03103, A03103. DOI: [10.1029/2007JA012733](https://doi.org/10.1029/2007JA012733) (cit. on pp. 7–9, 115).
- Štverák, Štěpán et al. (2009). « Radial evolution of nonthermal electron populations in the low-latitude solar wind: Helios, Cluster, and Ulysses Observations ». *J. Geophys. Res.* 114.A5, A05104, A05104. DOI: [10.1029/2008JA013883](https://doi.org/10.1029/2008JA013883) (cit. on pp. 7–9, 44, 66, 68, 72).
- Szabo, Adam et al. (2020). « The Heliospheric Current Sheet in the Inner Heliosphere Observed by the Parker Solar Probe ». *ApJS* 246.2, 47, p. 47. DOI: [10.3847/1538-4365/ab5dac](https://doi.org/10.3847/1538-4365/ab5dac) (cit. on p. 50).
- Thomsen, M. F. et al. (1985). « Gyration ions and large-amplitude monochromatic MHD waves upstream of the earth's bow shock ». *J. Geophys. Res.* 90, pp. 267–273. DOI: [10.1029/JA090iA01p00267](https://doi.org/10.1029/JA090iA01p00267) (cit. on p. 89).
- Tobias, S. M. (2005). « The solar tachocline: Formation, stability and its role in the solar dynamo ». *Fluid Dynamics and Dynamos in Astrophysics and Geophysics*. Ed. by Andrew M. Soward et al., p. 193. DOI: [10.1201/9780203017692.ch7](https://doi.org/10.1201/9780203017692.ch7) (cit. on p. 2).
- Tokar, Robert L., Gary, S. Peter, and Quest, Kevin B. (1987). « Electron heating by ion acoustic turbulence in simulated low Mach number shocks ». *Physics of Fluids* 30.8, pp. 2569–2575. DOI: [10.1063/1.866095](https://doi.org/10.1063/1.866095) (cit. on p. 16).
- Totten, T. L., Freeman, J. W., and Arya, S. (1995). « An empirical determination of the polytropic index for the free-streaming solar wind using Helios 1 data ». *J. Geophys. Res.* 100.A1, pp. 13–18. DOI: [10.1029/94JA02420](https://doi.org/10.1029/94JA02420) (cit. on p. 56).
- Tsurutani, B. T. and Rodriguez, P. (1981). « Upstream waves and particles - An overview of ISEE results ». *J. Geophys. Res.* 86, p. 4317. DOI: [10.1029/JA086iA06p04317](https://doi.org/10.1029/JA086iA06p04317) (cit. on p. 21).
- Tsurutani, Bruce T. and Stone, Robert G. (1985). « Collisionless shocks in the heliosphere: Reviews of current research ». *Washington DC American Geophysical Union Geophysical Monograph Series* 35. DOI: [10.1029/GM035](https://doi.org/10.1029/GM035) (cit. on p. 16).
- Tu, C. -Y., Marsch, E., and Qin, Z. -R. (2004). « Dependence of the proton beam drift velocity on the proton core plasma beta in the solar wind ». *Journal of Geophysical Research (Space Physics)* 109.A5, A05101, A05101. DOI: [10.1029/2004JA010391](https://doi.org/10.1029/2004JA010391) (cit. on p. 6).
- Verscharen, Daniel, Klein, Kristopher G., and Maruca, Bennett A. (2019). « The multi-scale nature of the solar wind ». *Living Reviews in Solar Physics* 16.1, 5, p. 5. DOI: [10.1007/s41116-019-0021-0](https://doi.org/10.1007/s41116-019-0021-0). arXiv: [1902.03448](https://arxiv.org/abs/1902.03448) [physics.space-ph] (cit. on pp. 6–9).
- Viall, Nicholeen M. and Borovsky, Joseph E. (2020). « Nine Outstanding Questions of Solar Wind Physics ». *Journal of Geophysical Research (Space Physics)* 125.7, e26005, e26005. DOI: [10.1029/2018JA026005](https://doi.org/10.1029/2018JA026005) (cit. on p. 45).

- Vinas, A. F. and Scudder, J. D. (1986). « Fast and optimal solution to the “Rankine-Hugoniot problem” ». *J. Geophys. Res.* 91.A1, pp. 39–58. DOI: [10.1029/JA091iA01p00039](https://doi.org/10.1029/JA091iA01p00039) (cit. on p. 78).
- Voitcu, Gabriel et al. (2014). « Collisionless transport equations derived from a kinetic exospheric solar wind model with kappa velocity distribution functions ». *arXiv e-prints*, arXiv:1410.3597, arXiv:1410.3597. arXiv: [1410.3597](https://arxiv.org/abs/1410.3597) [[astro-ph.SR](#)] (cit. on p. 4).
- von Rosenvinge, T. T. et al. (1995). « The Energetic Particles: Acceleration, Composition, and Transport (EPACT) investigation on the WIND spacecraft ». *SSRv* 71, pp. 155–206. DOI: [10.1007/BF00751329](https://doi.org/10.1007/BF00751329) (cit. on p. 38).
- Vourlidis, Angelos et al. (2016). « The Wide-Field Imager for Solar Probe Plus (WISPR) ». *SSRv* 204.1-4, pp. 83–130. DOI: [10.1007/s11214-014-0114-y](https://doi.org/10.1007/s11214-014-0114-y) (cit. on pp. 29, 42).
- Wang, Linghua et al. (2015). « Solar Wind ~20-200 keV Superhalo Electrons at Quiet Times ». *ApJL* 803.1, L2, p. L2. DOI: [10.1088/2041-8205/803/1/L2](https://doi.org/10.1088/2041-8205/803/1/L2) (cit. on pp. 9, 20, 22, 39, 76).
- Wang, Shan et al. (2019). « Observational Evidence of Magnetic Reconnection in the Terrestrial Bow Shock Transition Region ». *Geophys. Res. Lett.* 46.2, pp. 562–570. DOI: [10.1029/2018GL080944](https://doi.org/10.1029/2018GL080944). arXiv: [1812.09337](https://arxiv.org/abs/1812.09337) [[physics.space-ph](#)] (cit. on p. 14).
- Wang, Y. -M. (2010). « On the Relative Constancy of the Solar Wind Mass Flux at 1 AU ». *ApJL* 715.2, pp. L121–L127. DOI: [10.1088/2041-8205/715/2/L121](https://doi.org/10.1088/2041-8205/715/2/L121) (cit. on pp. 69, 72, 110).
- Wang, Y. -M. and Sheeley N. R., Jr. (1990). « Solar Wind Speed and Coronal Flux-Tube Expansion ». *ApJ* 355, p. 726. DOI: [10.1086/168805](https://doi.org/10.1086/168805) (cit. on p. 69).
- Wang, Y. X. et al. (2020). « MHD Modeling of the Background Solar Wind in the Inner Heliosphere From 0.1 to 5.5 AU: Comparison With In Situ Observations ». *Space Weather* 18.6, e02262, e02262. DOI: [10.1029/2019SW002262](https://doi.org/10.1029/2019SW002262) (cit. on pp. 53, 109).
- Wei, Wenwen et al. (2022). « Energy Spectra Variations of Energetic Ions Associated with A Stream Interaction Region ». *J. Geophys. Res.* 239.1-2, pp. 337–392. DOI: [10.1029/2022JA030652](https://doi.org/10.1029/2022JA030652) (cit. on p. 17).
- Wenzel, K. P. et al. (1992). « The ULYSSES Mission ». *A&AS* 92, p. 207 (cit. on p. 42).
- Whitham, G. B. (1999). « Linear and Nonlinear Waves ». *Wiley Book*. Vol. 1999. DOI: [10.1002/9781118032954](https://doi.org/10.1002/9781118032954) (cit. on p. 15).
- Whittlesey, Phyllis L. et al. (2020). « The Solar Probe ANalyzers—Electrons on the Parker Solar Probe ». *ApJS* 246.2, p. 74. DOI: [10.3847/1538-4365/ab7370](https://doi.org/10.3847/1538-4365/ab7370) (cit. on pp. 30, 31, 42, 43, 57, 64).
- Wilson Lynn B., III et al. (2018). « The Statistical Properties of Solar Wind Temperature Parameters Near 1 au ». *ApJS* 236.2, 41, p. 41. DOI: [10.3847/1538-4365/aab71c](https://doi.org/10.3847/1538-4365/aab71c). arXiv: [1802.08585](https://arxiv.org/abs/1802.08585) [[physics.plasm-ph](#)] (cit. on pp. 67, 71, 110).
- Wilson Lynn B., III et al. (2021). « A Quarter Century of Wind Spacecraft Discoveries ». *Reviews of Geophysics* 59.2, e2020RG000714. DOI: [10.1029/2020RG000714](https://doi.org/10.1029/2020RG000714) (cit. on pp. 37, 76).
- Wilson Lynn Bruce, III (2010). « The microphysics of collisionless shocks ». PhD thesis. University of Minnesota, Twin Cities (cit. on pp. 16, 18).
- Wilson, L. B. (2016). « Low Frequency Waves at and Upstream of Collisionless Shocks ». *Washington DC American Geophysical Union Geophysical Monograph Series* 216, pp. 269–291. DOI: [10.1002/9781119055006.ch16](https://doi.org/10.1002/9781119055006.ch16) (cit. on pp. 20–22, 27, 75, 76).
- Wilson III, L. B. et al. (2007). « Waves in Interplanetary Shocks: A Wind/WAVES Study ». *PhRvL* 99.4, 041101, p. 041101. DOI: [10.1103/PhysRevLett.99.041101](https://doi.org/10.1103/PhysRevLett.99.041101) (cit. on pp. 18, 20, 39, 91, 111).
- Wilson III, L. B. et al. (2009). « Low-frequency whistler waves and shocklets observed at quasi-perpendicular interplanetary shocks ». *J. Geophys. Res.* 114, A10106, A10106. DOI: [10.1029/2009JA014376](https://doi.org/10.1029/2009JA014376) (cit. on pp. 20, 39, 86).
- Wilson III, L. B. et al. (2012). « Observations of electromagnetic whistler precursors at supercritical interplanetary shocks ». *Geophys. Res. Lett.* 39, L08109, p. L08109. DOI: [10.1029/2012GL051581](https://doi.org/10.1029/2012GL051581) (cit. on pp. 39, 85, 89, 91, 112).
- Wilson III, L. B. et al. (2017). « Revisiting the structure of low-Mach number, low-beta, quasi-perpendicular shocks ». *J. Geophys. Res.* 122, pp. 9115–9133. DOI: [10.1002/2017JA024352](https://doi.org/10.1002/2017JA024352) (cit. on pp. 39, 84, 85).
- Wilson, L. B. et al. (2013). « Shocklets, SLAMS, and field-aligned ion beams in the terrestrial foreshock ». *Journal of Geophysical Research (Space Physics)* 118.3, pp. 957–966. DOI: [10.1029/2012JA018186](https://doi.org/10.1029/2012JA018186). arXiv: [1207.5561](https://arxiv.org/abs/1207.5561) [[physics.space-ph](#)] (cit. on pp. 20, 39).

- Wilson, L. B. et al. (2016). « Relativistic Electrons Produced by Foreshock Disturbances Observed Upstream of Earth's Bow Shock ». *PhRvL* 117.21, 215101, p. 215101. DOI: [10.1103/PhysRevLett.117.215101](https://doi.org/10.1103/PhysRevLett.117.215101). arXiv: [1607.02183](https://arxiv.org/abs/1607.02183) [[physics.space-ph](#)] (cit. on p. 31).
- Woodham, L. D. et al. (2021). « Enhanced proton parallel temperature inside patches of switchbacks in the inner heliosphere ». *A&A* 650, L1, p. L1. DOI: [10.1051/0004-6361/202039415](https://doi.org/10.1051/0004-6361/202039415). arXiv: [2010.10379](https://arxiv.org/abs/2010.10379) [[astro-ph.SR](#)] (cit. on p. 68).
- Woolfson, M. (2000). « The origin and evolution of the solar system ». *Astronomy and Geophysics* 41.1, p. 12. DOI: [10.1046/j.1468-4004.2000.00012.x](https://doi.org/10.1046/j.1468-4004.2000.00012.x) (cit. on p. 2).
- Wu, C. C. (1990). « Formation, structure, and stability of MHD intermediate shocks ». *J. Geophys. Res.* 95.A6, pp. 8149–8175. DOI: [10.1029/JA095iA06p08149](https://doi.org/10.1029/JA095iA06p08149) (cit. on p. 16).
- Wu, C. S. (1982). « Physical mechanisms for turbulent dissipation in collisionless shock waves. » *SSRv* 32.1-2, pp. 83–97. DOI: [10.1007/BF00225178](https://doi.org/10.1007/BF00225178) (cit. on p. 16).
- Wüest, Martin, Evans, David S., and von Steiger, Rudolf (2007). *Calibration of Particle Instruments in Space Physics* (cit. on p. 31).
- Yang, Liu et al. (2015). « The Angular Distribution of Solar Wind Superhalo Electrons at Quiet Times ». *ApJL* 811.1, L8, p. L8. DOI: [10.1088/2041-8205/811/1/L8](https://doi.org/10.1088/2041-8205/811/1/L8) (cit. on pp. 9, 17).
- Yang, Z. W., Lembège, B., and Lu, Q. M. (2012). « Impact of the rippling of a perpendicular shock front on ion dynamics ». *Journal of Geophysical Research (Space Physics)* 117.A7, A07222, A07222. DOI: [10.1029/2011JA017211](https://doi.org/10.1029/2011JA017211) (cit. on p. 76).
- Yang, Zhongwei et al. (2013). « Magnetic ramp scale at supercritical perpendicular collisionless shocks: Full particle electromagnetic simulations ». *Physics of Plasmas* 20.9, 092116, p. 092116. DOI: [10.1063/1.4821825](https://doi.org/10.1063/1.4821825) (cit. on p. 16).
- Yang, Zhongwei et al. (2018). « Impact of Shock Front Rippling and Self-reformation on the Electron Dynamics at Low-Mach-number Shocks ». *ApJ* 857.1, 36, p. 36. DOI: [10.3847/1538-4357/aab714](https://doi.org/10.3847/1538-4357/aab714) (cit. on p. 76).
- Yang, Zhongwei et al. (2020a). « MMS Direct Observations of Kinetic-scale Shock Self-reformation ». *ApJL* 901.1, L6, p. L6. DOI: [10.3847/2041-8213/abb3ff](https://doi.org/10.3847/2041-8213/abb3ff). arXiv: [2108.10856](https://arxiv.org/abs/2108.10856) [[physics.space-ph](#)] (cit. on pp. 16, 17).
- Yang, Zhongwei et al. (2020b). « PIC Simulations of Microinstabilities and Waves at Near-Sun Solar Wind Perpendicular Shocks: Predictions for Parker Solar Probe and Solar Orbiter ». *ApJL* 900.2, L24, p. L24. DOI: [10.3847/2041-8213/abaf59](https://doi.org/10.3847/2041-8213/abaf59). arXiv: [2008.06820](https://arxiv.org/abs/2008.06820) [[physics.space-ph](#)] (cit. on p. 16).
- Yao, Shuo et al. (2013). « Small-scale Pressure-balanced Structures Driven by Oblique Slow Mode Waves Measured in the Solar Wind ». *ApJ* 774.1, 59, p. 59. DOI: [10.1088/0004-637X/774/1/59](https://doi.org/10.1088/0004-637X/774/1/59) (cit. on p. 86).
- Yoon, Peter H. et al. (1994). « Theory of 2 ω_{pe} radiation induced by the bow shock ». *J. Geophys. Res.* 99.A12, pp. 23, 481–23, 488. DOI: [10.1029/94JA02489](https://doi.org/10.1029/94JA02489) (cit. on pp. 22, 75).
- Yu, Chunkai et al. (2022). « Electron Acceleration by Moderate-Mach-number Low- β Shocks: Particle-in-Cell Simulations ». *ApJ* 930.2, 155, p. 155. DOI: [10.3847/1538-4357/ac67df](https://doi.org/10.3847/1538-4357/ac67df) (cit. on p. 111).
- Zank, G. P. and Matthaeus, W. H. (1993). « Nearly incompressible fluids. II: Magnetohydrodynamics, turbulence, and waves ». *Physics of Fluids A* 5.1, pp. 257–273. DOI: [10.1063/1.858780](https://doi.org/10.1063/1.858780) (cit. on p. 14).
- Zank, G. P. et al. (2003). « The interaction of turbulence with shock waves ». *Solar Wind Ten*. Ed. by Marco Velli et al. Vol. 679. American Institute of Physics Conference Series, pp. 417–420. DOI: [10.1063/1.1618625](https://doi.org/10.1063/1.1618625) (cit. on p. 14).
- Zank, G. P. et al. (2006). « Particle acceleration at perpendicular shock waves: Model and observations ». *Journal of Geophysical Research (Space Physics)* 111.A6, A06108, A06108. DOI: [10.1029/2005JA011524](https://doi.org/10.1029/2005JA011524) (cit. on p. 14).
- Zarka, P., Cecconi, B., and Kurth, W. S. (2004). « Jupiter's low-frequency radio spectrum from Cassini/Radio and Plasma Wave Science (RPWS) absolute flux density measurements ». *J. Geophys. Res.* 109.A9, A09S15, A09S15. DOI: [10.1029/2003JA010260](https://doi.org/10.1029/2003JA010260) (cit. on p. 34).
- Zaslavsky, A. et al. (2011). « On the antenna calibration of space radio instruments using the galactic background: General formulas and application to STEREO/WAVES ». *Radio Science* 46.2, RS2008, RS2008. DOI: [10.1029/2010RS004464](https://doi.org/10.1029/2010RS004464) (cit. on pp. 34, 59–61, 101).
- Zaslavsky, A. et al. (2012). « Interplanetary dust detection by radio antennas: Mass calibration and fluxes measured by STEREO/WAVES ». *Journal of Geophysical Research (Space Physics)* 117.A5, A05102, A05102. DOI: [10.1029/2011JA017480](https://doi.org/10.1029/2011JA017480) (cit. on p. 36).

- Zhao, L. -L. et al. (2020). « Identification of Magnetic Flux Ropes from Parker Solar Probe Observations during the First Encounter ». *ApJS* 246.2, 26, p. 26. DOI: [10.3847/1538-4365/ab4ff1](https://doi.org/10.3847/1538-4365/ab4ff1). arXiv: [1912.02349](https://arxiv.org/abs/1912.02349) [[physics.space-ph](#)] (cit. on pp. 50, 65).
- Zhao, S. Q. et al. (2019a). « Observation of a Large-Amplitude Slow Magnetosonic Wave in the Magnetosheath ». *Journal of Geophysical Research (Space Physics)* 124.12, pp. 10, 200–10, 208. DOI: [10.1029/2019JA026924](https://doi.org/10.1029/2019JA026924) (cit. on p. 88).
- Zhao, S. Q. et al. (2021a). « Analysis of Magnetohydrodynamic Perturbations in the Radial-field Solar Wind from Parker Solar Probe Observations ». *ApJ* 923.2, 253, p. 253. DOI: [10.3847/1538-4357/ac2ffe](https://doi.org/10.3847/1538-4357/ac2ffe). arXiv: [2106.03807](https://arxiv.org/abs/2106.03807) [[astro-ph.SR](#)] (cit. on pp. 14, 36, 57, 86, 92, 112).
- Zhao, S. Q. et al. (2021b). « Observations of an Electron-Cold Ion Component Reconnection at the Edge of an Ion-Scale Antiparallel Reconnection at the Dayside Magnetopause ». *Journal of Geophysical Research (Space Physics)* 126.10, e29390, e29390. DOI: [10.1029/2021JA029390](https://doi.org/10.1029/2021JA029390). arXiv: [2109.10943](https://arxiv.org/abs/2109.10943) [[physics.space-ph](#)] (cit. on p. 14).
- Zhao, S. Q. et al. (2021c). « Observations of the Beam Driven Whistler Mode Waves in the Magnetic Reconnection Region at the Dayside Magnetopause ». *Journal of Geophysical Research (Space Physics)* 126.2, e28525, e28525. DOI: [10.1029/2020JA028525](https://doi.org/10.1029/2020JA028525) (cit. on pp. 14, 83).
- Zhao, S. Q. et al. (2022). « Multi-spacecraft Analysis of the Properties of Magnetohydrodynamic Fluctuations in Sub-Alfvénic Solar Wind Turbulence at 1 AU ». *arXiv e-prints*, arXiv:2204.05410, arXiv:2204.05410. arXiv: [2204.05410](https://arxiv.org/abs/2204.05410) [[astro-ph.SR](#)] (cit. on p. 14).
- Zhao, Xiaowei et al. (2017). « Propagation Characteristics of Two Coronal Mass Ejections from the Sun Far into Interplanetary Space ». *ApJ* 837.1, 4, p. 4. DOI: [10.3847/1538-4357/aa5ea3](https://doi.org/10.3847/1538-4357/aa5ea3). arXiv: [1702.04122](https://arxiv.org/abs/1702.04122) [[astro-ph.SR](#)] (cit. on p. 35).
- (2019b). « Quantifying the Propagation of Fast Coronal Mass Ejections from the Sun to Interplanetary Space by Combining Remote Sensing and Multi-point In Situ Observations ». *ApJ* 882.2, 122, p. 122. DOI: [10.3847/1538-4357/ab379b](https://doi.org/10.3847/1538-4357/ab379b). arXiv: [1908.04450](https://arxiv.org/abs/1908.04450) [[astro-ph.SR](#)] (cit. on pp. 17, 35, 75).
- Zhou, Zilu et al. (2022). « PSP Observations of a Slow Shock Pair Bounding a Large-Scale Plasmoid/Macro Magnetic Hole ». *Geophys. Res. Lett.* 49.6, e97564, e97564. DOI: [10.1029/2021GL097564](https://doi.org/10.1029/2021GL097564) (cit. on p. 65).
- Zouganelis, I. (2008). « Measuring suprathermal electron parameters in space plasmas: Implementation of the quasi-thermal noise spectroscopy with kappa distributions using in situ Ulysses/URAP radio measurements in the solar wind ». *Journal of Geophysical Research (Space Physics)* 113.A8, A08111, A08111. DOI: [10.1029/2007JA012979](https://doi.org/10.1029/2007JA012979) (cit. on p. 113).
- Zouganelis, I. et al. (2004). « A Transonic Collisionless Model of the Solar Wind ». *ApJ* 606.1, pp. 542–554. DOI: [10.1086/382866](https://doi.org/10.1086/382866). arXiv: [astro-ph/0402358](https://arxiv.org/abs/astro-ph/0402358) [[astro-ph](#)] (cit. on pp. 4, 56, 67, 71, 110).

Résumé

Le transport d'énergie dans la couronne et le vent solaires, qui n'est pas complètement compris, joue un rôle clé dans le chauffage de la couronne et l'accélération du vent. En raison de leur faible masse par rapport aux ions, les électrons dominent l'expansion thermique du vent solaire. Pour dériver leurs propriétés, la technique du bruit quasi-thermique (QTN) est un outil fiable : elle permet d'obtenir des mesures précises des paramètres des électrons dans le vent solaire, en particulier la densité électronique totale, sans aucun étalonnage. La technique QTN permet donc des vérifications croisées en routine pour les détecteurs de particules traditionnels. La sonde solaire Parker Solar Probe (PSP), en cours d'exploitation, dont les distances héliocentriques des périhélie de l'orbite passent de 35.7 rayons solaires (R_\odot) à 9.86 R_\odot en l'espace de cinq ans, offre une opportunité inédite d'examiner les propriétés du vent solaire au plus près du Soleil.

Tout d'abord, en utilisant les paramètres des électrons obtenus par la technique simplifiée du QTN et les paramètres des protons déduits des "coupes" de Faraday, nous avons étudié le flux d'énergie du vent solaire aussi près du Soleil que 27.8 R_\odot . Nous avons obtenu une valeur moyenne du flux d'énergie similaire aux résultats précédents basés sur des observations à long terme à de plus grandes distances et à diverses latitudes, ce qui confirme que cette quantité apparaît comme une constante solaire globale. De plus, les distributions normalisées du flux d'énergie sont presque symétriques et bien ajustées par des gaussiennes, ce qui implique des interactions limitées entre le vent solaire et les structures transitoires du plasma dans l'héliosphère interne.

Ensuite, nous avons examiné l'évolution radiale de la température totale des électrons (T_e), déduite de la technique du QTN en utilisant la partie haute fréquence des spectres radio, avec la distance héliocentrique variant d'environ 13 à 60 R_\odot . Nous obtenons que T_e décroît avec la distance comme $\sim R^{-0.66}$, qui est une variation beaucoup plus lente qu'un comportement adiabatique. La température T_e , basée sur les observations PSP, est cohérente avec la prédiction du modèle de vent solaire exosphérique extrapolé à 10 R_\odot , ainsi qu'aux observations Helios à 0.3 UA et aux observations de Wind à 1 UA, respectivement. De plus, lorsque le vent solaire est plus lent (ou dans un tube de flux avec un flux de masse plus important), les profils radiaux de V_p-T_e sont plus raides. Une anticorrélation plus prononcée de V_p-T_e est observée lorsque le vent solaire est plus lent et plus proche du Soleil. En complément, nous avons créé une base de données de spectres affectés par les ondes de Langmuir et/ou les émissions électromagnétiques, qui peut être utilisée pour une analyse plus approfondie et sera aussi utile pour un ajustement

en routine sur la totalité du spectre QTN dans le vent solaire.

En plus des propriétés du vent solaire, nous avons étudié un choc interplanétaire (IP) quasi-perpendiculaire supercritique, interagissant avec le pré-choc terrestre. De nouvelles caractéristiques sur les activités des ondes et la dynamique des particules, résultant de l'interaction choc-foreshock, ont été identifiées: (1) Des sursauts d'ondes de Langmuir intenses sont détectées en aval du choc IP, ce qui coïncide avec le fait que les faisceaux d'électrons pénétrant dans le pré-choc terrestre sont accélérés parallèlement au champ magnétique vers l'aval. (2) Le choc IP interagit avec les ondes/fluctuations d'Alfvén en amont, et est associé à un faisceau d'ions réfléchis en giration, d'intensité atypique par rapport à d'autres événements présentant des paramètres de choc similaires. Ces résultats soulèvent des questions et nécessitent des études supplémentaires concernant l'accélération des particules (par exemple par des whistlers précurseurs) et l'interaction choc-ondes d'Alfvén.

Mots clés : Parker Solar Probe, bruit quasi-thermique, vent solaire, chauffage et accélération, choc, ondes

Abstract

Heat transport in the solar corona and wind, which is not completely understood, plays a key role in corona heating and wind acceleration. Due to their small mass compared to ions, electrons dominate the thermally driven solar wind expansion. To derive their properties, the Quasi-thermal noise (QTN) technique is a reliable tool: it yields accurate measurements of the electron parameters in the solar wind especially the total electron density without any calibration. The QTN technique thus provides routine cross checking for traditional particle detectors. The ongoing pioneering Parker Solar Probe (PSP), whose heliocentric distances of orbit perihelia decrease from 35.7 solar radii (R_\odot) to 9.86 R_\odot within five years, offers an opportunity to examine the solar wind properties closer to the Sun than previously detected.

First, based on electron parameters obtained from the simplified QTN technique and the bulk proton parameters by Faraday Cups, we investigate the solar wind energy flux as close to the Sun as 27.8 R_\odot . We obtain that the averaged energy flux value is similar to the previous results based on long-term observations at greater distances and various latitudes, which confirms that this quantity appears as a global solar constant. Furthermore, the normalized energy flux distributions are nearly symmetrical and well fitted by Gaussians, implying the limited interactions between solar wind and transient plasma structures in the inner heliosphere.

Then, we examine the radial evolution of the total electron temperature (T_e), derived from the QTN technique using the high frequency part of the radio spectrum, with the heliocentric distance varying from about 13 to 60 R_\odot . We obtain that T_e decreases with the distance as $\sim R^{-0.66}$, which is much slower than an adiabatic behavior. The extrapolated T_e is consistent with the exospheric solar wind model prediction at around 10 R_\odot , Helios observations at 0.3 AU and Wind observations at 1 AU, respectively. Furthermore, when the solar wind is slower (or in flux tube with larger mass flux), the radial T_e profiles are steeper. More pronounced anticorrelated V_p-T_e is observed when the solar wind is slower and closer to the Sun. As a byproduct, we derive a database of spectra affected by bursty Langmuir waves and/or electromagnetic emissions, which will be useful for further analysis and routine full fit on the QTN spectra.

In addition to the solar wind properties, we study a supercritical quasi-perpendicular interplanetary (IP) shock interacting with the terrestrial foreshock via Wind observations. Some new features of wave activities and particle dynamics, resulting from the shock-foreshock interaction, are identified: (1) Intensive bursty Langmuir waves are detected downstream of the IP shock,

coninciding with that the penetrating terrestrial foreshock electron beams are accelerated parallel to the magnetic field toward downstream. (2) The IP shock is interacting with the upstream Alfvén waves/fluctuations, and associated with atypically intensive beam-like gyrating-reflected ions compared to other events with similar shock parameters. These findings raise questions and trigger further investigations regarding particle acceleration (i.e. through precursor whistlers) and interaction between a shock and Alfvén waves.

Keywords : Parker Solar Probe, Quasi-thermal noise, Solar Wind, heating and acceleration, Shock, Waves

